UNIVERSITY OF
COPENHAGEN

Photonic Quantum Information Processing with Quantum Dot Single-Photon Sources

Patrik Isene Sund

December 8, 2023

PhD Thesis

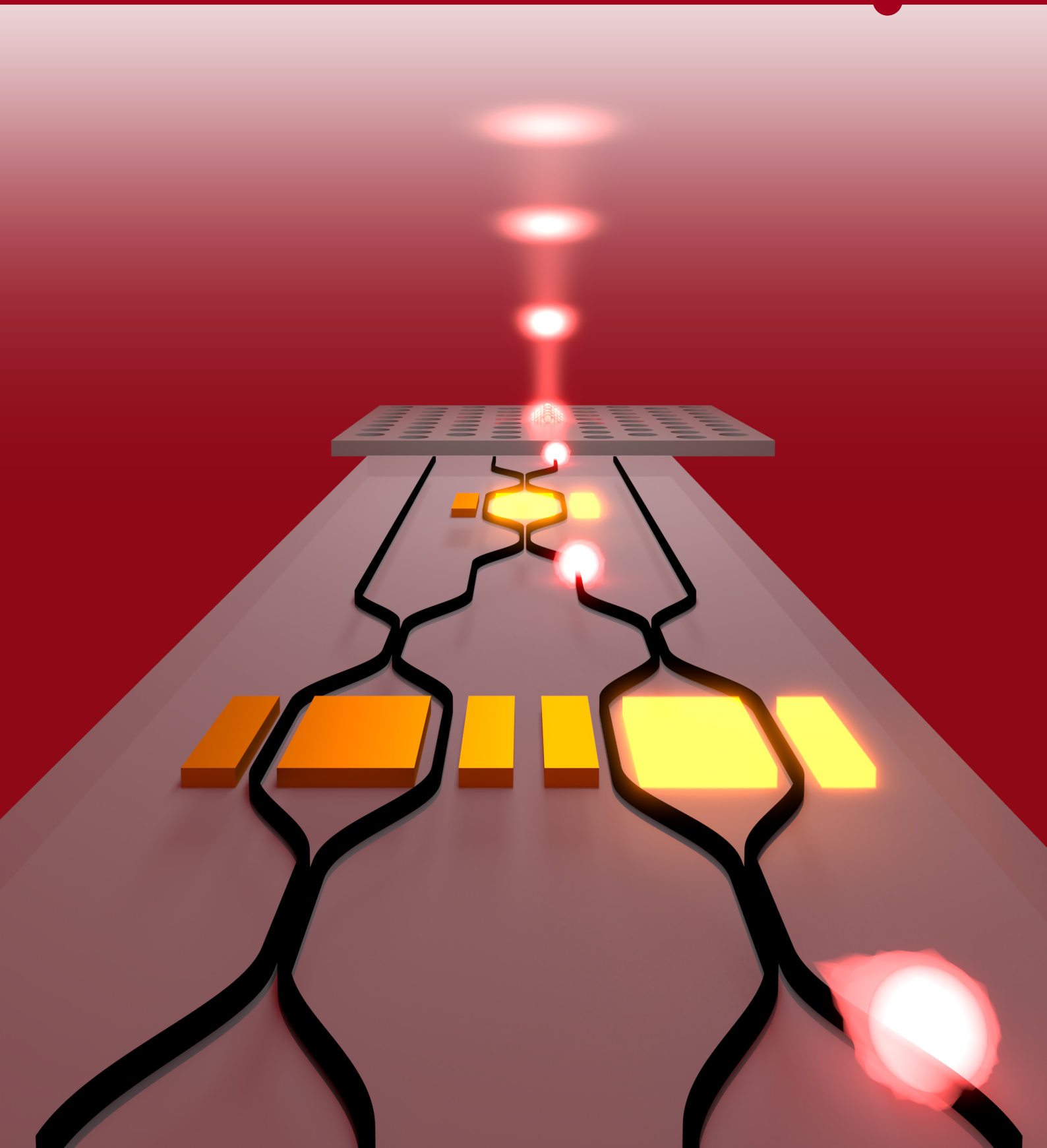

Professor Peter LODAHL Assistant Professor Stefano PAESANI

Photonic quantum information processing with quantum dot single-photon sources

Patrik ISENE SUND

UNIVERSITY OF
COPENHAGEN

Quantum Photonics
Center for Hybrid Quantum Networks
The Niels Bohr Institute

This thesis has been submitted to
the PhD School of The Faculty of Science
University of Copenhagen

December 8, 2023

Abstract

The fundamentally quantum mechanical properties of single photons present an exciting opportunity for the development of new technology. The fragile nature of quantum states makes this a challenging prospect, pressing stringent demands on the hardware used to generate and process the light. In this context, semiconductor quantum dots are emerging as a promising platform, enabling the realization of highly-efficient sources of near-identical single photons. In this thesis, we aim to expand the capabilities offered by these sources and state-of-the-art photonic technology. We present novel specialized interferometer architectures developed for the time-bin encoding naturally produced by quantum-dot single-photon sources (SPSs), that allow for significant reductions in loss. We proceed to leverage the advantageous properties of the time-bin encoding by constructing a resource-efficient interferometer used in an experimental demonstration of bosonic suppression laws and postselected entanglement using photons emitted from a quantum-dot SPS. Shifting the focus to photonic integrated circuits, we design a lithium-niobate-on-insulator (LNOI) chip tailored to the emission wavelength of our quantum dots. We perform two-photon interference experiments on two-mode and four-mode interferometers, carrying out the first demonstration of the Hong–Ou–Mandel effect on LNOI. Furthermore, we leverage the fast electro-optic modulators on LNOI to realize an on-chip demultiplexer, which is used to demonstrate active demultiplexing of the single-photon source. Finally, we extend the scope to larger scales by analyzing the hardware requirements for a quantum advantage demonstrations using the boson sampling algorithm with photons emitted from a quantum-dot SPS, determining it to be within reach for current state-of-the-art hardware.

Sammenfatning

Enkelt-fotoners fundamentale kvantemekaniske egenskaber præsenterer spænende muligheder for udvikling af ny teknologi. Kvantemekaniske tilstandes skrøbelige natur angiver udsigterne som udfordrende, og hardwaren brugt til at generere og behandle lyset skal derfor være meget effektiv. Her udviser halvledende kvanteøer et lovende potentiale for at lave nærideelle enkeltfotonskilder (EFKer). I denne afhandling tager vi sigte på at uddybe kapabiliteterne til EFKer og den nyeste kvantefotoniske teknologi. Vi præsenterer dugfriske specialiserede interferometerarkitekturer udviklet til den tidsbøtte-indkoding EFKer naturlig producerer, der fører til store reduktioner i tab af lys. Derefter benytter vi tidsbøtte-indkodningens gavnlige egenskaber for at konstruere et ressource-effektivt interferometer benyttet i en eksperimentel demonstration af bosonisk undertrykkelse og efterudvalgt kvantesammenfiltring med fotoner lavet af en kvanteø-EFK. Vi skifter dernæst fokus til fotoniske integrerede kredsløb på en lithium-niobat-på-isolator-chip (LNPI-chip) specielt designet til den bølgelængde som fotonerne udsendt fra kvanteørne har. Vi udfører to-foton-interferens-eksperimenter i et toarmede og firearmede interferometere, og laver så den første demonstration af Hong–Ou–Mandel-effekten i LNPI. Videre benytter vi de hurtige elektro-optiske modulatorer på LNPI for at realisere en on-chip demultiplekser der bruges til at demonstrere demultipleksering af en EFK. Til slut udvider vi omfanget til større skalaer ved at analysere hardware-krav for en demonstration af quantum advantage ved boson sampling af en kvanteø-EFK, og bestemmer at det er opnåeligt med nutidens bedste hardware.

Acknowledgements

Throughout my PhD, I have had had an amazing set of supervisors who have contributed greatly to my scientific and personal development. I would like to thank Peter Lodahl for giving me the opportunity to work on this exciting project, and for giving me valuable feedback at critical times. I want to thank Jacques Carolan, an amazing science communicator, for his encouraging guidance that extended well-after he left the group. I would also like to thank Ravitej Uppu, who drew upon his vast knowledge on all things photonic to guide my early work and for continuing to supervise me even after starting up his own group in Iowa. Finally, I am incredible grateful to the great Stefano Paesani, my day-to-day supervisor for most of the project, for the tremendous amount of knowledge and inspiration he has imparted during my time in Copenhagen.

My work and life as a PhD student has been shaped by a large number of people. First and foremost, many hours both in and out of the lab have been filled with discussions and help from former and current members of the quantum photonics group at NBI, including Leonardo, Alexey, Hanna, Xiaoyan, Liu, Camille, Martin, Ying, Atefeh, Ming-Lai, Freja, Nils, Arianne, Carlos, Celeste, Mikkel, Adam, Vasso, Bea, Yijian, Shikai, Sjaak, Rodrigo, Laurits. Hania, Kasper, Pratyush, Yu, Marcus, Nikolaos, Thomas, Christian, and Arnulf. I am especially grateful to Martin, Freja, Rodrigo, Nils, Bea, Carlos, Kasper, and Ying for giving me valuable assistance in the lab.

A lot of my time has been spent in the office, where I have been surrounded by a great group of people, including Björn, Erics Planz and Langman, Atefeh, Stefan, Felix, Sho, Carlos, and Hania. A special shoutout goes to Sho and Hania for supplying me with boosts of motivation in the form of chocolate during the critical last month of writing.

The three months I spent in Bristol with all the good people at QET Labs has filled my heart with fond memories. I am especially grateful to Anthony, Imogen, Owain, Naomi, Tom, Reece, Ed, and Patrick for welcoming me into the Laing gaing, and to Frazer for assisting me with incredible wirebonding precision.

I have also had the pleasure of collaborating with great people outside of NBI. Special thanks go to Francesco and Emma, who fabricated amazing lithium niobate chips. The week you came to visit in Copenhagen was one of the most fun, hectic, and scientifically rewarding weeks of my PhD.

I am especially grateful to Carlos, Kasper, Ying, Eric, Evi, and Ed for giving me valuable feedback during the writing process.

I would like to thank everyone at HyQ and the quantum optics section for creating a warm and welcoming environment. Special thanks to: Vasso,

for all of the thought-provoking conversations, and for the unique and exciting experiences we have shared. I couldn't have asked for a better PhD-twin! Carlos, for bringing quantum wonder and excitement into our office, and for being a great travel companion. Kasper, a world-class Lancier coach who picks up on new things entirely too quickly, with whom I've spent countless hours in the lab turning mirror knobs. Ying, for being an endless source of quantum-dot know-how, encouragement, and positivity. Marcus, for engaging me with equal-parts technical and whimsical discourse. Eric, who has an endless capacity for every kind of conversation, for the all of the good times both in and outside of Denmark, and for encouraging me to chase down rabbit holes. Milena, who enriched my life by decorating my monitor and the coffee machine, and by introducing me to One Piece. Julian, for the amazing photo shoot and for cooking up some seriously good pancakes. Sho, for tons of scientific discussions and for laughing at my bad Japanese puns. Felix, for bringing amazing board games into my life. Tesa, for your tireless contributions to improving our working environment, and for reminding me that I can always do two more pull-ups. Aida, for the great times, great pastries and great conversations. Oliver, for our many lengthy and sprawling discussions, both related and unrelated to science. Evi, for sharing with me a love of music and board games, and for almost convincing me that orthography is sensible. Ed, for being an amazing lab partner, and bringing great craic wherever you go.

Sist men ikke minst vil jeg takke Mai Ve, som gjør all mine gode opplevelser bedre, og alltid er der for meg når jeg trenger det.

The last three years have been filled with challenging, at times frustrating, but mostly rewarding work, and inspiring discussions and conversations (and thousands of pullups) with wonderful colleagues in an open and welcoming environment. As the journey comes to an end, I am filled with a sense of happiness and gratitude.

Patrik Isene Sund,
8th of December 2023
Copenhagen

List of publications

The main projects that were developed as part of this thesis resulted in the following publications, listed in chronological order.

Journal publications

A P.I. Sund, E. Lomonte, S. Paesani, Y. Wang, J. Carolan, N. Bart, A. D. Wieck, A. Ludwig, L. Midolo, W. H. P. Pernice, P. Lodahl, & F. Lenzini **"High-speed thin-film lithium niobate quantum processor driven by a solid-state quantum emitter "** Science Advances Vol 9 Issue 19 (2023)

B P.I. Sund, R. Uppu, S. Paesani, & P. Lodahl **"Hardware requirements for realizing a quantum advantage with deterministic single-photon sources "** arXiv:2310.10185

Conference publications

C P.I. Sund, E. Lommonte, S. Paesani, Y. Wang, J. Carolan, N. Bart, A. D. Wieck, A. Ludwig, L. Midolo, W. H. P. Pernice, P. Lodahl, & F. Lenzini **" Processing single-photons from a quantum dot using high-speed integrated photonic circuits on the thin film lithium-niobate-on-insulator platform "** CLEO San Jose 2023

During the PhD the author also contributed to the following publication, which has not been included in this thesis

Journal publication

D Y. Wang, C. F. D. Faurby, F. Ruf, P.I. Sund, K. H. Nielsen, N. Volet, M. J. R. Heck, N. Bart, A. D. Wieck, A. Ludwig, L. Midolo, S. Paesani, & P. Lodahl **"Deterministic photon source interfaced with a programmable silicon-nitride integrated circuit"** npj Quantum Information 9, no. 1 (2023): 94

Contents

1 Introduction

Scientific progress serves the dual-purpose of expanding what we know, in the form of knowledge, and what we can do, in the form of technology. These two aspects exist in a symbiotic relationship, where an initial understanding of nature enables the creation of technology, after which the limitations of this technology will direct and fund future research.

Quantum mechanics, since its advent in the early 20th century, has transformed our understanding of a variety of scientific disciplines—spawning several new fields—and fundamentally changed the technological landscape. In the first quantum revolution, a quantum mechanical description of nature was leveraged in a classical framework to enable the creation of computers and information processing. As these technologies have been developed to produce increasingly powerful devices, their fundamental limitations have become increasingly evident.

One such limitation, the apparent inability to simulate large quantum mechanical systems, has inspired the field of *quantum* information processing. Here, information is stored in the form of *quantum bits*, commonly shortened to *qubits*, that behave according to quantum mechanics, allowing for fundamentally different capabilities. In addition to the prospects of simulating large quantum systems, theoretical work from the 90s leveraged the properties of ideal qubit systems to develop novel quantum algorithms that surpassed the limitations of classical information processing, e.g. Shor's algorithm (Shor 1999). These developments marked the onset of a potential second quantum revolution, sparking an intense research effort across multiple potential material platforms—e.g. trapped ions, superconducting circuits, and quantum dots—and computing paradigms, each with distinctive strengths and drawbacks.

Photons play an important role in quantum technologies, as they can traverse vast distances at the speed of light and do not readily interact with one another or their environment, making them ideal information carriers. As such, quantum photonics is foundational to quantum communication and quantum cryptography (Bennett et al. 1984; Zahidy et al. 2023). However, though the lack of interaction allows for excellent transmission of quantum information, it also makes it exceedingly difficult to implement the controlled operations required for quantum computing. A turning point for photonic quantum computing came in 2001, when Knill, Laflamme, and

Milburn (Knill et al. 2001) showed that these interactions could be synthesized through photonic interference and detection. Photonic quantum computing has since matured to more advanced computing paradigms (Bourassa et al. 2021; Bartolucci et al. 2023) that incorporate protocols to correct the inevitable errors that will occur in any physical quantum computer. One such computing paradigm, *fusion-based quantum computing* (FBQC), provides a roadmap for fault-tolerant quantum computation using entangled states of single photons (Bartolucci et al. 2023).

A central requirement for quantum photonic technologies is the ability to prepare photons in a desired state with high efficiency and fidelity. Though lasers and light bulbs allow for easy generation of light in a coherent state or a thermal state, generating light in a quantum state that is useful for information processing is notoriously difficult. One approach is to generate single photons—indivisible particles of light—which can be produced either through nonlinear optical processes or the light–matter interaction of a single quantum emitter. The former approach allows for the probabilistic generation of correlated photon pairs where the detection of one photon can be used to herald the presence of the other. This probabilistic process can be made quasi-deterministic by multiplexing many sources with active feed-forward and high-speed switches, introducing an immense amount of resource overhead. Alternatively, single photons can be generated on-demand by employing single quantum emitters such as semiconductor quantum dots. Embedding such a quantum emitter into a nanophotonic structure provides a way to control the charge environment of the emitter and to enhance the light–matter interaction, enabling low-noise and highly-efficient operation. Recent experiments have demonstrated that on-demand single-photon sources (SPSs) based on semiconductor quantum dots are capable of producing long strings of highly indistinguishable photons (Uppu et al. 2020), with rapidly improving system efficiencies (Ding et al. 2023).

As fault-tolerant quantum computing is beyond the reach of current state-of-the-art hardware, *quantum advantage* marks an important intermediate milestone. A quantum system can demonstrate a quantum advantage by solving a specialized task with an insurmountable speedup compared to a classical computer. For single photon sources, this could be achieved by running the *boson sampling* algorithm (Aaronson et al. 2011), which replaces sophisticated controlled qubit transformations with a randomized linear optical interferometer.

With quantum-dot SPSs as a starting point, FBQC as a roadmap and quantum advantage as an intermediate milestone, there are still many steps and challenges that remain before we can realize the end goal of building a quantum computer. In this thesis, we aim to take a few steps forward. We develop novel interferometer architectures in the time-bin encoding that play to the strengths of on-demand SPSs, and showcase an advantageous combination of time-bin interferometers and quantum-dot SPSs in a resource-efficient experimental demonstration of bosonic suppression laws. Proceeding, we combine low-loss and rapidly reprogrammable

photonic integrated circuits in lithium-niobate-on-insulator (LNOI) with a quantum-dot SPS to realize a combined platform capable of demonstrating key functionalities required for FBQC. Lastly, we determine concrete hardware requirements for demonstrating *quantum advantage*, to evaluate how this milestone may be reached with near-term hardware.

1.1 Thesis outline

This thesis is structured as follows:

- Chapter 2 introduces the necessary background for the thesis. The chapter starts by introducing the working principles of a quantum-dot single-photon source and the key figures of merit for single photon states. We then proceed to introduce how the linear optical circuits used to transform our photonic states can be constructed, and the formalism of photonic qubits.
- Chapter 3 details interferometers encoded in the time-bin encoding that is naturally produced by on-demand single-photon sources. After an introduction of already-established architectures, we show how the time-bin encoding is particularly well-suited to implementing mode-permutations that enable novel interferometer architectures.
- Chapter 4 presents an experimental demonstration of bosonic suppression laws using a resource-efficient time-bin interferometer.
- Chapter 5 shows experimental results from single photons processed using photonic integrated circuits on a thin-film LNOI chip. The chapter introduces design considerations and experimental challenges that had to be addressed, and presents the results of experiments with single-photons using the fabricated devices.
- Chapter 6 establishes concrete hardware requirements for quantum advantage demonstrations of boson sampling using on-demand single-photon sources.
- Finally, Chapter 7 provides concluding remarks and outlook for future experiments.

2 Background

2.1 An introduction to single photons

In order to understand how single photons can be created and employed in quantum information processing, it's important to establish exactly what a single photon is, and how its behavior is different from the much-more readily available coherent states produced by lasers. To this end, we will examine three setups illustrated in Fig. 2.1, which will demonstrate how single photons manifest both sides of the famous wave–particle duality of quantum mechanics, and lay the foundation for evaluating the quality of a single-photon source. First, a mathematical framework of quantum mechanical multimode Fock states is introduced. The framework is introduced in multiple parts, starting with the properties of quantum mechanical states, followed by an introduction of how Fock states in a single mode and in multiple modes can be represented using bosonic operators, and how these states are transformed by beamsplitters and phase-shifters. After establishing the properties of single-photons, the same framework is used to represent coherent states, allowing for the introduction an experimental protocol to discriminate single-photon states from coherent states.

Before diving into a mathematical framework, consider that a single photon is a single quantized particle of light. This statement doesn't have to be assumed or accepted, but can (and should!) be verified experimentally. In order to do so, we can employ the experimental setup illustrated in Fig. 2.1a. Prospective single photons are sent into a 50/50 beamsplitter, and the two output ports are connected to detectors that register a detection event, i.e. "click", if there is any amount of light. The 50/50 beamsplitter will split incoming light equally between the two outputs, which means that, on average, both detectors should detect the same amount of light. However, if the light is truly composed of a single quantized particle, which cannot be split into smaller pieces, we should never observe the two detectors clicking at the same time, i.e. a coincidence. This effect, which is observed experimentally, is known as the *Hanbury Brown and Twiss* (HBT) effect (brown1954lxxiv), and relates more generally to the second-order autocorrelation function, $g^{(2)}(t = 0)$, which can be used to discriminate various photon states as will be shown in more detail later.

2.1.1 Quantum mechanical states

The following section will give a brief overview of the parts of quantum mechanics that are relevant to our calculations. A quantum mechanical state is described by a vector in Hilbert space, which spans all possible states that our system can take. For instance, in the simple case of the previous example of a single photon in two modes, the Hilbert space has two basis states, one where the photon is in the top mode, and one where the photon is in the bottom mode, which we will denote as $|0\rangle$ and $|1\rangle$. These states are vectors in Hilbert space in the bra-ket notation, where the Hermitian conjugate, i.e. the complex transpose is denoted as $|i\rangle^\dagger = (|i\rangle^T)^* = \langle i|$. Furthermore, basis states of the Hilbert space, $|s_i\rangle$, are required to be orthonormal, i.e. subject to the constraint that the inner product between two states $\langle s_i|s_j\rangle$ is equal to

$$\langle s_i|s_j\rangle = \delta_{ij},$$

where δ_{ij} is the Kronecker delta, defined as

$$\delta_{ij} = \begin{cases} 1, \ i = j, \\ 0, \ i \neq j. \end{cases}$$

The state of our system, $|\psi\rangle$, is allowed to take a linear combination of the basis states, $|s_i\rangle$, commonly referred to as a *superposition*

$$|\psi\rangle = \sum_i c_i \, |s_i\rangle \overset{\text{simple case}}{=} c_0 \, |0\rangle + c_1 \, |1\rangle \,, \tag{2.1}$$

where the coefficients c_i are subject to the constraint

$$\sum_i |c_i|^2 \overset{\text{simple case}}{=} |c_0|^2 + |c_1|^2 = 1. \tag{2.2}$$

To see why, we first note that the expectation value of an operator $\hat{O}$ in quantum mechanics is given by the inner product

$$\langle O\rangle = \langle\psi| \, \hat{O} \, |\psi\rangle \,. \tag{2.3}$$

We then consider the projection operator $\hat{P}_0 = |0\rangle \langle 0|$. Due to orthonormality, acting upon the state of the system yields

$$\hat{P}_0 \, |\psi\rangle = c_0 \, |0\rangle \langle 0|0\rangle + c_1 \, |0\rangle \langle 0|1\rangle = c_0 \, |0\rangle \,, \tag{2.4}$$

i.e. the system is left in the basis state $|0\rangle$. As such, the expectation value of $\hat{P}_0$ corresponds to the probability of finding the system in the state $|0\rangle$:

$$\langle\psi| \, \hat{P}_0 \, |\psi\rangle = \langle\psi|0\rangle \langle 0|\psi\rangle = c_0^* c_0 = |c_0|^2. \tag{2.5}$$

Thus, the complex coefficients c_i, corresponds to *probability amplitudes*, the absolute square of which correspond to the probability of finding the system

in the associated state.

The constraint on the probability amplitudes imposes a constraint on all transformations on the system. Transformations on the system should leave the system in a normalized state where the absolute squares of the probability amplitudes still sum to 1. Thus, transformations U_T on the system must be unitary, meaning

$$\begin{aligned} &|\det(U_T)| = 1, \\ &U_T^{-1} = U_T^\dagger \Leftrightarrow\ U_T U_T^\dagger = U_T^\dagger U_T = \mathbb{1}, \end{aligned} \tag{2.6}$$

where $\mathbb{1}$ is the identity matrix.

2.1.2 Mathematical framework

We typically represent single photons, or more generally Fock states of photons, using bosonic creation operators. The bosonic creation operator $\hat{a}^\dagger$, acting on the vacuum, $|0\rangle$, i.e. a state containing no photons, produces a state with a single photon, $\hat{a}^\dagger |0\rangle = |1\rangle$. In a similar manner, we can create a state with two photons by acting on the single-photon state with another creation operator, which behaves like $\hat{a}^\dagger |1\rangle = \sqrt{2}\,|2\rangle$, with a prefactor $\sqrt{2}$. The Hermitian conjugate of the creation operator, i.e. $\hat{a}$, will annihilate one excitation from the state, i.e. $\hat{a}\,|2\rangle = \sqrt{2}\,|1\rangle$, and is accordingly called an *annihilation* operator. The general transformations of the creation and annihilation operators acting on a Fock state $|n\rangle$, as well as their commutation relation can be defined as

$$\begin{aligned} \hat{a}\,|n\rangle &= \sqrt{n}\,|n-1\rangle\,, \\ \hat{a}^\dagger\,|n\rangle &= \sqrt{n+1}\,|n+1\rangle\,, \\ \left[\hat{a}, \hat{a}^\dagger\right] &= 1, \end{aligned} \tag{2.7}$$

where $[a, b] = ab - ba$. The prefactors, $\sqrt{n}$ and $\sqrt{n+1}$, lead to two important properties. First, they define the behavior of the annihilation operator acting on the vacuum state as $\hat{a}\,|0\rangle = 0$, which prevents Fock states with a negative number of photons. Second, they allow for the definition of the Hermitian *number operator* as $\hat{n} = \hat{a}^\dagger \hat{a}$, for which the Fock states $|n\rangle$ are eigenstates with eigenvalues $\hat{n}\,|n\rangle = n\,|n\rangle$.

This description only allows for the photons to occupy a single *mode*. A mode corresponds to a degree of freedom of the photon that is fixed. For instance, for photons occupying different spatial modes, the photons in the same mode have the same position and direction of propagation. If we want to describe two photons propagating in different directions, as will be the case after a beamsplitter, we must generalize to a multimode description. To this end, we associate a vacuum state to each mode we want to represent, such that for a two mode case, the vacuum state can be written as $|0\rangle \rightarrow |0\rangle_0 |0\rangle_1$, where the subscript denotes the mode. Each vacuum is associated to distinct creation and annihilation operators, $\hat{a}_i^\dagger$ and $\hat{a}_i$, subject to

the following relations

$$\begin{aligned} \hat{a}_i \left|n\right\rangle_i \left|\psi'\right\rangle &= \sqrt{n} \left|n-1\right\rangle_i \left|\psi'\right\rangle, \\ \hat{a}_i^\dagger \left|n\right\rangle_i \left|\psi'\right\rangle &= \sqrt{n+1} \left|n+1\right\rangle_i \left|\psi'\right\rangle, \\ \left[\hat{a}_i, \hat{a}_j^\dagger\right] &= \delta_{ij}. \end{aligned} \tag{2.8}$$

Here, the photonic state is given by $\left|\psi\right\rangle = \prod_i \left|n\right\rangle_i$, which we represent as $\left|n\right\rangle_i \left|\psi'\right\rangle = \left|n\right\rangle_i \prod_{j\neq i} \left|n\right\rangle_j$ for notational convenience.

Using this formalism, we define the operation of the beamsplitter as a transformation of the creation and annihilation operators. The 50/50 beamsplitter should take a photon incident in one of the modes, and split it into an equal superposition of the two modes:

$$\hat{a}_0^\dagger \overset{\text{BS}}{\rightarrow} \alpha \hat{a}_0'^\dagger + \beta \hat{a}_1'^\dagger, \ |\alpha|^2 = |\beta|^2 = 0.5. \tag{2.9}$$

Here, the output modes are represented by creation operators with primes, $\hat{a}_i'^\dagger$. For notational convenience, we will omit these primes. We can represent this as a unitary transformation acting on a vector of the form

$$\left|\psi\right\rangle = \left(c_0 \hat{a}_0^\dagger + c_1 \hat{a}_1^\dagger\right) \left|0\right\rangle_0 \left|0\right\rangle_1 = \begin{bmatrix} c_0 \\ c_1 \end{bmatrix}, \tag{2.10}$$

where we can define the unitary transformation as

$$U_{\text{BS}} = \begin{bmatrix} \alpha & \beta \\ \gamma & \delta \end{bmatrix}. \tag{2.11}$$

For a 50/50 beamsplitter which splits an input in one mode equally across the two outputs we know that,

$$|\alpha|^2 = |\beta|^2 = 0.5,$$

and we know from Eq. (2.6) that $|\det(U_{\text{BS}})| = 1$, implying

$$|\gamma|^2 = |\delta|^2 = 0.5.$$

There are (infinitely) many choices of parameters that satisfy these requirements. We will fix the beamsplitter transformation as

$$U_{\text{BS}} = \frac{1}{\sqrt{2}} \begin{bmatrix} 1 & 1 \\ 1 & -1 \end{bmatrix}. \tag{2.12}$$

In order to analyze the setup in Fig. 2.1b, we also have to define the transformation of the phase-shifter. This component shifts the phase of the

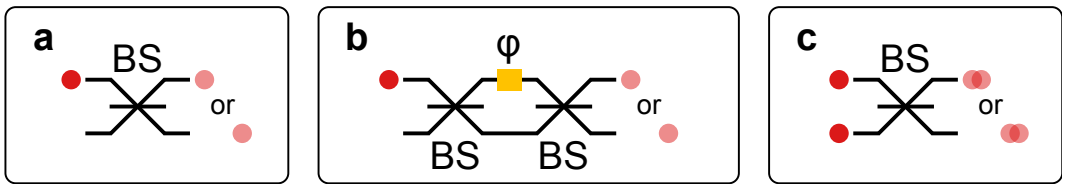

FIGURE 2.1: **a** A single-photon scattering on a beamsplitter. **b** A single-photon scattering on a Mach–Zehnder interferometer (MZI) comprised of two beamslpitters with a phase-shifter in the middle. **c** Two photons scattering on a beamsplitter.

probability amplitude in one mode, and does nothing to the probability amplitude in the other mode. As such, if we have two modes and the phase-shifter acts on the first mode, we can define its unitary transformation as

$$U_{\text{PS}}(\phi) = \begin{bmatrix} e^{i\phi} & 0 \\ 0 & 1 \end{bmatrix}. \tag{2.13}$$

2.1.3 Single photons scattering on beampslitters

In Fig. 2.1a, we have the input state

$$|\psi\rangle_{\text{input, a}} = \begin{bmatrix} 1 \\ 0 \end{bmatrix}. \tag{2.14}$$

Applying the beamsplitter transformation defined in Eq. (2.12) results in the output state

$$|\psi\rangle_{\text{output, a}} = U_{\text{BS}} |\psi\rangle_{\text{input}} = \frac{1}{\sqrt{2}} \begin{bmatrix} 1 \\ 1 \end{bmatrix}. \tag{2.15}$$

Upon detection, the photon will be found in either the top mode or the bottom mode, with equal probability $1/2$. In other words, as it is a single photon only one of the detectors can click at a time, i.e. the HBT effect.

In the second setup, we add a phase-shifter to one of the modes and add another beamsplitter between the two modes to construct a Mach–Zehnder interferometer (MZI). The transformations of the phase-shifter and beamsplitter given by Eq. (2.12) and Eq. 2.13, respectively, yields

$$|\psi\rangle_{\text{output, b}} = U_{\text{BS}} U_{\text{PS}}(\phi) |\psi\rangle_{\text{output, a}} = \frac{1}{2} \begin{bmatrix} e^{i\phi} + 1 \\ e^{i\phi} - 1 \end{bmatrix} = e^{i\phi/2} \begin{bmatrix} \cos(\phi/2) \\ i \sin(\phi/2) \end{bmatrix}. \tag{2.16}$$

The phase-shifter in the top mode leads to interference after the beamsplitter, where the exact value of the phase-shift determines the coefficients in the superposition. For instance, for the settings $\phi = 0$ and $\phi = \pi$, the photon will be found in the top mode or bottom mode, respectively, with probability 1, whereas for $\phi = \pi/2$ we get an equal probability of detecting the photon in either mode at the output. This showcases the wave–particle duality of single photons, with wave-like interference determined by the relative

phase between the two modes and particle-like detection, with the photon only being detected in a single mode at a time.

In the setup shown in Fig. 2.1c, two single-photons are incident on the beamsplitter. We can represent the initial state of these photons as the direct product of each single-photon

$$|\psi\rangle_{\text{input, c}} = \hat{a}_0^\dagger \hat{a}_1^\dagger \, |0\rangle_0 \, |0\rangle_1 \, . \tag{2.17}$$

The beamsplitter will act on each photon independently to produce the output state

$$\begin{aligned} |\psi\rangle_{\text{output, c}} &= \frac{1}{2}(\hat{a}_0^\dagger + \hat{a}_1^\dagger)(\hat{a}_0^\dagger - \hat{a}_1^\dagger) \, |0\rangle_0 \, |0\rangle_1 \\ &= \frac{1}{2}(\hat{a}_0^\dagger \hat{a}_0^\dagger - \hat{a}_1^\dagger \hat{a}_1^\dagger) \, |0\rangle_0 \, |0\rangle_1 \\ &= \frac{1}{\sqrt{2}}(|2\rangle \, |0\rangle - |0\rangle \, |2\rangle). \end{aligned} \tag{2.18}$$

Similarly to the first setup, coincidences will not occur, however, in this case they are prohibited by interference between the two input photons. This effect is known as the *Hong–Ou–Mandel* (HOM) effect (Hong et al. 1987), and requires that the two photons are *indistinguishable*, meaning that apart from being initialized in different modes, their internal degrees of freedom like polarization, wavelength, temporal shape are all exactly the same and that they overlap perfectly in time. To see why indistinguishability is crucial for the HOM effect, we can consider the case where the first photon is described by creation operators $\hat{a}_i^\dagger$ and the second photon is described by creation operators $\hat{a}_i'^\dagger$. The resultant output state will be

$$\begin{aligned} |\psi\rangle_{\text{output}} &= \frac{1}{2}(\hat{a}_0^\dagger + \hat{a}_1^\dagger)(\hat{a}_0'^\dagger - \hat{a}_1'^\dagger) = \frac{1}{2}(\hat{a}_0^\dagger \hat{a}_0'^\dagger + \hat{a}_0^\dagger \hat{a}_1'^\dagger - \hat{a}_1^\dagger \hat{a}_0'^\dagger - \hat{a}_1^\dagger \hat{a}_1'^\dagger) \\ &= \frac{1}{2}(|1, 1'\rangle \, |0\rangle + |1\rangle \, |1'\rangle - |1'\rangle \, |1\rangle - |0\rangle \, |1, 1'\rangle). \end{aligned} \tag{2.19}$$

As the two photons do not interfere with one another, the two detectors will click simultaneously to produce a coincidence with a probability of 50%.

2.1.4 Fock basis representation of coherent states

The Fock states can also be used as a basis to represent other types of states, such as coherent states and thermal states. We often make use of coherent states in experiments, as they can be generated using lasers. As such, it's useful to cover the description of coherent states in our framework, as we can see how their properties differ from the Fock states we're interested in. Coherent states $|\alpha\rangle$, are eigenstates of the annihilation operator, meaning that $\hat{a} \, |\alpha\rangle = \alpha \, |\alpha\rangle$. This is possible because coherent states are superpositions

of an infinite number of photons, which can be seen from its Fock-basis representation:

$$|\alpha\rangle = e^{-|\alpha|^2/2} \sum_{n=0}^{\infty} \frac{\alpha^n}{\sqrt{n!}} |n\rangle . \tag{2.20}$$

To get a physical intuition for the complex number α, we can take the expectation value of the number operator for a coherent state:

$$\begin{aligned} \langle\alpha| \hat{n} |\alpha\rangle &= (\langle\alpha| \hat{a}^\dagger) \cdot (\hat{a} |\alpha\rangle) = \alpha^* \cdot \alpha \langle\alpha|\alpha\rangle \\ &= |\alpha|^2. \end{aligned} \tag{2.21}$$

As such, $|\alpha|^2$ corresponds to the average number of photons in the coherent state. The number α is allowed to take any complex value, which means that the average number of photons can be any real number larger than or equal to zero. If $\alpha \ll 1$, then we can approximate the coherent state as

$$|\alpha\rangle \approx |0\rangle + \alpha |1\rangle + \frac{\alpha^2}{\sqrt{2}} |2\rangle + \mathcal{O}(\alpha^3). \tag{2.22}$$

In other words, mostly vacuum with a small probability of a single photon and a much smaller probability of two or more photons. However, no matter how low the number α is, we will not observe the HBT effect for a coherent state.

To outline why, we will first look at a coherent state impinging on one mode in a beamsplitter, and relate this experiment to the measurement of the second-order autocorrelation function $g^{(2)}(t = 0)$.

2.1.5 Coherent state scattering on a beamsplitter

Suppose we initialize a weak coherent state to the top input mode of the beamsplitter. We approximate the input state as

$$|\alpha\rangle \approx \left(1 + \alpha \hat{a}_0^\dagger + \frac{\alpha^2}{\sqrt{2}} \hat{a}_0^\dagger \hat{a}_0^\dagger + \mathcal{O}(\alpha^3)\right) |0\rangle . \tag{2.23}$$

In the same manner as in the HOM setup, the beamsplitter will act on each creation operator independently, yielding

$$\begin{aligned} |\alpha\rangle &\approx \left(1 + \frac{\alpha}{\sqrt{2}}(\hat{a}_0^\dagger + \hat{a}_1^\dagger) + \frac{\alpha^2}{2\sqrt{2}}(\hat{a}_0^\dagger + \hat{a}_1^\dagger)(\hat{a}_0^\dagger + \hat{a}_1^\dagger) + \mathcal{O}(\alpha^3)\right) |0\rangle \\ &= \left(1 + \frac{\alpha}{\sqrt{2}}(\hat{a}_0^\dagger + \hat{a}_1^\dagger) + \frac{\alpha^2}{2\sqrt{2}}(\hat{a}_0^\dagger \hat{a}_0^\dagger + 2\hat{a}_0^\dagger \hat{a}_1^\dagger + \hat{a}_1^\dagger \hat{a}_1^\dagger) + \mathcal{O}(\alpha^3)\right) |0\rangle . \end{aligned} \tag{2.24}$$

The term proportional to α^2 will invariably lead to the coincidental detector clicks. In an experiment, the rate at which coincidences are detected is proportional to α^2, i.e. a small number, which means the number of coincidences will depend on the *integration time* of the experiment, i.e. how long

we wait for coincidences to be detected. In order to be able to compare the statistics recorded in different experiments, one typically measures a normalized quantity, called the normalized second-order correlation function $g^{(2)}(\tau)$, which takes the lower overall detection rate into account by dividing by the square of the intensity. For this experiment, we allow for one detector to be delayed by τ and record the normalized coincidence count at the given time. It can be shown (Gerry et al. 2005) that this measure can be expressed in terms of creation and annihilation operators of the initial single-mode state before the beamsplitter as

$$g^{(2)}(\tau) = \frac{\langle \hat{a}^\dagger(t)\hat{a}^\dagger(t+\tau)\hat{a}(t+\tau)\hat{a}(t)\rangle}{\langle \hat{a}^\dagger(t)\hat{a}(t)\rangle\langle \hat{a}^\dagger(t+\tau)\hat{a}(t+\tau)\rangle}, \tag{2.25}$$

where the parameter τ corresponds to the time-delay between the detectors. The most interesting point is at zero time-delay $\tau = 0$. Assuming no time-dependence for the coherent state, i.e. an equal probability of detecting a photon at any given time, we can omit the time-dependence of the operators, such that

$$\begin{aligned} g^{(2)}(0)_{\text{coherent-state}} &= \frac{\langle\alpha|\,\hat{a}^\dagger\hat{a}^\dagger\hat{a}\hat{a}\,|\alpha\rangle}{\langle\alpha|\,\hat{a}^\dagger\hat{a}\,|\alpha\rangle\,\langle\alpha|\,\hat{a}^\dagger\hat{a}\,|\alpha\rangle} \\ &= \frac{|\alpha|^4}{|\alpha|^2\cdot|\alpha|^2} = 1 \end{aligned} \tag{2.26}$$

Assuming a similar time dependence for a single-photon state yields

$$\begin{aligned} g^{(2)}(0)_{\text{single-photon}} &= \frac{\langle 1|\,\hat{a}^\dagger\hat{a}^\dagger\hat{a}\hat{a}\,|1\rangle}{\langle 1|\,\hat{a}^\dagger\hat{a}\,|1\rangle\,\langle 1|\,\hat{a}^\dagger\hat{a}\,|1\rangle} \\ &= \frac{0}{1\cdot 1} = 0, \end{aligned} \tag{2.27}$$

which is in perfect agreement with the HBT effect.

2.1.6 Figures of merit for single-photon states

The power of single photons comes from their uniquely quantum mechanical behavior, which is manifestly different from that of other states of light such as coherent states emitted by lasers. The quantized nature of single photons can be validated experimentally by measuring the normalized second-order correlation function at zero time-delay, $g^{(2)}(0)$. Due to the HBT effect, the value of this function should be measured as zero for single-photon sources. A finite $g^{(2)}(0)$ implies the existence of multiphoton components in the photonic state, as showcased by coherent states for which we will always measure $g^{(2)}(0) = 1$, regardless of how low the average number of photons is. Furthermore, in order to make use of interference between multiple single-photons, the photons have to be indistinguishable over all internal degrees of freedom. This can be validated experimentally through the verification of the HOM effect, whereby the interference of two

single photons impinging on each input arm of a beamsplitter prohibits the measurement of a coincidence detection in the two output modes.

2.2 Operating principle of a quantum-emitter single-photon source

A quantum emitter is a system with an optically active transition between discrete energy levels allowing for the excitation of a single quantum, whereupon radiative decay will produce a single photon. In order to understand how this system can be operated as an on-demand single-photon source, we need to understand

1. How the quantum emitter can be prepared in the excited state.
2. How the excited state produces a single photon.
3. How the emitted single photon can be collected.

For each step, it is instrumental that the efficiency is as close to unity as possible to ensure deterministic generation of single photons. Insight into the principles behind each step will also allow us to understand the origins of specific errors that manifest in the measurements of $g^{(2)}(0)$ and the HOM effect.

2.2.1 Deterministic preparation of a quantum emitter using resonant excitation

There are various ways in which the quantum emitter can be prepared in an excited state, each with their own advantages and drawbacks. In the experiments covered in this thesis, we make use of an approach called *resonant excitation*, where we excite the system by driving it with a laser pulse that is resonant with the quantum emitter transition. The physics of resonant excitation can be understood from how a two-level system interacts with a driving light in the absence of damping. The details of the derivation will not be covered here, and we will instead make use of the results from Gerry et al. 2005. This derivation takes the semiclassical approximation by treating the light field as classical, which is reasonable for the laser pulses we want to drive the system with, and treats the light–matter interaction in the rotating wave approximation, which is valid as long as the interaction is not in the strong-coupling regime [1]. Furthermore, the derivation assumes that the two-level system has a dipolar interaction with the light field, with a dipole moment of $\mathbf{d}_{eg}$. When this two-level system interacts with a light field with electric field amplitude $\mathbf{E}_0$ and detuning Δ with respect to the transition,

[1] This means that the rate of exchange of energy between the two-level system and light field should be much slower than the resonance frequency of the transition.

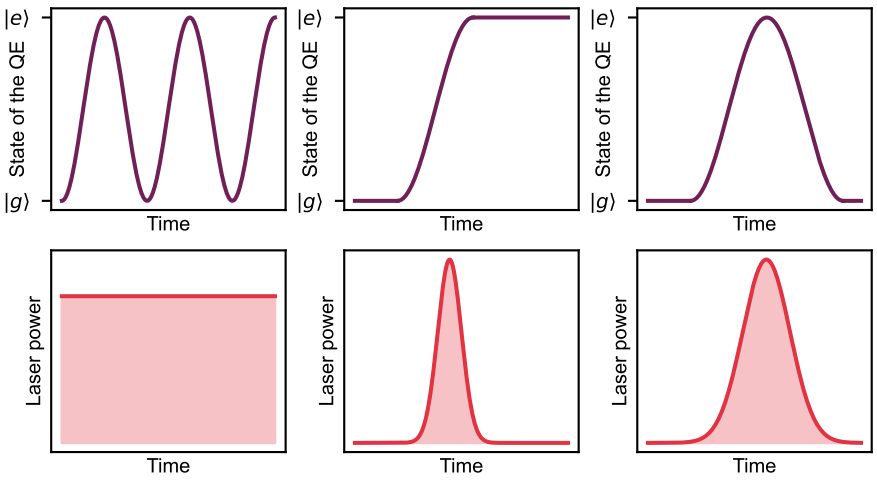

FIGURE 2.2: Illustration of the time-evolution of the state of a quantum emitter (QE) (top panels) upon interaction with three different kinds of laser fields (bottom). In the leftmost panel, the intensity of the laser is constant in time, leading to the state of the emitter oscillating between the ground state and excited state. In the middle panel and right-most panel, the laser is a pulse in time, where the pulse area leaves the system in the excited state for the middle panel, and back in the ground state in the rightmost panel.

the state of the system at time t will be given by (Gerry et al. 2005)

$$|\psi\rangle = e^{i\Delta t/2}\left[\cos(\Omega_{\mathrm{R}}t/2) - i\frac{\Delta}{\Omega_{\mathrm{R}}}\sin(\Omega_{\mathrm{R}}t/2)\right]|g\rangle + i\frac{\mathcal{V}}{\Omega_{\mathrm{R}}\hbar}e^{i\Delta t/2}\sin(\Omega_{\mathrm{R}}t/2)\,|e\rangle\,, \tag{2.28}$$

where $\mathcal{V} = -\mathbf{d}_{eg}\cdot\mathbf{E}_0$ i.e. the strength of the interaction between the light field and the two-level system, and where $\Omega_{\mathrm{R}} = \sqrt{\Delta^2 + \mathcal{V}^2/\hbar^2}$, which is known as the Rabi frequency. When the light field is resonant with the transition, such that the prefactors $\frac{\mathcal{V}}{\Omega_{\mathrm{R}}\hbar} = 1$ and $\frac{\Delta}{\Omega_{\mathrm{R}}} = 0$, the state of the two-level system oscillates coherently from being completely in the ground state to being entirely in the excited state, as illustrated in Fig. 2.2. These oscillations are known as Rabi oscillations. If the driving light is in the form of a pulse, the two level system will be left at a certain point in the fringe after the interaction. This end point is determined by the pulse area, which depends on the pulse length and amplitude. Fig. 2.2 shows two examples, one where the pulse area leads to half a period of oscillation, i.e. a phase of π, and one where the pulse area leads to a whole period of oscillation, i.e. a phase of 2π. The former pulse, which is called a π-pulse, can be used to deterministically invert the population of the quantum emitter from the ground state to the excited state.

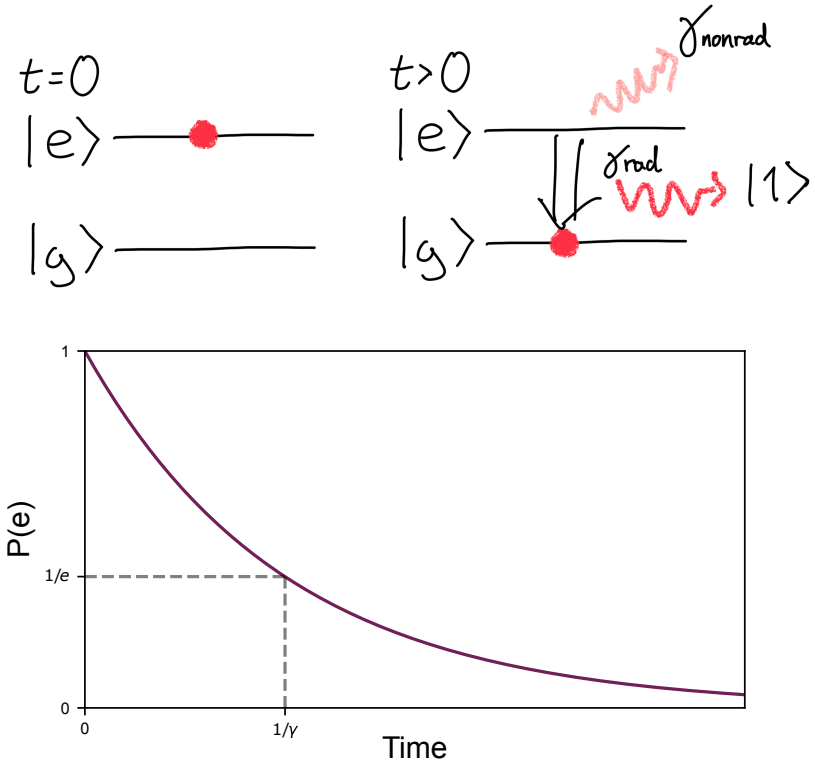

FIGURE 2.3: Spontaneous emission of a single-photon. The plot in the bottom panel shows the probability for the quantum emitter to remain in the excited state as a function of time.

2.2.2 Producing a single photon through spontaneous emission

The quantum emitter is not an isolated system, and our excited state will inevitably decay to lower energy levels through various channels, such as radiative emission of a single photon or nonradiative emission of a phonon, as illustrated in Fig. 2.3. This process can be described quantitatively by modeling the system accurately and treating the equations of motion for the system connected to thermal baths. Here, we will make use of results presented in Lodahl et al. 2015 to provide a qualitative picture of the process and see the sources of error that can arise.

We start by considering a quantum emitter that can only decay to the ground state radiatively by spontaneously emitting a single photon at a rate of γ, as seen in Fig. 2.3. Supposing this emitter is initialized in the excited state, we can express the state of the quantum emitter and the electromagnetic field at time t as

$$|\psi\rangle\,(t) = e^{-\gamma t/2}\,|e\rangle\,|0\rangle + \sqrt{1-e^{-\gamma t}}\,|g\rangle\,|1\rangle\,, \tag{2.29}$$

where $|e\rangle$ ($|g\rangle$) is the excited (ground) state of the quantum emitter. As time passes, it will be more and more likely for the quantum emitter to have decayed to the ground state by emitting a photon.

Though this example assumed the emitter was prepared in the excited

state, our preparation scheme of applying a π-pulse did not take spontaneous decay into consideration. As the π-pulse used for the preparation of the quantum emitter interacts with the emitter for a finite amount of time, it is possible for the system to spontaneously decay within the pulse duration, at which point it can be partially excited by the remainder of the pulse and emit an additional photon. As such, a single π-pulse can lead to the emission of multiple photons, which will manifest in the measurement of a nonzero $g^{(2)}(t = 0)$ value. As the probability for the system to have spontaneously decayed grows with time, the magnitude of the multiphoton noise will be higher for longer π-pulses. Accordingly, we typically restrict pulse lengths to be much shorter than the average time it takes for the system to emit a photon, characterized by the radiative decay rate, i.e.

$$\tau_{\pi\text{-pulse}} \ll 1/\gamma. \tag{2.30}$$

For a quantum emitter connected to multiple decay paths, we associate a decay rate for each decay path. The total decay rate γ will be equal to the sum of individual decay rates γ_i

$$\gamma = \sum_i \gamma_i. \tag{2.31}$$

We typically separate the decay rate into a radiative decay rate γ_{rad} for which the decay produces a single photon, and a nonradiative decay rate γ_{nonrad}, where no photon is produced. The decay rate of the emitter will then be equal to

$$\gamma = \gamma_{\text{rad}} + \gamma_{\text{nonrad}}. \tag{2.32}$$

Thus, upon excitation, the quantum emitter will produce a single photon with probability equal to

$$\frac{\gamma_{\text{rad}}}{\gamma_{\text{rad}} + \gamma_{\text{nonrad}}}. \tag{2.33}$$

2.2.3 Enhancing and collecting single-photon emission

Producing a single photon is not sufficient by itself. In order to use the single photon it will have to be collected into a well-defined mode, at which point it can be routed where it is needed, i.e. into an interferometer or a photonic circuit. If we consider a quantum emitter in a bulk material, the emitter can decay by emitting a photon in any direction, and it becomes practically impossible to collect all of the emission. Thus, in order to produce single photons with close to unity efficiency we have to ensure as high of a radiative decay rate as possible, and direct the emission into a well-defined mode. To this end, it's instructive to look at how the radiative decay rate is determined. We make use of a result from Lodahl et al. 2015, which derives the following expression for the radiative decay rate of a dipole emitter in

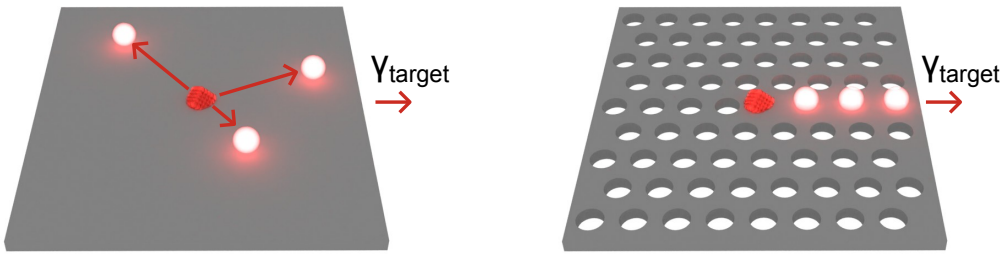

FIGURE 2.4: Enhancing the target emission of a quantum emitter (red pyramid) by altering the photonic environment

the Wigner–Weisskopf approximation:

$$\gamma_{\text{rad}} = \frac{\pi d^2}{\epsilon_0 \hbar} \omega_0 \rho, \tag{2.34}$$

where d is the dipole moment of the optical transition and ρ is the local density of states (LDOS). The LDOS is determined by the electromagnetic properties of the environment around the emitter and can be increased by placing the emitter in a photonic structure, such as an open microcavity (Ding et al. 2023) or a photonic crystal waveguide (Zhou et al. 2022). By sculpting the environment around the emitter, we can also ensure that the quantum emitter preferentially emits a photon into a specific mode, such as the guided mode of a photonic crystal waveguide. If we define the decay rate of the emitter into the mode we collect as γ_{target}, as illustrated in Fig. 2.4, we can define the probability of the quantum emitter producing a single-photon upon excitation, which we refer to as the β-factor, as

$$\beta = \frac{\gamma_{\text{target}}}{\gamma}. \tag{2.35}$$

Collection concerns itself with directing the photon emission into a specific spatial mode. However, we know from the HOM effect that photons have to be indistinguishable across all internal degrees of freedom to exhibit quantum interference. A source of error for the indistinguishability of photons emitted from *solid-state* quantum emitters, e.g. semiconductor quantum dots, is that the coupling to phononic modes in the solid-state material allows for *phonon-assisted* radiative decay. In this process, the emitter decays by emitting a photon with a lower (higher) energy than the

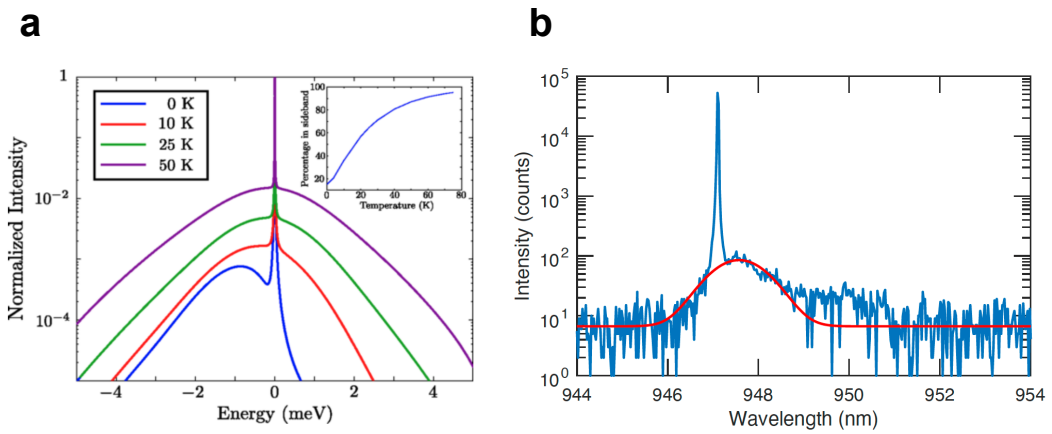

FIGURE 2.5: **a** Emission spectrum for an InGaAs quantum dot emitter for varying temperature. Adapted from Lodahl et al. 2015. **b** Measured emission spectrum from an InGaAs quantum dot emitter. Note that the x-axis is different compared to **a**, such that the red-detuned side-band is on the right-hand side. Adapted from Uppu et al. 2020.

excited-state–ground-state transition by simultaneously creating (annihilating) a phonon. This leads to an emission spectrum as shown in Fig. 2.5, where in addition to the sharp line corresponding to the emission of a photon resonant with the transition there is a *phonon sideband*. The blue-detuned part of the spectrum, requiring the annihilation of a phonon, will be proportional to the number of phonons present in the material, which will decrease with temperature. However, even as the number of phonons goes to zero, it is always possible for the emitter to produce a lower energy photon by simultaneously creating a phonon. In other words, the red-detuned phonon sideband will persist even as the temperature approaches absolute zero. To remove the error from phonon-assisted decay, we can send the emitted light through a narrow-band wavelength filter that admits the zero-phonon line and filters out the phonon sideband. This will, however, limit the efficiency of the single-photon source. Resultantly, quantum emitters with higher yield into the zero-phonon line, i.e. lower-amplitude phonon sideband are favored for use as on-demand single-photon sources.

It is crucially important when collecting single-photon emission that it is separated from the laser light used to prepare the quantum emitter in the excited state. Suppose we were to resonantly excite the emitter by sending a pulse into the mode used for collection of single-photon emission. In that case, it would be impossible to efficiently filter out the pump light, as it would be spectrally and temporally overlapped with the single-photon emission. For certain photonic structures, such as micropillar cavities, this renders efficient resonant excitation infeasible. Instead, one has to resort to non-resonant excitation schemes where wavelength filters can be used to separate the driving light from single-photon emission. In the case of an emitter embedded in a photonic crystal waveguide, this issue can be circumvented by driving the system from the out-of-plane emission mode and

collecting emission through the waveguide, as illustrated in Fig. 2.6. This is possible even if the system is only weakly coupled to the out-of-plane mode, as we can compensate for the weaker coupling by increasing the power of the driving pulse. Furthermore, as the out-of-plane mode is perpendicular to the propagating mode in the waveguide, there is little-to-no coupling from the out-of-plane pulse into the waveguide mode itself. However, as this excitation scheme relies upon the emitter being weakly coupled to the out-of-plane mode, characterized by the decay rate of the system to out-of-plane radiation, it is also inherently reliant on a nonunity β-factor.

2.2.4 Experimental realization of a quantum-dot single-photon source in a photonic crystal waveguide

To conclude this section, we will examine the single-photon source used for the experiments described in this thesis, which is based on an InGaAs quantum dot embedded in a one-sided photonic crystal waveguide. This source is the result of a long-standing collaboration between three academic groups in Copenhagen, Basel, and Bochum. The current device is based on an InGaAs wafer grown by Nikolai Bart in the group of Arne Ludwig and Andreas D. Wieck in Bochum, with nanophotonic devices fabricated by Ying Wang and Leonardo Midolo in Copenhagen, and builds on years of research and effort by previous group members.

An SEM image of the source is shown in Fig. 2.6a. To drive the source, short laser pulses with a pulse duration of $22\,\mathrm{ps}$ are sent orthogonally to the waveguide from the top, and single-photon emission is directed towards a grating coupler, which couples light out of the chip into a fiber. After fiber collection, the photons are routed into an narrowband etalon cavity that admits the zero-phonon line and filters out the phonon sideband. The efficiency of the etalon depends both on the transmission of the cavity at resonance, as well as the yield of the zero-phonon line. The zero-phonon line was not estimated for the source used here but has been estimated to be around 95% for previous sources developed in the group (Uppu et al. 2020). The efficiency of the source after the etalon was estimated as 21.7%. The β-factor was not estimated directly for this source, however it is included in the efficiency associated with reaching the shallow-etched grating, which is estimated to be over 90% (Wang et al. 2023). For previous quantum dot sources used in the group, the β-factor has been estimated to range from 92% (Uppu et al. 2020) to 95% (Zhou et al. 2022).

By sending the single-photon emission onto a beamsplitter and recording coincidences, as shown in Fig. 2.6c i, a $g^{(2)}(0)$ value of 0.008 was measured. To extract this value from the measured coincidences, the area of the peak at zero time-delay was normalized by the area of the peak at a time delay of 13.8 ns, i.e. the separation to the subsequent photon.

To quantify the indistinguishability of the photons, the Hong–Ou–Mandel interference *visibility* was measured by recording coincidences for two co-polarized single-photons interfering on a 50/50 beamsplitter, and normalizing by the coincidences for the interference of two cross-polarized photons,

i.e. completely distinguishable photons. This HOM visibility is a lower bound of the overlap integral of the wavefunction of the two photons, i.e. their mutual indistinguishability. The setup used to do so is schematically illustrated in Fig. 2.6d. In order to interfere two subsequent photons, the output photons are sent into an asymmetric MZI, where the lower arm contains a delay to synchronize the two photons. Supposing that the first of two photons is delayed in the bottom arm, and the second photon enters the top arm, they will coincide on a second beamsplitter. This has an overall success probability of 25%. In order to calibrate the number of recorded coincidence counts, a HWP in the upper arm can be set to $\pi/4$ radians to cross-polarize the photons, in which case the two photons entering the beamsplitter are completely distinguishable. The recorded coincidences for co- and cross-polarized photons are both shown in Fig. 2.6d. A HOM visibility of 94.5% $\pm$ 1.7% was measured.

2.3 Linear optics and photonic quantum computing

Single photons can enable quantum technologies with diverse applications, including quantum communication and networks, and quantum information processing (Degen et al. 2017; O'brien et al. 2009; Wang et al. 2020). Central to all of these applications is the ability to manipulate the state of the photons. This manipulation is typically performed using *linear optical* components, such as the MZI used to control the state of a single photon in two modes in the previous chapter. We will introduce how large multimode interferometers can be constructed by arranging a fixed number of MZIs to allow for the implementation of any linear optical transformation and introduce a mathematical formalism to translate this into a transformation on a general multimode multiphoton state.

In practice, we manipulate the photonic state using a variety of experimental components. We will give an overview of the components used in both bulk optics and photonic integrated circuits and how they relate to our mathematical formalism.

To understand how single photons can be used for quantum information processing, we give a basic introduction to and an overview of photonic quantum computing, and the requirements posed by photonic quantum computing on the optical circuitry.

2.3.1 Universal multimode interferometers

Linear optical components are components that perform the same optical transformation regardless of the number of photons. Linear optics is contrasted by *nonlinear optics*, where the transformation itself depends on the number of photons present. Nonlinear optical effects are typically too weak to make use of in the regime of single photons, and as such, most of our experimental setups will be composed of linear optical components.

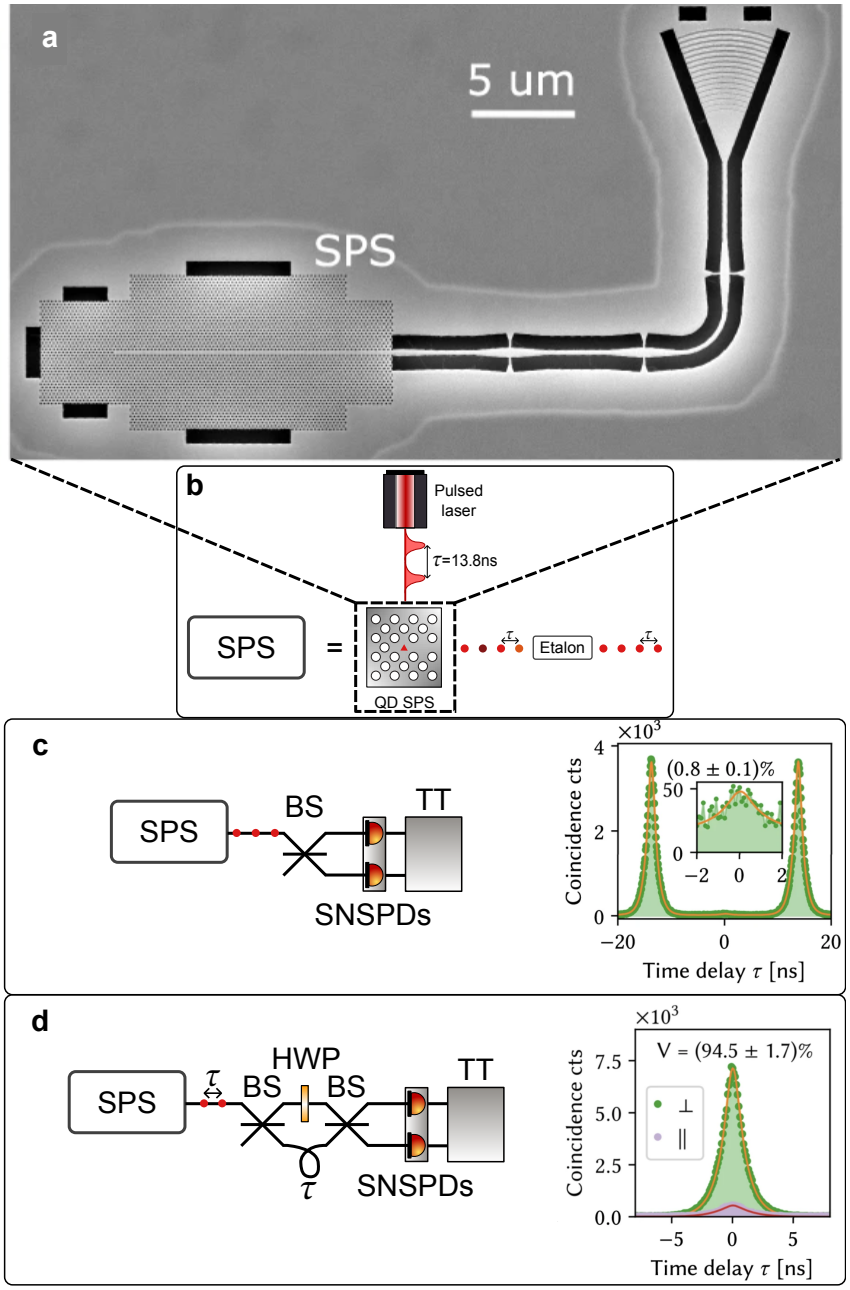

FIGURE 2.6: Experimental setup and results for the SPS used for the experiments detailed in this thesis. **a** SEM image of the quantum dot and single-sided photonic crystal waveguide. Adapted from Wang et al. 2023. **b** Illustration of the experimental setup used to operate a quantum dot as an on-demand single-photon source. **c-d** (Left) Schematic of the experimental setup used to measure $g^{(2)}(t)$ (**c**) and HOM visibility (**d**) for the single-photon source using a balanced beamsplitter (BS), superconducting nanowire single-photon detectors (SNSPDs) and a time tagger (TT). The setup in **d** has an additional beamsplitter with a half-wave plate (HWP) added to one arm and a delay added to the other (allowing for passive demultiplexing of pairs of photons). The HWP allows for the HOM visibility to be measured both in the co- and cross-polarized case, i.e. with indistinguishable and completely distinguishable photons.(Right) Experimentally measured data for $g^{(2)}(t)$ (**c**) and HOM visibility (**d**), adapted from Wang et al. 2023.

Linear optical transformations are described by unitary transformations that act on the *modes* of the photons. In the case of a single-photon state this is equivalent to the Hilbert space of the system. For multiple photons, however, as we examined in the setup used to demonstrate the HOM effect, each creation operator has to be transformed independently, i.e. the transformation on each photon is independent of the other photons present. We will cover how a unitary transformation on the modes can be mapped to a unitary transformation on the Hilbert space of a multiphoton state in a later section. For now, we restrict the focus to how we can construct arbitrary linear optical transformations.

The starting point for our foray is a modified MZI, as illustrated schematically in Fig. 2.7. As before, we have two beamsplitters with a phase-shifter in the middle, but we have now added a phase-shifter before the first beamsplitter and one after the second beamsplitter. Multiplying the transformation for each component together yields

$$\begin{aligned} U_{\text{MZI}}(\phi_1, \phi_2, \phi_3) &= U_{\text{PS}'}(\phi_3) U_{\text{PS}}(\phi_2) U_{\text{BS}} U_{\text{PS}}(\theta) U_{\text{BS}} U_{\text{PS}}(\phi_1) \\ &= e^{i\theta/2} \begin{bmatrix} e^{i(\phi_1+\phi_2)} \cos(\theta/2) & e^{i(\phi_2+\pi/2)} \sin(\theta/2) \\ e^{i(\phi_1+\phi_3+\pi/2)} \sin(\theta/2) & e^{i\phi_3} \cos(\theta/2) \end{bmatrix}. \end{aligned} \tag{2.36}$$

Here, the transformation $U_{\text{PS}'}$ denotes a phase-shifter on the bottom mode. By specifying the phases ϕ_1, θ, and ϕ_2, we can perform an arbitrary unitary transformation up to a global phase, whereas control of the phase ϕ_3 allows for the specification of the global phase as well. As the global phase does not lead to any measurable difference in the unitary transformation, this phase-shifter will often be omitted.

Universal unitary transformation on two modes

To illustrate the universality of the unitary transformation, we consider the example of transforming from an arbitrary input state $|\psi\rangle_{\text{in}}$ to an arbitrary output state $|\psi\rangle_{\text{out}}$, defined as

$$\begin{aligned} |\psi\rangle_{\text{in}} &= |\alpha| e^{i\phi_\alpha} |1\rangle |0\rangle + |\beta| e^{i\phi_\beta} |0\rangle |1\rangle \\ |\psi\rangle_{\text{out}} &= |\gamma| e^{i\phi_\gamma} |1\rangle |0\rangle + |\delta| e^{i\phi_\delta} |0\rangle |1\rangle . \end{aligned}$$

We start by rewriting the input state as

$$|\psi\rangle_{\text{in}} = e^{i\phi_\beta} \left(|\alpha| e^{i(\phi_\alpha - \phi_\beta)} | |1\rangle |0\rangle + |\beta| |0\rangle |1\rangle \right). \tag{2.37}$$

Setting the phase $\phi_1 = (\phi_\beta - \phi_\alpha) + \pi/2$ and transforming by the phase-shifter unitary, Eq. (2.13), yields

$$|\psi\rangle_1 = e^{i\phi_\beta} \left(i|\alpha| |1\rangle |0\rangle + |\beta| |0\rangle |1\rangle \right). \tag{2.38}$$

Here, the term $(\phi_\beta - \phi_\alpha)$ removes the relative phase difference, whereas the purpose of the $\pi/2$ term is to compensate for a phase offset introduced by the MZI transformation that will be applied next. The unitary matrix for an

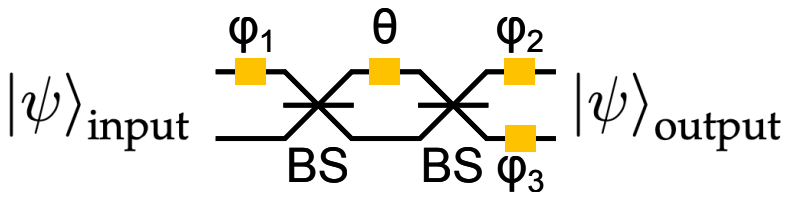

FIGURE 2.7: Universal two mode interferometer

MZI containing a single phase-shifter characterized by a phase shift of θ is equivalent to

$$U_{\text{MZI}}(\theta) = U_{\text{BS}}U_{\text{PS}}(\theta)U_{\text{BS}} = e^{i\theta/2}\begin{bmatrix}\cos(\theta/2) & i\sin(\theta/2)\\ i\sin(\theta/2) & \cos(\theta/2)\end{bmatrix}. \tag{2.39}$$

Thus, after the MZI transformation, the photonic state is equal to

$$e^{-i(\phi_\beta+\theta/2)}\left|\psi\right\rangle_2 = i\left[|\alpha|\cos(\theta/2) + |\beta|\sin(\theta/2)\right]|1\rangle\,|0\rangle \tag{2.40}$$
$$+\left[|\beta|\cos(\theta/2) - |\alpha|\sin(\theta/2)\right]|0\rangle\,|1\rangle\,. \tag{2.41}$$

We want the absolute value of the first and second prefactors to be equal to $|\gamma|$ and $|\delta|$, respectively. As we know that $|c_1|^2 + |c_2|^2 = |\gamma|^2 + |\delta|^2 = 1$, this is equivalent to the ratio of the prefactors being equal, i.e.

$$\frac{|\alpha|\cos(\theta/2) + |\beta|\sin(\theta/2)}{|\beta|\cos(\theta/2) - |\alpha|\sin(\theta/2)} = \frac{|\gamma|}{|\delta|}, \tag{2.42}$$

which can be solved for θ to find

$$\theta = 2\arctan\left(\frac{|\beta||\gamma| - |\alpha||\delta|}{|\beta||\delta| + |\alpha||\gamma|}\right), \tag{2.43}$$

yielding the state

$$|\psi_2\rangle = e^{i(\phi_\beta+\pi/2)}|\gamma|\,|1\rangle\,|0\rangle + e^{i(\phi_\beta)}|\delta|\,|0\rangle\,|1\rangle\,. \tag{2.44}$$

By setting the last phase-shifters to implement phase shifts of $\phi_2 = \phi_\gamma - \phi_\beta - \pi/2$ and $\phi_3 = -\phi_\beta$ the output state will be equal to

$$|\psi\rangle_{\text{out}} = \gamma\,|1\rangle\,|0\rangle + \delta\,|0\rangle\,|1\rangle\,, \tag{2.45}$$

completing the desired transformation.

Multimode interferometers

A natural follow-up question is: "what if we want a unitary transformation on *more than two modes*?" The answer to this question is that we can construct any unitary matrix by combining MZIs consisting of two beamsplitters and two phase-shifters, in addition to a phase screen. In practical terms, we take MZIs as shown in Fig. 2.7, chuck out the phase-shifter at the start and the one in the bottom mode at the end, weave these MZIs together

in a specific configuration, and then add phase-shifters to each of the output modes. The first universal interferometer architecture was introduced in a seminal paper by Reck and colleagues. The key insight of the approach is that a single MZI connected to an interferometer can be configured to zero out an element in the unitary matrix implemented by the interferometer. Suppose we have an m mode interferometer described by an $m \times m$ unitary matrix, which has $m(m-1)/2$ elements beneath the diagonal. By successively applying $m(m-1)/2$ MZI transformations in a cleverly chosen manner, all elements beneath the diagonal can be zeroed out. Due to the unitarity of the matrix, the result will be a diagonal matrix, where every element generally has a complex phase. By applying a phase shift on each of the modes, i.e. a phase screen, we can then transform the diagonal matrix to the identity matrix. As such, if we call the initial arbitrary unitary matrix $U^\dagger$, our network of MZIs will produce the Hermitian conjugate of this matrix, U. To give a better understanding of how this can be achieved, we will explain the decomposition method used in the Reck architecture, as the explanation is relatively straightforward.

Reck interferometer

The working principle behind the Reck architecture is most easily understood in terms of diagonal lines of MZIs and how they relate to columns in the unitary matrix. Suppose that we have a photon incident in the first mode of a four mode interferometer. The state at the output,

$$|\psi\rangle_{\text{out},1} = \begin{bmatrix} c_0 \\ c_1 \\ c_2 \\ c_3 \end{bmatrix} \tag{2.46}$$

will be equal to the first column of the unitary matrix implemented by the interferometer. Such a state can alternatively be produced using a diagonal line of MZIs, as shown on the right side of Fig. 2.8, with the following approach. For each MZI in the diagonal line, only the top mode of every MZI will have an incoming probability amplitude, such that the output probability amplitude in the top (bottom) mode will be equal to[2] the incoming probability amplitude multiplied by $\cos(\theta/2)$ ($\sin(\theta/2)$) where θ is the inner phase of the MZI. For the first MZI (M_1) we set θ to be equal to $\arccos(|c_0|)$, such that we have a probability amplitude of magnitude $|c_0|$ in the top output mode, and an amplitude of magnitude $\sqrt{c_1^2 + c_2^2 + c_3^2}$ in the bottom output mode. The bottom output of the first MZI is connected to the top input mode of the second MZI (M_2). We set the inner phase of this MZI to be equal to $\arccos\left(|c_1|/\sqrt{c_1^2 + c_2^2 + c_3^2}\right)$, such that the top output mode contains a probability amplitude of magnitude $|c_1|$ and the top mode a probability amplitude of magnitude $\sqrt{c_2^2 + c_3^2}$. For the final MZI (M_3)of the diagonal

[2] in addition to a phase

line, we set the inner phase equal to $\arccos\left(|c_2|/\sqrt{c_2^2+c_3^2}\right)$, ensuring an output of

$$|\psi\rangle_{\text{out}} = \begin{bmatrix} |c_0|e^{i\phi_0} \\ |c_1|e^{i\phi_1} \\ |c_2|e^{i\phi_2} \\ |c_3|e^{i\phi_3} \end{bmatrix}, \tag{2.47}$$

where the phases ϕ_0, ϕ_1, and ϕ_2 are determined by the outer phase-shifters of each of the three MZIs. We set the phase shifters to ensure the correct relative phase shift between the four elements. It will then be possible to compensate for any added phase by setting the phase shifter applied to the first mode in the phase screen at the start of the interferometer. Thus, we ensure $|\psi\rangle_{\text{out}} = |\psi\rangle_{\text{out},1}$. To see how we can proceed, consider the inverse of the circuit $M_3^\dagger M_2^\dagger M_1^\dagger$. The inverse circuit corresponds to running the circuit in reverse with all phases inverted $\phi \to -\phi$, i.e. the time-reversal of the circuit. Considering our circuit in reverse, we have fixed our last diagonal, and running the circuit in reverse yields

$$M_3^\dagger M_2^\dagger M_1^\dagger U_4 = \begin{bmatrix} 1 & 0 & 0 & 0 \\ 0 & & & \\ 0 & & U_3' & \\ 0 & & & \end{bmatrix}$$

i.e. the first column and row has been replaced with the first column and row of the identity matrix. This reduces the problem to three modes, and we can proceed by repeating the procedure with a three-mode diagonal line of MZIs addressing the first column in U_3 in the same way we did with the first column of U_4. By applying the Hermitian conjugate of this line of diagonals, i.e. $M_2'^\dagger M_1'^\dagger$, to the circuit we get

$$M_2'^\dagger M_1'^\dagger M_3^\dagger M_2^\dagger M_1^\dagger U_4 = \begin{bmatrix} 1 & 0 & 0 & 0 \\ 0 & 1 & 0 & 0 \\ 0 & 0 & & \\ 0 & 0 & U_2' & \end{bmatrix}$$

We can repeat this once more with a "diagonal line" consisting of a single MZI to yield

$$M_1''^\dagger M_2'^\dagger M_1'^\dagger M_3^\dagger M_2^\dagger M_1^\dagger U_4 = \begin{bmatrix} 1 & 0 & 0 & 0 \\ 0 & 1 & 0 & 0 \\ 0 & 0 & 1 & 0 \\ 0 & 0 & 0 & 1 \end{bmatrix} \tag{2.48}$$

By combining all of the diagonals in the correct order, we have constructed an interferometer that can implement an arbitrary four mode unitary matrix using 6 MZIs. This procedure can be generalized to m modes using $m-1$ diagonal lines of MZIs, i.e. $m(m-1)/2$ MZIs. An illustration of the completed

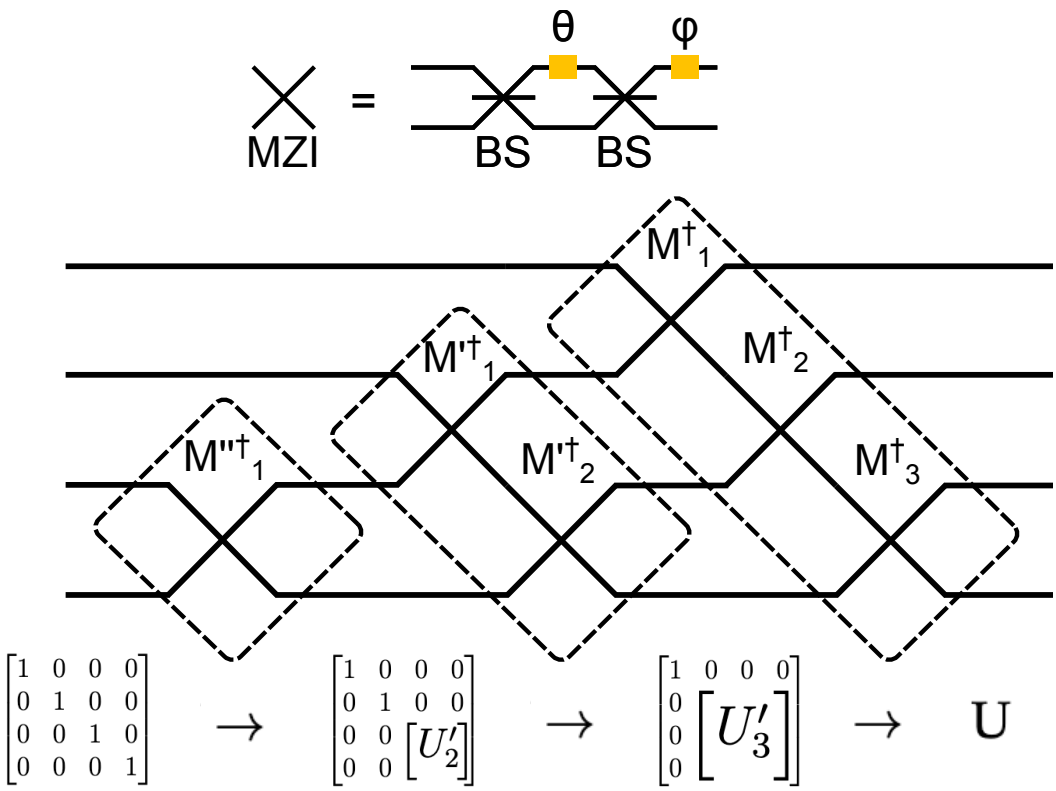

FIGURE 2.8: Reck decomposition for a four-mode unitary matrix. The decomposition is explained in detail in the main text.

Reck interferometer is shown in Fig. 2.8.

Clements interferometers

The Reck interferometer architecture is not the only valid configuration of MZIs. Clements et al. 2016 showed that one can make use of a more compact square layout of the same number of MZIs by making use of a different decomposition algorithm for the phases in the unitary. The smaller footprint means that the circuit leads to lower propagation loss, and the square configuration allows for more balanced loss for all input and output configurations. Thus, this architecture is more commonly employed in current-day experiments.

An illustration of both a Reck and a Clements interferometer for six modes is shown in Fig 2.9.

2.3.2 Linear optics with multiple photons

The unitary transformation of an interferometer describes the transformation on a single photon perfectly. However, this is not the case for states containing more than one photon. As the number of photons increases, so does the number of distinct configurations we can measure our photons in. All possible configurations are equivalent to basis states of the *Hilbert space* of our system. To describe the transformation of a multiphoton state, we

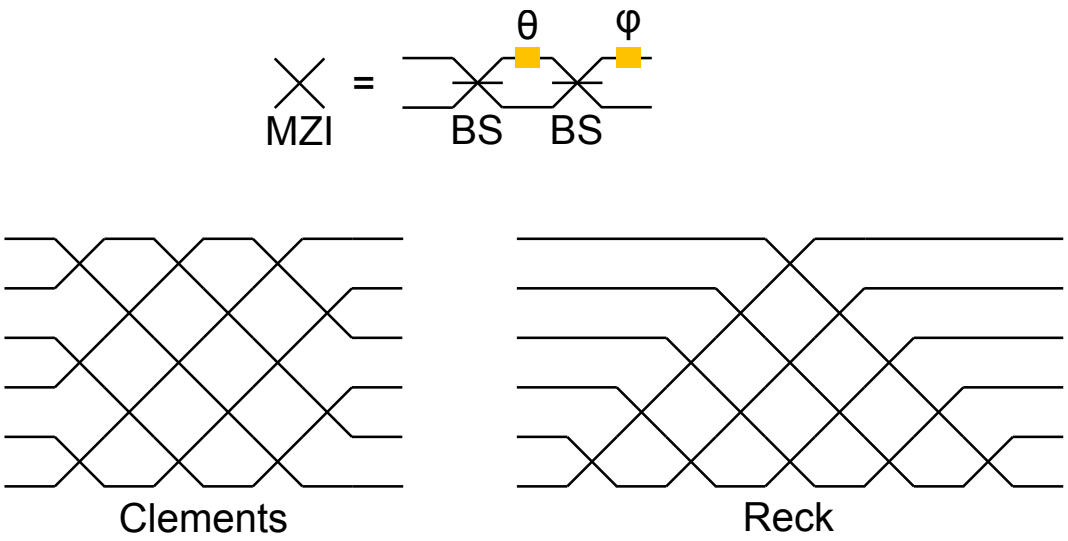

FIGURE 2.9: Clements and Reck interferometers for six modes.

need to map the interferometer's unitary matrix on the modes of the system to a unitary transformation on the multiphoton Hilbert space.

The Hilbert space for multiple photons

The Hilbert space for p photons in m modes is comprised of all possible configurations, i.e. the number of ways one can put p photons into m modes. This is equivalent to a well known result from combinatorics: p choices from m options with replacements, for which the number of combinations is:

$$\dim(\text{Hilbert space})(p,m) = \binom{m+p-1}{p}, \tag{2.49}$$

where $\binom{a}{b}$ is the binomial coefficient between a and b, otherwise known as "a choose b".

It is often useful to define two other subspaces, the *collision-free* space, and the *computational* space. In the collision-free space, we discard all states containing more than one photon in any given mode, i.e. any "collisions" between two photons. The size of this space is equal to the number of ways one can make p choices from m options *without* replacements

$$\dim(\text{Collision-free space})(p,m) = \binom{m}{p}. \tag{2.50}$$

The collision-free space is important in certain applications like boson sampling for reasons to do with the computational complexity of classical simulation. We will come back to this in Chapter 6. Another reason for why the collision-free space is important has to do with the detectors that are typically used in experiments. Some types of detectors, such as most superconducting nanowire single-photon detectors (SNSPDs), which are used for the experiments in this thesis, can only resolve the difference between any

number of photons and vacuum, and as such are often referred to as threshold detectors. Using such detectors, it is impossible to resolve the difference between states like $|2,0\rangle$ and $|1,0\rangle$. As photon loss will inevitably be present in the system, the only way we can make sure that our measurements have the right number of photons when using threshold detectors is to *postselect* the results to only include collision-free states with the correct number of photons, discarding all other measurement results as noise.

Finally, the computational space is related to the dual-rail encoding of photonic qubits, which will be explained further in Section 2.3.8. For now, we note that this encoding contains p photons in $2p$ modes, where each photon is restricted to two distinct modes. As we have two choices of modes for every photon, the size of the computational Hilbert space is

$$\dim(\text{Computational space}) = 2^p, \tag{2.51}$$

where the number of modes is fixed to $m = 2p$. The computational space is thus increasingly smaller than the collision-free space and full Hilbert space for an increasing number of photons and modes, as the latter two scale combinatorially with the numbers of photons and modes. To see an example of how the size of the collision-free Hilbert space and the computational Hilbert space compares to the full Hilbert space, see Table 2.1.

(p, m)	Full	Collision-free	Computational
(2, 4)	10	6	4
(4, 8)	330	70	16
(8, 16)	490314	12870	256

TABLE 2.1: The size of the full Hilbert space, the collision-free Hilbert space, and the computational Hilbert space for a given number of photons and modes.

2.3.3 Unitary transformation on the full Hilbert space

We now focus the attention on transforming the unitary matrix described by an interferometer, which transforms creation operators on the input modes into linear combination of creation operators on the output modes. We will make use of the matrix-permanent formalism popularized in Aaronson & Arkhipov's seminal paper introducing the boson sampling algorithm (Aaronson et al. 2011). To give an intuitive understanding of the approach, we start with a small-scale example of two photons incident on a four mode interferometer.

The Hilbert space for two photons in four modes is spanned by the following basis states

$$\text{basis}(p=2, m=4) = \begin{bmatrix} |0,0,1,1\rangle^{\text{cf}} \\ |0,1,0,1\rangle^{\text{cf, c}} \\ |0,1,1,0\rangle^{\text{cf, c}} \\ |1,0,0,1\rangle^{\text{cf, c}} \\ |1,0,1,0\rangle^{\text{cf, c}} \\ |1,1,0,0\rangle^{\text{cf}} \\ |0,0,0,2\rangle \\ |0,0,2,0\rangle \\ |0,2,0,0\rangle \\ |2,0,0,0\rangle \end{bmatrix}. \tag{2.52}$$

where the superscript cf denotes a collision-free state, and the superscript c denotes a computational state. As there are ten states in the Hilbert space, the transformation of the interferometer on the multiphoton state should be described by a 10×10 unitary matrix. We write the 4×4 unitary matrix describing the interferometer transformation as

$$U = \begin{bmatrix} u_{11} & u_{21} & u_{31} & u_{41} \\ u_{12} & u_{22} & u_{32} & u_{32} \\ u_{13} & u_{23} & u_{33} & u_{43} \\ u_{14} & u_{24} & u_{34} & u_{44} \end{bmatrix}. \tag{2.53}$$

Here, the matrix element u_{ij} corresponds to the probability amplitude associated with going from mode i to mode j, which we will call a transition amplitude. We can take a similar approach to define the unitary matrix on the full Hilbert space. In order to define the unitary transformation, we simply need to find the transition probability amplitudes between all basis states.

Suppose we want to find the transition amplitudes from state $|0,1,0,1\rangle$ to state $|1,0,1,0\rangle$. As illustrated in Fig. 2.10, this transition can be accomplished in two ways:

1. The photon in the second input mode goes to the first output mode with transition amplitude u_{21}, while the photon in the fourth input mode goes to the third output mode with transition amplitude u_{43}, or
2. The photon in the fourth input mode goes to the first output mode with transition amplitude u_{41}, while the photon in the second input mode goes to the third output mode with transition amplitude u_{23}.

To find the total transition amplitude, all we have to do is sum the two possible paths, i.e.

$$U_{|0,1,0,1\rangle \to |1,0,1,0\rangle} = u_{21}u_{43} + u_{41}u_{23}, \tag{2.54}$$

where the large $U_{|i\rangle \to |j\rangle}$ corresponds to transition elements in the full Hilbert space unitary matrix. Suppose now that we had three photons, and wanted

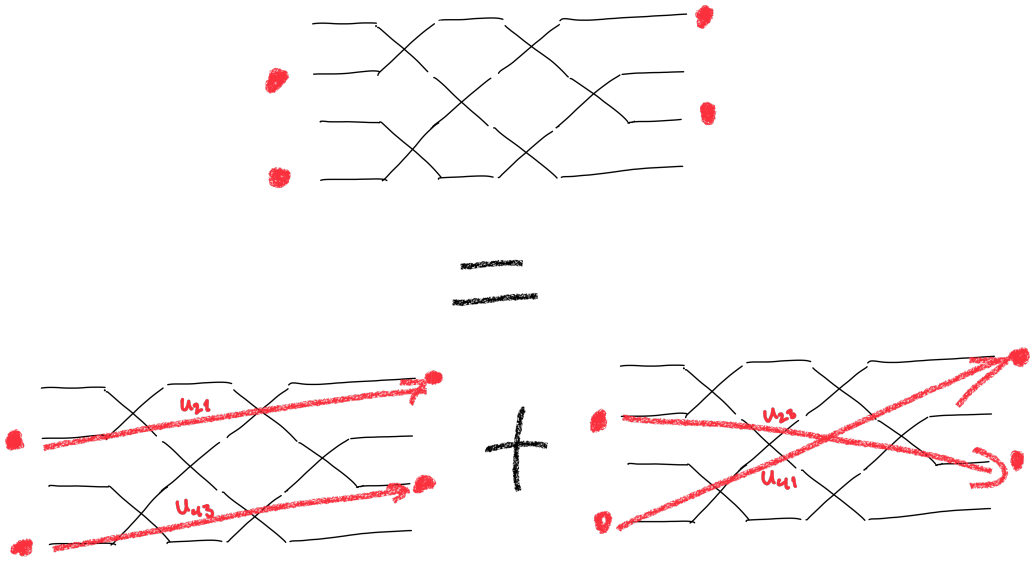

FIGURE 2.10: Transition amplitude of $U_{|0,1,0,1\rangle\to|1,0,1,0\rangle}$.

to find the transition probability amplitude $U_{|1,1,0,1\rangle\to|1,1,1,0\rangle}$. Part of this transition can be accomplished in the same way as before, if the photon in the second input mode goes to the third output mode, i.e.

$$U_{|1,1,0,1\rangle\to|1,1,1,0\rangle} = u_{12}\cdot U_{|0,1,0,1\rangle\to|1,0,1,0\rangle} + \text{Other paths.} \tag{2.55}$$

The other paths can also be represented in terms of other two photon transition amplitudes, i.e.

$$U_{|1,1,0,1\rangle\to|1,1,1,0\rangle} = u_{12}\cdot U_{|0,1,0,1\rangle\to|1,0,1,0\rangle} + u_{11}\cdot U_{|0,1,0,1\rangle\to|0,1,1,0\rangle} + u_{13}\cdot U_{|0,1,0,1\rangle\to|1,1,0,0\rangle}. \tag{2.56}$$

If we exchange the first two terms, the resulting expression is the same as the determinant of the following matrix

$$\Lambda_{|1,1,0,1\rangle\to|1,1,1,0\rangle} = \begin{bmatrix} u_{11} & u_{12} & u_{13} \\ u_{21} & u_{22} & u_{23} \\ u_{41} & u_{42} & u_{43} \end{bmatrix}, \tag{2.57}$$

only with all negative signs replaced with positive signs. This operation is called a *permanent*, such that we can (for collision-free states) find transition amplitudes according to

$$U_{|i\rangle^{\text{cf}}\to|j\rangle^{\text{cf}}} = \text{perm}(\Lambda_{|i\rangle^{\text{cf}}\to|j\rangle^{\text{cf}}}). \tag{2.58}$$

Before giving a general description for arbitrary numbers of photons and modes,let us consider what happens for collisional (i.e. not collision-free) states. Suppose we want to find the transition amplitude $U_{|2,0,0,0\rangle\to|1,1,0,0\rangle}$. Similarly to the case for $U_{|0,1,0,1\rangle\to|1,0,1,0\rangle}$, we can consider there to be two paths, as the first input photon can choose to go to the first mode or the

second mode, whilst our second input photon has to make the opposite choice. In addition to this, we need to account for the normalization of our initial state, which is written in terms of creation operators as

$$|2,0,0,0\rangle = \frac{\hat{a}_0^\dagger \hat{a}_0^\dagger}{\sqrt{2}} |0,0,0,0\rangle . \tag{2.59}$$

As the unitary matrix of the interferometer does not take this prefactor into account, we have to include a term in to find the transition amplitude for the full Hilbert space. Thus, we can write

$$U_{|2,0,0,0\rangle \to |1,1,0,0\rangle} = \frac{\text{perm} \begin{bmatrix} u_{11} & u_{12} \\ u_{11} & u_{12} \end{bmatrix}}{\sqrt{2}}. \tag{2.60}$$

We can describe the transition amplitude $U_{|1,1,0,0\rangle \to |2,0,0,0\rangle}$ in a similar manner. The first photon and second photon both have to go into the second mode. However, since there are two photons in the first mode of the output state, we include two terms as a way to describe how the first and the second output photon can originate from either of the two input photons. We have to include the same normalization factor in order for the output state to be normalized. As such, we can write

$$U_{|1,1,0,0\rangle \to |2,0,0,0\rangle} = \frac{\text{perm} \begin{bmatrix} u_{11} & u_{21} \\ u_{11} & u_{21} \end{bmatrix}}{\sqrt{2}}. \tag{2.61}$$

The generalization to transition amplitudes for an arbitrary number of photons and modes with an arbitrary number of collision is this. To find the columns in matrix $\Lambda_{|i\rangle \to |j\rangle}$, we first inspect the input state $|i\rangle = |n_1 n_2 n_3 ... n_m\rangle$ and take n_1 copies of the first column of the interferometer unitary matrix, n_2 copies of the second column, n_3 copies of the third column, and so on. For an output state $|j\rangle = |k_1 k_2 k_3 ... k_m\rangle$ we similarly take k_1 copies of the first row, k_2 copies of the second row, k_3 copies of the third row, and so on. In order for our output state to be normalized, we need to multiply by the prefactor

$$\frac{1}{\sqrt{n_1! \cdot n_2! \cdots n_m!}} = \frac{1}{\sqrt{\prod_l n_l!}} \tag{2.62}$$

for the input state and

$$\frac{1}{\sqrt{k_1! \cdot k_2! \cdots k_m!}} = \frac{1}{\sqrt{\prod_l k_l!}} \tag{2.63}$$

for the output state.

Thus, we can define the generalized expression for a transition amplitude from the input state $|i\rangle$ to the output state $|j\rangle$ as

$$U_{|i\rangle\to|j\rangle} = \frac{\text{perm}(\Lambda_{|i\rangle\to|j\rangle})}{\sqrt{\prod_l n_l!}_{n_l\in|i\rangle}\sqrt{\prod_l k_l!}_{k_l\in|j\rangle}} \tag{2.64}$$

A brief note on postselection

As mentioned, experiments may restrict the Hilbert space to the collision-free subspace or the computational subspace by discarding all measurements of basis states that are not within the desired subspace. We can represent postselection mathematically as discarding certain parts of the output state and renormalizing the remaining probability amplitudes. For example, for the two-photons in four modes case, we start with the vector

$$|\psi\rangle_{\text{out}} = \begin{bmatrix} c_0 \\ c_1 \\ c_2 \\ c_3 \\ c_4 \\ c_5 \\ c_6 \\ c_7 \\ c_8 \\ c_9 \end{bmatrix}, \tag{2.65}$$

where the corresponding basis states is shown in Eq. 2.52. For the collision-free basis, we only keep the elements with the superscript 'cf' in Eq. 2.52, and renormalize by the total probability of a collision-free output such that the total probability of our state is 1:

$$|\psi\rangle_{\text{out, cf}} = \frac{1}{\sqrt{|c_0|^2+|c_1|^2+|c_2|^2+|c_3|^2+|c_4|^2+|c_5|^2}} \begin{bmatrix} c_0 \\ c_1 \\ c_2 \\ c_3 \\ c_4 \\ c_5 \end{bmatrix}. \tag{2.66}$$

As the renormalization of elements depends on the probability amplitudes of the output state, which depend on the probability amplitudes of the input states, the unitary transformation in the collision-free subspace will depend on the input state, and as such we cannot represent it with a single unitary matrix.

2.3.4 Loss in quantum photonic experiments

Loss of photons plays a uniquely important role in experiments dealing with quantum states of light. As all optical components are associated with

some probability of an input photon being lost, we are by no means guaranteed that all of the photons produced at the start of our experiment will reach the detectors. Accordingly, loss is a big source of error for experiments and requires error mitigation or correction strategies. Classical information processing mitigates the effect of loss by making use of repeater stations, where the information stored in a lossy input state is copied over to a new output state. For quantum information processing however, this type of error mitigation strategy is much harder due to the *no-cloning theorem* (Nielsen et al. 2000) which prohibits direct copying of information from one state to another. Quantum repeater schemes (Borregaard et al. 2020) and error correction schemes (Bartolucci et al. 2023) are active areas of research, but current state-of-the-art proposals pose stringent requirements on hardware beyond state-of-the-art performance.

For experiments where Fock states are used, we can make use of the property that the total number of photons is fixed. Thus, by postselecting events where we detect the same number of output photons as input photons, we can mitigate the effect of loss at the output. This property is also referred to as loss being heralded, meaning that though loss has a certain 'success' probability, you know the events where a success has occurred.

Mathematical model

In order to see what happens to a photonic state upon loss and postselection, we need to be able to model it. A mathematical description of postselection was already introduced in the formalism of unitary transformation on the multiphoton Hilbert space. Thus, we need to be able to model loss in this formalism. We model loss for a given component by adding variable-reflectivity beamsplitters (i.e. MZIs) at the output of the component connected to ancillary modes. Recall that this transformation is written as

$$U_{\text{loss}} = \begin{bmatrix} \cos(\theta_{\text{loss}}/2) & i\sin(\theta_{\text{loss}}/2) \\ i\sin(\theta_{\text{loss}}/2) & \cos(\theta_{\text{loss}}/2) \end{bmatrix}. \tag{2.67}$$

Here, we can find the value for θ_{loss} by considering the probability that a photon is lost should be P_{loss}, such that $\sin^2(\theta_{\text{loss}}/2) = P_{\text{loss}}$. Thus, we can describe any level of loss by fixing the value of θ_{loss}.

In this model, it is important that every loss-beamsplitter is connected to its own separate loss-mode. Otherwise, it would be possible for a photon to be lost at one point through one loss-beamsplitter, and then re-enter the circuit at a later point through a different loss-beamsplitter. This leads to an important property: statistical independence. As the beamsplitter is a linear optical component, it treats every photon independently, and as a result, the loss of two different photons are statistically independent events. Moreover, as the other input port of the loss-beamsplitter is always connected to the vacuum, and since the output port is never connected back to the interferometer, interference will never play a role. Thus, it does not matter if the photons are indistinguishable or not.

A potential downside of this description is that adding an additional

mode for every component in our experiment results in a lot of additional modes, which quickly increases the size of our Hilbert space. However, we note that the output is postselected to not include the cases where photons are lost. As the first step of the postselection procedure is to discard all elements that we don't want, we can simply model loss by multiplying each component by the factor $\cos(\theta_{\text{loss}})$, disregarding all modes we are not interested in. As a result, the matrix describing the interferometer, and the matrix describing the transformation on the full Hilbert space will no longer be unitary, and we again have to ensure unity probability of the output state by renormalizing the initial output state, $|\psi\rangle'_{\text{out}}$, as

$$|\psi\rangle_{\text{out}} = \frac{1}{\sqrt{\sum_i |c_i|^2}_{c_i \in |\psi\rangle'_{\text{out}}}} |\psi\rangle'_{\text{out}} \,. \tag{2.68}$$

This has an important consequence: if there are multiple optical paths with an unequal number of optical components, i.e. such that loss is not balanced for all paths, the measured output distribution will be different from the case where there is no loss. Thus, the effect of unbalanced losses cannot be completely mitigated using postselection. An example of an unbalanced setup is the Reck interferometer. For an m-mode interferometer, the shortest path traverses a single MZI, whereas the longest path has to go through $2m-1$ MZIs. This makes the Clements interferometer more suitable for experiments.

Propagation loss

Up until now, we have talked about optical loss in terms of components, however, it is important to note that propagation through any medium except for vacuum will incur *propagation loss*. For a bulk material, propagation loss occurs due to the photon being absorbed, and if the material is shaped into a waveguide, surface roughness will lead to additional scattering-induced losses. We can model losses due to propagation in the exact same way, where we associate a probability of survival for every unit of length. As an example, if there is a $1 - P_{\text{prop}} = 10\%$ probability of losing a photon after 1 cm of propagation, then the probability of the photon surviving after 2 cm of propagation will be $P_{\text{prop}}^2 = 81\%$. It is usually more practical to express propagation loss, and indeed other losses, in units of decibel. The decibel loss, which we will denote with the Greek letter ρ, is defined as

$$\rho = 10 \cdot \log_{10}(P), \tag{2.69}$$

where P is the probability of survival. For the rest of the thesis, we will refer to percentage survival probabilities as *efficiencies* and decibel probabilities as *losses* for convenience. In units of decibel, we can define a propagation loss per unit length. Continuing our example where $90\,\%$ of the initial amount of light remains after one centimeter of propagation, the per-cm propagation

loss would be

$$\rho_{\text{prop}} = 10 \cdot \log_{10}(0.9)\text{dB/cm} \approx 0.46\text{dB/cm}.$$

To find the loss for any given length, we simply multiply this value by the length of propagation we're interested in. This can be done as products of efficiencies translate into sums of losses, as losses are logarithmic. Similarly, exponents translate into multiplication. Thus, instead of multiplying together the efficiency of every component, we can simply sum their decibel losses and translate this back into a probability at a later point.

2.3.5 Optical components

As we have established in a previous section, only two types of components—beamsplitters and phase-shifters—are needed to construct interferometers capable of implementing any linear optical transformation. The experimental implementation of these transformations differs depending on the degree of freedom used to encode the modes, i.e. we may use different components for the polarization encoding compared to the path encoding. Before introducing specific components, we will examine how the phase of light can be altered by altering the media in which it propagates. Proceeding, the focus is restricted first to the path encoding and then to the polarization encoding, introducing important optical components used in the construction of experimental setups. We round off by talking about the demultiplexer, which is used to convert from the time-bin encoding to the spatial encoding, which is instrumental for the use of single quantum emitters with path encoded interferometers. Note that time-bin encoded interferometers will be introduced later in Chapter 3.

The phase of a photon

The phase of a photon is related directly to its wave-like nature, and is best understood in this picture. As illustrated in Fig. 2.11, the phase of a photon changes along the propagation direction proportionally to the refractive index, n of the material. The refractive index is defined according to the speed of light, v in the material, such that

$$v = c/n, \tag{2.70}$$

where c is the speed of light in vacuum. Specifically, for light propagating in the direction z, we can describe the phase of the light according to the electric field, which evolves in space according to

$$E(z) \propto e^{ikz}, \tag{2.71}$$

where k, the wavenumber, is defined as

$$k = 2\pi n/\lambda, \tag{2.72}$$

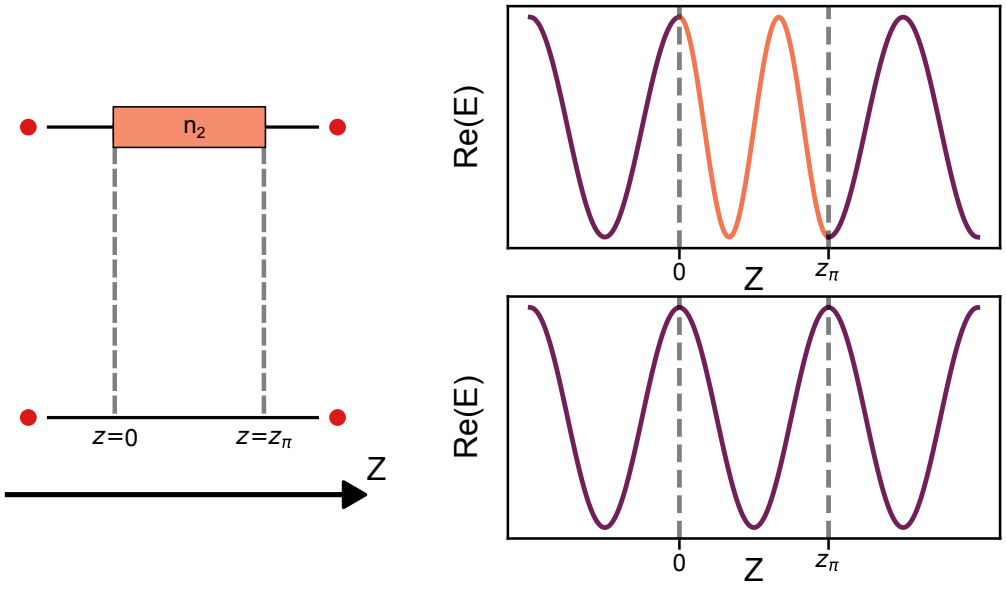

FIGURE 2.11: Illustration of how a phase-shifter can be implemented by letting one mode propagate through a medium with a different refractive index n_2. In the illustration, the length of the phase-shifter has been set to a specific value, z_π, to implement a specific relative phase-shift of π on the top mode compared to the bottom mode. z is the direction of propagation for both modes.

where λ is the vacuum wavelength of the light.

A phase-shifter between two modes can be implemented by altering the refractive index of one mode compared to the other, as indicated in Fig. 2.11. For instance, implementing a phase shift of π between the two modes is equivalent to finding a length of propagation, z_π such that

$$k_1 z_\pi - k_2 z_\pi = \frac{2\pi}{\lambda}(n_1 - n_2) z_\pi = \pi. \tag{2.73}$$

Path encoding in bulk optics and photonic integrated circuits

In path encoding, where different modes correspond to the photon propagating in different spatial paths, there are two main approaches used to implement phase-shifters.

The first option, which is exclusively used in bulk optics experiments, is to alter the relative length difference between different paths. To understand how this happens, consider that paths in bulk optics experiments are defined with mirrors, as seen in Fig. A.1 in Appendix A.1. Small perturbations to the angle and position of these mirrors, induced e.g. by vibrations, can easily lead to sufficient path length difference for significant phase shifts

(i.e. hundreds of nanometers). In order to stabilize such setups, one typically has to make use of piezoelectric mirrors that allow for electrical tuning of their position and angle. By implementing a feedback control protocol, one can maintain a fixed phase between the modes. Specifying this fixed phase amounts to specifying a specific phase shift within the interferometer.

The second option, which is the main method used in photonic integrated circuits, is to send the modes through materials with a tunable refractive index. By using media with electro-optic or thermo-optic effects, the refractive index of the material can be tuned by applying a voltage or changing the temperature, allowing for the specification of an arbitrary phase. Such electro-optic phase-shifters are used in the experiment detailed in Chapter 5.

To implement a beamsplitter in path encoding, we need an optical component that splits incoming light between two modes. In bulk optics, this is typically achieved by making use of beamsplitter prisms, which have a partially reflective coating. In photonic integrated circuits, on the other hand, we make use of the waveguides the light is already confined in to construct *directional couplers*. Directional couplers make use of the fact that the mode profile of the light confined in the waveguide has an evanescent tail outside of the waveguide. This means there's an exponentially decreasing component of the mode that exists outside of the waveguide. By bringing two waveguides together to a very small separation for a fixed length, the evanescent tail of the mode confined in one waveguide will enter into the other waveguide. This leads to the mode slowly leaking from one waveguide to the other. By fixing the length and separation of the directional coupler to suitable values, we can implement a beamsplitter with a perfect 50% splitting ratio described by the matrix

$$U_{\mathrm{DC}} = \frac{1}{\sqrt{2}} \begin{bmatrix} 1 & i \\ i & 1 \end{bmatrix}. \tag{2.74}$$

Additional considerations in the path encoding, such as alignment and coupling into and out of photonic integrated circuits is covered in Appendix A

Polarization encoding

In free-space, i.e. bulk optics experiments, the electric field of any photon is only restricted to be polarized[3] perpendicularly to the direction of propagation, such that we can always represent it as a linear combination of two perpendicular polarizations. Thus, we can encode two modes, corresponding to the photon being polarized either along a horizontal or along a vertical axis. For the polarization encoding, we have to make use of a different approach to implement phase shifts as the two modes share the same spatial path. To this end, we can exploit a material property called birefringence.

[3]One can also have *unpolarized* light, in which case the polarization is a statistical mixture.

For birefringent media, the refractive index is higher along the so-called ordinary axis than along the perpendicular extraordinary axis. As such, by aligning the ordinary axis of a birefringent material with the horizontal or vertical polarization axis, we can implement a phase shift between the two modes by letting them propagate through a specific length of material, or by tuning the strength of the birefringence with a fixed length of material. In the former approach, if the length of material leads to a phase shift of π ($\pi/2$), we call the resulting optical component a *half-wave plate* (*quarter-wave plate*). These components can also be used to implement beamsplitters, by rotating the orientation of the ordinary and extraordinary axis with respect to our horizontal and vertical modes. Specifically, rotating a half-wave plate $\pi/8$ radians with respect to the horizontal or vertical axis, results in a transformation described by the matrix

$$U_{\mathrm{HWP}}(\pi/8) = \frac{1}{\sqrt{2}} \begin{bmatrix} 1 & 1 \\ 1 & -1 \end{bmatrix}, \tag{2.75}$$

i.e. a 50/50 beamsplitter Hecht 2002. Thus, in polarization encoding, we can implement either a phase-shifter or beamsplitter between two modes by making use of birefringent materials with ordinary and extraordinary axes in specific orientations with respect to the horizontal and vertical axes defining the modes.

The polarization encoding is restricted to two modes per spatial path. If more modes are desired, we have to make use of a different degree of freedom, like spatial modes or time-bins. Here, we will consider the use of multiple paths, which is also a key requirement for time-bin interferometers based on polarization-and-time-bin encoding as will be explained in more detail in Chapter 4. We associate each spatial path with two polarization modes and can convert between polarization modes in a given path by using wave-plates. However, in order to implement multimode interferometers, we also have to be able to interfere specific modes that are not initially found in the same path. To this end, we can make use of *polarizing beamsplitters* (PBSs), which transmit one polarization and reflect the perpendicular polarization. This allows us to convert back and forth between polarization and path degrees of freedom. An example of how this works in practice is shown for a four mode interferometer in Fig. 2.12. For the third and sixth MZIs, the vertical polarization from the first spatial path is switched into the second spatial path using two PBSs, and after the MZI, another set of PBSs reverts the vertical polarizations back to their original paths.

Constructing a demultiplexer using time-dependent wave-plates

Birefringent media and PBSs allow for the easy construction of time-to-path *demultiplexers*, which are used to convert from a time-bin encoding to a path encoding. Recall that using a single quantum emitter, we can produce strings of single-photons in the same mode with a fixed temporal spacing. This is equivalent to a time-bin encoded state with one single-photon

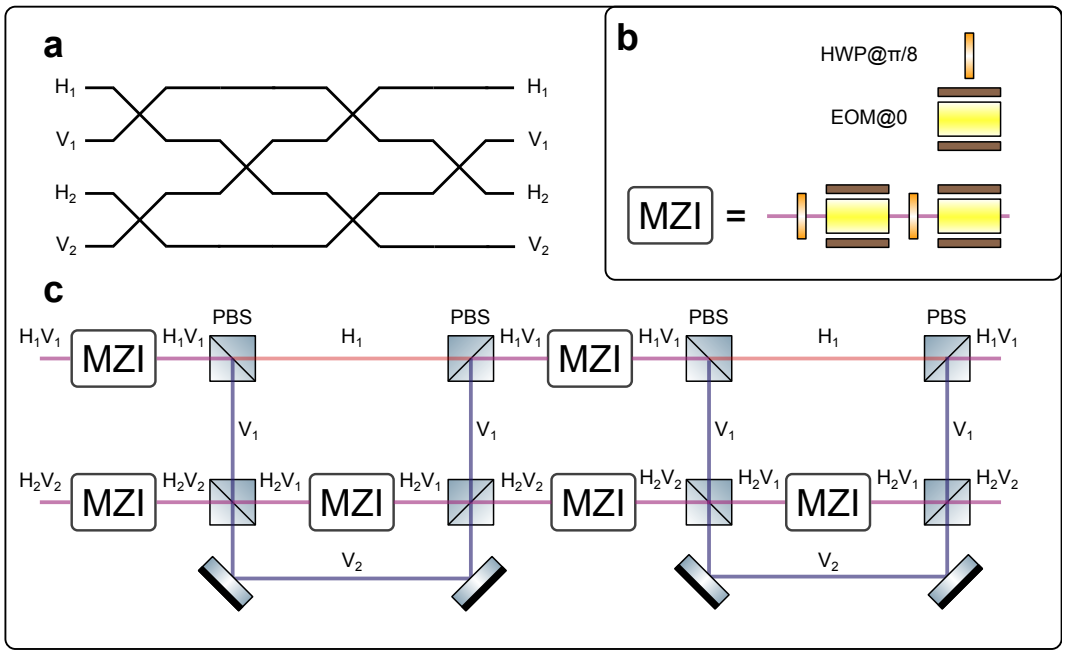

FIGURE 2.12: Schematic of an experimental setup to implement a universal four mode Clements interferometer with path-and-polarization encoding. **a** A schematic of the circuit in terms of MZIs (crosses). **b** Schematic of how an MZI can be implemented in the polarization, using two half-wave plates (HWPs) rotated by $\pi/8$ radians with respect to the horizontal polarization axis, and two birefringent electro-optic modulators (EOMs) with the fast axis oriented parallel to the horizontal polarization axis. **c** Circuit schematic of the four-mode Clements interferometer implemented in the polarization–path encoding using MZIs, polarizing beamsplitters (PBSs) and mirrors.

per time-bin. To be able to make use of this source in multiphoton experiments with path-encoded interferometers, we first need to use a demultiplexer to convert the input state to the path encoding. The most efficient way to construct a demultiplexer is to use a binary tree of *optical switches*, as illustrated for four modes in Fig. 2.13, after which the photons can be synchronized by adding an appropriate delay to each mode except for the last. Each optical switch should be able to switch photons coming in at different times into different modes, reconfiguring its transformation in-between time-bins. One option would be to use a completely path encoded MZI with time-dependent phases, however, it would have to be phase-stable. Instead, in our experiments, we make use of birefringent media, where the birefringence, i.e. the difference in refractive index between the ordinary and extraordinary axis, is proportional to an applied electric field. This effect is known as the *Pockels effect* (Saleh et al. 2007). Thus, by rotating the extraordinary axis $\pi/8$ radians with respect to the reflected polarization axis of a PBS, and applying either a half-wave voltage or a full-wave voltage, we can choose whether photons entering our device are transmitted or reflected, thus implementing an optical switch without the need for phase-stabilization. Thus, we can construct a demultiplexer by chaining together such electro-optic modulators and PBSs.

2.3.6 Building blocks for photonic quantum computing

The framework we have introduced serves to explain the properties of single photons and how they behave in a linear optical circuit. In this section we will contextualize this information by introducing the building blocks of quantum information processing, and how they can be realized in the photonic approach to quantum computing. We start with a description of the fundamental unit of a qubit and key properties of multiqubit states. We then show how linear optics with single-photons is well-suited to certain qubit operations, and less suited to others. To end the chapter, we introduce the building blocks required to implement fusion-based quantum computing (Bartolucci et al. 2023), a paradigm tailor-made for photonic quantum computing, and introduce the building blocks that are needed in this approach.

2.3.7 Qubits

A qubit is a system described by a quantum state $|\psi\rangle$ which can exist either in the mode $|0\rangle$, $|1\rangle$, or any superposition of the two

$$|\psi\rangle_{\text{single-qubit}} = \alpha\,|0\rangle + \beta\,|1\rangle\,, \tag{2.76}$$

subject to the constraint $|\alpha|^2+|\beta|^2 = 1$, i.e. α and β are complex-valued probability amplitudes. The state of a single-qubit can be visualized by mapping it onto the surface of the so-called *Bloch sphere*, illustrated in Fig. 2.14. With this mapping, the quantum state is described by vector pointing to a position on the surface of this sphere. The states $|0\rangle$ and $|1\rangle$ are mapped to the

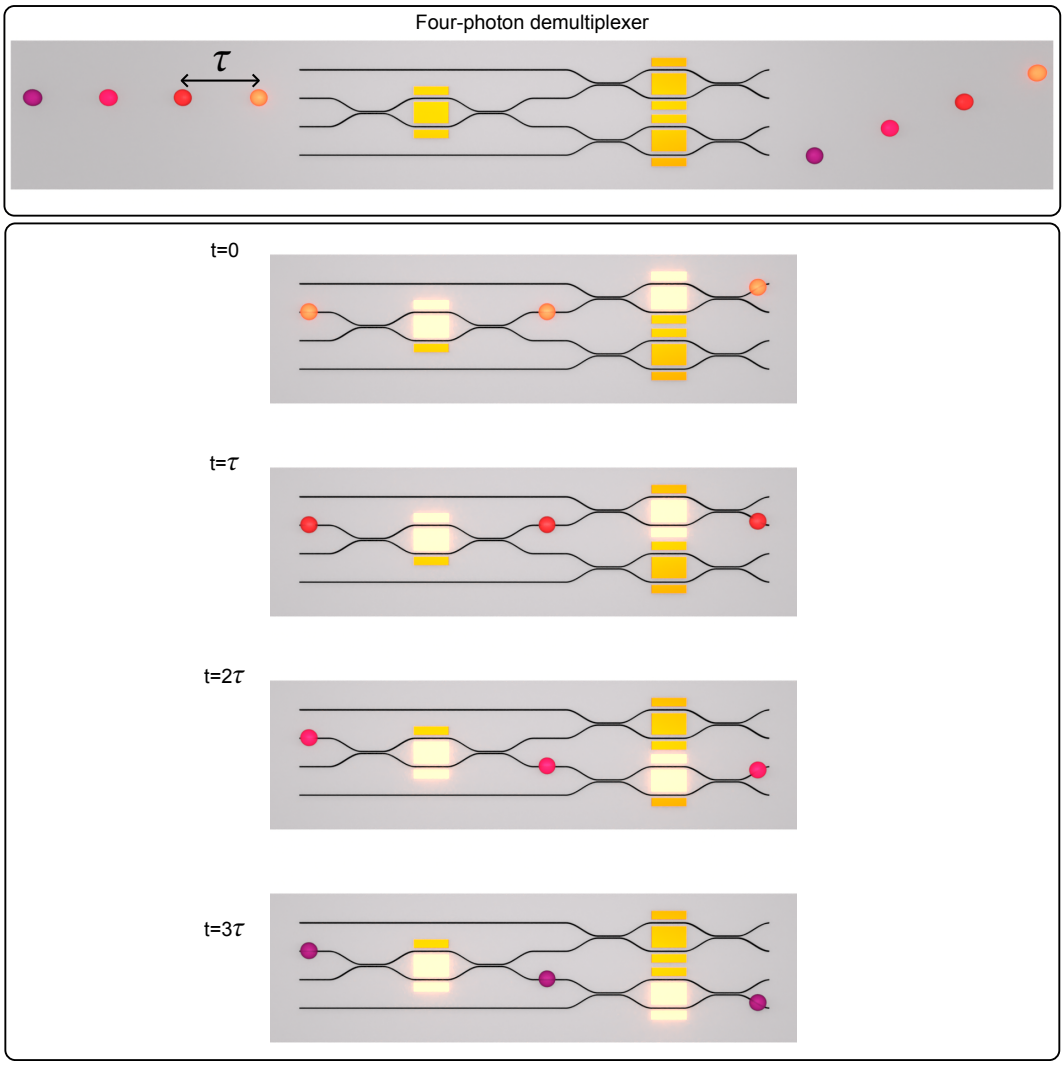

FIGURE 2.13: A four mode temporal-to-spatial demultiplexer based on a binary tree of reconfigurable switches. The switches can be configured to either switch photons to the top or bottom mode, as indicated for each time-bin. Color has been added to the photons for visual clarity, where the color corresponds to the arrival time of the photon. This color is not representative of the wavelength of the photons. The photons can be synchronized by adding a delay of 3τ to the first mode, 2τ to the second mode, and τ to the third mode.

north pole and the south pole, respectively, such that the polar angle θ determines the ratio between $|\alpha|^2$ and $|\beta|^2$, whereas the azimuthal angle ϕ determines the phase between α and β. Single-qubit transformations will shift the state from one point on the surface to another, which can be achieved by rotating the vector about some axis. As such, it is common to refer to single-qubit transformations as *rotations*.

Measuring the qubit will yield a result of $|0\rangle$ with a probability of $|\alpha|^2$ or $|1\rangle$ with a probability of $|\beta|^2$, which, in terms of the Bloch sphere, only gives information about the polar angle θ. This corresponds to a projection on the z-axis of the Bloch sphere, and as such is commonly referred to as a *z-basis* measurement. In order to characterize the complete state of the system, we have to additionally measure the state in two bases that are both mutually orthogonal and orthogonal to the z-basis, such as the x-basis and the y-basis. To this end, we can apply single qubit rotations to rotate 90 degrees about either the y-axis or x-axis. If a state were to point to one of the poles on the x-axis or y-axis, respectively, it would be transformed to a state pointing at the one of the poles on the z-axis. By measuring the now-altered state in the z-basis, we will effectively measure the original state in the x-basis or y-basis. This technique will be used to characterize the fidelity of a generated state with respect to a target state in Chapter 4.

An important property of quantum mechanical systems emerges for states of two qubits or more. The two-qubit state can be written as

$$|\psi\rangle_{\text{two-qubit}} = \alpha\,|00\rangle + \beta\,|01\rangle + \gamma\,|10\rangle + \delta\,|11\rangle\,, \tag{2.77}$$

where the first entry in the state vector refers to the state of the first qubit, and the second entry refers to the state of the second qubit. We can categorize two-qubit states as being either *separable* or *nonseparable*, determined by whether or not the state can be written as a product of two single-qubit states. An example of a separable state could be

$$|\psi\rangle_{\text{separable}} = \frac{1}{2}\,|00\rangle + \frac{1}{2}\,|01\rangle + \frac{1}{2}\,|10\rangle + \frac{1}{2}\,|11\rangle = \frac{1}{\sqrt{2}}\left(|0\rangle_0 + |1\rangle_0\right)\frac{1}{\sqrt{2}}\left(|0\rangle_1 + |1\rangle_1\right). \tag{2.78}$$

An example of a nonseparable state, on the other hand, is

$$|\phi_+\rangle = \frac{|00\rangle + |11\rangle}{\sqrt{2}}. \tag{2.79}$$

Nonseparable states exhibit a uniquely quantum mechanical property known as *entanglement*. For entangled two-qubit states, measuring the state of one qubit gives information of the state of the other qubit. For instance, by measuring the first qubit of the state $|\phi_+\rangle$, we can predict the state of the second qubit with certainty. Operations that transform separable states into nonseparable states are known as *entangling gates*, and play an instrumental role in quantum information processing.

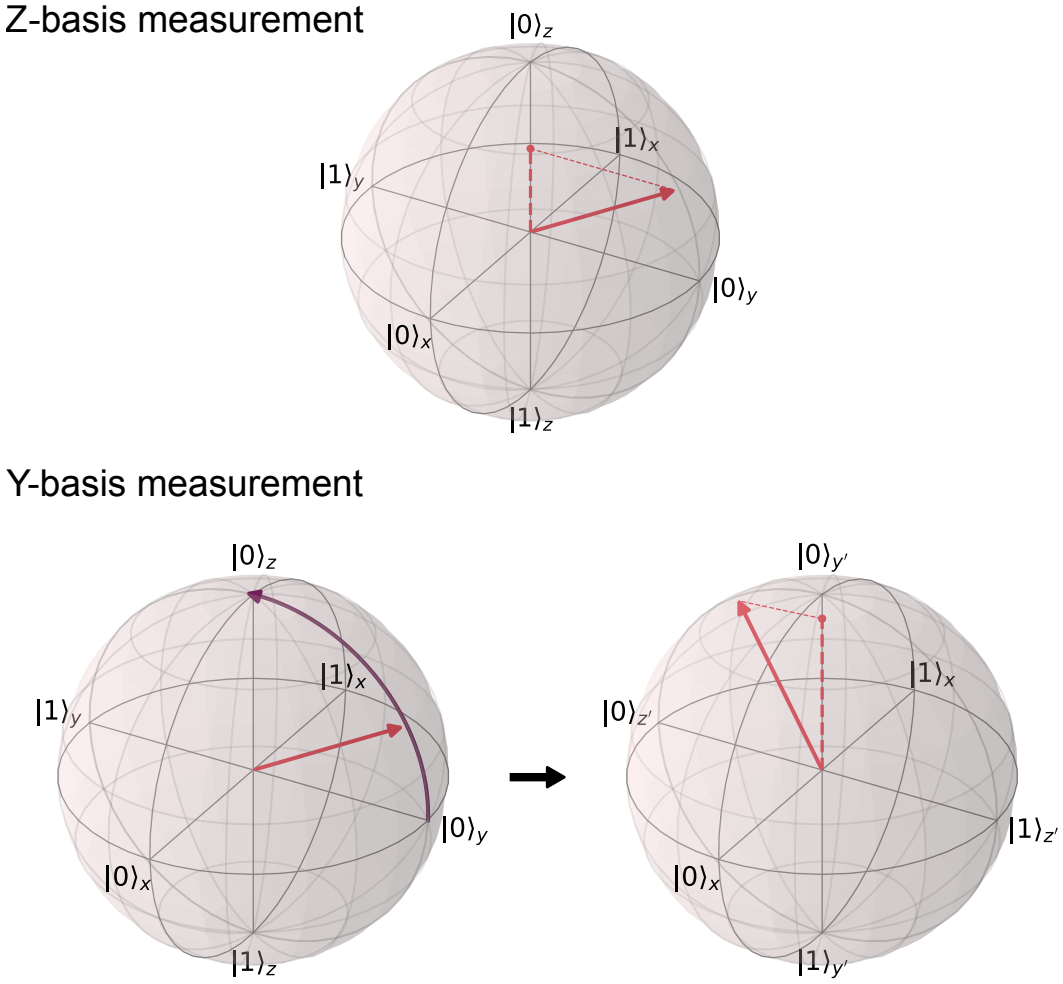

FIGURE 2.14: *Top* A z-basis measurement on a qubit. Associating a measurement of $|0\rangle$ with a value of 1 and a measurement of $|1\rangle$ with a value of -1, the expectation value of our measurement corresponds to the projection of the state $|\psi\rangle = \alpha|0\rangle + \beta|1\rangle$, indicated by the red vector, along the z-axis to the coordinate $z = |\alpha|^2 - |\beta|^2$. *Bottom* A y-basis measurement on a qubit. The qubit is first transformed by rotating the vector by $\pi/2$ about the x-axis, as indicated by the purple vector, effectively rotating the y-axis of the Bloch sphere to point along what was previously the z-axis. Thus, performing a z-axis measurement after the rotation effectively performs a y-axis measurement on the state before the rotation.

2.3.8 Photonic qubits

The attentive reader might have found the single-qubit state in Eq.(2.76) familiar, as it is equivalent to the state of a single photon in two modes with the following substitutions

$$\begin{aligned} |0\rangle_{\text{qubit}} &= |1,0\rangle_{\text{single-photon}}\,, \\ |1\rangle_{\text{qubit}} &= |0,1\rangle_{\text{single-photon}}\,. \end{aligned} \tag{2.80}$$

This encoding is called the *dual-rail* encoding, where each qubit is encoded as a single-photon in one of two modes. As was mentioned earlier in Section 2.3.2, for larger numbers of photonic qubits there is a discrepancy of the Hilbert space of the qubits, referred to as the *computational* Hilbert space, and the full photonic Hilbert space. Moreover, linear optics is limited in the types of operations that can be performed. For operations on individual qubits, we know from Section 2.3.1 that an MZI with a sufficient number of phase-shifters on the two photonic modes of the qubit is sufficient for any transformation. As linear optical components always transform each photon independently, it is impossible to use them to transform a separable state into a nonseparable state, i.e. there are no entangling gates.

However, this is only the case if we consider the whole output state. We can rewrite separable states as superpositions containing nonseparable states. Take, for instance, the separable state in Eq. (2.78). This state can be written as

$$|\psi\rangle_{\text{separable}} = \frac{|00\rangle + |11\rangle}{\sqrt{2}} + \frac{|01\rangle + |10\rangle}{\sqrt{2}}, \tag{2.81}$$

i.e. a superposition of two nonseparable states. As such, linear optics can be used for the *probabilistic* generation of entangled state. This probabilistic generation can be done either in a *heralded* manner or an *unheralded* (also called postselected) manner. In a heralded scheme, a successful event in the probabilistic scheme is accompanied by a specific measurement outcome of an ancilla photon. As this ancilla photon can be measured separately and independently from the photons used for the photonic qubit, it will *herald* the presence of an entangled state in the remaining unmeasured qubits, after which the state can be used e.g. in a computation. As for the unheralded case, the success is known upon the measurement of the photonic qubits, and as such, one typically has to remove unsuccessful events through post-selection.

Heralded generation of entanglement originates in a seminal paper by Knill, Laflamme, and Milburn (Knill et al. 2001), which introduced a scheme for universal quantum computing using linear optics and single-photons. In this scheme, named the KLM scheme after the initials of the authors, nonlinear operations (which are required for entangling operations) are implemented by introducing additional ancillary modes containing an additional ancilla photon. A small interferometer is used to interfere the ancilla photon with the computational photons, after which the state in the ancilla

modes is measured. The detection of a specific output state in the ancilla modes heralds a nonlinear phase shift on the photonic state in the computational mode. Though the success probability of the scheme with one ancilla photon is limited to $1/4$, additional ancillary photons and modes can be introduced to increase the success probability close to unity using a protocol called *gate teleportation* (Knill et al. 2001). The downside of the KLM scheme is that it does little to introduce resilience to errors, which become increasingly dominant as the system is scaled up. However, heralded entanglement generation provides an excellent way to generate entangled resource states of a limited number of qubits, which are the starting point for fusion-based quantum computing.

In fusion-based quantum computing (FBQC), error correction and computation are performed by arranging a large number of entangled resource states of a small number of qubits and *fusion gates* between them in a *fusion network* (Bartolucci et al. 2023). A *fusion gate* is a probabilistic entangling operation performed on two qubits in two separate entangled states. Both computations and error correction require the use of a photonic circuits and switches that can be reconfigured to implement various fusion gates, and single-qubit measurements in a set of different bases. As such, the hardware required for FBQC is:

1. An entangled resource state generator.

2. Rapidly reconfigurable linear optical interferometers to perform fusion switching, fusion gates, and single-qubit measurements.

3 Time-bin interferometer architectures

An on-demand single-photon source can be triggered periodically to produce a string of single photons with a fixed temporal separation. Considering the creation time of each single photon as a mode, this approach produces a *time-bin* encoded multimode state. As the time-bin encoding is the natural encoding of on-demand single-photon sources, we will explore how interferometers can be implemented in this encoding. We start by introducing the single-path and two-path time-bin encodings, and show how they are well-suited to implement time-bin versions of the Reck and Clements architecture, respectfully. We proceed to show that the time-bin encoding is uniquely well-suited for the implementation of *mode crossings* and identify how this can be used to implement a variety of permutation matrices on the modes. With this knowledge, we develop novel interferometer architectures with the aim of reducing optical depth and time-delay, resulting in specialized architectures where the optical depth scales logarithmically with the number of modes. We show how a similar approach allows for a *demultiplexing* (*multiplexing*) architecture, taking a time-bin encoded (path encoded) input state and producing a path encoded (time-bin encoded) output state. We end by showing how logarithmic-depth interferometer architectures can be used to enact discrete Fourier transform matrices up to a relabeling of inputs and outputs when the number of modes is a power of two.

3.1 Time-bin interferometers with one or two spatial paths

In Section 2.3.1 we saw how multimode interferometers can be constructed using the basic building block of two-mode MZIs, consisting of two beamsplitters and two phase shifters. For spatially encoded states, where each state occupies its own spatial path, interferometers can be constructed by arranging MZIs in either a triangular (Reck) or square (Clements) architecture. For temporally encoded states, where modes occur at different times, the construction is slightly more complicated, and the ideal architecture depends on the exact number of spatial paths used in the time-bin encoding. In the following we will focus on two distinct time-bin encodings: 1. The *single-path* encoding, where all modes occupy individual time-bins in the

same spatial path, and 2. The *two-path* time-bin encoding, where every time-bin contains two modes defined by corresponding spatial paths.

A brief comment on the symbols used in the figures

The figures in this chapter represent time-bins using ⊔ symbols. The time-bins travel at the speed of light toward the right. As such, time-bins to the right will be earlier than time-bins to the left. The colors of the time-bins are added for visual clarity.

3.1.1 MZIs in the single-path time-bin encoding

We start by considering in the single-path time-bin encoding, where all of the modes are encoded using the temporal degree of freedom, for which the first interferometer architecture was proposed by Motes et al. 2014, and has been experimentally implemented in Carosini et al. 2023. In order to implement an MZI on such a state, we need a phase shifter that can be reconfigured between time-bins, as well as a beamsplitter taking two inputs only separated by time. There is no single component that acts like a beamsplitter in time, but we can construct one from three configurable MZIs connected by a delay, as shown in Fig. 3.1b. Here, we temporarily add an additional spatial path. The first time-bin is switched into the newly-added bottom mode by enacting a swap transformation with the first MZI, after which the MZI is reconfigured to enact a unity transformation to let the second time-bin into the top mode. The bottom mode contains a delay of one time-bin such that the two modes arrive at the middle MZI simultaneously. At this point, we have converted the first two modes to a spatial encoding, such that we can use a spatially encoded MZI to enact the desired unitary transformation, i.e. the same transformation as is used in Fig. 3.1a. The top output mode of the second MZI is connected to a delay, restoring the temporal separation between the modes. The final MZI then switches the first output time-bin into the top output mode with a swap transformation and lets the second time-bin pass into the top output mode with a unity transformation, restoring the original time-bin encoding to a single spatial path.

The same result can be achieved by using only a single MZI, by connecting one of the output modes of the MZI to an input mode through a delay, as is shown in Fig. 3.1c. This MZI plays the role of all three MZIs, enacting a swap transformation during the first and last time-bins, and enacting the desired transformation during the middle time-bin. If we add an additional third time-bin to this looped MZI, then top output of the interference between the first two time-bins will meet the third time-bin after being looped back through the delay to meet the third time-bin. As such, a single looped MZI allows for the implementation of a diagonal of MZIs. This makes the single-path time-bin encoding particularly suitable for the implementation of the Reck architecture. We identify this as a building block which we will call the "Reck MZI". In order to construct a complete Reck-style interferometer, as shown in Fig. 2.9, we need to implement multiple diagonals.

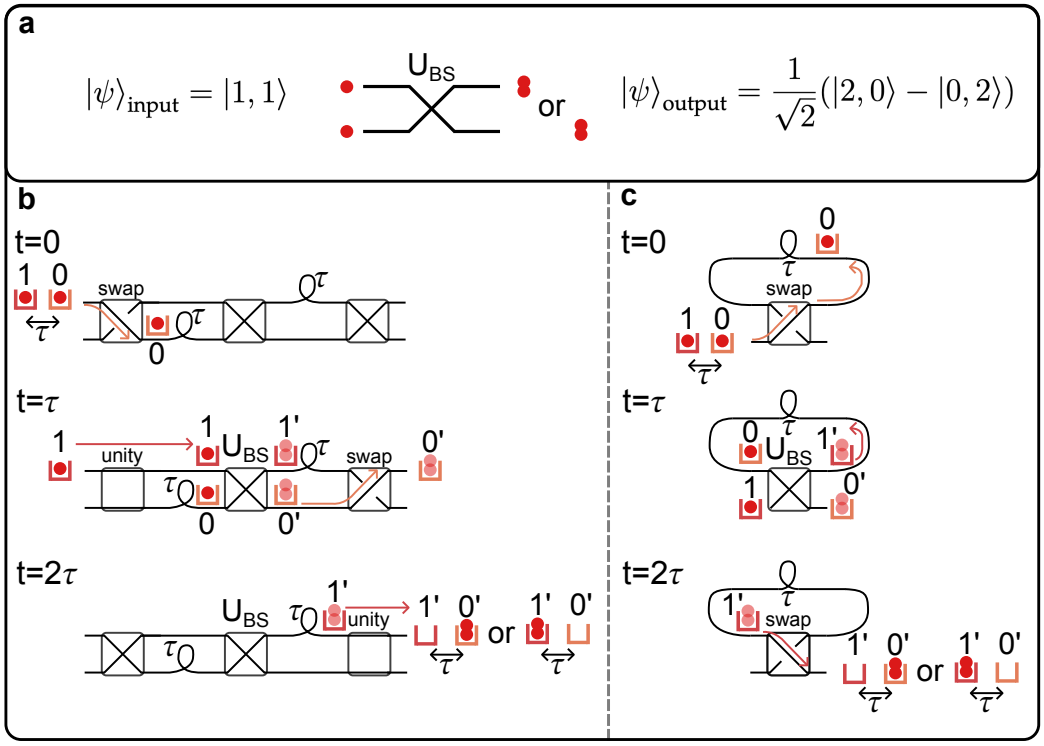

FIGURE 3.1: Schematic showing an MZI can be implemented in the single-path time-bin encoding. **a** Schematic of two single-photons scattering on an MZI. The photons are illustrated as filled red circles, which upon interference bunch in either the top or bottom mode. **b** The implementation of scattering of two single-photons in different time-bins with a temporal separation of τ interfering in a time-bin encoded MZI constructed from three spatially encoded reconfigurable MZIs. **c** The implementation of a time-bin encoded MZI using a single reconfigurable physical MZI with the top output mode connected to the top input mode through a delay loop.

3.1.2 Loop interferometers and cascaded interferometers.

There are two main approaches to implementing multiple diagonals which will result in either a *loop* time-bin interferometer, used in Motes et al. 2014 and He et al. 2017, or a *cascaded* time-bin interferometer, as introduced in Qi et al. 2018 for single-path encodings and Sund et al. 2023b for two-path encodings[1]. Both approaches are illustrated in Fig. 3.2a. In the loop approach, we connect the output of a Reck MZI to its own input through a delay loop, which we will call the *outer loop*. In order to get time-bins into and out of the interferometer, we have to add an extra switch to the input, and ideally the output of the Reck MZI. It is crucial that the delay in the outer loop is sufficient to delay the first output mode from the Reck MZI to arrive after the final input mode to the Reck MZI[2]. For convenience, we will set the delay in outer loop to delay the first output time-bin to arrive back at the input of the MZI exactly one time-bin after the first input time-bin, i.e. $M - 1$ time-bins of delay, where M is the number of modes/time-bins.

In the cascaded approach, additional diagonals are added by routing the output of one Reck MZI to the input of another, as shown in the right side of Fig. 3.2a. The total number of Reck MZIs required is then equivalent to the number of diagonals in the Reck architecture, which is equal to $M - 1$. This requires a number of MZIs which scales with the number of modes, but comes with the benefit of shorter delay lines, as each Reck MZI only needs a delay line with one time-bin of delay. As such, there is a tradeoff[3] between resource requirements and propagation loss, where loop architectures allow for the use of fewer resources at the expense of higher propagation loss. An additional downside of loop architectures is that the interferometer is only able to process one multimode at a time, and one has to wait for it to be finished before it can process another multimode state. As there are $M - 1$ diagonals that are connected by delays of $M - 1$ time-bins, the repetition rate of the time-bin interferometer scales $\propto 1/M^2$. Cascaded time-bin interferometers, on the other hand, don't require any waiting time, and you can insert an additional state immediately after the first one. One still needs to wait for the whole state to get into the interferometer, so the repetition rate in this case scales $\propto 1/M$.

3.1.3 Interferometers in the two-path time-bin encoding

In the two-path time-bin encoding, M modes are encoded across two spatial paths and $M/2$ time-bins. This encoding allows for the natural encoding of dual-rail qubits using a single on-demand single-photon source.

[1] However, it should be noted they were implemented in the experiment detailed in Chapter 4 and Nielsen 2022 before this paper was published.

[2] Technically you could have delayed time-bins arriving in-between the input time-bins, but that gets *really* messy.

[3] It is also possible to do a "partial" cascade, where a fraction of the MZIs (i.e. fewer than the full cascade, 1/2, 1/3, etc.) are cascaded with the output mode of the final MZI connected to the input of the first MZI with a shorter time-delay compared to the single-MZI loop architecture.

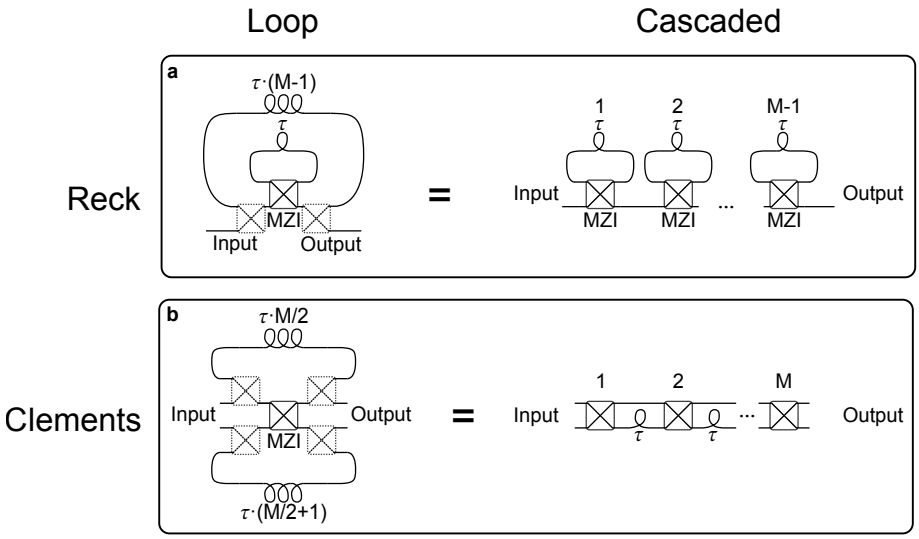

FIGURE 3.2: Schematic showing how the Reck and Clements architectures can be implemented using either cascaded or loop approaches. The symbol τ corresponds to the temporal separation between time-bin, and loops corresponds to a delay of the indicated duration. **a** Schematic of a Reck time-bin interferometer. The loop-architecture shown on the left side has input and output switches indicated with dashed lines. These are used to switch the input state into the time-bin interferometer, and the output states out of the time-bin interferometer. The cascaded approach shown in the right panel consists of $M - 1$ physical Reck MZIs in a series. **b** Schematic of a Clements time-bin interferometer. The loop-architecture shown on the left side has input and output switches indicated with dashed lines. These are used to switch the input state into the time-bin interferometer, and the output states out of the time-bin interferometer. The cascaded approach shown in the right panel consists of M physical MZIs with a delay of τ in the bottom mode between each MZI.

The on-demand source will emit a single photon per time-bin into the same path, such that every time-bin contains a photonic qubit initialized in the same state. The two-path time-bin encoding is particularly well-suited for implementing interferometers with a Clements architecture. Contrary to the single-path encoding, the two path encoding already has two spatial modes that MZIs can be implemented on, so no ancillary modes are needed. One output mode has to be connected to a delay before both output modes are connected to the input modes of the next MZI either through a loop or cascaded approach, as illustrated in Fig. 3.2b.

Fig. 3.3a shows a cascaded implementation of a four mode interferometer, where each physical MZI acts like a column of MZIs in the Clements scheme. The delay in the bottom output mode of the Clements MZI allows for the columns to alternate which pairing of neighboring modes interfere. However, as a consequence of the asymmetric delay, the output state from odd-indexed columns is asymmetrically distributed across time-bins and contains an additional time-bin compared to the input state. To ensure a fixed number of output modes from the interferometer, each even-numbered physical MZI must enact a swap transformation on the first and last time-bins, where only one of the input modes is occupied, as shown in Fig 3.3e. A Clements interferometer with an arbitrary even number of modes M can be constructed by combining $M/2$ pairs of an odd and an even column.

It is also possible to implement a full interferometer using a loop approach, as illustrated in Fig. 3.2b. In the loop approach, two outer delay loops are added to connect both output modes to their corresponding input mode, through a delay of $M/2$. The factor of $1/2$ compared to the Reck architecture comes from the property that there are half as many time-bins for any given number of modes. This results in a lower amount of propagation loss compared to the Reck case. As the total number of modes is equal to the number of paths multiplied by the number of time-bins, which will always be an even number, the two-path time-bin encoding is suitable for interferometers with an even number of modes. It is possible to omit one input and output mode to realize a two-path time-bin interferometer with an odd number of modes, and this naturally lends itself to a peculiar (although seemingly not very useful) architecture for loop time-bin interferometers where the modes effectively have periodic boundary conditions, as detailed in Appendix B.2.

Using the polarization modes in two-path time-bin interferometers

The polarization degree of freedom provides an alternative way to implement beamsplitter transformations, as waveplates and birefringent electro-optic modulators can be used to implement beamsplitter and reconfigurable phase-shifter transformations. As such, two-path time-bin interferometers can also be implemented using two polarization modes for every time-bin.

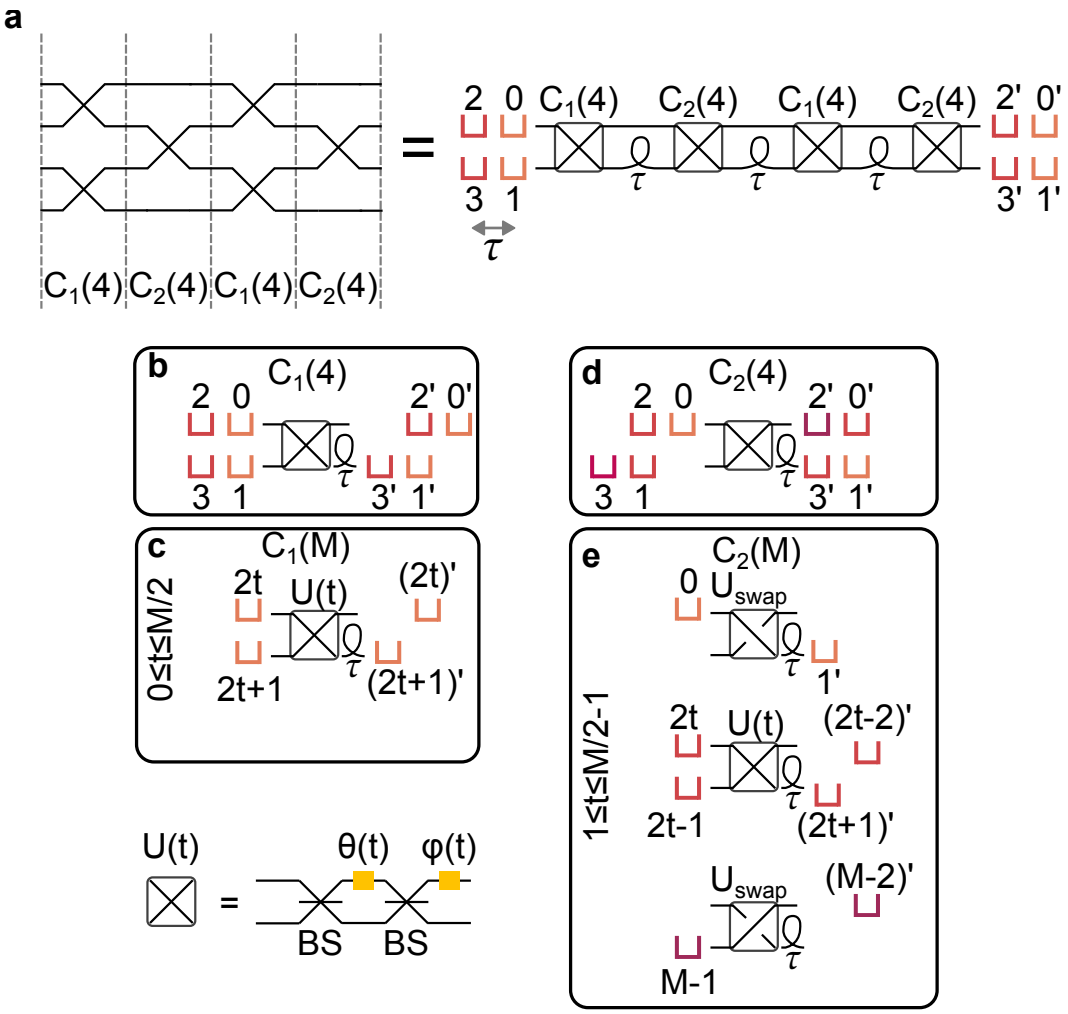

FIGURE 3.3: Schematic showing how a four-mode Clements interferometer can be implemented in the two-path time-bin encoding. The label t corresponds to time in units of time-bins, where the first time-bin occurs at time $t = 0$, the second time-bin at $t = 1$, etc.**a** Architecture and cascaded implementation. Labels without primes denote input modes, whereas labels with primes denote output modes. **b** Operation of odd-indexed MZI column. Illustration of how time-bin interferometers can be constructed to implement specific features in interferometer architectures. This results in an asymmetric output state. **c** Operation protocol for an odd-indexed MZI column. **d** Operation of an even-numbered MZI column. This takes in an asymmetric input state and produces a symmetric output state. **e** Operation protocol for an even-indexed MZI column. The MZI must be configured to enact a swap transformation on the first and final time-bin in order to restore the symmetric state.

It should be noted that the asymmetric delay between Clements MZIs requires the use of separate paths[4], which can be achieved by employing polarizing beamsplitters to convert back and forth between polarization encoding and path encoding. An example of an experimental implementation of such an interferometer can be seen in He et al. 2017 and in Chapter 4.

3.2 Mode-crossings in time

A unique feature of time-bin interferometers is that they allow for a simple way to implement *mode crossings*. In the path encoding, crossing two modes requires the use of specialized components such as waveguide crossings, or additional pathing for every mode-crossing. In the time-bin encoding, however, mode crossings can be implemented by letting two time-bins cross one another in delay lines in separate spatial modes. The most versatile way[5] to add mode crossings is to add additional MZIs acting as switches connected to ancillary spatial paths in the middle of the interferometer. These mode crossings can be configured to implement a permutation matrix on the modes. Fig. 3.4 and Fig. 3.5 show two different types of permutations, which we will call *exchange permutations* and *alternating permutations*, respectively.

An exchange permutation exchanges the chronological order of two sets of modes, one consisting of the first T modes and the other consisting of the remaining $(\mathrm{M}-\mathrm{T})$ modes. We will start by considering the example shown in Fig. 3.4a, where the first mode ($\mathrm{T}=1$) of three is exchanged with the latter two. To this end, we use a switch—which can be constructed using an MZI with time-dependent phase shifters—where the top output is connected to the top input through a delay loop of length 3τ, where τ is the separation between time-bins. At time $\mathrm{t}=0$, the switch is configured to swap the first mode into the delay loop. At time $\mathrm{t}=\tau$ and $\mathrm{t}=2\tau$, the switch is set to unity, such that the input modes are passed through without delay. Finally, at time $\mathrm{t}=3\tau$, the delayed mode arrives back at the switch, which is configured to swap the mode out of the delay loop, completing the permutation.

The general algorithm for exchange permutations is illustrated in Fig. 3.4b. The algorithm to implement a permutation is split into three parts. For the first T time-bins, the switch is configured to implement a swap transformation, sending the incoming mode into a delay loop of length M. After this, the second stage of the algorithm sends the remaining modes through the switch with no delay. In the third stage, which starts at time $\mathrm{t}=\mathrm{M}$, the switch is again to enact a swap transformation such that the delayed modes from the first stage are sent back out of the delay loop. This stage has the same duration as the first stage, such that all of the delayed time-bins are switched out of the delay loop.

The exchange permutation swaps the order of only two sets of modes. However, it is also possible to split the modes into a larger number of sets

[4] In order to be feasible, birefringence is not strong enough for the delay we want.

[5] Mode crossings can also be added without additional MZIs or paths in certain special cases, as detailed in Appendix B.2

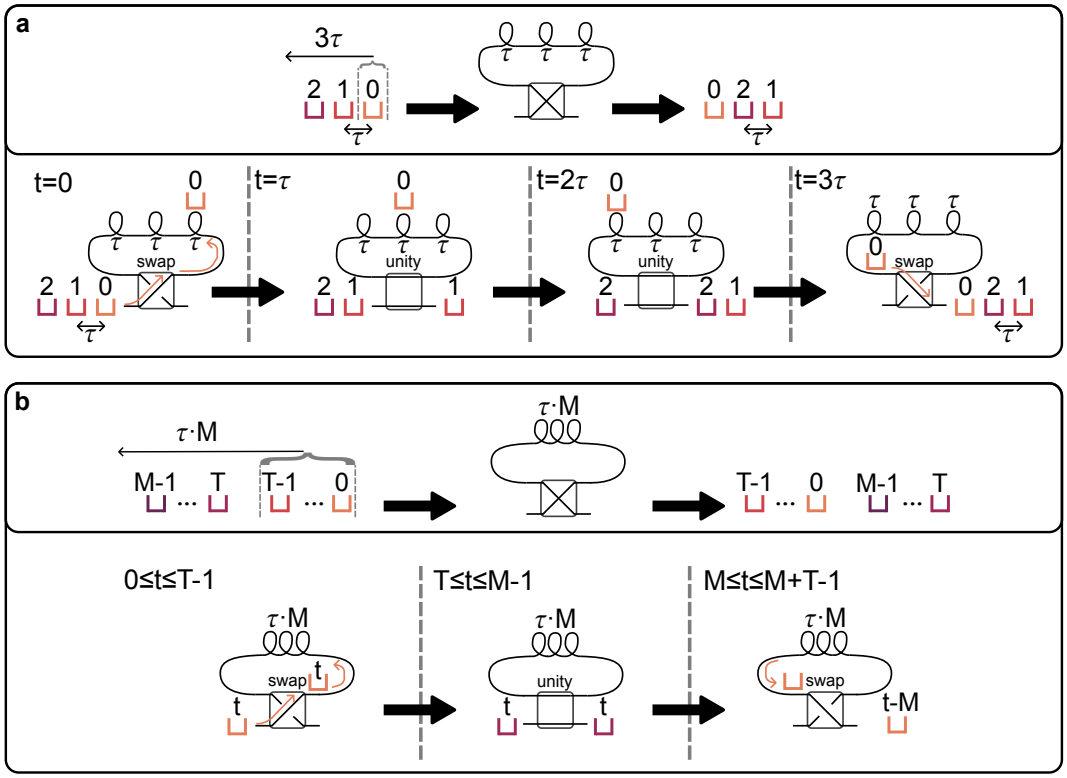

FIGURE 3.4: Single-path exchange permutation, reordering time-bins with respect to the input state. **a** A single-path exchange permutation with three time-bins, exchanging the first time-bin with the latter two. The separation between time-bins in both input and output states is equal to τ. An explanation of the procedure is given in the main text. **b** The general procedure for a single-path exchange permutation with M time-bins. The ordering of the set containing the first T time-bins and the last M − T time-bin is exchanged. An explanation of the procedure is given in the main text.

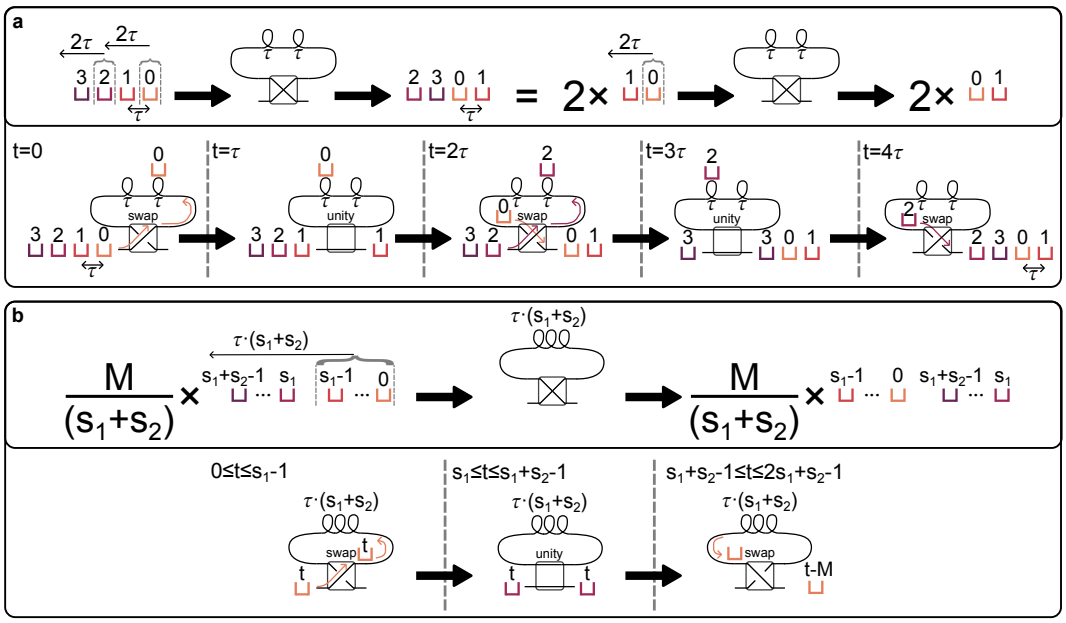

FIGURE 3.5: Single-path alternating permutation, reordering time-bins with respect to the input state. **a** A single-path alternating permutation with four time-bins, exchanging the order of the first pair of time-bins and the second pair of time-bins. This is equivalent to a series of exchange permutations between pairs of time-bins. The separation between time-bins in both input and output states is equal to τ. An explanation of the procedure is given in the main text. **b** The general procedure for a single-path alternating permutation with M time-bins. For every set of $s_1 + s_2$ time-bins, the ordering of the subset containing the first s_1 time-bins and the last s_2 time-bin is exchanged. An explanation of the procedure is given in the main text.

and swap the position of subsequent pairs of sets. The alternating permutation, illustrated in Fig. 3.5, splits the M modes into groups of modes of size $s_1 + s_2$, and applies an exchange permutation between the first s_1 and last s_2 modes in each group. This is possible because the third stage of the exchange permutation for one group overlaps perfectly with the first stage of the exchange permutation of the next group. It is also possible to have groups of varying sizes as long as the value for s_1 is always greater or equal to the value for s_1 in the previous group.

An example of an alternating permutation with four modes and $s_1 = 1$ is shown in Fig. 3.5a. The switch alternates between swap and unity, such that the first and third time-bins are both delayed, while the second and fourth time-bin are transmitted with no delay. The procedure for a single group of a general alternating permutation is shown in Fig. 3.5b. It should be noted that the third section shown in the bottom panel overlaps with the first section of the next group.

3.3 Logarithmic-depth time-bin interferometers

In order to make use of these permutations, we need to develop new interferometer architectures. There are two main aspects that determine the merit of an interferometer architecture. First, for the interferometer to be useful, it needs to be able to implement a desired unitary transformation. Second, it is crucial that the interferometer introduces as little loss as possible, as this ultimately determines the scale (i.e. the numbers of photons and modes) at which it can be used. Thus, in our development of new architectures, we should minimize the amount of loss caused by propagation through MZIs and delay lines, and show that the developed architectures can implement useful unitary transformations.

This section will focus on interferometer architectures that make use of permutations with increasing sizes T of exchanged sets. Each unique permutation requires a distinct amount of delay, which is impractical to implement in a loop architecture, Thus, we will restrict the focus to cascaded architectures. For novel loop-architectures, including an architecture conjectured to be universal with improved depth and delay loss compared to the loop-Clements scheme, the reader is referred to Appendix B.3.

The optimal number of MZIs for a fully populated unitary matrix

The Reck and Clements architectures do not make use of permutations, and instead implement MZIs between nearest-neighboring modes for each diagonal or column. As a result, it takes (M-1) columns or diagonals until the unitary matrix describing the interferometer can be fully populated, i.e. where no element in the matrix is equal to zero. However, an optimal architecture should be able to produce a fully-populated unitary matrix, also referred to as a fully connected interferometer, by sending each mode through only $\lceil \log_2(\mathrm{M}) \rceil$ MZI. To understand why this is the case, we can examine the maximum number of modes encountered after three layers of MZIs, as illustrated in Fig. 3.6. Each MZI has two inputs and two outputs. After the first MZI, all output modes can contain contributions from at most two modes. If we send two modes containing contributions from different modes into a second MZI, then the output modes from the second MZI can contain at most contributions from four modes. Similarly, output modes from a third MZI can contain contributions from at most eight modes. In conclusion, every set of MZIs doubles the maximal number of modes connected. As such, $\lceil \log_2(\mathrm{M}) \rceil$ layers of MZIs are required to connect all modes.

Thus, in order to implement a fully-connected time-bin interferometer with as low depth as possible, we want to permute the modes between time-bins such that we double the number of modes encountered for each layer, as this enables the construction of interferometers with optimal depth.

There are two additional considerations we will take into account, one having to do with MZI diagonals, and the other having to do with *optimal delay*. Single-path time-bin interferometers are constructed from MZI diagonals, for which the optical depth is hard to determine as different paths through the interferometer will encounter a different number of MZIs. To

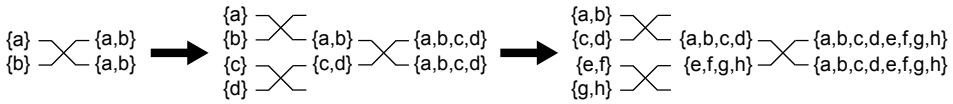

FIGURE 3.6: An illustration of how the number of modes connected in an interferometer consisting of layers of MZIs can be doubled for every layer. The number of connected modes is denoted with curly brackets, meaning that a mode labeled with a,b contains contributions from the initial modes a and b, or in other words, the mode is connected to modes a and b.

avoid this complication, we will restrict the focus to two-path interferometers, where every MZI column introduces an additional component in every path.

Optimal delay for a time-bin interferometer

The only way for an earlier time-bin to interfere with a later time-bin is to synchronize the two by delaying the earlier time-bin. As such, for a fully connected interferometer, the first output time-bin can at the earliest occur simultaneously with the last input time-bin. Conversely, if the first output time-bin were to exit the interferometer *before* the last input time-bin enters the interferometer, it would be impossible to connect the two modes. Thus, we can say that interferometers have an optimal delay if the first output time-bin happens at the same time as the last input time-bin. This is the case for a cascaded single-path Reck-style interferometer, consisting of $M-1$ diagonals of MZIs, each of which delays the state by one time-bin, i.e. delaying the output state with $M-1$ time-bins—which is equal to the temporal separation between the first and last input modes. As for the cascaded Clements interferometer, it consists of $M/2$ pairs of MZI columns, each delaying the state by one time-bin. As the separation between the first and last time-bin is $M/2-1$, this means that the cascaded Clements interferometer is one time-bin short of optimal delay.

Regardless of the delay configuration, there will be a delay loss associated with every path through the interferometer. Each element in the unitary matrix, describing the probability amplitude for going from a specific input to a specific output, can be associated with a delay that is equal to the temporal separation between the input mode and the output mode. In other words, every path through the interferometer that starts in the same input mode and ends in the same output mode will necessarily go through the same amount of delay. Thus, for the purposes of optimizing delay, we only have to concern ourselves with the time difference between input modes and output modes.

3.3.1 Time-bin interferometer architectures with logarithmic depth and optimal delay

To construct time-bin interferometer architectures with as low optical depth as possible, we want to double the number of modes encountered for every layer of MZIs. A layer of MZIs consists of an MZI followed by a permutation, which itself contains a switch. The switch is omitted for the last layer of MZIs, as it is unnecessary to permute the output modes. For two-path time-bin encodings, we need to generalize the permutations introduced in the previous section to two modes. We will make use of the permutation algorithms shown in Fig. 3.7 and Fig. 3.8.

Two-path permutations

The exchange permutation for two paths applies a single-path exchange permutation on the top mode, and delays the bottom mode by $T \cdot \tau$ time-bins. This ensures that the bottom-modes from the first T time-bins overlap perfectly with the top time-bins from the subsequent set of $M/2 - T$ time-bins. Thus, the sets of top modes are exchanged, and all top modes are synchronized with a bottom mode. An example for six modes with set-size $T = 1$ is shown in Fig. 3.7a, and the procedure for a general number of modes and set-size, ExchangePermutation(M, T), is illustrated in Fig. 3.7b.

As for the alternating permutation, we again apply the permutation to only the top mode, and delay the bottom mode. In this case, we set the numbers s_1, s_2 to be equal to a power of two, i.e. $s_1 = s_2 = 2^{c-1}$ for a positive integer c. This is motivated by the argument illustrated in Fig. 3.6, as we want to double the size of the groups we're exchanging for every layer of MZIs. This requires that the number of time-bins $M/2$ is divisible by the group size $s_1 + s_2 = 2^c$, which ultimately requires that the number of modes is a power of two. Similarly to the exchange permutation, the delay in the bottom mode is set to be equal to the size of the exchanged set, i.e. $\tau \cdot 2^{c-1}$. In this case, this ensures that the bottom modes from one set are synchronized with the top modes from the exchanged set. An example with eight modes and order $c = 1$ is shown in Fig. 3.8, and the procedure for the first group of a general number of modes and order, Pow2Permutation(M, c), is illustrated in Fig. 3.8b.

Cascaded logarithmic-depth interferometers for power-of-two numbers of modes

As the number of modes connected can maximally double for every MZI layer, the most simple case has the number of modes equal to a power of two. In this case, doubling the number of modes connected for every layer will eventually result in a fully connected interferometer.

After an MZI, the top and bottom modes in a given time-bin will contain contributions from the same modes, as illustrated in Fig. 3.6. Therefore, we should make sure that the paths the top and bottom modes take never overlap for the rest of the interferometer. To ensure that this happens, the

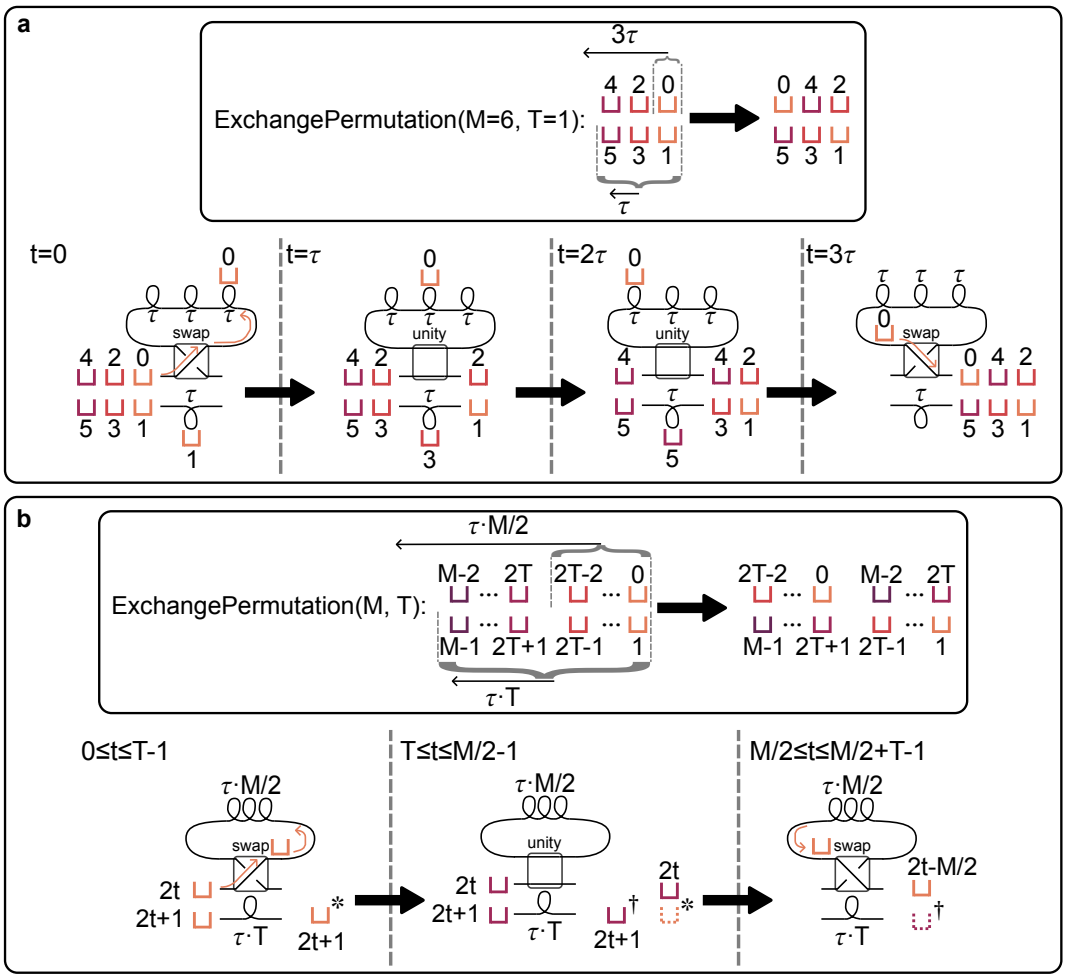

FIGURE 3.7: Two-path exchange permutation, consisting of a single-path exchange permutation in the top mode and a delay in the bottom mode. The delay ensures that all top modes are synchronized with a bottom mode. **a** A two-path exchange permutation with three time-bins, exchanging the order of the top mode in the first time-bin with the top modes in the two subsequent time-bins. The separation between time-bins in both input and output states is equal to τ. **b** The general procedure for a two-path exchange permutation with $M/2$ time-bins. The ordering of the set containing the top modes in the first T time-bins and the top modes in the last $M - T$ time-bin is exchanged.

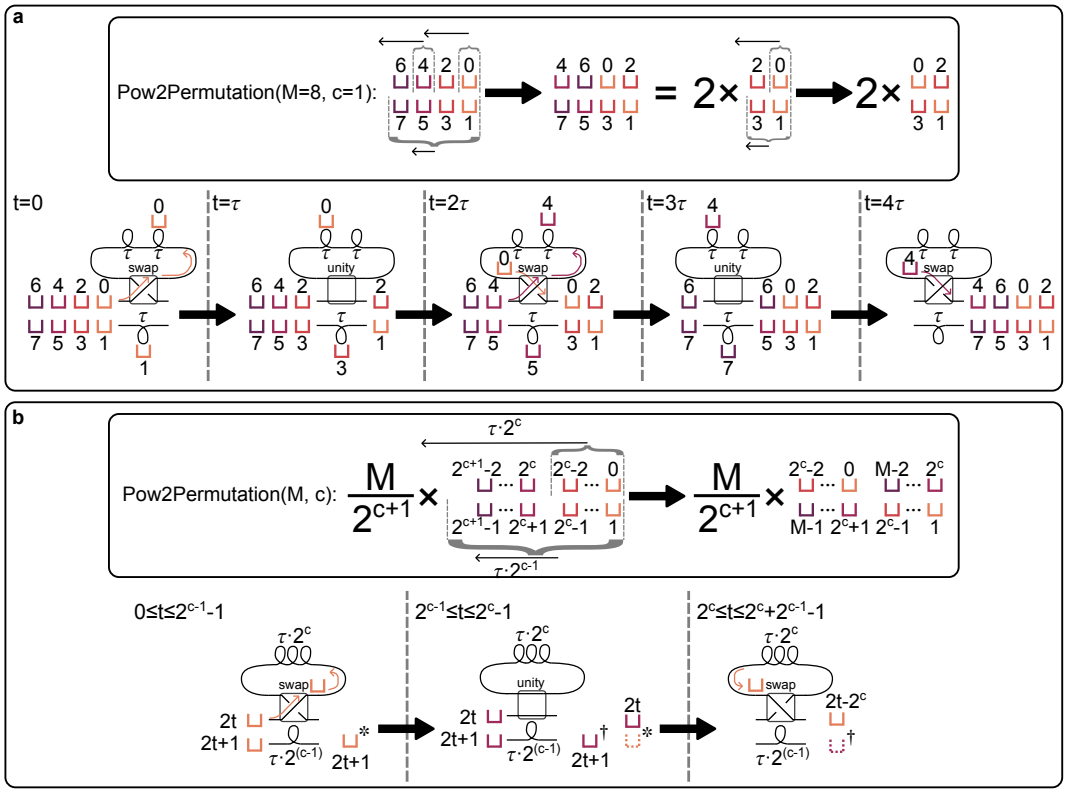

FIGURE 3.8: Two-path power-of-two permutation, reordering sets of time-bins in the top modes with respect to the input state and delaying the bottom modes. The delay ensures that all top modes are synchronized with a bottom mode. The number of modes is assumed to be divisible by 2^{c+1}. **a** A two-path alternating permutation with four time-bins, exchanging the order of the top modes in the first pair of time-bins and the top modes in the second pair of time-bins. This is equivalent to a series of exchange permutations between pairs of time-bins. The separation between time-bins in both input and output states is equal to τ. **b** The general procedure for a two-path power-of-two permutation with $M/2$ time-bins. For every set of 2^c time-bins, the ordering of the subset containing the top modes in the first 2^{c-1} time-bins and the top modes in the last 2^{c-1} time-bin is exchanged. The bottom delay ensures all bottom modes are synchronized with a top mode from the other subset.

delay in the bottom mode will be set to a fixed value for a given MZI layer. If we index the MZI layer as L (for "layer"), we want the bottom delay to be equal to $2^{\mathrm{L}-1}$. This corresponds to ExchangePermutation$(\mathrm{M},\ \mathrm{T}=2^{\mathrm{L}-1})$, and Pow2Permutation$(\mathrm{M},\ \mathrm{c}=\mathrm{L})$.

In the exchange permutation, the top mode will either not be delayed, or be delayed by $\mathrm{M}/2 = 2^{\log_2(\mathrm{M})-1}$ time-bins, which only happens once for the case of power-of-two number of modes. The bottom modes will go through a delay of $\sum_{\mathrm{L}=1}^{\log_2(M)-1} 2^{\mathrm{L}-1} = 2^{\log_2(\mathrm{M})-1} - 1$, where we note again that there is no permutation in the final MZI layer. As such, the path taken by the top mode and the bottom mode will never overlap for the first $\log_2(M)$ MZI layers.

For the power-of-two permutation, a slightly different approach is taken. Between the MZI and the permutation in the Lth MZI layer, we can split the time-bins into $2^{\log_2(\mathrm{M})-1-\mathrm{L}}$ contiguous groups where all of the modes in each group are connected to one another. As the number of modes is equal to a power of two, we can use the permutation layer to merge pairs of groups together, doubling the number of modes connected. As the number of time-bins in each group is 2^{L-1}, this can be accomplished with the permutation Pow2Permutation$(\mathrm{M},\ \mathrm{c}=\mathrm{L})$.

Examples of cascaded interferometers with power-of-two numbers of modes using exchange permutations or power-of-two permutations are shown in Fig. 3.9 and Fig. 3.10, respectively. These figures also show how zero elements are eliminated from the unitary matrix associated with the interferometer for every MZI layer.

Before proceeding, we should evaluate if these interferometers have optimal delay by checking whether or not the first output time-bin is synchronous with the last input time-bin. As the modes should be fully connected, this corresponds to the case where there is a path from the last input time-bin to the end of the interferometer which goes through no delay. As the bottom mode is always delayed between MZI layers, we only need to consider the top modes. Every permutation delays the current first 2^{L-1} time-bins. By summing the number of time-bins delayed for every layer, we can find how many of the initial time-bins have been delayed at the output of the interferometer as

$$\sum_{\mathrm{L}=1}^{\log_2(\mathrm{M})-1} 2^{\mathrm{L}-1} = 2^{\log_2(\mathrm{M})-1} - 1 = \mathrm{M}/2 - 1.$$

As such, the first $\mathrm{M}/2-1$ out of all $\mathrm{M}/2$ time-bins have been delayed, which means that the final input time-bin has not been delayed, verifying that the exchange-permutation-based approach allows for the construction of optimal-delay time-bin interferometers with logarithmic depth.

We have to use a slightly different approach for the power-of-two permutation. For every 2^{L} time-bins, this permutation delays the first 2^{L-1}. If we index time-bins starting from 1, then every input time-bin that has an index not divisible by 2^{L} will have been delayed after layer L, up to the last

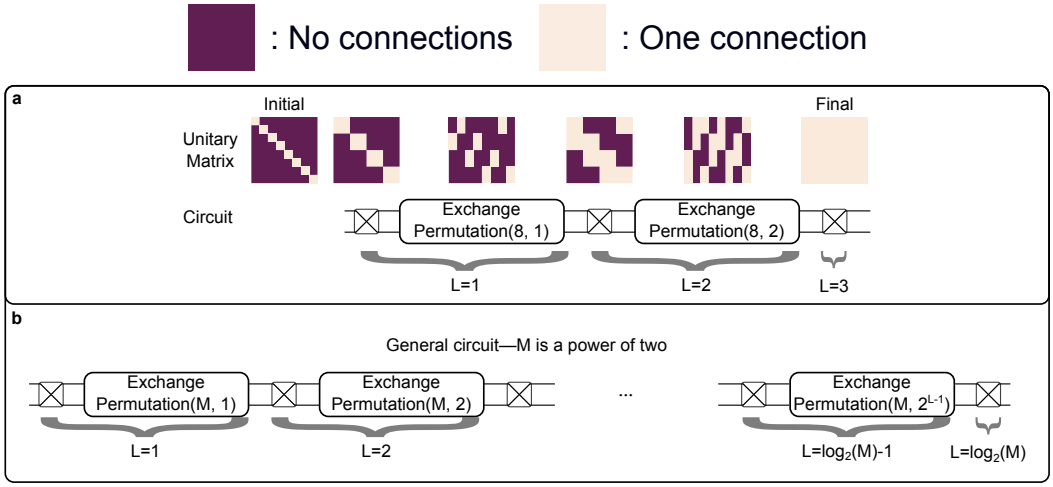

FIGURE 3.9: Circuit schematic for a logarithmic depth cascaded time-bin interferometer based on exchange permutations for power-of-two numbers of modes. **a** Example of an implementation for eight modes consisting of three MZIs and two two-path exchange permutations with increasing set-size T. The plots above the circuit show how the number of nonzero elements in the unitary matrix increases for each step in the circuit. A nonzero element for row i and column j corresponds to a connection from input mode i to output mode j. **b** Circuit schematic for a general power-of-two number of modes, consisting of $\log_2(\mathrm{M})$ MZIs sandwiching $\log_2(\mathrm{M}) - 1$ two-path exchange permutations.

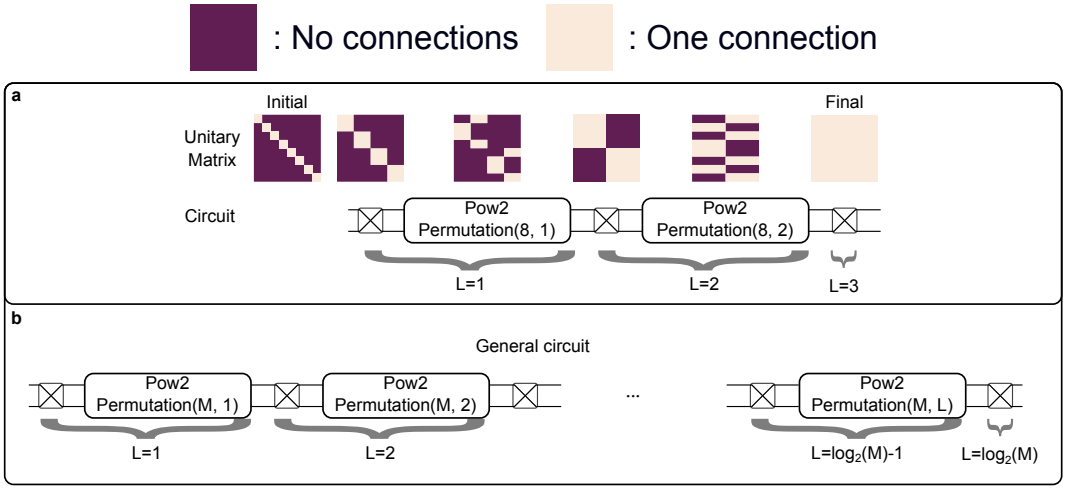

FIGURE 3.10: Circuit schematic for a logarithmic depth cascaded time-bin interferometer based on power-of-two permutations for power-of-two numbers of modes. **a** Example of an implementation for eight modes consisting of three MZIs and two two-path power-of-two permutations with increasing order c. The plots above the circuit show how the number of nonzero elements in the unitary matrix increases for each step in the circuit. A nonzero element for row i and column j corresponds to a connection from input mode i to output mode j. **b** Circuit schematic for a general power-of-two number of modes, consisting of $\log_2(\mathrm{M})$ MZIs sandwiching $\log_2(\mathrm{M}) - 1$ two-path power-of-two permutations.

layer where there is no permutation. At the second to last layer our time-bin index has to be divisible by $2^{\log_2(M-1)} = M/2$, i.e. the index of the final input time-bin. As such, at the output of the interferometer the only input time-bin that has not been delayed is the final input time-bin, verifying that the power-of-two-permutation-based approach allows for the construction of optimal-delay time-bin interferometers with logarithmic depth.

3.3.2 Exchange based permutations vs power-of-two based permutations

Thus far, the exchange permutation and power-of-two permutation seem to accomplish the same thing. However, their differing properties lead to unique advantages. The exchange permutation is particularly well-suited to the case where the number of modes is not equal to a power of two. The approach is the same for the first $\lfloor \log_2(M) \rfloor$ columns, after which more than half of the modes have been connected, meaning the number of connections can not be doubled again. The first output time-bin from this layer is $2^{\lfloor \log_2(M) \rfloor - 1} - 1$, whereas the last input time-bin is $M/2 - 1$. Furthermore, all unconnected modes will be found in this section. Thus, we can fully connect the interferometer with optimal delay by adding the permutation ExchangePermutation$(M, T = M/2 - 2^{\lfloor \log_2(M) \rfloor - 1})$. As the connected number of modes cannot be doubled, this means that there will be a finite number of overlapping paths in the interferometer. This is illustrated in Fig. 3.11, where having two connections is indicated with an orange color. Thus, using exchange permutations, we can implement a fully connected interferometer for any even number of modes with optimal delay and optical depth of $\lceil \log_2(M) \rceil$.

The power-of-two permutation, on the other hand, has a different property that we can exploit. After each interferometer layer, the modes can be split into $2^{\log_2(M)-c}$ groups where all of the modes in each group are connected to one another. Thus, we should be able to split the groups into $2^{\log_2(M)-c}$ paths, where each path contains one mode from each group. In other words, we can double the number of spatial paths for each layer of MZIs, thereby allowing for the construction of a *demultiplexing* interferometer. A schematic for how this can be accomplished is illustrated in Fig. 3.12. The permutation here is slightly different, as top modes (bottom modes) are permuted to interfere with top modes (bottom modes). By operating a demultiplexing interferometer in reverse, it is also possible to make a *multiplexing interferometer*. As the output modes must be synchronized at the end of a demultiplexing interferometer, the overall delay loss will also be lower for later output time-bins compared to the case of a non-demultiplexed interferometer where they must be delayed to have a temporal separation with respect to the first output time-bin.

Demultiplexing (multiplexing) interferometers can also be extended to single-path time-bin encodings by sending the single-path into a reconfigurable switch at the start (end) of the interferometer, where one path is connected to a delay of the time-bin separation τ. This requires that all

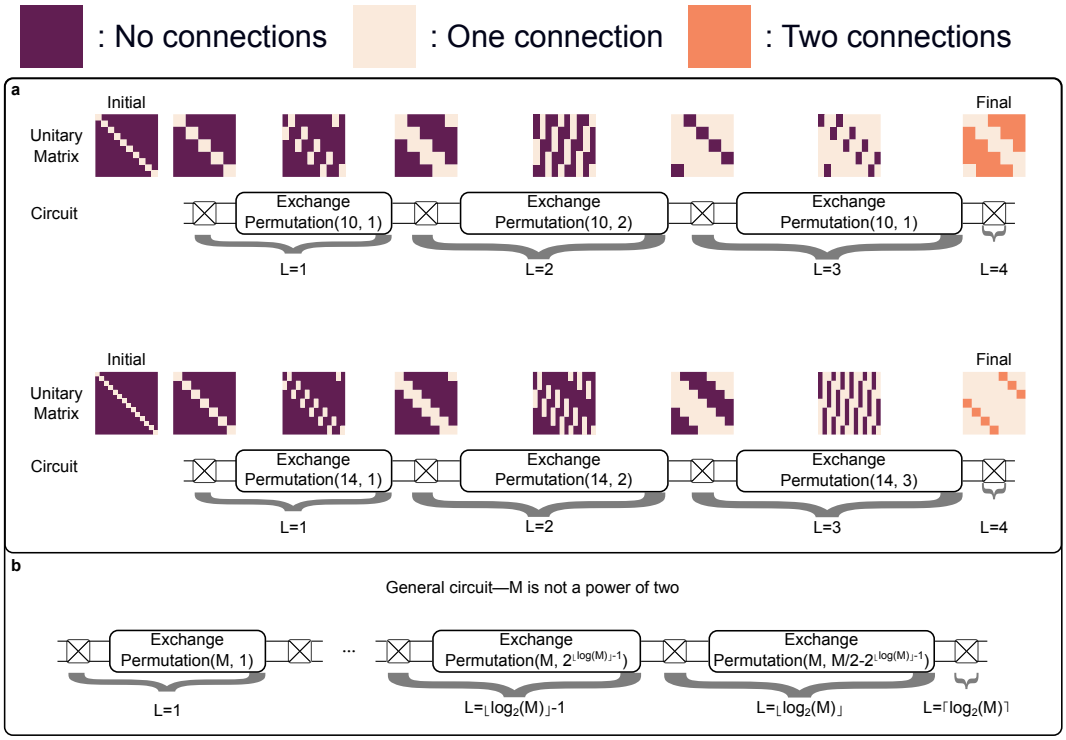

FIGURE 3.11: Circuit schematic for a logarithmic depth cascaded time-bin interferometer based on exchange permutations for even numbers of modes not equal to a power of two. **a** Top: Example of an implementation for ten modes consisting of four MZIs and three two-path exchange permutations with varying set-size T. The plots above the circuit show how the number of nonzero elements in the unitary matrix increases for each step in the circuit. A nonzero element for row i and column j corresponds to a connection from input mode i to output mode j. For certain input–output combinations there will be two connecting paths through the interferometer as opposed to one, indicated by an orange color. **b** Circuit schematic for a general even number of modes not equal to a power of two, consisting of $\lceil \log_2(\mathrm{M}) \rceil$ MZIs sandwiching $\lfloor \log_2(\mathrm{M}) \rfloor$ two-path exchange permutations.

other delays in the two-path demultiplexing (multiplexing) interferometer are multiplied by a factor of two.

3.3.3 Specialized unitary matrices with logarithmic-depth interferometers

The utility of the logarithmic-depth interferometer architectures only extends as far as the utility of the unitary matrices they can implement[6]. To this end, we will show in this section that for power-of-two numbers of modes, we can implement discrete Fourier transform (DFT) matrices using a single cascaded interferometer.

DFT matrices using demultiplexing interferometers

In the following we will focus on the use of demultiplexing interferometers, as this maps naturally onto the algorithm introduced by Barak et al. 2007. This is fairly simple to translate into a cascaded power-of-two-permutation-based time-bin interferometer, by implementing a swapped beamsplitter instead of a beamsplitter for every MZI layer, i.e.

$$U_{\text{swap-bs}} = U_{\text{beamsplitter}} U_{\text{swap}} = \frac{1}{\sqrt{2}} \begin{bmatrix} 1 & 1 \\ -1 & 1 \end{bmatrix}.$$

The procedure introduced by Barak et al. 2007 provides a way to implement a DFT matrix using linear optical components. Multimode photonic Fock states exhibit specific bunching and antibunching behavior similar to the HOM effect when scattering on a DFT matrix, which is denoted as *bosonic suppression laws*. This has been demonstrated in a number of experiments Crespi et al. 2016; Wang et al. 2023, one of which is detailed in the next chapter of this thesis.

An example of the DFT interferometer algorithm for eight modes is illustrated in Fig. 3.13, reproduced from Barak et al. 2007.

If we ignore the labels and start at the bottom, we can see that the interference pattern is identical to that of a demultiplexing interferometer. The interference between modes is given by the beamsplitter matrix

$$U_{\text{beamsplitter}} = \frac{1}{\sqrt{2}} \begin{bmatrix} 1 & 1 \\ 1 & -1 \end{bmatrix}.$$

Thus if we set the MZIs to implement a beamsplitter transformation in addition to a time-dependent phase for the modes requiring a phase-shift, we can implement a DFT matrix up to relabeling the input and output modes. The elements in the DFT matrix all have the same absolute value, such that the only difference between the elements is their phase. The phases of DFT matrices of increasing sizes are shown in the leftmost column in Fig. 3.14.

[6] For certain applications, such as running the boson sampling algorithm, they might prove advantageous without the need to dial specific unitaries, as will be discussed in more detail in Chapter 6

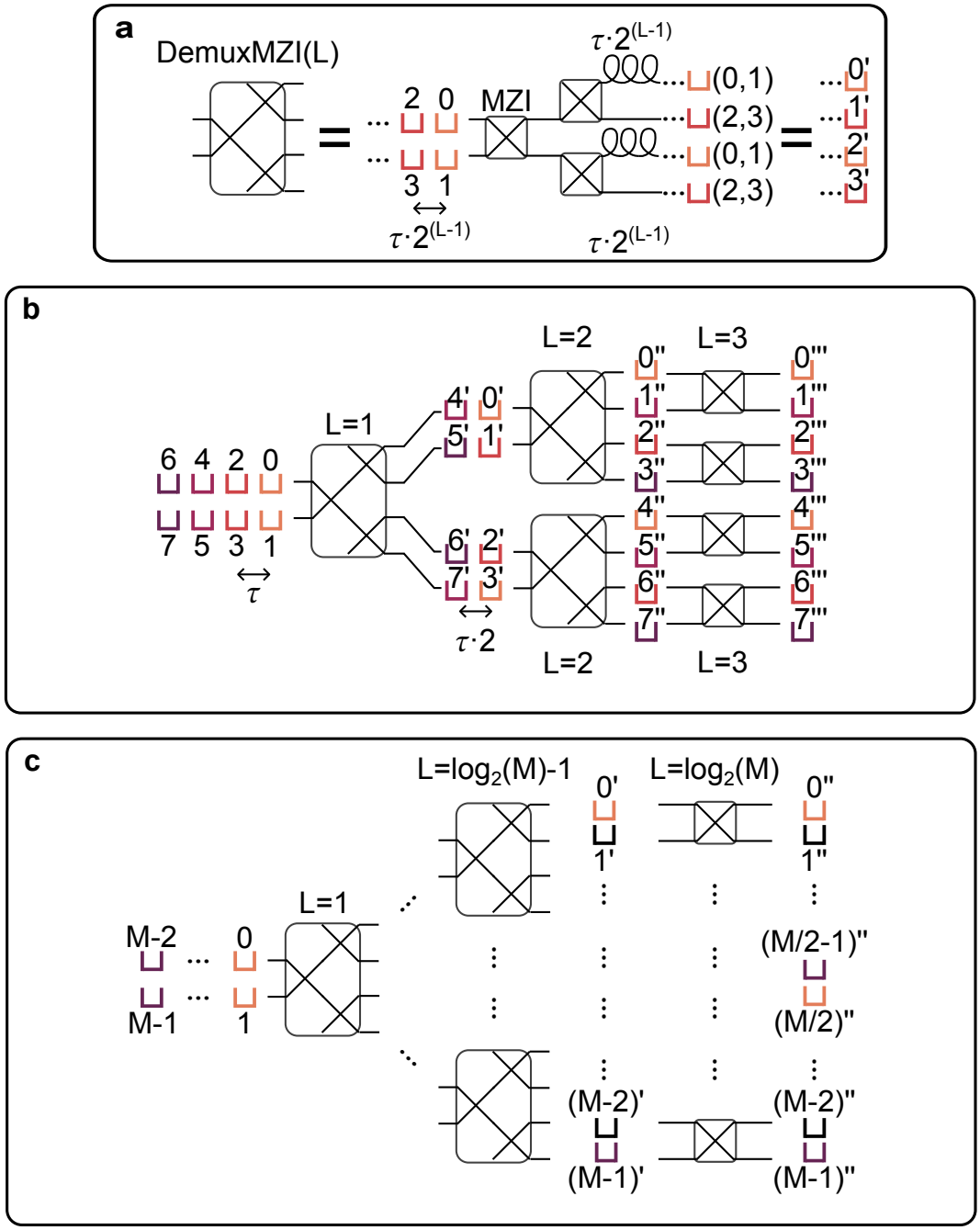

FIGURE 3.12: Circuit schematics for demultiplexing interferometers. Multiplexing interferometers can be constructed by running the circuit in reverse. Modes with primes denote the ordering of modes after interference and permutation. The color of each bin corresponds to the end position of the input time-bins for the case where all MZIs are set to enact the unity transformation. **a** Schematic for the basic building block which we call a 'DemuxMZI'. The DemuxMZI takes incoming sets of four modes in two time-bins where the time-bins have a temporal separation of $\tau \cdot 2^{L-1}$. The two modes in each time-bin interfere at the MZI and the outputs are demultiplexed and synchronized to four modes. **b** Example schematic of a demultiplexing interferometer with eight modes, requiring three layers of MZIs, where the first two layers are DemuxMZIs demultiplexing and permuting the modes after interference. **c** A schematic for a demultiplexing interferometer with a general number of modes. The black time-bins correspond to modes that were not illustrated in the input state.

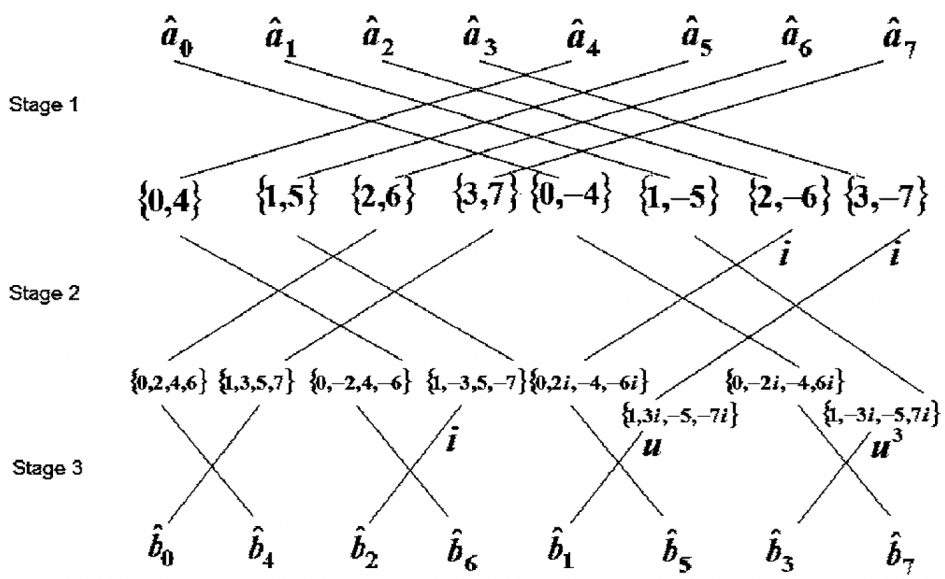

FIGURE 3.13: Schematic of a linear optical implementation of the Cooley–Tukey algorithm for the DFT matrix in eight modes. The crosses represent beamsplitter transformations between the two incident modes. The operators $\hat{a}_i$ denote input modes, whereas the operators $\hat{b}_i$ denote output modes. The values i, u and u^3 correspond to phase shifts applied to the corresponding modes. Adapted from Barak et al. 2007.

The middle column in Fig. 3.14 shows the phase of the corresponding unitary matrix made by running the DFT matrix algorithm with a demultiplexing interferometer without relabeling the input and output modes. This relabeling corresponds to permuting rows and columns and can be implemented by permuting the input and output modes before and after the interferometer. The rightmost column in Fig. 3.14 shows the unitary implemented by the demultiplexing interferometer with the correct permutation matrix applied to the input and output. The code used to generate the DFT matrix and the permutation matrix for the input and output is provided in Appendix B.5.

3.4 Conclusion and outlook

In summary, we have shown various time-bin interferometer architectures using either loop or cascaded approaches in the single-path and two-path time-bin encodings. We have demonstrated how the time-bin encoding is uniquely suited to employing permutation matrices between the modes, and how this can be used to construct specialized interferometer architectures with a significant reduction in the optical depth. Though these specialized interferometers cannot implement arbitrary unitary matrices, we have shown that they are capable of implementing discrete Fourier transform matrices, which have been used in several quantum optics experiments, including the one detailed in the next chapter.

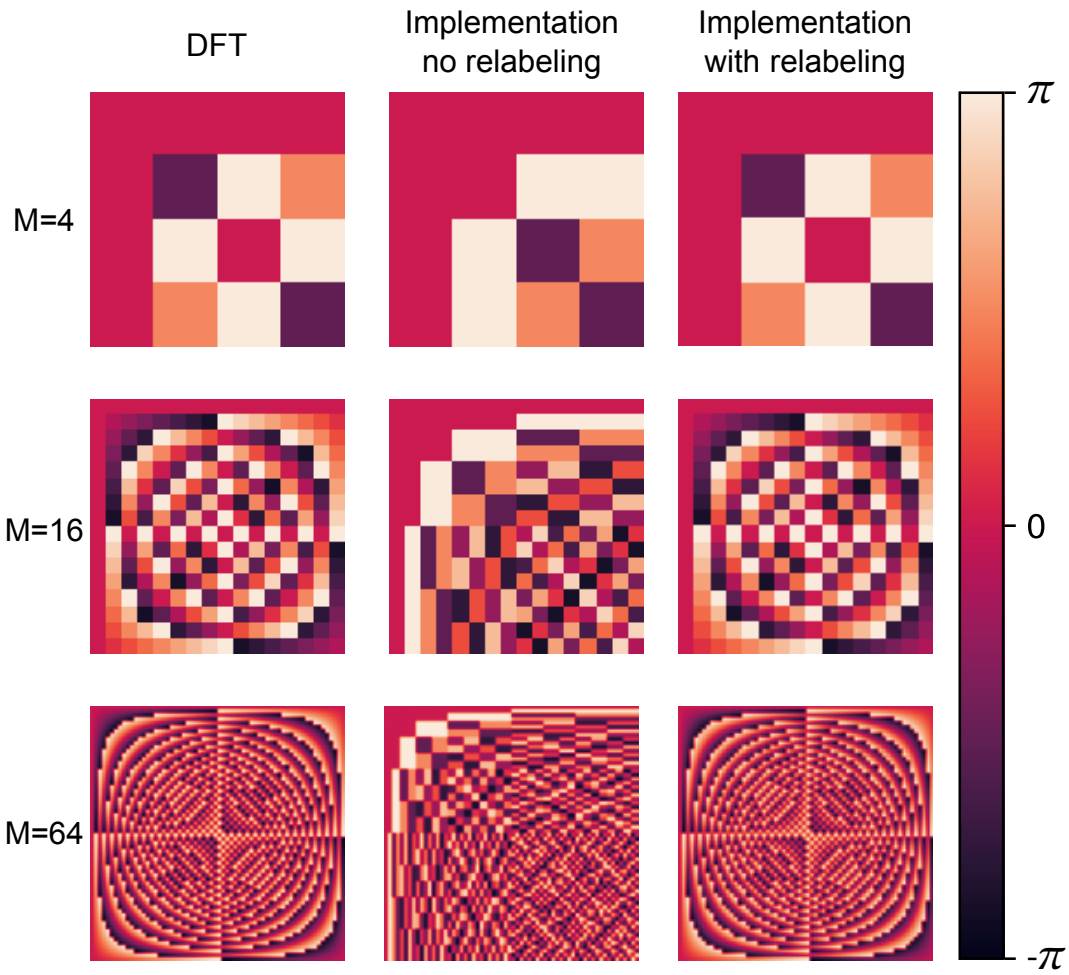

FIGURE 3.14: Heatmaps of the phase of the complex elements of unitary matrices with numbers of modes equal to increasingly higher powers of two. The first column shows the phase of the elements of the discreet Fourier transform. The second column shows the result of the implementation of the reverse circuit from Barak et al. 2007 implemented with a demultiplexing time-bin interferometer. The third column is the result from the second column with a specific permutation matrix applied to the input and output modes.

For the two-path time-bin encoding, we have demonstrated two different types of permutation matrices, the exchange permutation and the power-of-two permutation, each of which has unique advantages. Specifically, the exchange permutation can be used for the construction of logarithmic-depth interferometers with optimal delay for any even number of modes. Power-of-two-permutations on the other hand, which are restricted to power-of-two numbers-of-modes, enable the construction of demultiplexing (multiplexing) interferometers, which take time-bin encoded (path encoded) input states and produce path encoded (time-bin encoded) output states. The resource cost for implementing demultiplexing interferometers is similar to that of a demultiplexer, as both consists of binary trees of switches. Specifically, the interferometer variant requires the addition of one MZI per switch, where all MZIs apart from the last set generally has to be reconfigurable in time. As such, the resource requirements are approximately a factor of two higher for any power-of-two number of modes.

The demultiplexing interferometer allows for a reduction in propagation loss compared to other optimal-delay architectures, as no temporal separation is required between output modes. Multiplexing interferometers, on the other hand, provide a way to interface path-encoded devices with quantum emitters, which could be useful e.g. in experiments aiming to use a quantum dot as a nonlinearity.

There are a number of ways in which the work presented here could be expanded upon, some of which are outlined in Appendix B. By counting the resources required to construct universal interferometer architectures, we can conjecture improved architectures for the two-path time-bin encoding, both with a loop approach and with a cascaded approach. However, these result are only useful if we know how to implement unitary matrices of interest using these architectures. To verify that the conjectured universal architectures are, in fact, universal, a decomposition method would have to be developed, as was done by Reck et al. 1994 and Clements et al. 2016 for their respective architectures.

Alternatively, we could expand the scope to architectures for time-bin encodings with n paths, which would be the natural encoding of n or $n/2$ on-demand single-photon sources, for which specialized interferometer architectures have already been developed (Su et al. 2019).

As demonstrated by the results presented in Chapter 4 and Fig. 6.6 of Chapter 6, specialized interferometer architectures have practical advantages in a variety of experiments. To establish the full utility of these architectures, we would have to:

1. Find the full range of unitary matrices that can be implemented.

2. Develop a decomposition method to implement any specific possible unitary matrix.

On a final note, demultiplexing interferometers can be developed for any even number of modes by making use of MZIs, permutations, and possibly Reck MZIs in each mode at the start or in the middle of the interferometer. In the worst case, you could always combine a cascaded exchange-based

logarithmic-depth interferometer with a standard demultiplexer. This would have a logarithmically scaling depth but would have twice as much delay compared to the optimal delay. As of yet, it is uncertain how much delay and how many switches and MZIs would be required for an optimized architecture.

4 Demonstration of bosonic suppression and postselected entanglement using a time-bin interferometer

Statement of work

The experiment was conceived of and designed by Stefano Paesani and I. We built the time-bin interferometer together with Kasper H. Nielsen. The experiments and data analysis were conducted by Kasper and I with supervision from Stefano. The single-photon source was set up and characterized by Ying Wang.

Although the results presented in this chapter are original, the methods and classical characterization of this work was presented in Kasper H. Nielsens master thesis (Nielsen 2022), and much of this chapter draws upon chapters 6 and 7 of his thesis.

4.1 Introduction

As the time-bin encoding is the natural encoding of on-demand single-photon sources, no mode-conversion (e.g. using a demultiplexer) is required for experiments employing time-bin interferometers. Additionally, time-bin interferometers allow for a further reduction in the number of required physical components compared to the path encoding, as a single physical resource can be reused over multiple time-bins in place of multiple components. However, this typically requires the use of more complex resources that can be reconfigured rapidly between time-bins. In this experiment we construct a cascaded time-bin interferometer which is used to demonstrate bosonic suppression laws and postselected entanglement using only a single reconfigurable electro-optic modulator, showcasing how the time-bin encoding is particularly advantageous for certain specialized tasks. We start the chapter by introducing a simple four-mode photonic circuit that can be used both to demonstrate bosonic suppression laws and postselected entanglement. Proceeding, we explore how this circuit can be implemented in the two-path time-bin encoding using two polarization modes in place of the two paths. The experimental setup is used to demonstrate bosonic suppression laws with a fidelity of 0.934 ± 0.001 and postselected generation of Bell states with a fidelity of 0.963 ± 0.001.

4.2 Background

The HOM effect is the cornerstone of photonic quantum computing and is the gold-standard in quantifying the indistinguishability of two photons. The HOM effect can be considered a special two-mode two-photon case of of so-called *bosonic suppression laws*. The following explanation is adapted from Crespi et al. 2016, drawing upon results from Tichy et al. 2010 and Tichy et al. 2012. Bosonic suppression laws occur when Fock states composed of p photons in a *cyclic* collision-free input state are transformed by interferometers enacting DFT matrices with $m = p^n$ modes for an integer n. For a cyclic input states, the occupied modes j_r^s satisfy the rule

$$j_r^s = s + (r-1)p^{n-1},$$

where $r = 1, \cdots, p$ and $s = 1, \cdots, p^{n-1}$. For the purposes of this chapter, where we have $p = 2$ photons in $m = 2^2 = 4$ modes, there are only two possible cyclic input states, $|1,0,1,0\rangle$ and $|0,1,0,1\rangle$. After evolution by the DFT matrix, the output states with a finite probability amplitude have to fulfill the following condition

$$\mathrm{mod}\left(\sum_{l=1}^{p} k_l, n\right) = 0, \tag{4.1}$$

where k_l is the output mode of the lth photon. As all other outputs have been suppressed, we call this effect a *bosonic suppression law*. This has been demonstrated in a number of experiments, e.g. Crespi et al. 2016, Carolan et al. 2015a, and Wang et al. 2023.

In order to observe bosonic suppression, we will make use of the circuit illustrated in Fig. 4.1a. Though the unitary matrix this circuit produces is not exactly the same as the DFT matrix, it reproduces the same bosonic suppression laws. This circuit bears a striking resemblance to the circuit for a *postselected Bell-state generator*, illustrated in Fig. 4.1b, which is also equivalent to a circuit representation of the type-II fusion gate introduced in Browne et al. 2005. The bosonic suppression law circuit is equivalent to the XX-basis configuration (i.e. both photonic qubits are measured in the X-basis). The circuit for a generalized postselected GHZ state generator is illustrated in Fig. 4.1c (This type of circuit has seen implementation in e.g. Pont et al. 2022 and Li et al. 2020).

These circuits have the useful property that the output statistics are insensitive to phase shifts between the elements in the circuit as long as they are applied to both the first and third mode, or the second and fourth mode, as shown in more detail in Appendix C.1. These pairs of modes are only separated in time, meaning that the interferometer only has to be phase-stable between pairs of time-bins, i.e. on a nanosecond timescale. As mechanical fluctuations are significantly slower than this, an interferometer implementing these circuits will not have to be phase-stabilized.

The circuits in Fig 4.1 are similar to specific instances of a Clements

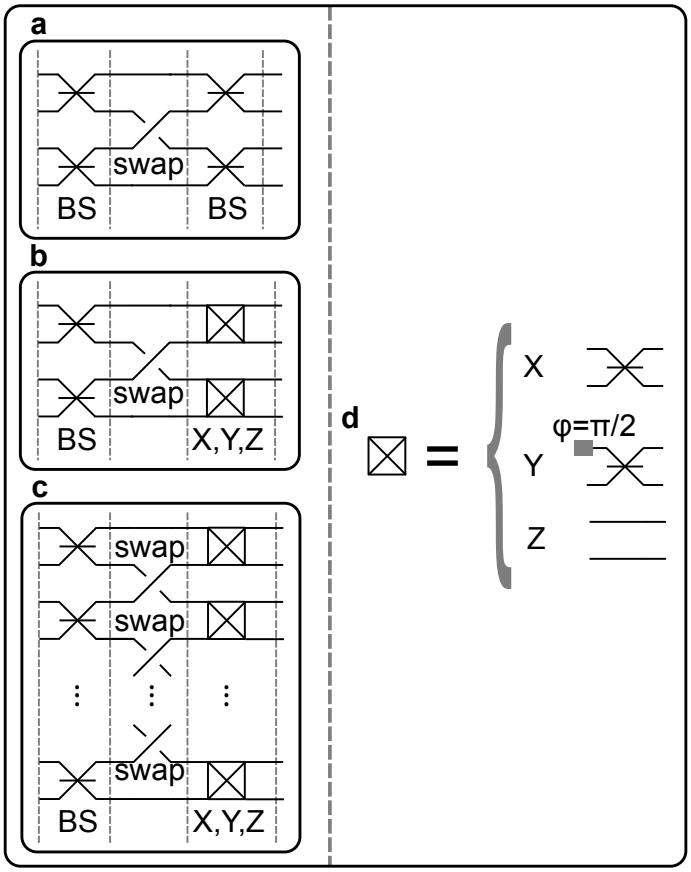

FIGURE 4.1: **a** Schematic of a circuit implementation of a four-mode DFT matrix. **b** Schematic of a circuit implementation of a postselected Bell state generator. **c** Schematic of a circuit implementation of a postselected GHZ state generator. **d** A component that can be reconfigured between three settings to project the measurement in the X, Y, and Z bases.

scheme in four modes, where the last column of MZIs have been removed. As such, we can implement the circuits using a cascaded two-path time-bin interferometer with three physical MZIs. From Fig. 3.3, we know that for even numbered time-bins, the physical MZI has to implement a swap transformation on the first and last time-bin. However, no such restriction is placed on the first and third column, and as our schematic has the same unitary operation applied across the whole column, we can implement these columns using a fixed unitary transformation for all time-bins. As such, both the boson suppression circuit and the postselected Bell state generator can be implemented using the circuit schematic shown in Fig. 4.2b, using two *static* (i.e. not time-dependent) unitary transformations and one time-dependent unitary transformation.

4.3 Setup

The two-path time-bin circuit shown in Fig. 4.2b is implemented using the polarization degree-of-freedom in bulk optics in place of the two paths, resulting in an effective circuit schematic shown in Fig. 4.2a. The polarization degree-of-freedom in bulk optics has the advantage that static unitary transformations can be implemented using wave plates for which the two polarizations share the same path. It will be necessary to convert back-and-forth with a two-path encoding to selectively delay one of the modes, which is achieved by inserting polarizing beamsplitters (PBSs). As all modes propagate in free-space, they should in principle not experience any propagation loss. However, the dealyed paths should ideally be perfectly aligned with the undelayed paths after recombination on the PBS. In practice, imperfect alignment will result to an imbalanced fiber coupling efficiency at the end of the interferometer for different paths.

The full experimental setup is shown in Fig. 4.3, where three sections have been outlined: the source, the interferometer, and measurement.

The **Source** consists of a pulsed laser (Coherent Mira) periodically exciting the quantum dot to produce a string of polarized single-photons separated by $13.8\,\mathrm{ns}$. This initializes the input state of the two-path time-bin interferometer to $|1,0,1,0\rangle = |\mathrm{HE},\mathrm{HL}\rangle$. Part of the laser is split off into a separate path using a beamsplitter, where it is detected using a photodiode to provide a clock signal used for synchronization of the experiment and measurement.

The **Interferometer** employs sets of wave plates (U_1 and U_3) for static unitary transformations, and employs an electro-optic modulator ($U_2(t)$) to perform a time-dependent unitary transformation.

As the desired time-dependent unitary transformation oscillates between two settings, we use a *resonantly enhanced* EOM from QUBIG with resonant frequency tuned to half of the repetition rate of the laser, i.e. around $36\,\mathrm{MHz}$. Resonantly enhanced EOMs can take higher-frequency driving signals than their nonresonant counterparts, but are limited to sinusoidal driving signals at their resonant frequency. To alternate between a maximum and minimal driving signal for every time-bin, we want to apply a sinusoidal signal

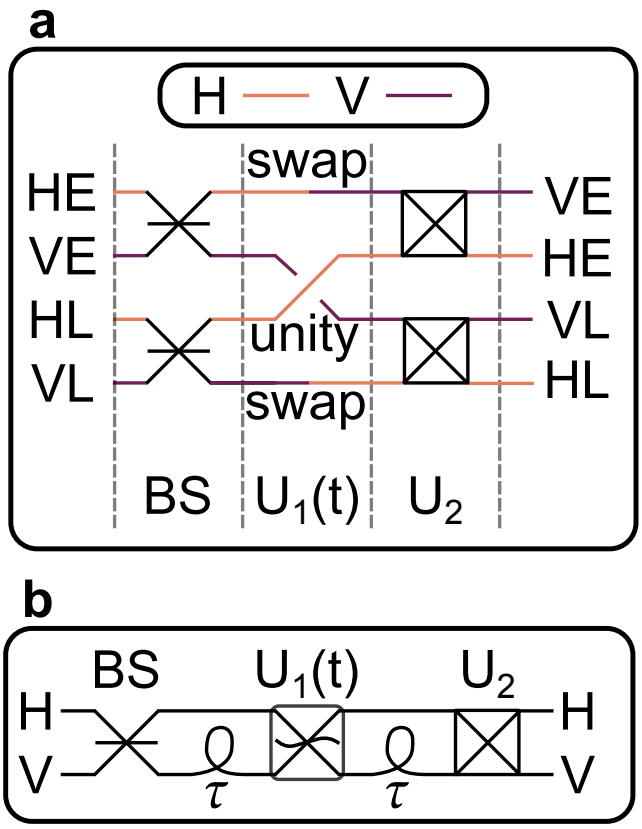

FIGURE 4.2: **a** Schematic of a time-bin circuit implementation used to implement a four-mode DFT matrix and postselected Bell-state generator. Horizontal and vertical modes are denoted by color. "E" denotes the "early" time-bin, and "L" denotes the "late" time-bin. **b** Schematic of the physical circuit implementation of a postselected Bell state generator. The first beamsplitter (BS) and the reconfigurable basis projection unitary (U_2) are implemented using wave plates, whereas the unitary matrix ($U_1(t)$) is implemented using a reconfigurable electro-optic modulator. As indicated in **a**, the electro-optic modulator alternates between applying a swap transformation (H $\rightarrow$ V, V $\rightarrow$ H) and a identity transformation (H $\rightarrow$ H, V $\rightarrow$ V).

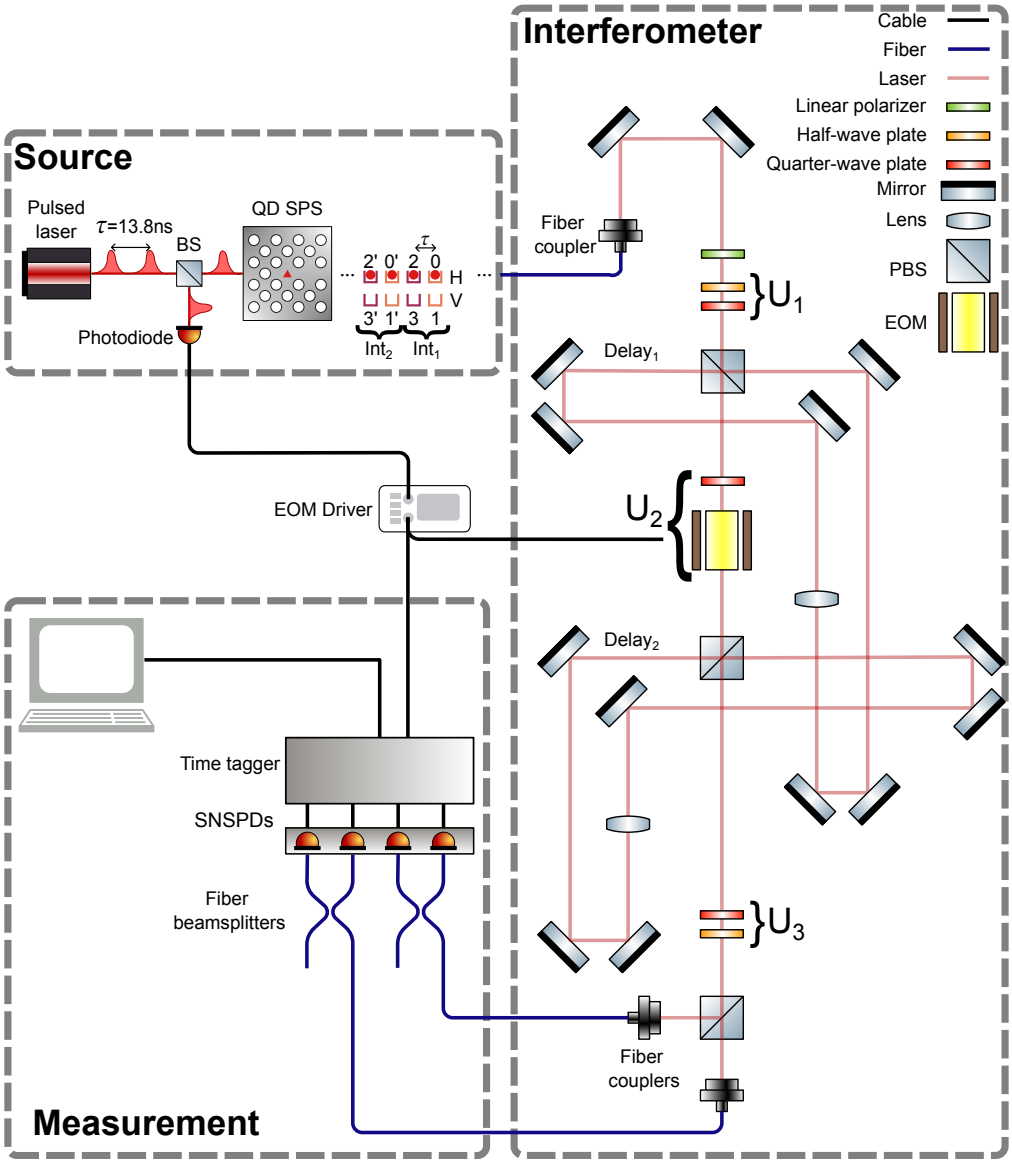

FIGURE 4.3: Schematic of the setup used for the experiments. An explanation of the schematic is provided in the main text.

with frequency equal to half of the repetition rate of the pulsed laser driving the source. The driving signal is produced by our EOM driver, which is phase-locked to the pulsed laser through a clock signal produced by the photodiode in the source section. By aligning the phase of the EOM driving signal precisely to the arrival time of the photons at the EOM, we can alternate between applying the maximum and minimum of the driving signal on every other time-bin. By setting the appropriate maximum and minimum values, we can then alternate between a swap transformation and a identity transformation, satisfying the requirements for the time-dependent unitary transformation.

After the first and second unitary transformations, a PBS is used to send vertically polarized light into a delay of exactly one time-bin, which corresponds to approximately four meters of propagation in free-space. The length of the delay was tuned by interfering laser pulses from the pulsed laser. The laser pulses have a pulse-length of around $6\,\mathrm{ps}$, and we only observe interference when they are overlapped. As the lifetime of the quantum dot was measured to be $917\,\mathrm{ps}$ (Wang et al. 2023), this ensures that any temporal mismatch between a delayed early input photon and an undelayed late input photon is negligible, ensuring that the delay does not introduce any partial distinguishability. A lens is added to each delay to correct for divergence of the beam waist. The delays are aligned such that the vertical polarization is aligned with the transmitted polarization after a second reflection on the PBS. The lens and alignment allows us to decrease the mismatch between the fiber coupling efficiencies of delayed and transmitted paths. After the third unitary transformation, a PBS is used to split the horizontal and vertical polarization into different modes for detection. The fiber coupling efficiencies for each path through the interferometer, characterized by configuring the wave plates in the interferometer with the EOM turned off, are shown in Table 4.1.

The wave plates in U_3 can be configured to implement measurements in the XX-basis, the YY-basis, or the ZZ-basis. For the XX and YY basis, the half-wave plate is rotated by $\pi/2$ with respect to the horizontal polarization, such that it implements a beamsplitter transformation on the two polarization modes. The quarter-wave plate is rotated by $\pi/2$ between the two bases, resulting in a relative phase difference of π added between the modes. For the ZZ-basis measurements, the ordinary axis of the half-wave plates was aligned with the horizontal polarization, resulting in an effective identity transformation[1].

For the **Measurement** of the state, the two polarized outputs are split using fiber beamsplitters and each of the four outputs are sent into a corresponding detectors. The fiber beamsplitters serve two purposes. First, they allow for measuring coincidences between early and late time-bins of the same polarization mode, which would otherwise be difficult due to the deadtime of the detectors, which has been measured to be $55\,\mathrm{ps}$ by a former

[1] In principle this adds a phase shift of π to the horizontal mode, but as there is no more interference before detection, it cannot affect the output statistics.

Path configuration	Measured fiber coupling
TTH	0.89
TTV	0.82
DTH	0.80
DTV	0.81
TDH	0.78
TDV	0.77
DDH	0.75
DDV	0.75

TABLE 4.1: Measured fiber coupling efficiency for each path through the interferometer illustrated in Fig. 4.3. The two first letters in the path configuration indicates whether the light was delayed in the first or second delay loop (with "T" denoting the path being transmitted at the PBS and "D" denoting the path being delayed by being reflected at the PBS). The final letter corresponds to the output detector the output coupling was measured at, with "H" ("V") denoting the fiber coupling to the horizontal (vertical) polarization detectors.

member of the group (Appel 2021). Second, the fiber beamsplitters in conjunction with two detectors allow for probabilistic resolution of two-photon Fock states as an output state containing two-photons in the same mode will antibunch on the fiber beamsplitter with a probability $50\,\%$. We can correct for this probabilistic detection by doubling the number of detected counts for each state with two photons in the same mode.

All detectors, as well as a clock signal from the EOM driver, are connected to the time-tagger used to measure two-fold photon coincidences between various pairs of detectors. The clock signal from the EOM allows for us to define the time-bin of two detector coincidences. By adding a deadtime to the clock signal channel on the time-tagger, we can effectively downsample the clock signal by a factor of two to produce a clock signal for the time-bin interferometer. Table 4.2 shows the appropriate detector configuration and time-delay for coincidence measurements for each basis state of the full Hilbert space.

4.3.1 Sources of error in the experimental setup

Before proceeding to the results, we will introduce two important sources of errors, and a model used to simulate the experimental setup with imperfections. We will consider two types of errors: 1. *Partial distinguishability* between the two photons in our input state, and 2. Finite *extinction* of the EOM leading to leakage between earlier and later time-bin interferometers.

Partial distinguishability is a model used to explain nonunity HOM visibility. A set of partially distinguishable photons are considered as a statistical mixture of two fully *in*distinguishable photons, which do interfere with one another, and two fully distinguishable photons, which transform

State	Detector configuration
$\|2,0,0,0\rangle$	HH:$E_1E_2^*$
$\|1,1,0,0\rangle$	HV:E_1E_2
$\|1,0,1,0\rangle$	HH:$(E_1L_2 + L_1E_2)$
$\|1,0,0,1\rangle$	HV:E_1L_2
$\|0,2,0,0\rangle$	VV:$E_1E_2^*$
$\|0,1,1,0\rangle$	HV:L_1E_2
$\|0,1,0,1\rangle$	VV:$(E_1L_2 + L_1E_2)$
$\|0,0,2,0\rangle$	HH:$L_1L_2^*$
$\|0,0,1,1\rangle$	HV:L_1L_2
$\|0,0,0,2\rangle$	VV:$L_1L_2^*$

TABLE 4.2: Detector coincidence configuration settings to measure a specific output state. The two first letters in the detector configuration corresponds to the polarization of each detector, with H denoting horizontal polarization and V denoting vertical polarization. Two detectors are available per polarization. The two last letters denote the measured time-bin for the corresponding detector, such that HV:E_1L_2 denotes a coincidence between an H detector and a V detector, where the H detector clicks in the early time-bin whereas the V detector clicks in the late time-bin. The states $|1,0,1,0\rangle$ and $|0,1,0,1\rangle$ are measured by two different detector configurations each. All basis states containing two photons in the same mode, marked with the * superscript, will have a $50\,\%$ lower chance of being detected.

independently of one another. In our model, we set the proportion of indistinguishable photons equal to the HOM visibility of the source. As the HOM visibility was measured to be $94.5\,\%$ (Wang et al. 2023), the output statistics should correspond to 0.945 multiplied with the output probability distribution from an input state of two indistinguishable photons in addition to 0.055 multiplied by the output probability distribution from an input state of two distinguishable photons.

The second source of error that we consider is that of nonunity extinction of our EOM. The extinction of the EOM was measured by sending horizontally polarized single photons through the EOM with the delayed paths

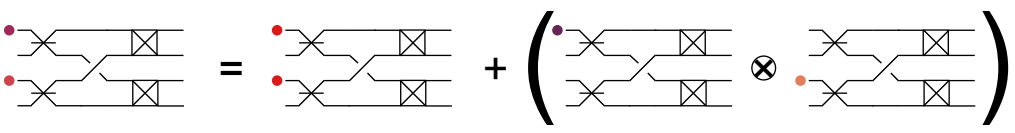

FIGURE 4.4: An illustration of how partial distinguishability is modeled. A set of partially distinguishable photons in an interferometer are considered as a statistical mixture of two fully *in*distinguishable photons interfering with one another and two fully distinguishable photons scattering independently (as indicated with the tensor product).

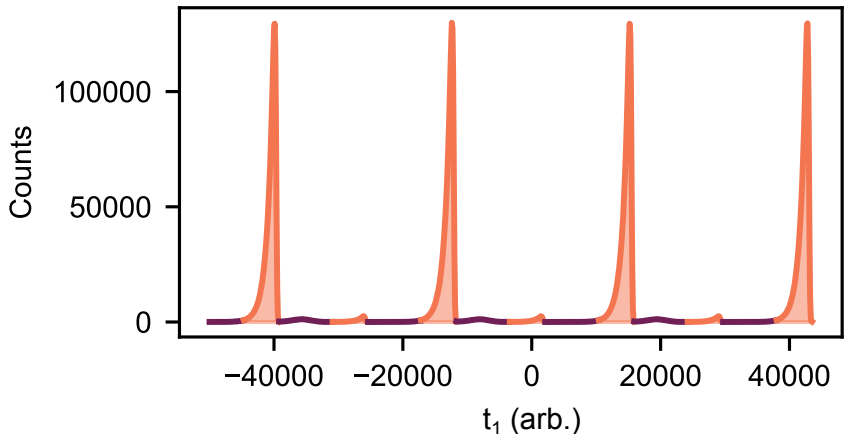

FIGURE 4.5: Measurement of the extinction of the electro-optic modulator used in the time-bin interferometer. The measurement is a coincidence measurement between the clock signal from the pulsed laser used to excite the source and one of the horizontal polarization detectors. Peak areas are indicated with a yellow color. An extinction of 51 was calculated by dividing the low intensity peak areas and the high intensity peak areas.

blocked. As every other photon should be swapped to vertical polarization, we should ideally only see peaks for every other time-bin. However, as we can see from the measurement shown in Fig. 4.5, we will instead see a strong suppression at every other time-bin. The result of this is illustrated in Fig. 4.6. From this measurement, we can estimate an extinction of 51. However, we note that this extinction was not stable, and drifted on a timescale of minutes. As the experiments required integration times of ten minutes, it is likely that the average extinction throughout the experiment was lower.

As finite extinction leads to some of the light being transmitted when it should be delayed and vice versa, light in the first (last) time-bin of an interferometer can be exchanged with the late (early) time-bin of the previous (subsequent) interferometer. We can model this by considering all combinations of the four photons highlighted in Fig. 4.6, where we use the inverse of the extinction as the transmission between interferometers. Each pair of photons are also modeled as partially distinguishable.

A brief comment about relabeling of outputs in the measurement

In our experiments we measured suppression of the states $|1,0,1,0\rangle$ and $|0,1,0,1\rangle$ instead of the expected states $|1,0,0,1\rangle$ and $|0,1,1,0\rangle$. Though this is not consistent with the output statistics expected from the circuit shown in Fig. 4.1a, it would be consistent with a circuit where the EOM applies an additional phase of $\pi/2$ to both modes when implementing only the swap or identity operation (or a phase shift of π to one mode for only one of the operations). Therefore, we attribute this discrepancy to such a phase shift, and proceeding we will compare with a relabeled distribution, i.e. one with suppression of $|1,0,1,0\rangle$ and $|0,1,0,1\rangle$.

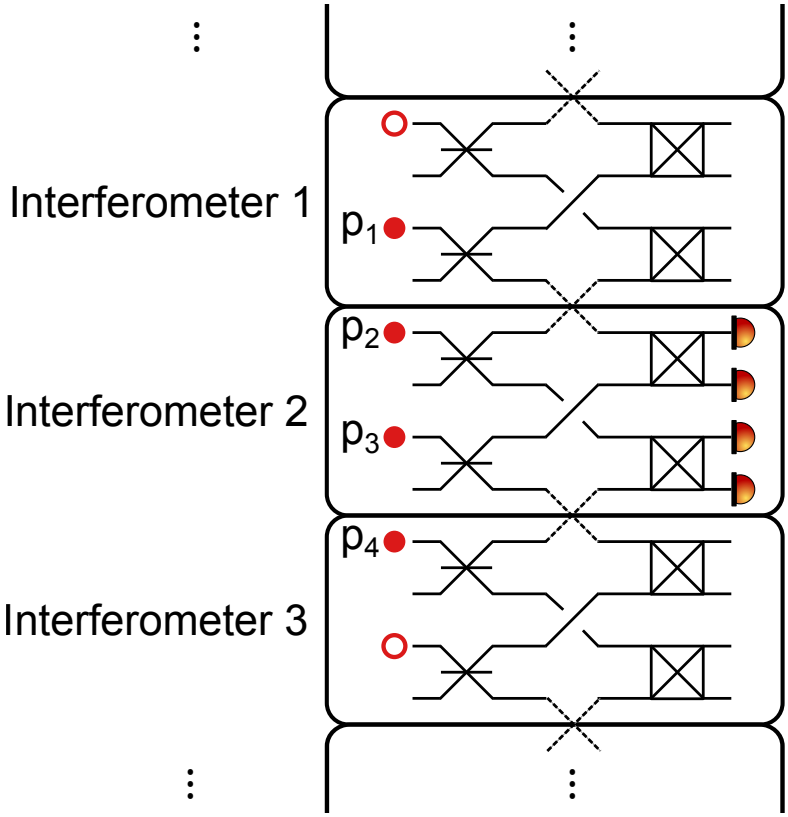

FIGURE 4.6: An illustration of how finite extinction leads to multiple connected time-bin interferometers. The dashed grey lines correspond to the EOM not implementing a perfect swap operation which would isolate each interferometer, instead scattering small portions of light between two interferometers. The filled red circles correspond to the input photons that contribute to detection events considered for Interferometer 2. The circles with a red outline correspond to input photons that do not contribute to the output statistics measured for Interferometer 2.

4.4 Results

A three-fold coincidence measurement between two photon clicks as well as the time-bin clock signal is shown in Fig. 4.7 for the two horizontal polarization detectors. This 2D histogram has the time-delay t_1 between the first detector and time-bin clock on the x-axis, and the time-delay t_2 between the second detector and the time-bin clock on the y-axis. In this measurement, the deadtime on the time tagger had to be set to downsample the clock signal by a factor of 12[2] as the time tagger had a maximum count rate of $8\,\mathrm{MHz}$. As a result, we can see six separate time-bin interferometers along the diagonal of the 2D histogram. Each point on the diagonal corresponds to the two detectors clicking at the same time with some time-delay compared to the time-bin interferometer clock. Moving up along the y-axis from the diagonal corresponds to the first detector clicking early and the second detector clicking late, and moving to the right along the x-axis from the diagonal corresponds to the first detector clicking late and the second detector clicking early. In Fig. 4.7 all interferometers along the diagonal have been summed together, effectively reversing the effect of the time-bin clock downsampling on the 2D histogram. The outlined areas are labeled according to which time-bin combinations they correspond to.

In order to reconstruct the output probability distribution for all basis states in the full Hilbert space, we have to combine the results of all detector configurations outlined in Table 4.2. We can then find the probability for a given output configuration by dividing by the total number of counts for all basis states considered. In order to correct for uneven coupling and detector efficiency, we normalize the coincidence counts for a given pair of detectors, d_1 and d_2 as

$$\text{coincidences}_{\text{normalized}}(d_1, d_2) = \text{coincidences}(d_1, d_2)/\sqrt{\text{counts}(d1) \cdot \text{counts}(d2)},$$

where $\text{counts}(d_i)$ is the total number of detected counts for detector i over the whole integration time.

The results of the measurements are shown in Fig. 4.8. This figure also shows a comparison to a simulation of the setup taking partial distinguishability and finite EOM extinction into account. The uncertainty of the measured results and the measured fidelity is estimated using Monte Carlo simulation where the number of detected counts have been assumed to follow a Poissonian distribution. The uncertainties of the measurements are shown in Table 4.3 for the bosonic suppression law and Table 4.4 for the postselected Bell state generator.

The fidelity of the measurements compared to the target probability distributions is estimated using two different approaches for the bosonic suppression law measurement and the postselected Bell state generator. To estimate the fidelity of the bosonic suppression law, we use the statistical

[2] Technically, a factor of 10 would have been sufficient.

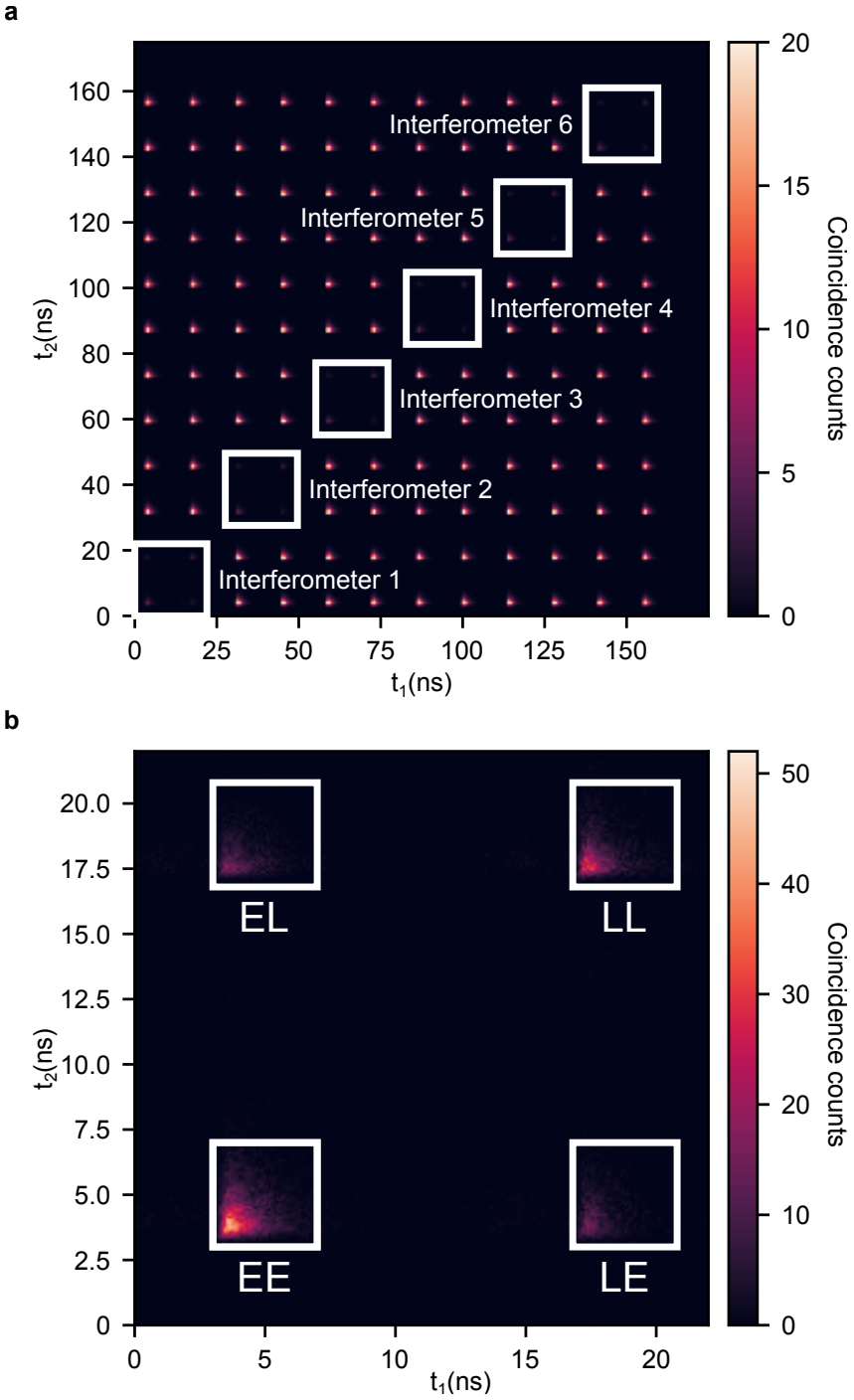

FIGURE 4.7: **a** 2D histogram measured for the HH detector configuration. Separate interferometers are labeled along the diagonal. The x-axis (y-axis) corresponds to the delay between detection of the downsampled clock cycle and the first (second) detector. **b** Sum of the separate interferometers illustrated in **a**. The four outlined regions correspond to different time-bin detection configurations where the first (second) letter refers to the detection time of the first (second) detection. The letter "E" corresponds to detection of the "early" time-bin and the letter "L" corresponds to detection of the "late" time-bin.

Bosonic suppression	
State	± uncertainty
$\|2,0,0,0\rangle$	0.0020
$\|1,1,0,0\rangle$	0.0006
$\|1,0,1,0\rangle$	0.0004
$\|1,0,0,1\rangle$	0.0019
$\|0,2,0,0\rangle$	0.0020
$\|0,1,1,0\rangle$	0.0020
$\|0,1,0,1\rangle$	0.0004
$\|0,0,2,0\rangle$	0.0019
$\|0,0,1,1\rangle$	0.0006
$\|0,0,0,2\rangle$	0.0019

TABLE 4.3: 95 % confidence interval for the measured counts in the bosonic suppression law measurement, estimated using Monte Carlo simulation assuming a Possonian distribution of detected counts.

fidelity between two distributions, defined as

$$F = \left(\sum_i \sqrt{p_i q_i} \right)^2 , \tag{4.2}$$

for distributions **p** and **q**. For the Bell state generator, we use the same approach as Vigliar et al. 2021, where the fidelity is defined as

$$F = \frac{1}{2} \left(F_{XX} + \frac{1}{2} \left(F_{YY} + F_{ZZ} \right) \right) , \tag{4.3}$$

where F_{ii} is the statistical fidelity for the computational ii-basis calculated using Eq.(4.2).

We measure a fidelity of 0.934 ± 0.001 for the bosonic suppression law, and a fidelity of 0.963 ± 0.001 for the postselected Bell state generator, where the uncertainties have been estimated using a Monte Carlo approach. Additionally, we estimate fidelities of 0.992 and 0.995 compared to simulations for the bosonic suppression law circuit and postselected Bell state generator, respectively.

4.5 Conclusion and outlook

In summary, we have demonstrated bosonic suppression laws and postselected Bell state generation with fidelities exceeding $90\,\%$, using a resource-efficient time-bin interferometer. Our results are limited by finite EOM extinction and partial photon distinguishability, as corroborated by simulations taking these effects into account showing a high fidelity compared to the measured results. Our experiments make it clear that time-bin interferometers can be particularly well-suited for the implementation of specific

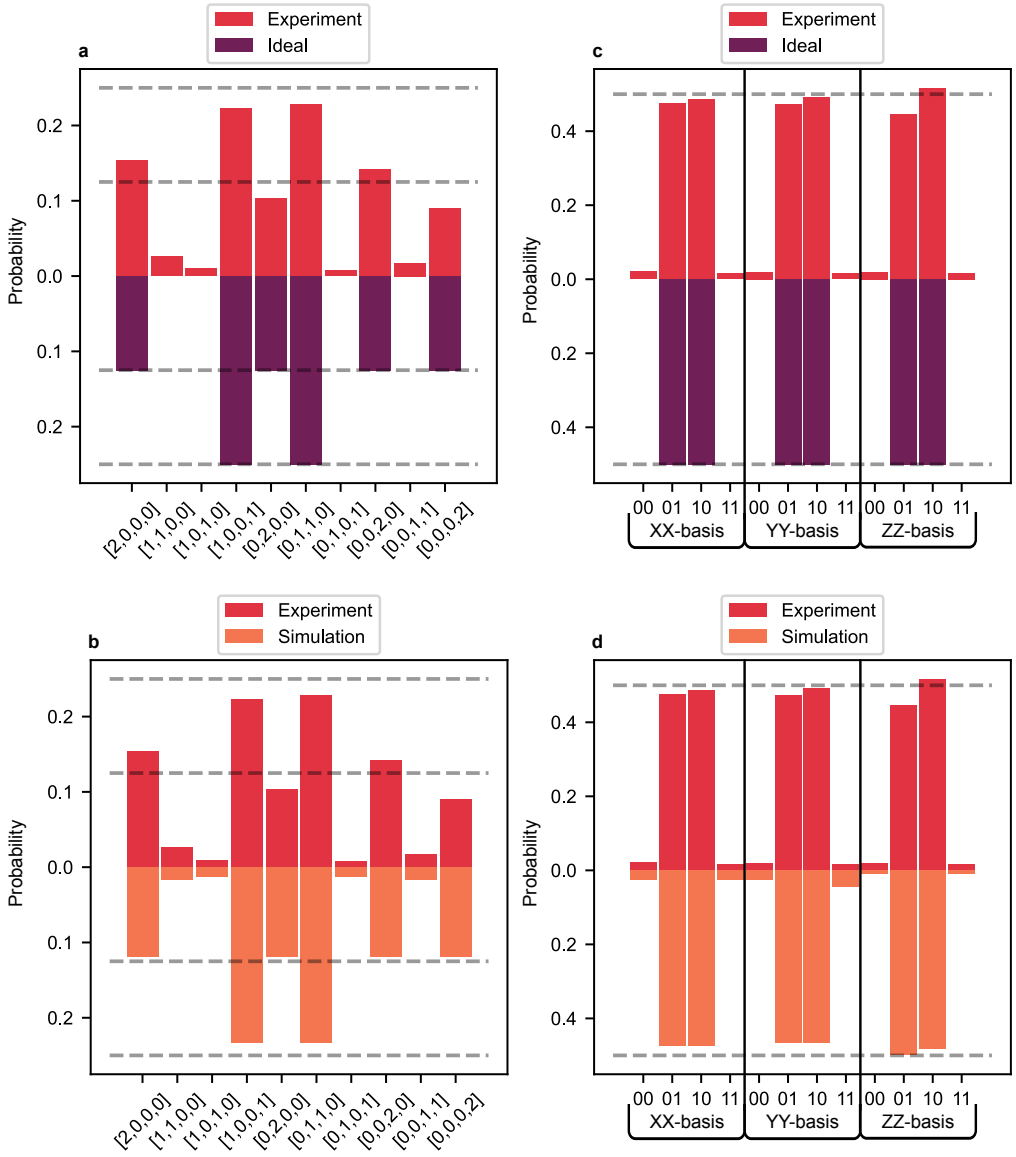

FIGURE 4.8: Measured output probability distributions compared to the ideal case and a simulation of the experimental setup. **a** The measured output probability distribution of the bosonic suppression law compared to the ideal case. The measured distribution reach a fidelity of 0.934 ± 0.001 compared to the ideal distribution. **b** The measured output probability distribution of the bosonic suppression law compared to a simulation of the experimental setup. The simulated distribution displays a fidelity of 0.992 compared to the measured distribution.**c** The measured computational output probability distribution of the postselected Bell state generator in the XX, YY, and ZZ basis compared to the ideal case. The measured result reach a fidelity of 0.963 ± 0.001 compared to the ideal case. **d** The measured computational output probability distribution of the postselected Bell state generator in the XX, YY, and ZZ basis compared to a simulation of the experimental setup. The simulation displays a fidelity of 0.995 compared to the measurement.

Postselected Bell-state generation	
State	+/- uncertainty
XX-basis	
$\|00\rangle$	0.0008
$\|01\rangle$	0.0032
$\|10\rangle$	0.0032
$\|11\rangle$	0.0008
YY-basis	
$\|00\rangle$	0.0017
$\|01\rangle$	0.0072
$\|10\rangle$	0.0017
$\|11\rangle$	0.0008
ZZ-basis	
$\|00\rangle$	0.0018
$\|01\rangle$	0.0336
$\|10\rangle$	0.0329
$\|11\rangle$	0.0025

TABLE 4.4: 95 % confidence interval for the measured counts in the postselected Bell state generator measurement, estimated using Monte Carlo simulation assuming a Possonian distribution of detected counts.

unitary transformations.

Our results highlight particular advantages and disadvantages of constructing time-bin interferometers in free-space using bulk optics. Bulk optics has the advantage that long delays can be implemented with low loss. However, as each delay introduces additional paths through the interferometer, all of which have to be coupled into the same detectors, it is difficult to achieve balanced coupling efficiency, as shown in Table 4.1.

Scaling up to larger experiments will face additional challenges. For our particular circuit, we were able to exploit the structure of the target circuit to limit the number of time-dependent components to one, using a single resonantly enhanced EOM. Future larger-scale experiments could similarly target larger-scale circuits with a similar structure. The postselected GHZ state generator[3] shown in Fig. 4.1c is an example of one such circuit, which could be implemented with the same experiemntal setup used here with a crucial substitution. In order for the EOM used for the second MZI column to implement swap transformations (or more likely, identity operations) on all time-bins except the first and the last, one would have to use a nonresonant EOM, also known as a broadband EOM. However, the use of broadband EOMs typically require the use of more sophisticated electronics, and the EOMs typically cannot operate at sufficiently high repetition rates. Experiments employing broadband EOMs instead rely on grouping

[3]It is important to note that *postselected* entanglement is more limited in utility than *heralded* entanglement, as detailed in Adcock et al. 2018.

multiple copies of the same time-bin into sequences where the same operation is applied to all time-bin in a given sequence. As the EOM only has to be reconfigured between each sequence, one can effectively lower the requirements on how rapidly it needs to be reconfigured by increasing the number of time-bins in each sequence. In this approach, each time-bin in the sequence only sees one time-bin from other sequences, as is done in e.g. Li et al. 2020 and Hummel et al. 2019. This has the consequence that the separation between interfering time-bins has to be increased, requiring longer delays.

Another disadvantage of bulk-optics setups is that they require a large amount of physical space. In the path encoding, this issue can be overcome by integrating all optical components onto a photonic chip, allowing for large-scale experimental setups on a small footprint, with the additional advantage that the interferometer stays phase-stabilized. However, the prospects of integrating time-bin interferometers on chips is limited by their excessive propagation loss, where even the best integrated photonics platforms exhibit propagation loss orders of magnitude worse than the standard propagation loss in optical fibers. One way to overcome this issue could be to route photons into off-chip fiber delays, however, typical current-day fiber-to-chip coupling loss is too high for this approach to be viable.

5 High-speed thin-film lithium niobate quantum processor

Statement of work

The work presented in this chapter is the result of a collaboration with Emma Lomonte and Francesco Lenzini who were working in Wolfram Pernice's group at the University of Münster, and Stefano Paesani and I from the Quantum Photonics group at the Niels Bohr Insitute in Copenhagen. The photonic integrated circuits were designed by Stefano and I using components developed by Francesco and Emma, and were fabricated in Münster by Francesco and Emma. Francesco and Emma also carried out classical characterization of the bandwidth of the on-chip EOMs, and took the beautiful microscope images of the chip shown in the figures in this chapter. The rest of the measurements were carried out by Stefano and I at the Niels Bohr Institute, using a single-photon source setup and characterized by Ying Wang. The work resulted in a publication (Sund et al. 2023a) and much of this chapter, particularly the introduction, results, and conclusion and outlook, will be reproduced from this manuscript with minor adjustments.

5.1 Introduction

Through substantial effort, quantum technologies are steadily advancing toward the promise of surpassing the limitations of classical information processing. Quantum photonics stands out as a promising candidate platform, with computing paradigms such as fusion-based quantum computing (FBQC) providing roadmaps for the realization of fault-tolerant quantum computing (Bartolucci et al. 2023). FBQC poses stringent requirements on the capabilities of the photonic hardware utilized, and although many key functionalities are satisfied by individual platforms, a singular platform satisfying every requirement has yet to emerge. Two key functionalities stand out as particularly challenging: the efficient generation of a large number of indistinguishable photons and rapidly-reconfigurable low-loss circuit for their routing and processing. In recent years, on-demand single-photon sources based on semiconductor quantum dots have demonstrated impressive progress, enabling highly efficient generation of near-ideal single-photons. Concurrently, thin-film lithium-niobate-on-insulator (LNOI) has rapidly matured as a platform for photonic integrated circuits (PICs) owing to a wide transparency window, low loss waveguides, and fast

and cryogenically compatible electro-optic modulators (Zhang et al. 2017; Wang et al. 2018a; Lomonte et al. 2021b). In this chapter, we combine the advantageous properties of a quantum-dot single-photon source with low-loss and rapidly reconfigurable circuits on LNOI to realize a device capable of demonstrating key functionalities for photonic quantum computing. The chapter is structured as follows. The first section introduces the LNOI platform and covers the design of the photonic chip. The proceeding sections cover the experimental setup, including workarounds of issues uncovered in classical characterization of the device. Finally, the results, discussion and outlook are presented as they appear in Sund et al. 2023a.

5.2 Background

This section will focus on the properties of lithium niobate that were relevant to the design of the photonic integrated circuits and experiments. For a more detailed account of LNOI fabrication, see e.g. the Ph.D. thesis of Jeffrey C. Holzgrafe (Holzgrafe 2022).

5.2.1 Electro-optic phase modulators

Lithium niobate (LN) is a material with a high nonlinear $\chi^{(2)}$ coefficient, leading to a strong Pockels effect (Saleh et al. 2007), where application of an electric field along a specific crystalline axis of the material will change the refractive index. In LN, the nonlinear coefficient, and hence the change in refractive index, is strongest along for an electric field is oriented along crystalline z-axis of the material.In order to induce a phase shift between modes, we need to apply an electric field which is perpendicular to the propagation direction of the light. To this end, we make use of the modulator design illustrated in Fig. 5.1a, adapted from Lomonte et al. 2021b. Here, two electrodes are deposited on top of a cladding layer on either side of a LN waveguide. By applying a positive voltage to one electrode while grounding the other, an electric field flowing through the cladding and waveguide to the other electrode will be created. As there will be an electric field inside the waveguide aligned with the crystalline z-axis, the resultant electro-optic effect will alter the refractive index of the material, altering the phase of any light that propagates through the waveguide.

In order to increase the relative phase shift between two modes, we can construct *push–pull* modulators as shown in Fig. 5.1b. Here, a positive electrode is situated in the middle of two waveguide, with ground electrodes on the other side of each waveguide. By applying a positive voltage to the middle electrode, the voltage will flow in opposite directions across each waveguide, applying a positive phase shift to the light in one waveguide (a phase "push") and a negative phase shift in the other (a phase "pull"), effectively doubling the phase shift.

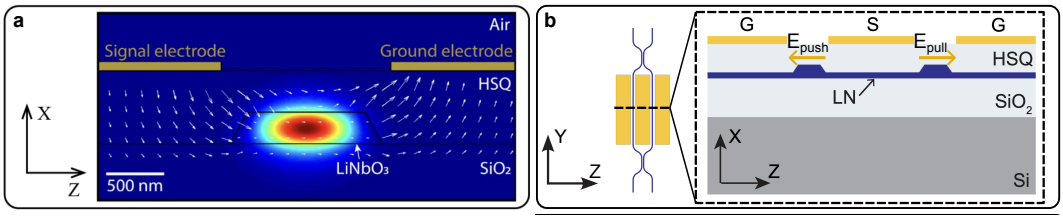

FIGURE 5.1: **a** Electrode configuration allowing for the application of an electric field along the z-axis within a thin-film LN waveguide. The white field lines indicate the direction and amplitude of the electric field. The heatmap shows the mode profile of the first-order TE mode in the waveguide. This figure is adapted from Lomonte et al. 2021b. **b** A top-view schematic and cross-section view of a push–pull phase-shifter. By applying a voltage to the signal eletrode (S), an electric field will be oriented in the negative z-direction for the left waveguide and in the positive z-direction for the right waveguide. This results in phase shifts with opposite signs (a "push" and a "pull") on the two waveguides. This figure is adapted from Sund et al. 2023a with modifications.

A brief acknowledgement of DC bias drift

A well-known issue with LN EOMs is *DC bias drift*, which results in instability of phase shifts when static (DC) voltages are applied to the modulators. The effect this has on our devices mirrors the one described in Lomonte et al. 2021b for room temperature operation, where upon application of a DC signal or AC signal with a DC bias the modulated signal returns to the same state as a zero DC voltage in less than a second. Though this had a profound impact on the experimental protocols, the origin of the DC bias drift is beyond the scope of this thesis. The interested reader is directed to Holzgrafe 2022 and/or Salvestrini et al. 2011. The effect of this DC bias on our modulators is partly covered in Appendix D.1.

5.2.2 Waveguides

Because of the large refractive index contrast between LN ($n_{\mathrm{LN}} \approx 2.24$ for wavelengths around $940\,\mathrm{nm}$) and the silicon oxide bottom cladding (($n_{\mathrm{SiO_2}} \approx 1.45$ for wavelengths around $940\,\mathrm{nm}$)) and HSQ top cladding ($n_{\mathrm{HSQ}} \sim 1.4$ for wavelengths around $940\,\mathrm{nm}$), light can be confined tightly, enabling relatively small waveguide cross-sections and small bending radii, particularly when compared to titanium-diffused LN which is still widely used in commercial EOMs. The mode profile for the single-mode waveguides used in our devices, as well as the mode-profile of a titanium diffused LN waveguide, is shown in Fig. 5.2.

A large portion of propagation loss in the waveguides comes as a result of roughness on the boundary between the LN and cladding materials, often referred to as waveguide roughness, which leads to scattering of the light. In order to reduce this source of propagation loss, we can make use

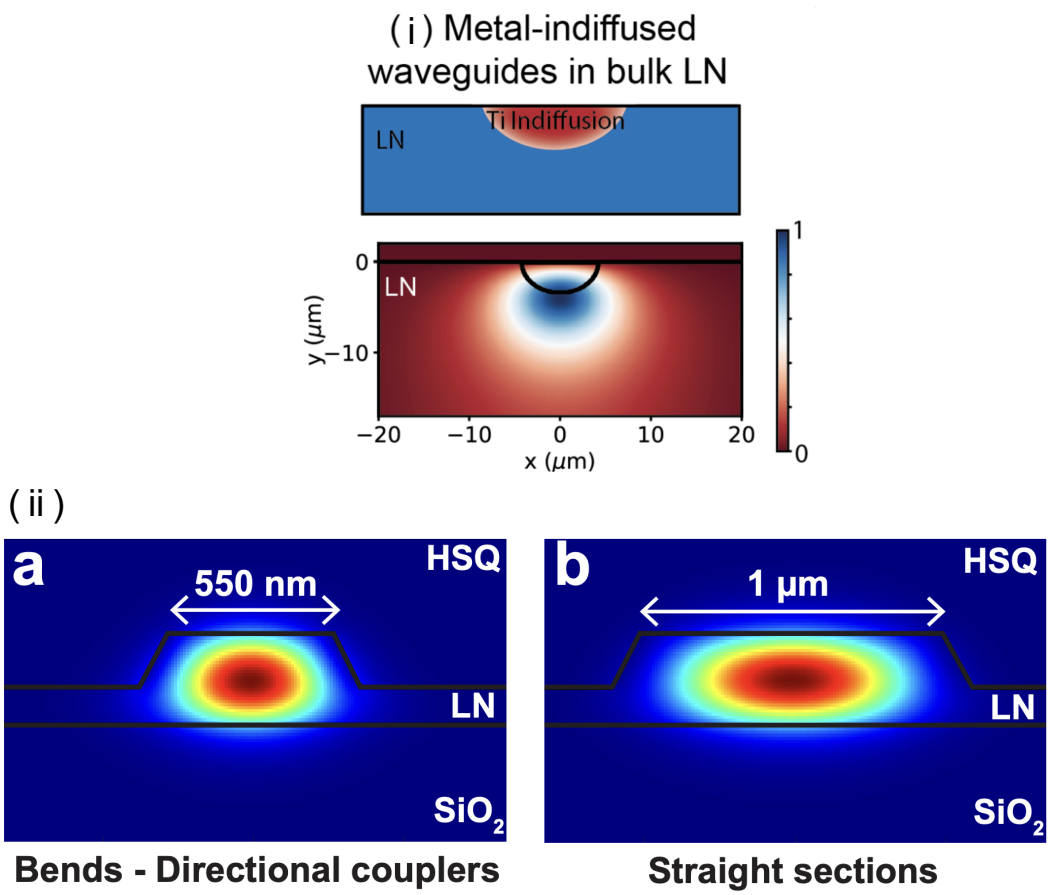

FIGURE 5.2: (i) A waveguide in bulk titanium-diffused LN. Adapted from Zhu et al. 2021. The colors indicate electric field amplitude. (ii) Mode-profiles for the fundamental TE mode in **a** a single-mode waveguide with a width of $550\,\mathrm{nm}$. **b** a multimode waveguide with a width of $1\,\mu\mathrm{m}$. The color indicates electric field amplitude where darker red is larger. Adapted from Sund et al. 2023a

of multimode waveguides with a width of $1\,\mu\mathrm{m}$. The mode profile for such a waveguide (adapted from Sund et al. 2023a) is shown in Fig. 5.2, which also shows the mode profile for a single-mode waveguide with a width of $550\,\mathrm{nm}$. The mode-profile for the multimode waveguide has a smaller proportion of the mode overlapping with the boundaries between materials compared to the case for a single-mode waveguide, and hence proportionally less of the mode will be scattered by waveguide roughness. In our final device we use $550\,\mathrm{nm}$-wide single-mode waveguides for sections with bends, where there would be a risk of mode conversion between different guided modes for multimode waveguides, and use $1\,\mu\mathrm{m}$-wide multimode waveguides for straight sections. We convert back and forth between single-mode waveguides and multimode waveguides using tapers of length $30\,\mu\mathrm{m}$.

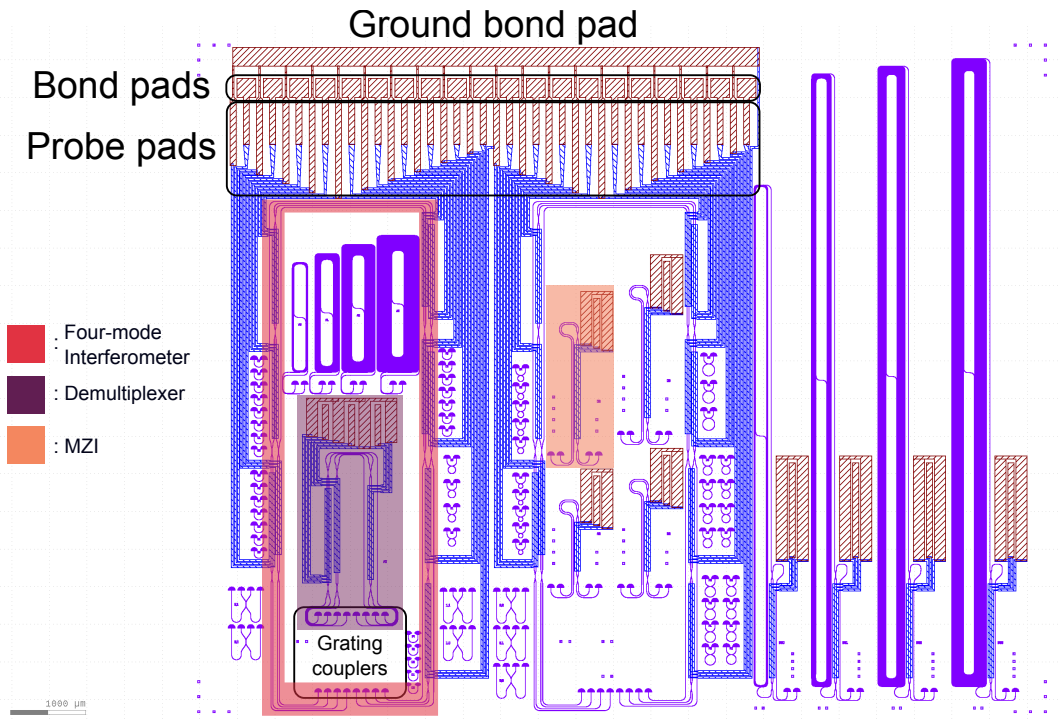

FIGURE 5.3: Screenshot of the GDS file used for the fabrication of the LNOI chips employed in this chapter. Structures used for experiments, i.e. a four-mode interferometer, a four-mode demultiplexer and an MZI, are highlighted. Sections with bond-pads, probe-pads and the grating couplers for the four-mode interferometer structure and demultiplexer are outlined.

5.3 Device design

A screenshot of the full layout of the chip is shown in Fig. 5.3, with the three structures used for experiments highlighted. The design of these devices was informed by a number of constraints and experimental considerations. The two most important constraints were: 1. A fixed orientation for all modulators, and 2. Fixing the relative orientation of all grating couplers and electronics.

The first constraint was motivated by the higher electro-optic coefficient for the crystalline z-axis, as previously mentioned. The second constraint, on the other hand, was put in place to simplify the experimental setup. Placing all grating couplers on the same side, as seen in Fig. 5.3, allowed for the coupling to be done with a single fiber-array. Routing all electronics towards the opposite side of the chip, on the other hand, made it simpler to place and align the optics and electronics using two camera angles, as detailed in Appendix D.2.

To simplify electronic access to all structures, the electronic connection of all electrodes included elongated pad-sections as outlined in Fig. 5.3, intended for use with electronic probes. For the four-mode interferometer, all signal electrodes were designed to include a wirebonding pad section,

whereas all ground electrodes were shorted together, effectively reducing the number of required bonds by a factor of two. Ultimately, no wirebonding was performed, with electronic probes used to connect to all modulator electrodes.

A microscope image of a fabricated MZI is shown in Fig. 5.7a and a microscope image of a fabricated four-mode interferometer and a demultiplexer is shown in Fig. 5.8a. For the four-mode interferometer, there will be multiple interfering paths between MZIs. The lengths of these different paths were not matched. The longest on-chip delay between two paths is approximately $1\,\mathrm{mm}$, which would correspond to a time-delay of approximately $3\,\mathrm{ps}$ in free-space, which is more than two orders of magnitude smaller than the measured lifetime of the quantum dot, i.e. the temporal length of a given single-photon. As such, we neglect the effect of any path-length mismatch on the indistinguishability of two output photons. This path-length mismatch instead results in an effective phase-shift, but which can be compensated for by using the phase-shifters in the interferometer.

5.4 Experimental setup

Many of the decisions made in the construction of the experimental setup were made to tackle issues that became apparent during classical characterization. The procedures and results of this preliminary classical characterization are presented in Appendix D.1. This section will focus instead on the final state of the experimental setup with explanations of the issues that had to be taken into consideration for each component.

Overcoming the DC bias drift

The biggest obstacle in performing experiments on the chip was the electronic control of the modulators. The first problem was that we needed to be able to send in DC signals and signals with DC offsets. This problem was exacerbated by the apparent high impedance of the modulators (see Appendix D.1). We solved both issues by making use of an arbitrary waveform generator (AWG) able to drive high load impedances (a Rigol DG 4202). In order to effectively drive DC signals, we used the AWG to drive $100\,\mathrm{kHz}$ square wave signals, i.e. a signal switching between a high voltage and a low voltage, and postselected on detected events coinciding with the high voltage. The demultiplexer required additional workarounds, as we had to be able to drive fast AC signals with a DC offset. As the DC bias drift removed any DC offsets to AC signals, we implemented the desired AC signal in *pulses* with a low duty cycle, i.e. only applying the AC signal containing the "DC" offset for a short period of time.

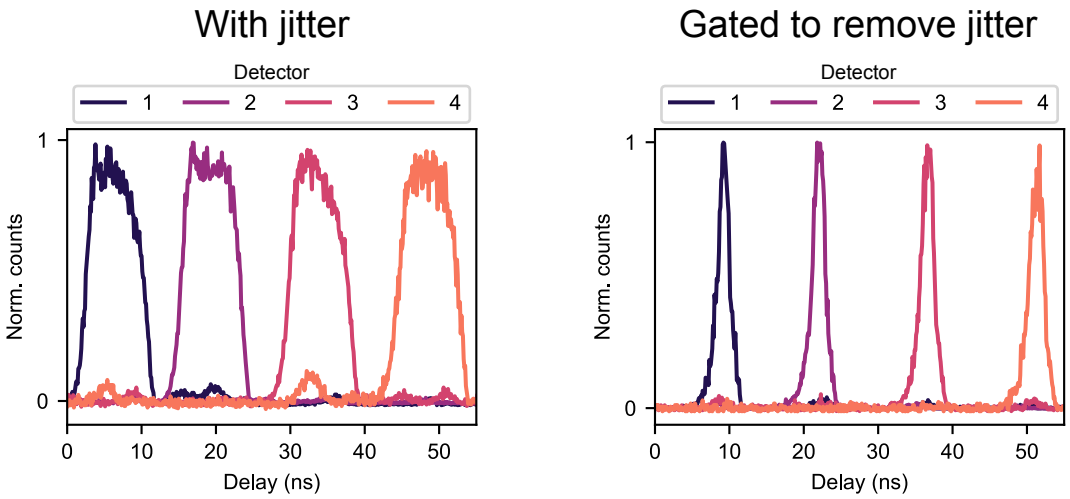

FIGURE 5.4: Experimentally measured demultiplexed signal with and without jitter filtering. The different colors corresponds to detected events using different detectors. The detector counts have been normalized, and calibrated background counts have been subtracted.

Overcoming the limitations of the Rigol AWG

As the repetition rate of the pulsed laser used to drive our single-photon source is approximately $72\,\mathrm{MHz}$, the pulse sequence for a four-photon demultiplexer should in principle be the same rate divided by four, i.e. approximately $18\,\mathrm{MHz}$. To introduce a lower duty cycle, we instead pulsed a single iteration of the pulse sequence with a pulse rate of $5\,\mathrm{MHz}$. Thus, in order to use the Rigol AWG to drive the modulators in the demultiplexer experiment, we had to be able to trigger low-duty cycle pulses with a repetition rate around $5\,\mathrm{MHz}$ in-phase with the photon emission at a repetition rate of around $72\,\mathrm{MHz}$. This required downsampling the frequency of the clock signal from the single-photon source to approximately the repetition rate of the AWG pulses. To this end, we made use of a complicated scheme where the clock signal was first downsampled by a factor of two through an FPGA, and then used to trigger a $5\,\mathrm{MHz}$ clock signal on a faster AWG (Active Technologies Arb Rider AWG-5064). This resulted in a downsampled clock signal at approximately $5\,\mathrm{MHz}$, but the introduction of an FPGA and another AWG resulted in substantial jitter on the signal. This jitter was removed by postselecting on detector coincidences where the synchronization signal from the Rigol AWG coincided within a short temporal window with a clock signal from the SPS. The effect of this postselection can be seen in Fig. 5.4. This complicated setup was not necessary, and it would have been much easier to make use of a conventional frequency divider in place of the FPGA and AWG.

A final challenge with using the Rigol AWG was that only two channels were available to drive the three EOMs on the demultiplexer or ten EOMs in the four-mode interferometer. For the demultiplexer, two channels were sufficient as one channel could be reused for two EOMs. The demultiplexer

splits four photons in the same spatial input mode into four separate spatial output modes in two stages. In the first stage a single EOM is used to split the incoming photons between two spatial modes, and in the second stage one EOM per mode is used to route the photons from two spatial modes to four. The EOM in the first stage applies a transformation to all four photons, sending the first two photons into one arm through an identity transformation, and the latter two photons into the other arm with a swap transformation. The EOMs in the second stage only applies a transformation to two photons each, and so we can use the same signal to address the first EOM for the first two photons, and the other EOM for the second two photons. The pulse sequence implemented in the experiment is illustrated in Fig. 5.8d.

A different approach was taken for the four-mode interferometer. Here, we use a single channel to drive all of the modulators in reverse by applying a signal to the ground pad. In this configuration, the push–pull MZIs, as illustrated in Fig. 5.1, now act as pull–push MZIs where the ground electrodes on the side act as signal electrodes, and the signal electrodes act as floating ground electrodes. In this configuration, we were able to configure different unitary matrices with limited programmability.

Modeling of the four-mode interferometer

In order to validate the experimental results from this configuration, we mathematically modeled the circuit with a single phase being applied to the internal phase-shifter of all MZIs and individual phases applied to each external phase-shifters. Though the same phase would be applied to the external phase-shifters, the external phase shifts were kept as free parameters as path-length mismatch between MZIs within the interferometer also adds an effective phase shift to the light. We then extrapolated the implemented unitary by numerically fitting the expected output statistics from the model to the experimentally measured output distributions.

Two-mode off-chip demultiplexer

As our four-mode interferometer and MZI experiments require spatially encoded input states with two photons in two separate modes, we have to make use of a two-mode demultiplexer. To this end we make use of the experimental setup introduced in Chapter 4, which has the capability of switching and synchronizing pairs of photons to two different modes. To this end, the first delay loop was blocked, and the unitary transformations U_1 and U_3 shown in Fig. 4.3 were set to identity.

Schematic of the experimental setup

Schematics of the full experimental setup are shown in Fig. 5.5, adapted from the Supplementary Materials of Sund et al. 2023a. The following is a quote of the figure caption from the supplementary materials of Sund et

al. 2023a. **a** Schematic of the experimental setup used to perform measurements of two-photon interference in two-mode and four-mode interferometers. *Optics*: A pulsed laser operated at $72\,\mathrm{MHz}$ is used to drive a quantum-dot (QD) single-photon source, producing a stream of single photons, which is routed into a two-mode demultiplexer consisting of an electro-optic modulator (EOM) and a polarizing beamsplitter (PBS). The demultiplexer splits subsequently emitted photons into two modes, one of which is delayed such that the photons are synchronized. The synchronized photons are subsequently sent to the chip via a fiber array (FA) and on-chip grating couplers, and extracted from different grating couplers and coupled to the same fiber array. The output photons are detected using superconducting nanowire single-photon detectors (SNSPDs) and the arrival times are recorded on a time-tagger (TT). *Electronics*: A fraction of the pulsed laser is split off using a beamsplitter and measured using a photodiode (PD). The resulting clock signal is used to trigger the EOM. An arbitrary waveform generator (Rigol AWG) is used to drive the modulators with an AC signal, and a synchronization signal is sent to the TT to allow for coincidence measurements between the control signal and single-photon detection events. **b** Schematic of the experimental setup used to perform active 1×4 demultiplexing of a stream of single-photons produced by a quantum-dot (QD) single-photon source. *Optics*: A pulsed laser operated at $72\,\mathrm{MHz}$ is used to drive a QD single-photon source, producing a stream of single photons. The stream of photons is routed directly into the chip via a fiber array (FA) and on-chip grating couplers, and output photons are extracted from different grating couplers with the same fiber array. These output photons are detected using superconducting nanowire single-photon detectors (SNSPDs) and the arrival times are recorded on a time-tagger (TT). *Elecronics*: A fraction of the pulsed laser is split off using a beamsplitter and measured using a photodiode (PD). Part of this clock signal is downsampled using a field-programmable gate array (FPGA) and used to trigger a square waveform with a repetition rate of $\sim 5\,\mathrm{MHz}$ on an arbitrary waveform generator (AT AWG). This $\sim 5\,\mathrm{MHz}$ signal is used to trigger an arbitrary waveform generator (Rigol AWG) which drives the modulators in an on-chip demultiplexer structure. A synchronization signal from the Rigol AWG and the other part of the clock signal from the PD is sent into a time-tagger to enable coincidence detection between the input photon clock signal, the electronic control signal, and the single-photon detection events.

5.5 Results

The remaining text and figures of this chapter have been quoted from Sund et al. 2023a with an additional two sentences added to the conclusions and outlook and minor formatting adjustments.

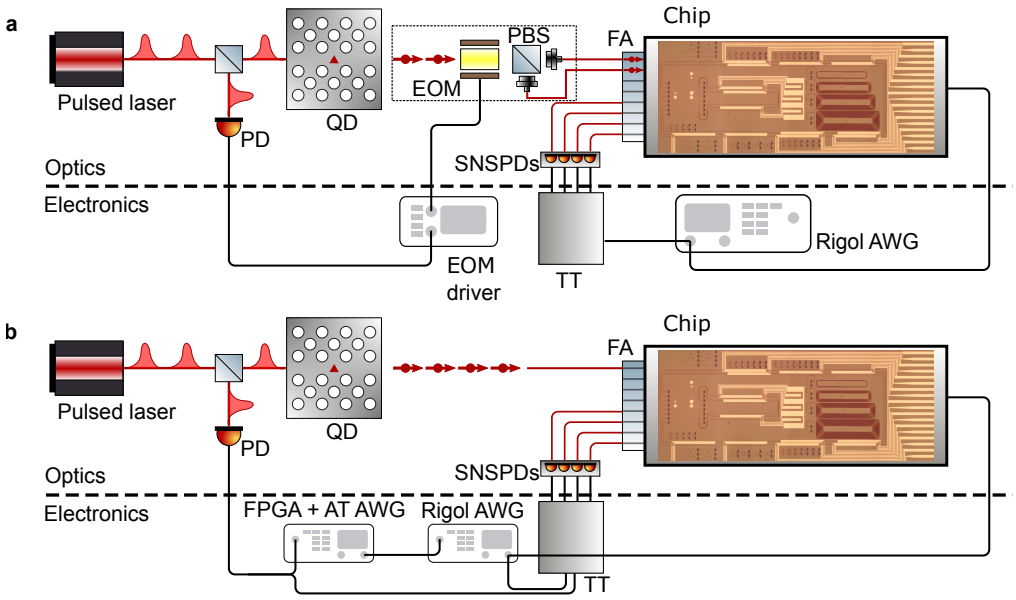

FIGURE 5.5: This figure is adapted from the from the supplementary material of Sund et al. 2023a. **a** Shows the setup used for two-photon interference, used with the MZI structure and four-mode interferometer. **b** Shows the setup used for the demultiplexer experiment. The caption is quoted from the supplementary material of Sund et al. 2023a in the main text.

5.5.1 Integrated photonic platform

In Fig. 5.6a we report a schematic of the geometry employed for the realization of single-mode (SM) LNOI waveguides. Optical circuits are implemented as rib waveguides with a 180 nm etching depth, fabricated by electron-beam lithography (EBL) and argon etching on a 300 nm thick X-cut LN film bonded on a silica-on-silicon substrate. After etching, the waveguides are clad with a $\simeq 550$ nm thick electrically cured hydrogen silsesquioxane (HSQ) layer. The angle of the waveguide sidewalls (measured with an AFM) is $\simeq 60°$, and the top waveguide width of 550 nm ensures single-mode operation around 940 nm wavelength, the typical emission wavelength for InGaAs QDs employed in this work, for TE-polarized light.

The fabrication of photonic integrated circuits (PICs) operating at the short emission wavelength of InGaAs QDs comes with the disadvantage of increased propagation loss due to sidewall scattering, whose magnitude scales as $1\lambda^3$ (Lacey et al. 1990) when compared with the values attainable for telecom LNOI waveguides. For this reason, we chose to employ SM waveguides only for the realization of bends and directional couplers—where it is more likely to excite higher order modes—and to adiabatically enlarge the waveguide width up to 1 µm in the straight sections of the optical circuitry to reduce the overlap between the TE optical mode and the waveguide sidewalls (see Fig. 5.6b). By the use of this approach, we were able to measure a low propagation loss coefficient down to 0.84 dB/cm at $\lambda = 940$ nm.

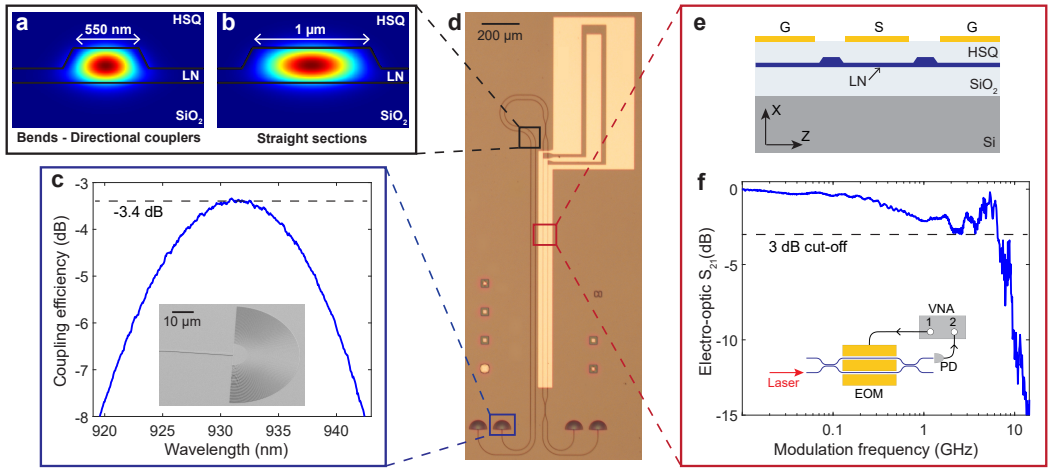

FIGURE 5.6: **Overview of the platform.** **a-b** Schematics of the designed waveguide geometry, tailored for the quantum emitter $\lambda \simeq 940$ nm operation wavelengths, for **a** single-mode waveguides used in bends and directional couplers, and **b** multi-mode straight waveguides. Color-coded is the field intensity of the fundamental TE waveguide mode. **c** Measured coupling efficiency of the fabricated grating couplers as a function of the input laser wavelength, with a peak efficiency of -3.4 dB. The inset shows a scanning electron micrograph image of the coupler. **d** Optical microscope image of an electrically tunable MZI. **e** Schematic of the cross-section of the electro-optic phase-shifter. **f** Modulation bandwidth of the MZI measured with a VNA. The data shows a 3 dB cut-off at approximately 6.5 GHz. Inset: schematic of the setup employed in the measurement.

The LNOI PIC is optically coupled to SM fibers by the use of apodized grating couplers with a negative diffraction angle, designed by following the approach of Lomonte et al. 2021a. The best coupling efficiency of our gratings was measured around 930 nm wavelength, and found to be -3.4 dB (see Fig. 5.6c for further details). This measured value compares well with the best ones obtained at telecom wavelength for gratings etched on a pure LNOI platform, i.e., without any use of a back-reflector for improving the grating directivity or additional material layers for increasing the grating strength (see, e.g., Chen et al. 2022 for a review on recent progress). We numerically estimate that with the aid of a metal back-reflector underneath the buried oxide layer, our couplers can achieve an insertion loss of < 1 dB. The LNOI PICs demonstrated here can therefore offer an efficient approach for interfacing fast optical switches and circuits to optical fibers.

For the realization of electro-optically tunable waveguide circuits we use as a main building block Mach–Zehnder interferometers (MZIs) consisting of two 50:50 directional couplers and an electrically tunable phase-shifter (see Fig. 5.6d). The phase-shifter is implemented by patterning three 1.25 mm long gold electrodes in a ground–signal–ground configuration along the Y axis of the crystal, in order to provide an efficient overlap between the fundamental TE mode of the waveguide and the z-component of the applied electric field via the highest electro-optic component ($r_{33} \simeq 30$ pm/V) of the LN susceptibility tensor. Unlike more common implementations of EOMs in LNOI, where signal and ground electrodes sit at the two sides of the waveguide (Wang et al. 2018b; Wang et al. 2018a), here we opted to pattern them atop of the HSQ cladding (see Fig. 5.6e). This choice is made to enable a nearly lossless crossing of the electrodes with the waveguides without any need for additional fabrication steps. The fabricated modulators displayed a half-wave voltage (V_π) of approximately $4.5\,\mathrm{V}$, corresponding to a small voltage-length product $V_\pi L \simeq 0.6$ V $\cdot$ cm, and a high extinction ratio $\simeq 21$ dB. The insertion loss of a single MZI, which includes two directional couplers, propagation loss in the waveguides, and metal-induced absorption loss due to the presence of the electrodes, was estimated from measurements to be equal to $\simeq$0.8 dB.

To test the high-speed performance of the modulators, we make use of the setup schematically depicted in the inset of Fig. 5.6e. The phase-shifter is driven with a small-amplitude RF signal from port 1 of a vector network analyzer (VNA), while port 2 is connected to a fast photodiode (Newport - 1544 B) optically coupled to one of the two outputs of the MZI. The resulting S_{21} parameter—defined as the ratio between the power measured at port 2, and the power leaving from port 1—is plotted in Fig. 5.6f normalized to its maximum value, and provides a direct estimation of the MZI electro-optic bandwidth. From the data, we record a 3 dB cut-off frequency of the modulator at approximately 6.5 GHz, demonstrating the high-speed capabilities of the fabricated PICs.

5.5.2 On-chip quantum interference

A central figure of merit in photonic quantum information processing is the visibility of multiphoton quantum interference, typically quantified as the two-photon interference visibility in Hong–Ou–Mandel (HOM) experiments. Incorporating simultaneously the detrimental effects of imperfect photonic circuitry, source distinguishability, and purity, this quantity is essential in determining the dominant stochastic noise in photonic quantum computing schemes (Rudolph 2017) and the computational complexity limits in photonic sampling algorithms (Renema et al. 2018a). We thus start by performing on-chip HOM experiments to test the performance of our platform for photonic quantum information processing with the experimental scheme depicted in Fig. 5.7b. For single-photon generation we use a self-assembled InAs QD embedded in a GaAs photonic and electronic nanostructure in a 1.6K cryostat. The device comprises a single-sided photonic crystal waveguide and a shallow-etched waveguide grating for efficient photon generation, and a hetero-diode to suppress electrical noise and Stark-tune the emission wavelength (Uppu et al. 2020). We create a two-photon input state from a stream of single photons emitted by the QD using an off-chip demultiplexer to split up pairs of consecutive photons into two distinct paths, one of which is delayed such that the photons arrive at the chip simultaneously. The photons are sent into an integrated MZI containing a tunable electro-optic phase-shifter. The electrodes constituting the phase-shifter are connected to an electronic probe, allowing for control of the internal phase in the MZI. Photons are then routed off-chip to SNSPDs for coincidence detection. On-chip HOM interference is studied by applying a varying phase to the high-speed modulator of the MZI interferometer, and measuring the fringe of the coincidence counts at the output (Rarity et al. 1990; Adcock et al. 2019; Paesani et al. 2020). The measured HOM fringe visibility of $92.7\% \pm 0.7\%$, see Fig. 5.7c, is consistent with the corresponding HOM visibility measured off-chip. This testifies that the fabricated PIC does not add stochastic noise on the processed photonic states (e.g., due to imperfect phase shifting or beam splitting, temporal mismatches, excitation of higher order modes in the waveguides, or TE-TM intermodal conversion (Kaushalram et al. 2020)), certifying the high quality of the developed circuits as quantum photonic processing units.

5.5.3 Integrated single-photon router

Fast photon routers play an important role in photonic quantum computing schemes. For example, routers can be used in conjunction with measurement and feed-forward to construct multiplexing schemes, turning inherently probabilistic quantum photonic processes into near-deterministic operations (Migdall et al. 2002; Varnava et al. 2008; Gimeno-Segovia et al. 2015). Alternatively, taking advantage of the capability of deterministic quantum emitters, streams of emitted photons can be routed into multiple spatial outputs to enable networking schemes that reduce resource overheads in photonic quantum computing architectures (Bombin et al. 2021),

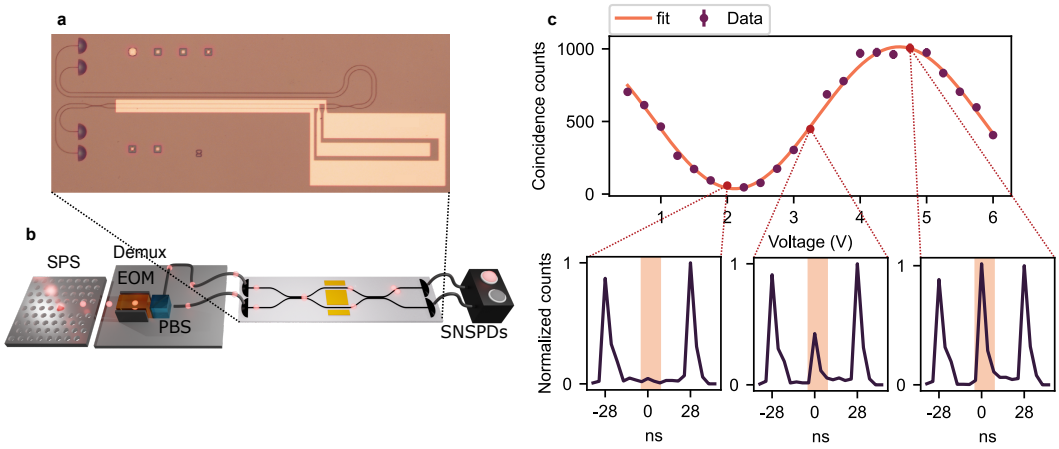

FIGURE 5.7: **Measurement of on-chip quantum interference.** **a** Optical image of the chip. **b** Schematic of the experimental setup. Photons generated by a QD single-photon source (SPS) are sent into a two-mode demultiplexer consisting of a resonantly enhanced electro-optic modulator (EOM) and a polarizing beam-splitter (PBS). The photons are subsequently collected into fibers and injected into the LNOI chip by a fiber array. Controlling the delay on one of the demultiplexer arms ensures that the photon pairs arrive at the device simultaneously, and fiber polarization controllers are used to optimize coupling into the TE mode. The output photons are collected via the same fiber array and routed to SNSPDs for coincidence detection. **c** Recorded coincidence data at zero time-delay (shaded red areas in the insets) for varying applied voltages. Minima and maxima in the observed HOM fringe correspond to applied phases of $\phi_{\text{min}} = \pi/2 + k\pi$ and $\phi_{\text{max}} = k\pi$, respectively, with k an integer number. The error bars are estimated from Poissonian statistics and are smaller than the data points. The HOM visibility of the quantum interference is determined from a curve fit (orange line) to be $92.7\% \pm 0.7\%$. Insets: coincidence histograms for three different applied voltages.

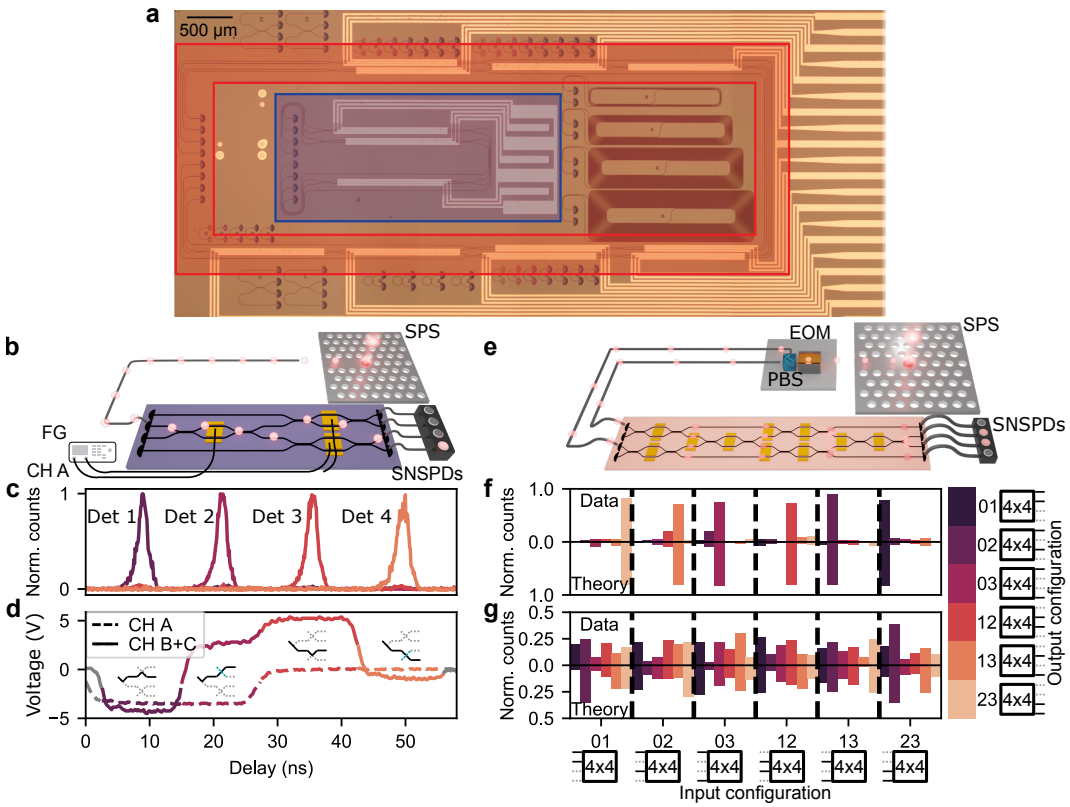

FIGURE 5.8: **Photon processing in multimode high-speed integrated circuits.** **a** Optical image of the chip. The photon router structure is highlighted in blue, and the 4×4 universal interferometer in orange. **b** Schematic of the experimental setup used to perform active 1×4 demultiplexing of a stream of single-photons produced by the QD. Photons are directly coupled in and out of the chip using a fiber array, and their time of arrival recorded via SNSDPs and a time-tagger. Fast electrical control is performed via a function generator (FG) connected to the modulators via a probe station, where a channel is used to individually address the MZI in the first layer and the other channel is split to drive both MZIs in the second layer in parallel. **c** Normalized photon counts in the four output waveguides within the time interval of a four-photon sequence. **d** Associated pulse sequences, with corresponding switching network configurations shown as insets. **e** Schematic of the experimental setup for the universal 4×4 interferometer. The optical part is equivalent to that described in Fig. 5.7. The ten high-speed modulators employed are electrically connected via a probe station and driven by a multichannel function generator. **f-g** Experimental data (top) and estimated theoretical (bottom) collision-free input–output probability distributions when programming the interferometer to implement an approximate permutation matrix (**f**) and a randomized unitary matrix (**g**), with estimated statistical fidelities of 96.3% and 95.5%, respectively. The horizontal index indicates the input configuration in terms of the mode indices of the first and second photon, and the color corresponds to the output configuration. Dashed lines separate different input configurations.

as well as demultiplexing schemes that turn a single deterministic single-photon source into multiple sources (Wang et al. 2019).

Making use of the capability to integrate fast phase-shifters on the LNOI platform compatible with the quantum emitter wavelengths, we demonstrate a fully on-chip photon router for the QD-emitted photons. In particular, starting from a stream of single photons emitted from the QD at a fixed rate, we implement a 1×4 demultiplexer. The demultiplexer consists of three fast electro-optic MZI switches, which are cascaded in a tree-shaped network, as schematised in Fig. 5.8b (see Fig. 5.8a for a device microscope image). It processes sequences of four single photons emitted by the QD with a temporal separation of $13.8\,\mathrm{ns}$, switching each photon deterministically into its own dedicated spatial mode. Fig. 5.8c shows time traces for four output detectors with respect to the pulse sequence. The average probability of switching a photon in the four-photon sequence to its dedicated mode is measured to be 96.2%, corresponding to an average suppression of -14.2 dB for unwanted photons. Such success probability is conditional upon photon detection (i.e. does not include loss) and shows the performance of rapidly programming the device to implement the desired time-dependent routing transformation. This directly illustrates the highly promising potential of the LNOI platform for photon routing of deterministic resource states produced by QDs.

5.5.4 Universal four-mode interferometer

Programmable multimode quantum photonic interferometers are central in the implementation of core functionalities in photonic quantum technologies, e.g., multi-photon gates and fusion measurements (Carolan et al. 2015b; Bartolucci et al. 2023), and to realize circuits for quantum computational advantage experiments or analog quantum simulation (Zhong et al. 2020; Madsen et al. 2022; Huh et al. 2014; Sparrow et al. 2018). To showcase the capabilities of the QD-LNOI platform for this class of tasks, we implement a universal 4×4 interferometer constructed from a network of 6 MZIs containing 10 phase modulators, as shown in Fig. 5.8e. The interferometer implements a scheme from Clements et al. (Clements et al. 2016), whereby the unitary transformation enacted by the interferometer is controlled by the phases applied to the modulators, allowing for the device to implement any arbitrary linear-optical unitary transformation on the four input waveguides.

We show that the interferometer can be programmed from implementing a structured matrix (an approximate permutation matrix resulting from applying no voltage to the modulators) to implementing a randomized matrix obtained by driving all the phase-shifters simultaneously. In Figures 5.8f, g we report the measured input–output probability distributions for the two cases, obtained by photon coincidence detection for all possible collision-free two-photon configurations, i.e. combinations with no more than one photon per mode. The different input states were prepared by demultiplexing a stream of photons from the QD off-chip into two separate fibers and

routing these two fibers to all possible collison-free two-photon input configurations (see Fig. 5.8e). The measured distributions are compared with theoretical predictions obtained by reconstructing the unitary matrices from the experimental data. We find a mean statistical fidelity to the implemented transformation of 96.3% for the approximate permutation matrix, and of 95.5% for the randomized matrix.

5.6 Discussion

The demonstrated circuits show the promise of the developed LNOI platform for processing photons from emerging solid-state deterministic sources. In order to fully enable scalable quantum technologies, further optimization of the platform is, however, required. Firstly, though limited reconfigurability was demonstrated with the four-mode interferometer, universal operation and particularly the implementation of fusion gates are important future milestones. This can either be achieved by upgrading the electronic circuity used for the experiment, or alternatively by addressing the DC bias drift problem of the modulators. Various measures can be taken to address DC bias drift, such as cooling down the chip to cryogenic temperatures (Lomonte et al. 2021b), or removing the cladding between the electrodes and LN (Holzgrafe 2022, Puma et al. 2022). To improve the transmission loss at the relevant wavelengths for quantum-dot sources, besides improving our current fabrication process to reduce roughness, the use of a thinner LN film would allow for the width of SM waveguides to be increased while maintaining single-mode operation. As proportionally less of the mode in such wider waveguides would overlap with the sidewalls of the waveguide, this would mitigate the effect of sidewall scattering. The use of a cladding with a higher refractive index than HSQ (e.g., silicon oxynitride) can also be beneficial, at the expense of a larger waveguide footprint at the expense of a larger footprint as the bend radius would have to be increased. A large improvement in the efficiency of the grating couplers can be achieved by patterning a metal back-reflector underneath the buried oxide layer. This can, for example, be accomplished via back-side etching of the silicon handle, with a fabrication process analogous to the one preliminary demonstrated in Lomonte et al. 2022.

System integration of all the employed quantum devices on LNOI—sources, circuits, and detectors—provides an additional promising direction for lowering the overall system loss. In this direction, direct integration of SNSPDs together with a reconfigurable LNOI component has been recently experimentally demonstrated using the same material stack employed in this work (Lomonte et al. 2021b). Heterogeneous integration of quantum emitters directly onto the LNOI waveguides could be realized with pick-and-place techniques that has recently emerged as a highly promising approach (Aghaeimeibodi et al. 2018). Alternatively, photonic wire bonds fabricated by two-photon absorption lithography might be employed for interfacing optical circuits implemented in heterogeneous photonic platforms (Lindenmann et al. 2012).

In conclusion, high-speed LNOI quantum processors provide a route to scale up quantum photonic technologies by leveraging the mature and advanced on-demand sources realized with solid-state quantum emitters in photonic nanostructures. Moving forward, further optimization of the platform is required in order to reduce coupling and propagation loss, which will be realized in a close interplay between device design and PIC fabrication optimization. Fault-tolerant quantum computing architectures demand typical loss levels of $\lesssim 10\%$ per photon (Borregaard et al. 2020; Bartolucci et al. 2023), which appears feasible with the technology after full-circle optimization of source, processor, and detector, and will be an exciting future research and engineering challenge. With such an approach, only a few tens of interconnections between individual quantum emitters and GHz-speed reconfigurable devices suffice for fault-tolerant photonic quantum computing at scale (Bombin et al. 2021).

6 Hardware requirements for a quantum advantage demonstration using deterministic single-photon sources

Statement of work

The work presented in this chapter is the result of a collaborative effort between my former supervisor Ravitej Uppu, Stefano Paesani, Peter Lodahl, and I.

The work resulted in a manuscript (Sund et al. 2023b), and much of this chapter will be reproduced from this manuscript. Specifically, the introduction and most of the results, discussion and outlook are presented as they appear in the manuscript with minor formatting adjustments. Larger changes were made to the section detailing the boson sampling setup so as to not repeat information presented in earlier chapters, and hardware requirement benchmarks for the demultiplexing interferometer architecture presented in Chapter 3.3.2 have been included in the results and discussion.

6.1 Introduction

Devices based on quantum systems can potentially outperform the capabilities of classical computers (Preskill 2012; Preskill 2018). Quantum technologies are rapidly progressing towards this goal and new computational regimes are being explored (Arute et al. 2019; Madsen et al. 2022; Morvan et al. 2023). While fault-tolerance is generally thought to be necessary to reach most practical applications, reaching this regime necessitates hardware requirements that are far from current capabilities, limiting demonstrations to small-scale experiments (Maring et al. 2023; Quantum et al. 2020). Quantum advantage (QA), where specialized algorithms can demonstrate speed-ups over classical computers, has been identified as an intermediate milestone computational regime amenable for near-term hardware using readily available quantum hardware components (Aaronson et al. 2011; Hamilton et al. 2017; Boixo et al. 2018). While it is currently not known if any practical applications are possible in this regime, it serves as an entry point to beyond-classical capabilities and an important benchmark for developing scalable platforms that can evolve towards fault-tolerance. In this context, we analyze the hardware requirements for achieving QA using photonic quantum hardware, where fusion-based approaches for fault-tolerant quantum computing have been proposed (Bartolucci et al. 2023; Paesani et al. 2023).

Aaronson and Arkhipov proposed boson sampling of photonic quantum states (Aaronson et al. 2011) as a route for demonstrating QA with near-term quantum hardware. The key insight is the connection between the correlations induced by linear interference operations on N indistinguishable photons in an M-mode linear optical interferometer and the matrix permanent, a quantity that is #P-hard to compute on a classical machine (Valiant 1979; Scheel 2004). However, imperfections in photon sources and losses in optical interferometer networks and detectors rapidly diminish the degree of quantum correlations and overthrow the quantum advantage. This loss of QA has been captured in models on 'noisy' boson samplers that proposed efficient classical computation algorithms, thereby imposing strict bounds on the indistinguishability of photons and the overall optical loss (Brod et al. 2019; Renema et al. 2018a; Renema et al. 2018b). As quantum photonic hardware continues to rapidly advance (Elshaari et al. 2020; Uppu et al. 2021; Pelucchi et al. 2021; Moody et al. 2022), the formulation of quantitative benchmarks for realizing QA is a critical need as they provide milestones for guiding the hardware development.

In this paper, we present a comprehensive analysis quantifying the performance metrics of the constituent building blocks essential for surpassing efficient classical algorithms with boson sampling. By benchmarking our framework against state-of-the-art single-photon sources and photonic integrated circuits, we identify a realistic regime for conducting QA experiments. Our analysis focuses on the case of boson samplers based on single-photon sources (discrete variable photonic qubits), where several proof-of-concept experiments have been carried out to date (see e.g. Broome et al. 2013; Spring et al. 2013; Crespi et al. 2013; Tillmann et al. 2013; Wang et al. 2019).

Recent advances in deterministic photon sources employing semiconductor quantum dots have demonstrated the generation of $>$100 nearly-identical photons Uppu et al. 2020; Tomm et al. 2021, setting the stage for scaling up from proof-of-concept experiments. A remaining challenge is to realize large photonic circuits with sufficiently low loss such that the large photonic resource can be processed and measured to demonstrate QA Brod et al. 2019; Pelucchi et al. 2021. As the optical loss in an interferometer circuit is highly dependent on its design, i.e., the spatial arrangement of Mach-Zehnder interferometers (MZI), we analyze the requirements of the individual MZIs and their integration into an optimal architecture. Combining the analysis of the source imperfections and optical circuit loss, we identify two key optimizations, a rectangular circuit architecture and the encoding of modes in multiple degrees of freedom, that could enable an unequivocal demonstration of QA. We determine that an insertion loss of $3.5\,\mathrm{mdB}$ per MZI interferometer, i.e., a transmittance of $99.92\,\%$ is sufficient for the optimal architecture using state-of-the-art photon sources and detectors. This sets a clear target metric for ongoing advances in photonic integrated circuits (Stojanović et al. 2018; Bao et al. 2023), and is already within reach for the specialized, fixed circuits employed in Wang et al. 2019 and Zhong et al. 2020.

6.2 The boson sampling algorithm and its validation

Boson sampling is the task of sampling from the output photon distribution after multiple independent photons have interfered in a multimode linear optical interferometer. The setup for implementing boson sampling is schematically illustrated in Fig. 6.1a) highlighting the key components: an input consisting of multiple indistinguishable photons, a large multimode interferometer module, and single-photon detectors.

The computational complexity of simulating boson sampling arises from the connection between multi-photon correlations and the calculation of matrix permanents. However, the computational hardness of calculating the matrix permanent decreases when duplicate rows or columns occur from multiple photons occupying the same input or output mode. To preserve the computational complexity, it is crucial to ensure collision-free states at both the inputs and outputs (Aaronson et al. 2011), meaning that each mode contains at most one photon. Collision-free input states can be guaranteed by choosing the initial condition, where no more than one photon is injected into each input mode. Ensuring collision-free outputs demands the interferometer to possess a large number of modes per photon. Specifically, the number of modes m must scale at least quadratically with the number of photons p, i.e., $m \propto p^2$, a requirement arising from a phenomenon called the *bosonic birthday paradox* (Aaronson et al. 2011; Arkhipov et al. 2012). In experiments, collision-free outputs can be ensured through postselection of events where photons are detected in the same number of output modes as input modes while discarding all other events. This postselection strategy remains applicable even when the detectors lack number-resolving capabilities, thereby enabling near-term implementations of QA with efficient single-photon detectors (Wang et al. 2019; Zhong et al. 2020; Bulmer et al. 2022).

To demonstrate QA, it is essential that the output samples can be validated as being computationally hard to produce by classical means Brod et al. 2019. Due to the computational hardness, direct validation of the samples by comparison with exact distributions is infeasible. Within these constraints, the validation of QA through boson sampling requires two steps. First, we must require that deviations in the experimental setup are small enough that approximate classical algorithms cannot simulate the output distribution efficiently. Secondly, instead of validating that the samples are produced from the exact distribution, one verifies that the outputs are not reproduced by a computationally efficient distribution (Brod et al. 2019; Wang et al. 2019). Specifically, statistical tests performed on the output samples obtained in a boson sampling experiment verify that the experimentally observed distribution differs significantly from a set of efficiently computable distributions. These statistical tests provide a termination condition for the experiment, whereby the boson sampler is run until a sufficient number of output samples are generated to establish the statistical tests' convergence unequivocally. Thus, a QA demonstration will be feasible if a

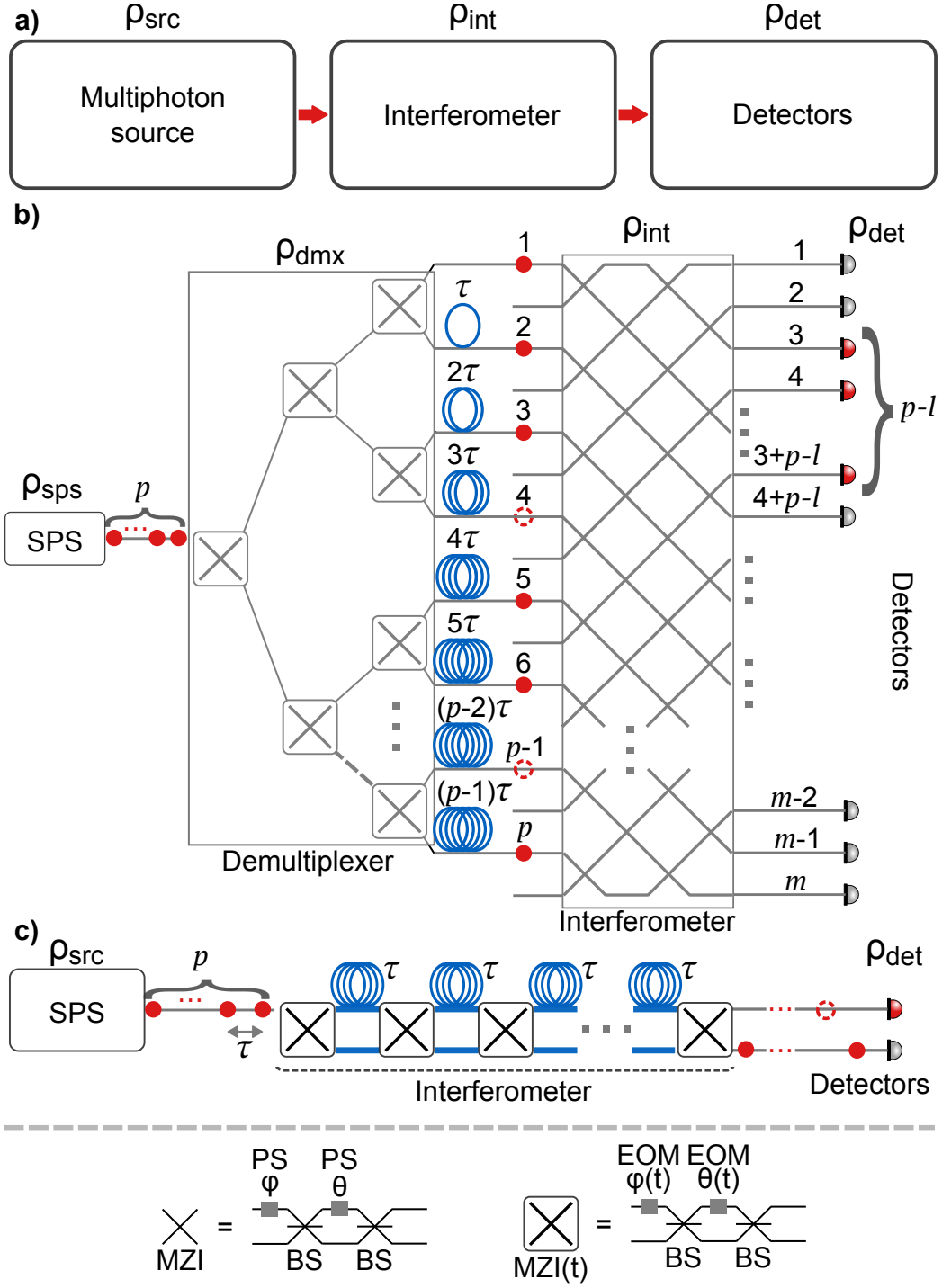

FIGURE 6.1: **a)** A general boson sampling setup, consisting of a source of multi-photon input states, a multi-port interferometer, and detectors. The associated system losses ρ are indicated for each sub-component. Up to l photons may be lost in the experiment, illustrated red circles with dashed outlines in **b)** and **c)**. **b)** A boson sampling setup based on a deterministic single-photon source (SPS) and a spatially encoded interferometer. The SPS and demultiplexer produces spatially encoded input states of p photons, illustrated as filled red circles. The input state is transformed using a spatially encoded interferometer, constructed from a network of MZIs. **c)** A boson sampling setup employing a time-bin interferometer constructed from reconfigurable time-dependent MZIs connected by delay lines (blue lines) each applying a single time-bin τ of delay.

sufficient number of samples can be produced over an experimentally viable integration time, proportional to the sample acquisition rate, r_{sample}. The sample acquisition rate in an experiment is equal to the product of the generation rate of the multiple photon input state r_{input} and the probability of the state reaching the detectors, P_{sample}:

$$r_{\text{sample}} = P_{\text{sample}} \cdot r_{\text{input}}. \tag{6.1}$$

The probability of sampling a p-photon coincidence at the output is related to the total per-photon efficiency of the system P_{sys} as

$$P_{\text{sample}} = P_{\text{sys}}^{p}. \tag{6.2}$$

For convenience, we express these probabilities in decibels, i.e., $\rho_{\text{i}} = -10\log_{10}(P_{\text{i}})$. For brevity, we refer to the decibel probability, ρ_{i} as loss, while P_{i} is referred to as efficiency.

6.3 Experimental setup and imperfections

As illustrated in Fig. 6.1a), the loss in the boson sampling architecture can be broken down into component-level losses as

$$\rho_{\text{sys}} = \rho_{\text{src}} + \rho_{\text{int}} + \rho_{\text{det}}, \tag{6.3}$$

where ρ_{src} is the source loss, ρ_{int} is the interferometer loss, and ρ_{det} is the detector loss. In this section, we detail the implementation and requirements on the components and discuss strategies to tackle experimental limitations in each component.

6.3.1 Input state preparation

The input state in the boson sampling algorithm consists of multiple indistinguishable single photons in a collision-free input state. In the following, we discuss how such an input state can be produced, and the imperfections that are introduced in real experiments.

The pair-wise indistinguishability between photons, here refered to as x^2, is an important figure-of-merit for boson sampling experiments. The indistinguishability can be quantified experimentally by measuring the HOM visibility in an interference experiment (Hong et al. 1987) (e.g. as done in Chapter 5). To ensure computational hardness, photon indistinguishability approaching near-unity visibility is necessary.

One approach to generating highly indistinguishable single-photons is to employ single quantum emitters such as semiconductor quantum dots in nanophotonic structures to realize on-demand single-photon sources, as detailed in Chapter 2. However, there is an additional approach that has

seen widespread use in experiments: using nonlinear optics to make *heralded* single-photon sources. This approach exploits the energy-time correlations in optical processes in nonlinear media like spontaneous parametric down-conversion and spontaneous four-wave mixing to generate correlated photon pairs. The resulting squeezed state can be used directly for Gaussian Boson Sampling (Hamilton et al. 2017; Zhong et al. 2020; Madsen et al. 2022), or alternatively, the detection of one photon in the pair can be used to herald the presence of the other. Despite being probabilistic, the heralded nature can be exploited through active feed-forward and multiplexing to realize a near-deterministic photon source (Migdall et al. 2002). As the sources suffer from an intrinsic trade-off between the photon number purity (the probability of having one and only one photon pair per pulse) and the photon pair generation rate, this requires massive multiplexing of many probabilistic sources to reach near-deterministic operation with high number purity, which is an active area of research (Bartolucci et al. 2021).

On-demand single-photon sources (SPSs) based on quantum emitters do not suffer from these challenges and tradeoffs. Such sources have recently been demonstrated to enable the on-demand generation of >100 highly indistinguishable single photons operational up to a GHz rate, thus highlighting an avenue for realizing boson sampling in the QA regime (Uppu et al. 2020).

A single on-demand SPS will naturally produce multimode input states in the time-bin encoding, which can be converted to a spatial encoding by employing a demultiplexer. In both cases, the repetition rate at which the source produces new input states, which we will call the *input state generation rate* r_{input}, is limited by the time it takes for the source to produce all of the photons. If the SPS produces single-photons at a rate of $r_{\text{single-photon}}$, the input state generation rate of p photons will be

$$r_{\text{input}} \leq r_{\text{single-photon}}/p, \tag{6.4}$$

where the lesser sign can apply to the time-bin encoding, as will be explained in Section 6.3.5.

We specifically consider and benchmark the case of a single deterministic source but note that access to multiple deterministic quantum-dot sources would allow for spatially encoded experiments with higher input state generation rates and lower demultiplexer losses. The simultaneous use of multiple sources relies on the development of local tuning methods for overcoming intrinsic inhomogeneities of quantum-dot sources, and important progress has recently been reported both for quantum dots in bulk samples (Zhai et al. 2022) and in nanophotonic waveguides (Papon et al. 2022).

Recall from Chapter 2.3.5 that a time-to-spatial mode demultiplexer can be realized by sending the emitted photon stream through a binary tree of switches. Each step in the tree doubles the number of spatial modes, as illustrated in Fig. 6.1b), such that the full demultiplexer requires a depth of $\lceil \log_2(p) \rceil$. Each output mode from the demultiplexer requires a specific optical delay to synchronize all photons. We associate a loss of ρ_{switch} with

each switching operation, such that the overall loss of the demultiplexer is:

$$\rho_{\text{dmx}} = \lceil \log_2(p) \rceil \, \rho_{\text{switch}}.$$

The output of the demultiplexer has to be connected to the input of the interferometer, which is typically implemented using a different photonic platform. This incurs a coupling loss, ρ_{coupling}, such that the overall source loss is

$$\rho_{\text{src}} = \rho_{\text{sps}} + \rho_{\text{dmx}} + \rho_{\text{coupling}},$$

where ρ_{sps} is the loss associated with the single-photon source itself, accommodating for inefficiencies associated with the generation of single photons and subsequent coupling from the cavity or waveguide the source is embedded in (Lodahl et al. 2022).

Photon loss and Aaronson–Brod sampling

We note that the number of photons generated should ideally be kept as low as possible while maintaining intractability, as the sample acquisition rate will decrease exponentially with system efficiency for an increasing number of input photons in accordance with Eq. (6.2). In order to increase acquisition rates, experimental efforts typically employ a related algorithm called *Aaronson–Brod* boson sampling (Aaronson et al. 2016), where an additional l photons are added to the p input photons, while the outputs are postselected to contain the same number of photons as before. The probability of detecting the correct number of photons, i.e. the probability of generating a sample, $P_{\text{sample}}(p, l)$ can then be expressed as

$$P_{\text{sample}}(p, l) = P_{\text{sys}}^{p-l}(1 - P_{\text{sys}})^l \binom{p}{l}, \tag{6.5}$$

where the factor $\binom{p}{l}$ is the number of combinations in which one can lose l photons from p input photons. This leads to a speed-up in the sample acquisition rate, which increases combinatorially with the number of lost photons l. The downside is that postselection increases the deviation from the ideal case and lowers the computational complexity. In practice, the simulation algorithm in Renema et al. 2018a can approximate the output of such an experiment within an error E bounded by

$$\frac{x^{2(k+1)}\left(\frac{p-l}{p}\right)^{k+1}}{1 - \left(x^2 \frac{p-l}{p}\right)} \geq E^2, \tag{6.6}$$

where x^2 is the indistinguishability of the photons. Thus, the number of lost photons allowed depends on the indistinguishability of the photons in the input state.

6.3.2 Interferometer design and operation

So this should in principle be adapted to fit better with the stuff that's already in the thesis

The interferometer is constructed from layers of MZIs applied to pairs of modes arranged according to a specific architecture. The per-photon loss for an interferometer architecture depends on the number of optical components, i.e. MZIs, a photon passes through from the input to the output. Referring to this number of MZIs as the optical depth, $D(m)$, the interferometer loss can be written as

$$\rho_{\text{int}} = D(m) \cdot \rho_{\text{MZI}}.$$

The depth will increase for a higher number of modes where the exact dependence is given by the specific architecture employed.

Ideally, the interferometer should be reconfigurable and constructed using a universal architecture, such as the Clements architecture (Clements et al. 2016) in order to facilitate a random sampling of the unitary transformation implemented by the interferometer. Additionally, the number of modes should scale at least quadratically with the number of photons, i.e. $m = \mathcal{O}(p^2)$, to ensure that collision-free output states dominate the output distribution, which is important to ensure computational hardness. However, as interferometer losses present a major bottleneck to experimental demonstrations, two main strategies have emerged to reduce loss: 1. Reducing the number of modes, and 2. Employing interferometer architectures with a lower optical depth for a given number of modes.

6.3.3 Reducing the number of modes

Due to the challenges in scaling up low-loss interferometers, experiments involving a large number of photons ($p > 10$) have employed interferometers with the number of modes m smaller than p^2. Consequently, this choice yields a proportionally reduced depth $D(m)$. Although this reduction in the number of modes mitigates optical loss within the interferometer, the bosonic birthday paradox no longer holds, i.e., the outputs cannot be assumed to be collision-free. In this scenario, the output event where multiple photons occupy the same mode will be indistinguishable from photon loss unless detectors with number-resolving capabilities are utilized. However, using the framework established in Ref. Chin et al. 2018, it can be shown that the computational complexity of boson sampling with collisions is at least as high as the computational complexity of collision-free boson sampling with the same number of nonzero elements. For more details, we refer to Appendix E.1.

Assuming a postselection criterion where the detection of photons is restricted to d ($< p$) modes, with p representing the number of input photons, Eq. (6.5) can be reformulated to derive the total sample efficiency $P_{\text{sample, lin}}$

for a linear number of modes ($m \propto p$)

$$P_{\text{sample, lin}}(p,d) = \sum_{l=0}^{d} P_{\text{sys}}^{(p-l)}(1-P_{\text{sys}})^{l}\binom{p}{l} P_{\text{ps}}(p,d,l,m). \tag{6.7}$$

Here, $P_{\text{ps}}(p,d,l,m)$ is the probability of detecting an output state with $d-l$ collisions and $p-l$ photons from an interferometer with m modes–essentially quantifying the effective postselection efficiency. This equation involves summing the probabilities of all possible collision and photon loss configurations that result in photodetection in d modes. These probabilities are then multiplied by the occurrence probability of the given combination of losses and collisions. The computation of Eq. (6.7) relies on the knowledge of the effective postselection efficiency $P_{\text{ps}}(p,d,l,m)$. To estimate this quantity, we assume uniform sampling of Haar-random scattering matrices in the Hilbert space. Thus, we can estimate the effective postselection efficiency as the ratio between the size of the Hilbert space with $p-l$ photons in m modes with $p-l-d$ collisions—essentially the postselected portion of the Hilbert space—and the full Hilbert space for $p-l$ photons in m modes. This is expressed as:

$$P_{\text{ps}}(p,d,l,m) = \frac{\binom{m}{d}\cdot\binom{p-l-1}{p-l-d}}{\binom{m+p-l-1}{p-l}}, \tag{6.8}$$

where $\binom{a}{b}$ represents the binomial coefficient for a and b. For more details, we refer to Appendix E.2.

6.3.4 Path-encoded boson sampling circuit architectures

The physical design of the interferometer architecture depends on the mode encoding employed. We will first present the architectures for path encoding. While theoretical works typically assume the use of universal interferometer architectures Aaronson et al. 2011, larger-scale experimental endeavors have so far featured interferometers constructed from non-universal architectures Wang et al. 2019; Zhong et al. 2020; Madsen et al. 2022 with lower optical depth. Formally, the complexity arguments from Refs. Aaronson et al. 2011; Aaronson et al. 2016 are valid only in the universal case, but practically, quantum advantage experiments are hard to simulate even in nonuniversal cases. To provide an overview of how the different approaches compare, we will examine three interferometer architectures: a universal architecture, a fully-connected architecture with single mode-encoding, and a fully-connected hybrid-mode-encoded architecture. Here, “fully connected" signifies that all of the output ports of the interferometer are connected to all of the input ports, generally resulting in a unitary matrix where all elements are non-zero, but that in general can be non-universal. In all three cases, the architectures were chosen to balance the loss per photon to the best possible degree for all input–output configurations. In the Clements case, and to a lesser extent the Rectangular case,

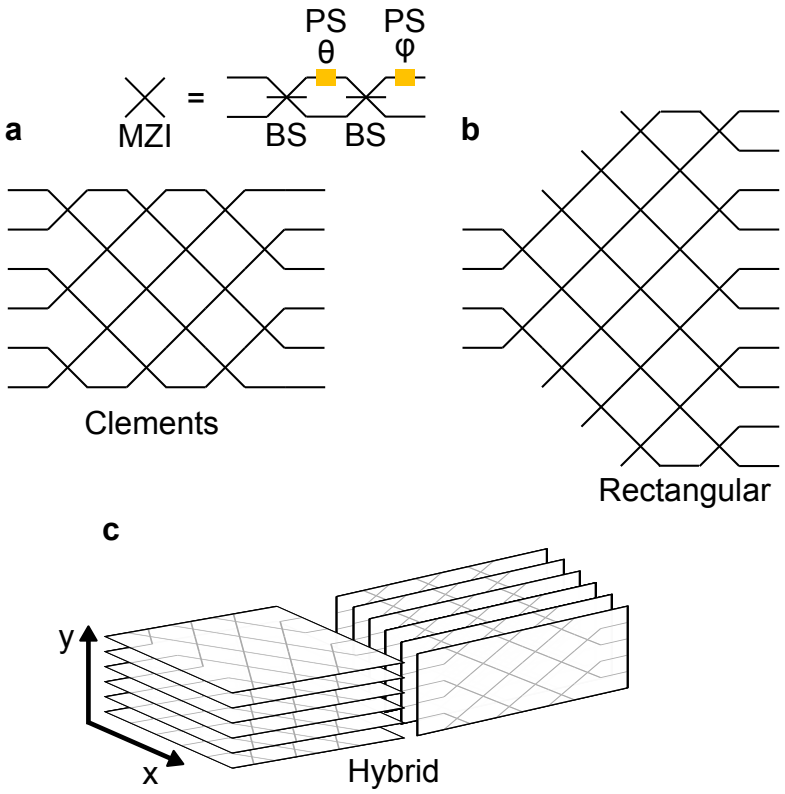

FIGURE 6.2: **a** Illustration of the Clements interferometer architecture, as detailed in Ref. Clements et al. 2016. Each cross corresponds to an MZI, which can be constructed from two 50:50 beamsplitters (BSs) and two phase-shifters (PSs). **b** Illustration of a rectangular interferometer with a larger number of output modes than input modes, the latter of which is equal to the number of input photons. The interferometer can be described by a rectangular matrix, hence the name. **c** Illustration of an interferometer with multiple mode-encodings, i.e. a hybrid mode-encoding. In this case, one mode encoding has spatial modes separated in the x-direction, while the other has modes separated in the y-direction.

paths along the edges traverse fewer MZIs. Since the number of such edge cases is negligible, we assume uniform loss for all input–output configurations in our analysis.

The Clements architecture (Clements et al. 2016) introduced in Chapter 2.3.1, is constructed from m columns of MZIs, as shown in Fig. 6.1a), such that the interferometer loss is given by $\rho_{\text{int}} = m \cdot \rho_{\text{MZI}}$.

The interferometer loss can be optimized by employing non-universal architectures. We propose a non-universal 'Rectangular' interferometer architecture (see Fig. 6.1b)), which maintains full connectivity but reduces the depth D. This is achieved by reducing the number of input modes to be equal to the number of input photons p, while maintaining the same number of output modes m. The interferometer consists of an initial section where two modes are added at the edges of each additional column of MZIs, and a second section fully connecting every input mode to all output modes. In practice, the Rectangular architecture is equivalent to starting a Clements architecture partway in, distributing input modes starting from the middle, and removing unused MZIs. The interferometer loss, ρ_{int}, given by the number of MZI columns multiplied by the MZI insertion loss, is $\left(\left\lceil \frac{m}{2} \right\rceil + \left\lceil \frac{p}{2} \right\rceil - 1\right) \cdot \rho_{\text{MZI}}$. Notably, when the number of output modes is much larger than the number of input modes, i.e. the number of input photons, such that $m \gg p$, ρ_{int} is approximately halved compared to the Clements architecture.

Next, we introduce a 'hybrid mode interferometer architecture' inspired by recent experiments Wang et al. 2019; Zhong et al. 2020; Madsen et al. 2022. These interferometers encode modes over multiple degrees of freedom, e.g. path or polarization, resulting in a hybrid mode encoding. For instance, one degree of freedom might represent spatial modes separated in the x-direction, while another represents spatial modes separated in the y-direction as shown in Fig. 6.2c. Concatenating fully connected interferometers in each direction results in an interferometer that is fully connected across all modes. The power of this approach lies in the way the number of modes and the depth scale with degrees of freedom. The total number of modes in the interferometer is equal to the product $m = \prod_i m_i$, where m_i is the number of modes encoded over the ith degree of freedom. The optical depth, however, is equal to the sum of individual optical depths $\rho_{\text{int}} = \sum_i D_i \cdot \rho_{\text{MZI},i}$, where D_i is the depth for the interferometer connecting all modes for the ith degree of freedom, and $\rho_{\text{MZI},i}$ is the MZI insertion loss for the ith degree of freedom. As an example, if we encode modes over two degrees of freedom, with $m_x = \sqrt{m}$ modes in the x direction and $m_y = \sqrt{m}$ modes y direction, the total number of modes remains as $m_x \cdot m_y = m$. A fully connected interferometer can then be constructed from Clements interferometers over the m_x modes followed by Clements interferometers over the m_y modes, as illustrated in Fig. 6.2c. The total optical depth will then be $D_x + D_y = m_x + m_y = 2\sqrt{m}$. This approach allows for efficient scaling of both modes and depth, and it's worth noting that the Clements interferometers in each mode encoding can be replaced with Rectangular interferometers to reduce depth further.

The optical depth scalings for the different architectures can be summarized as follows

$$\rho_{\text{int}} = \begin{cases} m \cdot \rho_{\text{MZI}} & \text{Clements,} \\ \left(\left\lceil \frac{m}{2} \right\rceil + \left\lceil \frac{p}{2} \right\rceil - 1\right) \cdot \rho_{\text{MZI}} & \text{Rectangular,} \\ \sum_i D_i \cdot \rho_{\text{MZI},i} & \text{Hybrid.} \end{cases} \tag{6.9}$$

6.3.5 Time-bin encoded interferometer architectures

As detailed in Chapter 3, time-bin interferometers make use of time-dependent MZIs and fiber delays to implement multimode interferometers with significantly fewer physical resources than their spatially encoded counterparts. Time-bin interferometer architectures have been both proposed (Motes et al. 2014; Qi et al. 2018) and implemented in (He et al. 2017) boson sampling experiments. Experiments have implemented both single-path time-bin interferometers (Carosini et al. 2023) and two-path time-bin interferometers (Chapter 4 and He et al. 2017). In this chapter we will focus on cascaded two-path interferometer architectures, such as the one implemented in Chapter 4, due to their lower total propagation loss and higher input state generation rate. A more detailed comparison between loop architectures and cascaded architectures is provided in Appendix E.3. We will also consider a demultiplexing interferometer architecture and point out potential pitfalls with this approach.

Fig. 6.3 shows how a Rectangular interferometer can be implemented using a time-bin interferometer. Specifically, we can construct the equivalent of spatial interferometers by combining three different MZI column types as shown in Fig. 6.3a. All of the interferometer columns have the exact same construction for the time-bin interferometer architecture, a time-dependent MZI with a delay in one of the output modes, with the only difference being the sequence of transformations. The first MZI column type, labeled C_1 interferes all modes pairwise, starting with the first mode. The time-bin implementation of C_1 increases the total number of time-bins at the output by 1 due to the time delay, where the first mode and last mode will occupy their own time-bins. The second interferometer column type, C_2 differs from C_1 in the nature of the input state, where the first and last time-bins of the input states are occupied by only one mode, as shown in Fig. 6.3c. The operation of the MZI on this asymmetric input state results in two additional modes (time-bins) at the output in addition to the time delay. The final interferometer column type, C_3, takes an input state where the first and final time-bins are only occupied by one of the modes and enacts a swap transformation on the first and last time-bins, as shown in Fig. 6.3d. This reduces the number of time bins by one compared to the input state. This type of column effectively interferes the modes pairwise starting with the second mode, such that the first and last modes don't interfere with any other mode.

The type of architecture that is implemented is determined by the order and type of MZI columns implemented. Recall that a Clements interferometer can be implemented by combining $m/2$ pairs of $C_1(m)$ and $C_3(m)$ columns, such that the optical depth, i.e. the number of physical MZIs in

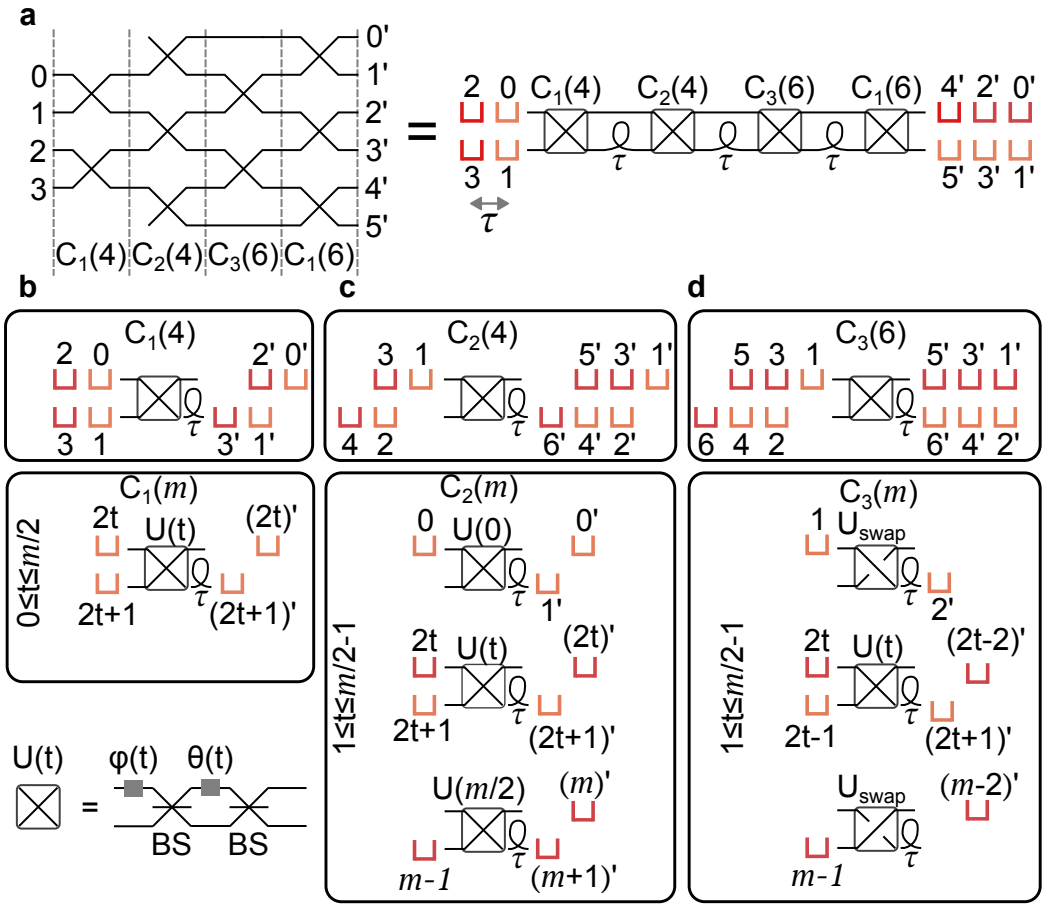

FIGURE 6.3: Illustration of how time-bin interferometers can be constructed to implement specific features in interferometer architectures. The bin symbols ⊔ correspond to the modes of the interferometer, and τ is the temporal separation between photons, which is equal to the inverse of the SPS emission rate $\tau = r^{-1}_{\text{single-photon}}$. Numbers correspond to input modes, and numbers with primes correspond to output modes. Colors are added for visual clarity, and the color of output time-bins correspond to how the time-bins move if the unitary transformations U(t) are set to identity (except for in the first and final time-bin). **b** and **d** are identical to **b** and **c** in Fig. 3.3, where the latter has been relabeled. **c** Operation protocol for a C_2 MZI column. This takes in an asymmetric input state and produces an asymmetric output state with two additional modes.

the interferometer, is m. The Rectangular interferometer consists of a $\mathrm{C}_1(2p)$ column followed by $(m-2p)/2$ $\mathrm{C}_2(m')$ columns where m' is increased from $2p$ at the input of the interferometer to m at the interferometer by increasing the number of modes by 2 for every column. This is followed by $p-1$ pairs of $\mathrm{C}_3(m)$ and $\mathrm{C}_1(m)$ columns, resulting in an optical depth of $(m+2p)/2-1$. Note that we have increased the number of input modes from p in Eq. (6.9) to $2p$ as one SPS can only populate one of the spatial input modes as shown in Fig. 6.1, i.e. half of the input modes of the Rectangular interferometer.

To account for the effect of delay lines when establishing hardware requirements for time-bin interferometers, we can adjust the MZI insertion loss to include the propagation loss of the output with the longest delay

$$\rho_{\text{MZI, time-bin}} = \rho_{\text{MZI}} + \tau \cdot \rho_{\text{prop}} + \rho_{\text{coupling}}, \tag{6.10}$$

where τ is the separation between time-bins, ρ_{prop} is the propagation loss per unit time for the delay lines, and ρ_{coupling} is the coupling loss associated with going from one MZI to the next, i.e. coupling into and out of delay lines.

The input state generation rate of a single cascaded interferometer is determined by the number of time-bins in the input state, as opposed to the number of input photons, as we have to wait for the full input state to be inserted into the time-bin interferometer before sending in the next state. For two-path interferometers the number of time-bins will be the number of modes divided by two, yielding

$$r_{\text{input, time-bin}} = \frac{2r_{\text{single-photon}}}{m}. \tag{6.11}$$

This rate can be increased by running multiple interferometers in parallel as is discussed in Appendix E.4, which can lead to slightly advantageous hardware requirements.

In addition to the Clements and Rectangular architectures used in the spatial encoding, the time-bin encoding allows for the construction of demultiplexing interferometers, as detailed in Chapter 3.3.2. The demultiplexing architecture, shown in Fig. 3.12, has some important differences compared to the Clements and Rectangular architecture. The main difference is that the optical depth is much lower, scaling logarithmically with the number of photons rather than linearly. However, this also means that the number of phase-shifters used to specify the unitary transformation implemented by the interferometer is significantly reduced. Though the unitary matrix will be fully populated, this opens for the possibility that there are simplifications that could allow for the experimented to be (approximately) simulated by a classical algorithm with lower computational complexity. One such example is explained in Appendix E.5. As such, though we will show benchmarks for the demultiplexing architecture, it should be noted that these benchmarks represent experiments that are more susceptible to classical simulation through development of improved classical algorithms.

6.4 System benchmark for implementing the Aaronson–Brod boson sampling algorithm

Before delving into the component-level hardware benchmarks, we address the overall system requirements, focusing on the two key system parameters, photon indistinguishability x^2 and system loss ρ_{sys}. We analyze the interplay between these two parameters in implementing Aaronson–Brod's boson sampling algorithm with lost photons. To provide a practical assessment of hardware performance, we choose realistic experimental conditions for run time and error rate of approximate classical algorithms for QA demonstrations with $p \geq 50$ photons.

We use the coupon collectors problem Ferrante et al. 2012; Uppu et al. 2020 to estimate the number of samples required for validation

$$r_{\text{sample}} \cdot t_{\text{integration}} \approx m \log(m)/p, \tag{6.12}$$

where $t_{\text{integration}}$ is the total run time of the boson sampler and $r_{\text{sample}} \cdot t_{\text{integration}}$ is the total number of samples acquired. We set the target for r_{sample} to be 100 samples per day, $r_{\text{sample}} = 100/(24 \cdot 3600)\,\text{Hz}$, which is in line with the measured $6/3600\,\text{Hz}$ photon coincidence rate reported in Ref. Wang et al. 2019 that allowed validating the boson sampling experiment.

We analyze the boson sampling experiment for a deterministic single-photon source at the input that emits photons at a rate of 1 GHz. We consider both the case with a demultiplexer and a spatially encoded interferometer as well as the case with a time-bin interferometer. In the former, the p photon input state is generated at a rate of $r_{\text{input, spatial}} = 1/p\text{GHz}$. In the latter, the input state containing $M/2$ time-bins is generated at a rate of $r_{\text{input, time-bin}} = 2/m\text{GHz}$. We consider two circuit architectures of the interferometer: one with a quadratic number of modes $m = (p-l)^2$ and another with a linear number of modes $m = 10 \cdot (p-l)$, as detailed in Sec. II.A and II.C, respectively. By comparing the two cases we can examine the influence of mode scaling on the trade-off between photon indistinguishability and system loss tolerance. We combine Eq. (6.1) with Eq. (6.5) (Eq. (6.7))for the quadratic (linear) case, to find the level of loss that results in an r_{sample} of 100 samples per day.

We choose an error rate of $E \leq 0.01$, given by Eq. (6.6), for approximating the noisy boson sampling output using classically computed permanents of order $k = 49$. We plot this relation for a varying number of detected photons $(p-l)$, where the number of lost photons l has been set as high as possible while keeping the error of the approximation below the threshold of $E \leq 0.01$.

Results for mode scalings $m = (p-l)^2$ and $m = 10 \cdot (p-l)$ are shown in the upper and lower rows of Fig. 6.4, respectively. The lowest indistinguishability $x^2 \approx 0.805$, found by setting $l = 0$ and $p = 50$ in Eq. (6.6), corresponds to the maximal per-photon loss for Aaronson–Arkhipov boson sampling, i.e.

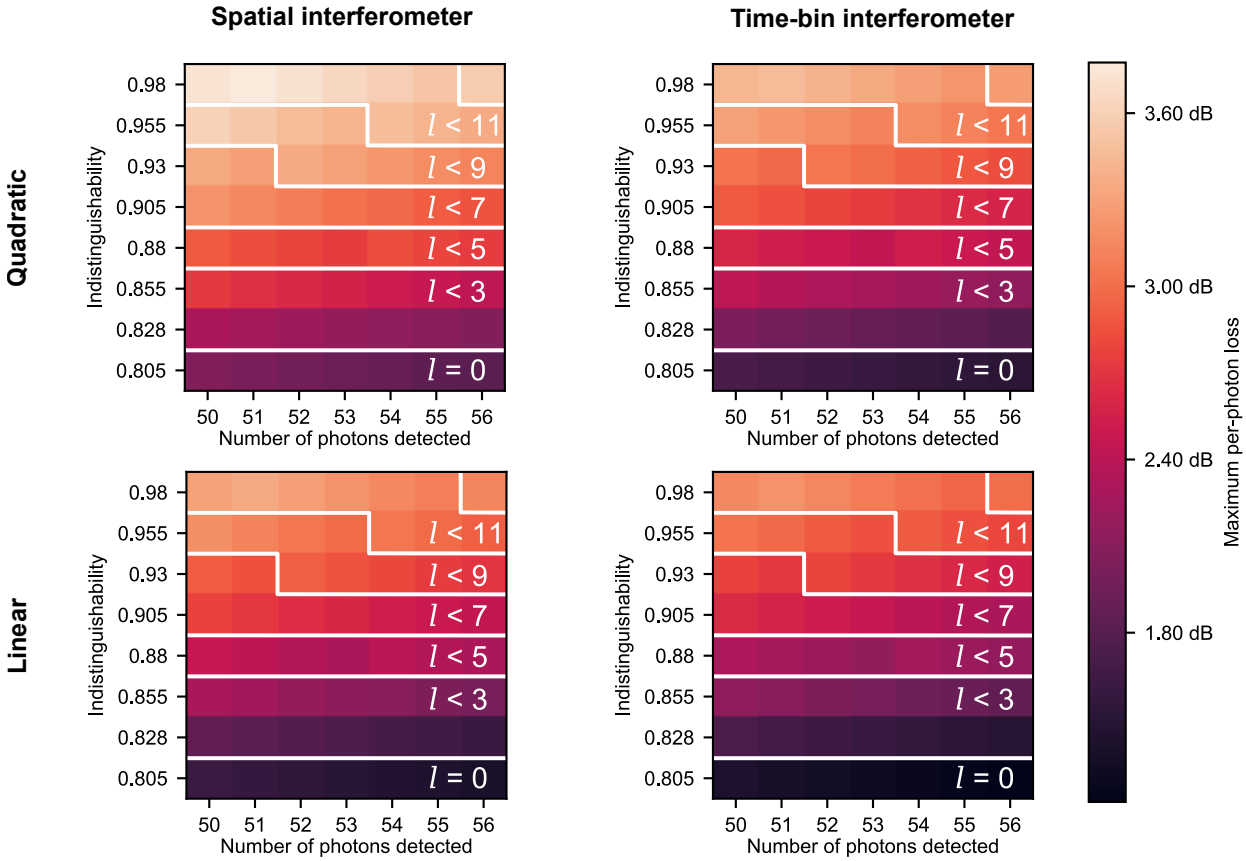

FIGURE 6.4: Maximum per-photon loss for the full circuit to perform boson sampling in the QA regime versus degree of indistinguishability and number of detected photons and for different values l of lost or colliding photons. The two upper plots are for the case where the number of modes scales quadratically with the number of photons $m = (p-l)^2$, and the two bottom plots are for the case where the number of modes scales linearly with the number of photons $m = 10 \cdot (p-l)$. The two plots to the left are for spatial interferometers with a demultiplexed source, whereas the two plots on the right are for time-bin interferometers. White contours indicate the added number of lost photons l, which increases with the indistinguishability, and detected number of photons.

with no photon loss or collisions. Increasing the photon indistinguishability allows for a higher number of lost photons with Aaronson–Brod sampling, increasing the per-photon loss that can be tolerated. We find that $>$ 3 dB (i.e. 50%) loss tolerance for realistic degrees of indistinguishability of quantum-dot SPSs Lodahl et al. 2022 for all four cases. We find the highest maximal loss values at an indistinguishability of $x^2 = 0.98$ to be, from highest to lowest: $3.78\,\mathrm{dB}$ for the quadratic spatial case, $3.46\,\mathrm{dB}$ for the quadratic time-bin case, $3.35\,\mathrm{dB}$ for the linear spatial case, and $3.20\,\mathrm{dB}$ for the linear time-bin case. For comparison, in the limit of perfect indistinguishability, $x^2 = 1$ where up to $l = 12$ photons can be lost with 50 detected photons, the highest maximal loss values would be $3.96\,\mathrm{dB}$ for the quadratic spatial case, $3.65\,\mathrm{dB}$ for the quadratic time-bin case, $3.53\,\mathrm{dB}$ for the linear spatial case, and $3.39\,\mathrm{dB}$ for the linear time-bin case.

As the number of detected photons increases the total loss of the system typically increases, leading to a decreased maximum per-photon loss. However, for a fixed degree of indistinguishability, gradually increasing the number of detected photons can lead to abrupt changes when an additional lost photon can be tolerated according to Eq. (6.6). Thus, the optimum number of lost photons and the detected photons will both depend on the exact photon indistinguishability in the experiment.

In comparing the different plots it is evident that quadratic mode scalings and spatial interferometers lead to higher overall loss tolerance compared to the linear mode scaling and time-bin interferometers. The advantage of quadratic mode scaling can be attributed to the added effective postselection loss associated with linear mode-scaling, described by Eq. (6.8). Specifically, the average difference between quadratic and linear mode scalings is $0.430\,\mathrm{dB}$ for spatial interferometers and $0.277\,\mathrm{dB}$ for time-bin interferometers, in favor of quadratic interferometers. The advantage of spatial interferometers can be attributed to the lower input state generation rate for time-bin interferometers. The average difference between spatial and time-bin interferometers is $0.298\,\mathrm{dB}$ for a quadratic number of modes and $0.145\,\mathrm{dB}$ for a linear number of modes, both in favor of spatial interferometers.

Although quadratic mode-scalings allow for higher per-photon loss, the interferometers consist of more MZIs. As such, there is a trade-off between lower effective postselection loss for quadratic interferometers and lower interferometer loss for linear mode scalings where the MZI insertion loss determines which mode scaling is favored.

Time-bin interferometers have a similar trade-off, as they have a lower maximal per-photon loss due to the lower input state generation rate, but do not require the use of a demultiplexer. However, a demultiplexer can be constructed from the same MZIs that are used to construct a time-bin interferometer, and as such, this trade-off can also be quantified in terms of MZI insertion loss. Specifically, a demultiplexer has an optical depth of $\lceil \log_2(p) \rceil = 6$, where the equality holds for the optimal number of detected and lost photons for all indistinguishabilities considered in Fig. 6.4. The demultiplexer also involves a delay on all except the last photon, where the

first photon has to go through the longest delay of $(p-1)$ time-bins. As for the time-bin interferometer, all of the $D(m)$ MZIs in the interferometer will in the worst case include one time-bin of delay which is not present in the spatial case. If we compare the added per-photon loss from the demultiplexer in the spatial case with the added delay and lower maximum per-photon loss in the time-bin case, we can find the following inequality for the regime where time-bin interferometers are less favorable implementations than spatial interferometers:

$$\begin{aligned} 6 \cdot \rho_{\text{MZI}} + (p-1)\rho_{\text{prop}} &\leq (D(m)-1)\rho_{\text{prop}} + \Delta, \\ \Delta &= \rho_{\text{sys, spatial}} - \rho_{\text{sys, time-bin}}. \end{aligned} \tag{6.13}$$

The average of the value for Δ, i.e. the difference between maximal per-photon loss for spatial and time-bin interferometers, was found to be $0.145\,\text{dB}$ for the case where $m = 10(p-l)$ and $0.298\,\text{dB}$ for the case where $m = (p-l)^2$. If we neglect propagation loss, $\rho_{\text{prop}} = 0$, and insert the average values we can estimate this inequality in the two cases considered in Fig. 6.4:

$$\begin{aligned} \rho_{\text{MZI}} &\leq 0.05\,\text{dB} \quad m = (p-l)^2, \\ \rho_{\text{MZI}} &\leq 0.024\,\text{dB} \quad m = 10 \cdot (p-l). \end{aligned} \tag{6.14}$$

In practice, coupling into the delay between MZIs will inevitably incur loss, and as such, these inequalities present a best-case scenario in favor of time-bin interferometers.

6.5 Benchmarking hardware requirements

The requirements on component losses for a given interferometer architecture can be found by combining Eqs. (6.3), (6.9), with either Eq. (6.5) or Eq. (6.7). To simplify the analysis, we note that only the interferometer loss scales with the number of modes, and separate the losses into the interferometer loss, ρ_{int}, and the remaining system loss, $\rho_{\text{sys}} - \rho_{\text{int}} = \rho_{\text{sps}} + \rho_{\text{dmx}} + \rho_{\text{coupling}}$. We fix the degree of indistinguishability to $x^2 = 0.96$, which is readily achievable with present-day quantum-dot single-photon sources Ding et al. 2016, while routes to achieve even higher values have been laid out Dreeßen et al. 2018. This allows us to fix the number of input photons to $p = 59$ with up to $l = 9$ lost photons in accordance with Eq. (6.6). We also consider the requirements for Aaronson–Arkhipov sampling where we postselect on detecting the same number of photons as are sent into the interferometer, i.e. fixing the number of input and output photons to $p = 50$. The hardware requirements on the interferometer can be formulated as specific requirements on the MZI insertion loss by specifying the architecture and number of modes used for the interferometer.

Single mode-encoding: The first two columns of Fig. 6.5 show the requirements for three different choices of mode scaling for both Clements and Rectangular interferometer architectures, where the top figures show requirements for Aaronson–Brod Aaronson et al. 2016 boson sampling, and

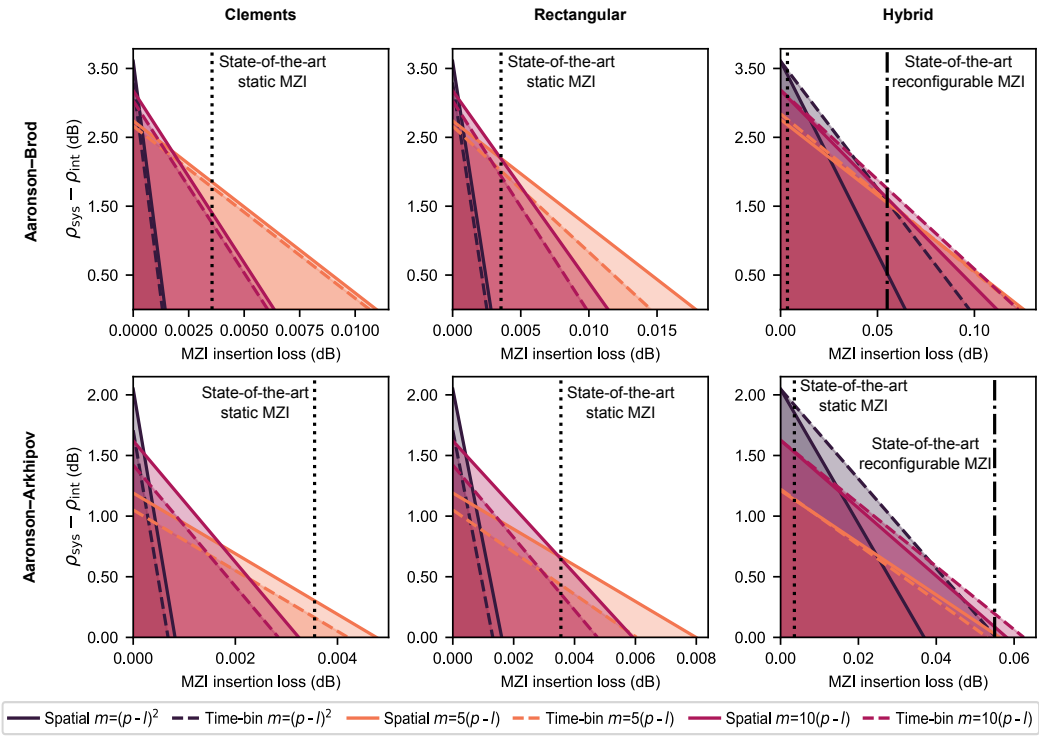

FIGURE 6.5: Plot of the requirements on MZI insertion loss (x-axis) and $\rho_{\text{sys}} - \rho_{\text{int}}$ (y-axis) with photon indistinguishability set to $x^2 = 0.96$. The upper plots show the requirements for Aaronson–Brod boson sampling, where the input state consists of 59 photons with the outputs postselected to contain 50 photon detection events. The lower plots show the requirements for Aaronson–Arkhipov boson sampling, where we send in 50 photons and detect 50 photons, not allowing for photon loss or collisions. The first, second, and third column shows hardware requirements for setups where the interferometers are constructed according to the Clements architecture, the Rectangular architecture, and a set of Hybrid architectures, respectively. For the Clements and Rectangular architectures, the solid lines correspond to the requirements for spatially encoded architectures, whereas dashed lines correspond to the requirements for time-bin architectures. For the Hybrid architectures, the solid lines correspond to requirements for an interferometer encoded over two spatial mode-encodings, whereas dashed lines correspond to requirements for an interferometer encoded over time-bins and two spatial mode encodings. The dotted vertical lines mark the estimated MZI loss for a state-of-the-art experimental realization with static, nonprogrammable MZIs Wang et al. 2019. The dash-dotted vertical line in the plots for Hybrid interferometers marks the estimated MZI loss for a state-of-the-art experimental realization with programmable MZIs Taballione et al. 2023.

Efficiency	Current Best	Near-term estimated best
P_{sps}	0.717 (Ding et al. 2023)	0.78 (Uppu et al. 2020)
P_{coupling}	0.902 (Wang et al. 2019)	0.902 (Wang et al. 2019)
P_{dmx} (p)	0.83 (20) (Wang et al. 2019	0.92 (Uppu et al. 2020)
P_{det}	0.95 (Madsen et al. 2022)	0.95 (Maring et al. 2023)
Total efficiency	0.510	0.615
x^2	0.964 (Ding et al. 2016)	0.985 (Ding et al. 2016, Pedersen 2020)

TABLE 6.1: Table of state-of-the-art system efficiencies. In the column for demultiplexer efficiency, the number of modes of the demultiplexer employed is indicated in parentheses. For the current best indistinguishability, we have used the measured photon indistinguishability, whereas for the near-term estimated best we have used the estimated intrinsic photon indistinguishability which has been corrected for experimental imperfections.

the bottom figures show requirements for Aaronson–Arkhipov boson sampling Aaronson et al. 2011, i.e. with postselection on the same number of detected photons as input photons. The figures include a vertical dotted line corresponding to the state-of-the-art insertion loss for a static MZI, estimated to be $-10 \cdot \log_{10}(0.987)/(10+6)\,\text{dB} \approx 0.0035\,\text{dB}$, which is the overall interferometer efficiency in Ref. Wang et al. 2019 divided by the number of MZIs corresponding to the optical depth of a 10-mode interferometer followed by a 6-mode interferometer.

Comparing the requirements on MZI insertion loss with the Eqs. (6.14), we find that we are in the regime where demultiplexing and spatial mode encoded interferometers are favorable in terms of loss even with access to the rapidly reprogrammable MZIs required to construct a time-bin interferometer.

As seen from the figure, a QA demonstration using single-mode-encoding architectures would be within reach if one could use interferometers with state-of-the-art efficiency in conjunction with a source and detection efficiency of around $P_{\text{sps}} \cdot P_{\text{dmx}} \cdot P_{\text{coupling}} \cdot P_{\text{det}} \geq 0.65$. This overall efficiency is currently beyond the state-of-the-art values reported with quantum-dot sourcesMaring et al. 2023; Wang et al. 2019; Chen et al. 2023; Wang et al. 2023, see Table 6.1 for an overview of parameters already reported in the literature. Further expected near-term improvements of the approach is also listed in the table, indicating that explicit QA demonstration with single-mode encoding is not far outside reach.

Hybrid mode encoding: Hybrid encoding schemes make the algorithms more robust to optical loss and hence put QA demonstrations within closer reach. We consider two distinct Hybrid architectures, one with two spatial mode encodings, like the one employed in Refs. Wang et al. 2019; Zhong et al. 2020 and illustrated in Fig. 6.2c, and one with two spatial mode encodings and one time-bin encoding. For the former, the number of modes in each encoding was chosen to optimize the optical depth, as described by Eq. (6.9). This optimization procedure allowed for the total number of modes to be

slightly increased if it led to favorable optical depth. Rectangular interferometers were employed in each mode encoding to minimize depth. For the latter encoding, we considered an architecture where the input state is partially demultiplexed, whereby sets of two spatial modes are inserted into a time-bin interferometer. By ensuring that there are no empty time-bins in the time-bin interferometer, we avoid the issue of a lowered input state generation rate for time-bin interferometers. The output modes of the time-bin interferometers are then sent into a two-spatial-mode-encoding Hybrid interferometer employing Rectangular interferometers across the two spatial encodings. The total optical depth of this interferometer, including the initial demultiplexer is equal to:

$$D(n, p, m_1, m_2) = n + 2\left\lceil \frac{p}{2^n} \right\rceil + \left\lceil \frac{m_1}{2} \right\rceil + \left\lceil \frac{m_2}{2} \right\rceil + \frac{2^n}{2}, \tag{6.15}$$

where n is the depth of the demultiplexer, such that there are 2^n spatial modes and $\lceil \frac{p}{2^n} \rceil$ time-bins after the demultiplexer, and where m_1 and m_2 correspond to the number of output modes in each spatial encoding. Similarly to the case of the spatial hybrid interferometer, we allow for the number of modes to be increased if it leads to a lower optical depth, only requiring that

$$m_1 \cdot m_2 \cdot \left\lceil \frac{p}{2^n} \right\rceil \geq m,$$

where the left-hand side is the actual number of modes, and the right-hand side is the target number of modes, calculated from the mode scaling. The depth of the demultiplexer and the number of spatial modes were optimized in order to minimize Eq. (6.15). For the case of a quadratic number of time-bins, the ideal demultiplexer depth was found to be $n = 3$, with $m_1 = m_2 = 18$, whereas for the linear mode scalings, the ideal demultiplexer depth was found to be $n = 4$ with the number of spatial modes equal to $m_1 = 11,\ m_2 = 12$ and $m_1 = 8,\ m_2 = 9$ for the case where $m = 10(p - l)$ and $m = 5(p - l)$, respectively.

The resulting hardware requirements for Aaronson–Brod (Aaronson–Arkhipov) boson sampling are shown in the top (bottom) plot of the right column of Fig. 6.5, where the solid lines ('Spatial') refer to the case with two spatial mode encodings, and the dashed lines ('Time-bin') refer to the case with time-bin and two spatial encodings. In addition to the dashed line for the state-of-the-art static MZI insertion loss, the plots include a dashed-dotted line marking the state-of-the-art insertion loss for a reconfigurable MZI, estimated from Ref. Taballione et al. 2023 to be $1.1\,\mathrm{dB}/20 = 0.055\,\mathrm{dB}$, which is the interferometer insertion loss divided by the number of MZIs.

The hybrid encoding with the time-bin encoding performs better at larger mode-scalings but seems to perform comparably or slightly worse for the case where $m = 5(p-l)$. The advantage at higher mode-scalings comes from the fact that the number of modes is distributed over three encodings, which means that the sum of the number of modes can be smaller. This is less of

an advantage for the case where $m = 5(p - l)$, where the additional demultiplexer loss included in the time-bin case gives a higher overall depth. It should be noted that the spatial hybrid interferometer requires the addition of a demultiplexer at a depth of $n = \lceil \log_2(p) \rceil$, which should be included as part of the source efficiency. As such, the time-bin hybrid interferometer would be expected to perform advantageously even for low mode-scaling.

Figure 6.5 clearly shows that the MZI insertion loss determines whether a quadratic mode scaling or linear mode scaling is favorable. Specifically, at the state-of-the-art static MZI insertion loss, employing an interferometer with a quadratic mode-scaling is best, whereas linear mode scalings are favored when using MZIs with the state-of-the-art reconfigurable MZI insertion loss. This is not the case for Clements or Rectangular architectures except for the case where the MZI insertion loss is vanishingly low. The discrepancy between the Clements and Rectangular architectures and the Hybrid architecture is attributed to how the optical depth scales with the number of modes, as shown in Eq. (6.9). With modes distributed across two mode-encodings, the optical depth of Hybrid interferometers scales with $\sim \sqrt{m}$, as opposed to linearly in m. As increasing the number of modes has a smaller impact on interferometer loss, the added effective postselection loss associated with linear mode-scalings has a proportionally higher impact on the system loss for hybrid interferometers.

Demultiplexing time-bin interferometer: Demultiplexing interferometers allows for the construction of interferometers where the optical depth scales logarithmically with the number of modes, allowing for the optical depth to be reduced even further compared to Hybrid architectures. For the requirements shown in Fig. 6.6, we have set the number of modes to a power of two larger than the corresponding mode-scaling for the hybrid interferometer architecture. The number of MZI layers, where each MZI layer except for the last requires two switches (as shown in Fig. 3.12), will then be equal to the logarithm of the number of modes such that

$$m = 2^c, D(m) = 2c - 1,$$

where c is an integer. This allows for the requirements of MZI insertion loss, as shown in Fig. 6.6, to be relaxed substantially, particularly if the other sources of loss are kept low.

Much like time-bin interferometer architectures, it is important to keep in mind that demultiplexer loss has not been included for the hybrid interferometer architecture, and that propagation loss has not been taken into account for either interferometer. The propagation loss will scale proportionally to the number of modes in the demultiplexing time-bin interferometer, whereas it will scale with the number of photons for a spatially encoded Hybrid interferometer. Additionally, the demultiplexing interferometer will have to couple into delay lines one time per MZI (except for the very last one), as opposed to only once for the spatially encoded hybrid interferometer.

Though the hardware requirements for demultiplexing interferometers are attractive and promising for future research endeavors, they require the

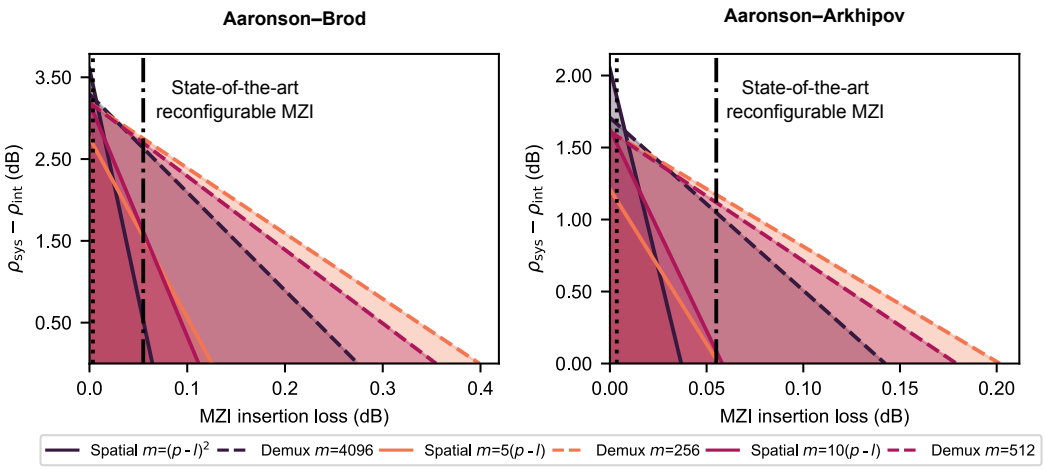

FIGURE 6.6: Plot of the requirements on MZI insertion loss (x-axis) and $\rho_{\text{sys}} - \rho_{\text{int}}$ (y-axis) with photon indistinguishability set to $x^2 = 0.96$. The plot to the left shows the requirements for Aaronson–Brod boson sampling, where the input state consists of 59 photons with the outputs postselected to contain 50 photon detection events. The plot to the right shows the requirements for Aaronson–Arkhipov boson sampling, where we send in 50 photons and detect 50 photons, not allowing for photon loss or collisions. The solid lines correspond to the requirements for Hybrid architectures encoded over two spatial mode-encodings, whereas dashed lines correspond to the requirements for demultiplexing time-bin architectures. The dotted vertical lines mark the estimated MZI loss for a state-of-the-art experimental realization with static, nonprogrammable MZIs Wang et al. 2019. The dash-dotted vertical line marks the estimated MZI loss for a state-of-the-art experimental realization with programmable MZIs Taballione et al. 2023.

integration of low-loss electro-optic modulators and delay lines beyond the capabilities of state-of-the-art hardware. As such, the next section will restrict the focus to Hybrid spatial interferometer architectures.

6.6 Hardware requirements for near-term QA demonstrations

From Fig. 6.5 we observe that an explicit QA demonstration is within reach with a deterministic quantum-dot source. Indeed using state-of-the-art static interferometers would imply that QA can be reached for $P_{\text{sps}} \cdot P_{\text{dmx}} \cdot P_{\text{coupling}} \cdot P_{\text{det}} \geq 0.45$, where the required efficiency of each sub-component was already realized experimentally, see Table 6.1. As time-bin interferometers require the use of reprogrammable MZIs, one could not make use of hybrid architectures with time-bin encoding in this case. As for state-of-the-art reconfigurable interferometers, this would require a setup with combined source and detection efficiencies around 0.65 (0.7) for the time-bin (spatial)

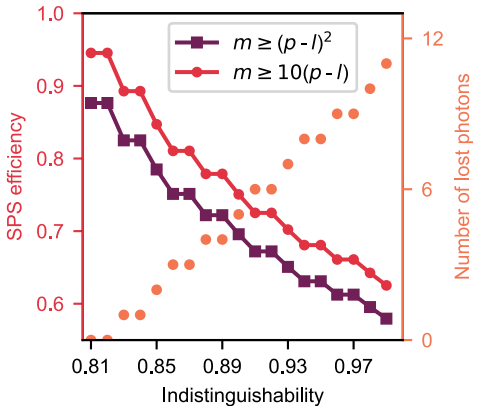

FIGURE 6.7: Requirements on source efficiency for a given indistinguishability with a hybrid interferometer encoded in two mode-encodings. Rectangular interferometers have been used within both mode encodings. The requirements are defined to allow for 100 samples to be obtained per day with a 1 GHz single-photon generation rate. For each value of indistinguishability, the number of photons detected and lost has been optimized to increase the loss tolerance while maintaining an error bound higher than 1% for the approximation algorithm. The purple line corresponds to a quadratic mode scaling, and the red line corresponds to a linear mode scaling

Hybrid architectures. These values are reachable with the estimated near-term values of the approach, cf. Table 6.1. It is important to note that the state-of-the-art values of MZIs hold for thermo-optic phase-shifters, which are unsuitable for realizing time-bin interferometers due to their slow response time. Consequently, this would limit the present implementations of Hybrid time-bin architectures. On the other hand, Hybrid interferometers with spatial mode encodings appear to be promising candidates for near-term QA demonstrations with quantum-dot single-photon sources.

It is clear from Table 6.1 that the source efficiency is the main bottleneck in realizing a demonstration of QA. In the following, we restrict the focus to the exact requirements for the single-photon source by fixing other losses to state-of-the-art values. We fix the MZI insertion loss to the state-of-the-art value for static MZIs shown in Fig. 6.5. The demultiplexer efficiency and coupling losses are fixed to realistic parameters extrapolated from Refs. Zhong et al. 2020; Uppu et al. 2020:

$$\rho_{\text{dmx}} = \frac{0.458}{5} \lceil \log_2(p) \rceil \, \text{dB},$$
$$\rho_{\text{coupling}} = 0.458 \, \text{dB}.$$

We examine how the requirements on the source efficiency change as a function of the photon indistinguishability. The resulting curves for quadratic and linear mode-scalings are shown in Fig. 6.7. It is clear from the figure

that quadratic mode-scaling is favored regardless of photon indistinguishability. For realistic photon indistinguishability, $x^2 \geq 0.96$, the results show that a QA demonstration is within reach for single-photon source efficiencies greater than 0.6, which has been demonstrated experimentally Chen et al. 2023. The challenge will be to construct a demultiplexer and an interferometer that are sufficiently large while maintaining sufficiently low loss, and connecting them to an exceedingly large number of low-loss detectors.

6.7 Conclusion

In conclusion, we have presented an in-depth analysis of the hardware requirements for realizing boson-sampling in the QA regime with deterministic single-photon sources, notably quantum dots in nanophotonic cavities and waveguides. The estimated benchmarks provide precise requirements on optical circuits and single-photon sources that must be reached, thereby offering a roadmap for future engineering efforts to realize that goal. Our analysis elucidates the precise advantages and disadvantages of strategies that are commonly employed in experiments to lower hardware requirements, such as making use of specialized interferometer architectures and employing interferometers with linear mode scaling. We have identified interferometers with hybrid mode encoding and quadratic mode scaling as a key strategy to demonstrating QA, an approach that has yet to see realization in experiments. Specifically, we have shown that a QA experiment based on single-photon boson sampling is within reach of current state-of-the-art hardware, provided that one can reach source efficiencies as high as 60%-70%.

In examining the requirements for time-bin encoded interferometers, we have found time-bin interferometers utilizing the Clements and Rectangular architectures to be inferior to equivalent spatial interferometers for QA demonstrations. This is due to the disadvantages associated with empty time-bins in the input state in the regime where MZI insertion loss is low enough for a QA demonstration to be feasible. For hybrid interferometer architectures, however, encoding a subset of the modes in time-bins leads to improved hardware requirements on MZI insertion loss. As such, developing rapidly reconfigurable photonic integrated circuits with bandwidth to support time-bin-compatible MZIs with sufficiently low loss is a promising direction to enable QA demonstrations.

Our analysis has focused on the requirements of the interferometers and single-photon sources, however, an underlying assumption for parts of the analysis was that the loss associated with coupling photons from the source and into the interferometer were comparable with the losses quoted in Wang et al. 2019 and Zhong et al. 2020. Achieving ultra-low-loss chip-to-fiber coupling is an important engineering challenge and an area of active research (see e.g. Tiecke et al. 2015; Notaros et al. 2016; Marchetti et al. 2019). Ultimately coupling losses could be further mitigated by a partial or full-scale system integration, whereby sources, demultiplexer, interferometers, and detectors would be combined in a single device (Uppu et al. 2021), which

constitutes an important future research direction.

7 Conclusion

At the start of this PhD project three years ago, the promising prospects of quantum-dot single-photon sources were becoming increasingly evident (Uppu et al. 2020; Wang et al. 2019). This thesis presents developments and experiments that utilize and further expand the capabilities offered by these sources and state-of-the-art photonic technology. In Chapter 3, we exploited the unique properties of the native time-bin encoding of on-demand single-photon sources to introduce novel interferometer architectures allowing for the implementation of specialized unitary transformations with a substantial reduction in optical depth. In Chapter 4, we employed a time-bin interferometer in an experimental demonstration of bosonic suppression laws and postselected entanglement with photons emitted from our quantum-dot SPS. Our experimental setup leveraged the properties of both the time-bin encoding and the desired transformation to simplify the experimental requirements, resulting in an interferometer constructed from only one active component with no need for phase stabiliziation. In Chapter 5, we designed photonic integrated circuits on thin-film LNOI for use with single photons emitted by the quantum dot, enabling the first experimental demonstration of the HOM effect on LNOI. Two additional experiments were carried out, demonstrating two-photon interference in a four-mode interferometer, and employing the fast electro-optic modulators offered by LNOI to show on-chip demultiplexing of the single-photon source. Finally, in Chapter 5 we determined concrete hardware requirements for a demonstration of quantum advantage using boson sampling of single-photons from an on-demand single-photon source, establishing that a demonstration of quantum advantage is within reach using current state-of-the-art hardware. Our comprehensive analysis highlighted key strategies in interferometer architecture design and choice of mode encoding that lead to substantially reduced demands on hardware performance.

7.1 Outlook

The presented results highlight a variety of improvements and prospects, both in the near-term and in the longer term.

Near-term improvements

Chapter 3 explored time-bin interferometers with two or fewer spatial paths. Expanding the scope to additional paths would allow for interferometer architectures tailored to multiple on-demand sources, and might reveal more unique properties. Additionally, determining the full range of unitary transformations that can be implemented with the newly developed architectures would firmly establish their utility.

A natural follow-up to our time-bin interferometer experiment in Chapter 4 is to demonstrate postselected entanglement with an increased number of photonic qubits. For the optical setup, this would only require a single substitution, exchanging the resonant EOM with a broadband EOM, which would allow for the interferometer to be scaled to an arbitrary number of qubits. Alternatively, identifying other transformations with similar properties could expand the versatility of similarly resource-efficient time-bin interferometers. Circuits that can be used for *heralded* entanglement generation would be of a particular interest as they have greater utility, e.g. enabling the generation of resource states for FBQC.

The main challenge we faced in the experiments on LNOI was the electronic control of the modulators, which limited the programmability of the four-mode interferometer. Addressing this challenge is crucial for enabling more complex and larger-scale experiments. To this end, we could e.g. alter the design and fabrication of the electrodes as outlined in Puma et al. 2022, or cool the chip down to cryogenic temperatures, as explained in Lomonte et al. 2021b.

Long-term prospects

The results presented in the thesis span a variety of platforms for photonics, and highlight the strengths of each. Gallium arsenide enables the realization of on-demand single-photon sources through the growth of quantum dots and fabrication of nanophotonic structures. Bulk-optics allows for the integration of megahertz-bandwidth electro-optic modulators and low-loss delay for resource-efficient time-bin interferometers, and is compatible with high-efficiency fiber-coupled detectors. LNOI enables the miniaturization of large-scale photonic circuits that can be operated and reconfigured with gigahertz bandwidths. The main challenge that limits the scale of our experiments to proof-of-principle demonstrations is the high amount of loss related to connecting these different platforms together. Though the planar SPS platform enables efficient emission into waveguides, a significant proportion is lost when the photons are routed off-chip to a fiber. Similarly, though LNOI enables fast switches that would be ideal for time-bin interferometers, this prospect would require either ultra-low propagation loss for on-chip delay, or highly-efficient fiber-to-chip interfaces. In the absence of a monolithic material platform capable of all desired functionalities, the efficient integration of distinct platforms is vital. There are two main approaches that are pursued to tackle this challenge, increasing the efficiency of fiber-to-chip interfaces (Tiecke et al. 2015; Notaros et al. 2016;

Marchetti et al. 2019), and *heterogeneous integration* (Lau 2019; Uppu et al. 2021), where light is coupled directly from one platform to another without going through fiber interfaces. As this technology matures, future endeavors can combine the strengths of the individual platforms to unlock the full potential of photonic technology, which is crucial to meet the extreme demands posed by fault-tolerant quantum computers.

Ultimately, there are many difficult challenges ahead, and it's not yet clear exactly how or even if they can be overcome. For the time being, the best that we can do is to leverage, adapt and improve our knowledge and technological capabilities one step at a time.

A Appendices for Chapter 2

A.1 Alignment in the path encoding

The alignment of optical paths is crucial in bulk optics experiments for two main reasons:

1. Increasing the probability that the output of the bulk optics setup reaches the detectors to minimize loss

2. Aligning reflected and transmitted paths from beamsplitters to ensure they occupy the same mode.

We note that bulk optics setups are commonly only part of the experimental setup, where light is routed into and out of the setups through fiber coupling. As such, the extraction of photons out of the bulk optics setup is dependent on how well the optical modes are coupled *into* the fibers. This requires that the angle and position of the light beam, as well as its beam profile, i.e. it's size, is as aligned with the fiber mode as possible, as illustrated in Fig. A.1. The second experimental challenge has to do with the fact that we want to interfere initially separate paths on beamsplitters. Beamsplitters can be considered mathematically as having two input modes and two output modes, where a given output mode will contain a contribution from the transmission of one input mode and a contribution from the reflection of the other input mode. In order for photons from reflection and transmission to interfere, they need to overlap perfectly. As we typically want to route this linear combination of modes into the same fiber coupling at the end of the setup, it's also crucial that they overlap to achieve a high coupling efficiency. In order to solve both challenges, we use mirrors to align the positions and angles of our light beams, and we use lenses to adjust the beam profile, i.e. the size of the beam spot and rate of convergence/divergence.

A.2 Coupling into and out of photonic integrated circuits

In the experiments with photonic integrated circuits described here, as well as most current-day experiments in integrated quantum photonics, we have to be able to couple light into and out of the chip. This is because we make use of separate platforms for the generation of light, the construction

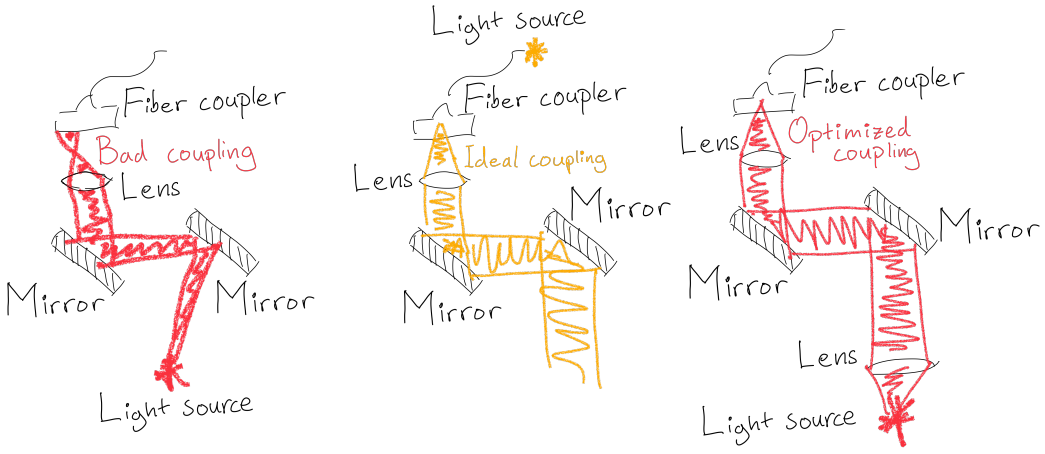

FIGURE A.1: Illustration of the process of alignment. As shown in the second panel, the ideal alignment would overlap perfectly with the case where light is inserted in the reverse direction.

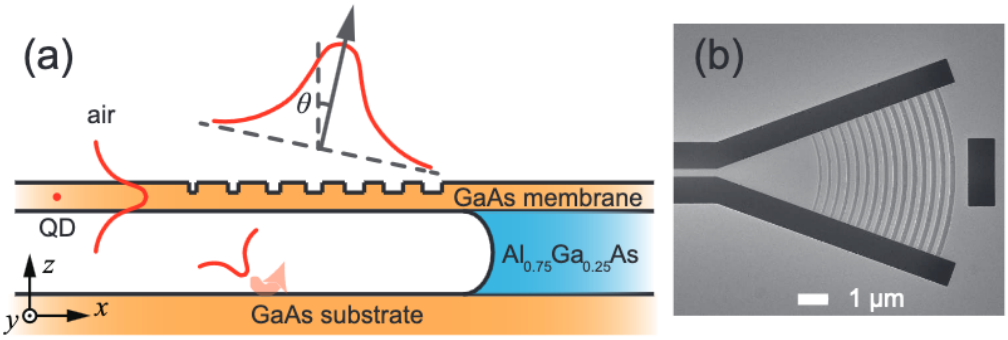

FIGURE A.2: Illustration of the operation of a grating coupler. Adapted from Zhou et al. 2018.

of interferometers, and for detection. Also here, fibers are employed to route the photons between components, and as such, what we need is a fiber-to-chip interface. In the experiments covered in this thesis, this is achieved by the use of *grating couplers*, illustrated in Fig. A.2. These photonic structures are gratings that scatter light from waveguides out of the plane of the chip, or the inverse, scattering out-of-plane light into the chip. In order to direct the light in a specific out-of-plane direction, i.e. up rather than both up and down, we also require a reflective layer beneath the grating coupler. Otherwise, the maximum efficiency of a grating coupler is 50%. Another common coupling strategy is to couple light directly into the waveguide from the side, also known as *butt coupling*. This does not require the use of reflectors to direct the coupling, but comes with the disadvantage that light has to be coupled in from the side, which means light has to be routed from the side of the chip to the desired structure. With side-couplers we have one dimension of access around the circumference of the chip, whereas grating couplers allow for two-dimensional access across the surface of the chip.

B Appendices for Chapter 3

These appendices present a variety of results that either haven't been fully developed, or don't present any obvious utility for experiments and applications. I nevertheless think the results are interesting, and worth presenting in some form. The first section introduces line-and-circle diagrams that are useful for representing time-bin interferometer architectures quickly and easily. In the second section we present loop and partially cascaded time-bin interferometer architectures that exhibit peculiar periodic boundary conditions even without the permutation matrices we introduced in the main chapter. Though these architectures have interesting geometries, it's hard to see any obvious use cases for them, so they are presented without much discussion of utility or outlook. The rest of the appendices for this chapter concern results that have not been fully developed. Using a resource counting argument as a basis for constructing a universal architecture, I develop potentially improved universal cascaded and loop interferometer architectures for the two-path time-bin encoding, as well as one for the path encoding. The final section presents a potential starting point for developing interferometer architectures for time-bin encodings with an arbitrary number of paths.

B.1 Line-and-circle diagrams

To illustrate many of the two-path time-bin interferometer architectures we will present here, we will make use of the graphical representation introduced in He et al. 2017. An example of the representation for a four-mode Clements interferometer is shown in Fig. B.1. This representation divides the interferometer into separate columns of MZIs (column i is labeled as C_i in the figure). For loop interferometers, as illustrated in we can go from one column to the next by going through the delay loop, and as such, the column index corresponds to the number of times a photon has travelled through this delay loop. In this case, the number in the circles representing the MZIs in Fig. B.1b denotes the time-bin the MZI occurs at, i.e. an MZI *event*. As such, time increases both along the horizontal and vertical axis. For cascaded interferometers, each column is implemented using separate MZIs, and in this case the column index corresponds to which physical MZI is implementing the column. In the cascaded case, time only increases along the vertical axis.

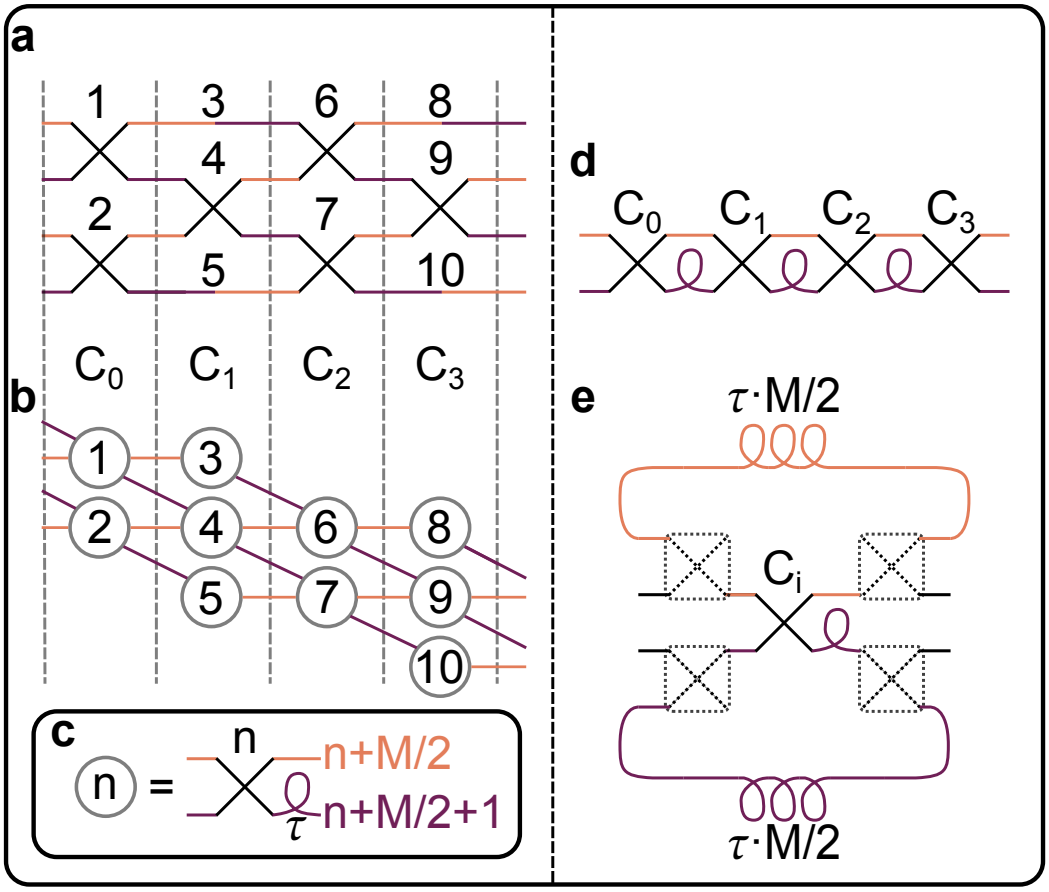

FIGURE B.1: Line-and-circle representation of a two-path time-bin encoded four-mode Clements interferometer. The ith MZI column is labaled as C_i starting with 0, and the two colors correspond to specific spatial modes. **a** Schematic of a four-mode Clements interferometer. **b** Line-and-circle diagram of the circuit shown in **a**. **c** Cascaded implementation of the four-mode interferometer. **d** Loop implementation the four-mode interferometer.

B.2 Time-bin interferometers with interesting geometries and dubious utility

The diagram in Fig. B.1c shows how different MZI events are connected for specifically Clements interferometers. As shown in Fig. 3.3 in the main text, the MZIs will specifically implement swap transformations on the first and last time-bins of even columns (odd columns in this case since we start counting them at 0). It is natural to wonder what would happen if we allowed the MZI to implement an arbitrary unitary transformation instead? The answer to this question is different for cascaded and loop interferometers. In the cascaded case, this adds more modes to the interferometer, as shown in Fig. 6.3c. In the case of loop interferometers, however, this causes the first delayed mode to overlap with one of the last input modes, as shown in Fig. B.2 creating an odd-numbered time-bin interferometer with periodic boundary conditions. This architecture is similar to the optimal-delay loop-architecture with an even number of modes, shown in Fig. B.5 we will present later in Section B.3.2, with two key differences:

1. The odd-numbered interferometer does not require any extra switches to introduce periodic boundary conditions.

2. The odd-numbered interferometer connects the first mode to the last mode in the *same* column, where as the even-numbered interferometer connects to the last mode in the *subsequent* column.

The second property in particular is quite peculiar, and makes the concept of an MZI column ill-suited to describe the interferometer architecture.

Similar properties can be found for *partially cascaded* interferometers. Here, rather than cascading as many MZIs as there are columns, only a subset P of the MZI columns are cascaded as physical MZIs, as shown in Fig. B.3a. Though this approach can be used to implement Clements interferometer architectures by setting the right delay and enacting swap transformations on the first and last time-bins of every other MZI columns, Fig. B.3b illustrates what happens if an arbitrary unitary transformation is enacted for every MZI event. Whereas the loop interferometer connected the first output mode to the last input mode of every MZI "column", the partially cascaded interferometer instead connects the last "column" of the cascade back to the first "column" of the cascade. For the first two "columns" there is also a new connection in the lastd time-bin of every column that connects to the first time-bin $P+1$ columns in advance.

B.3 Resource counting conjecture for universal interferometer architectures

A unitary matrix with M modes contains M^2 elements. Using the unitary constraint, we can reduce this to M^2-1 unique elements, and as such, a universal interferometer architecture should be able to specify at least M^2-1

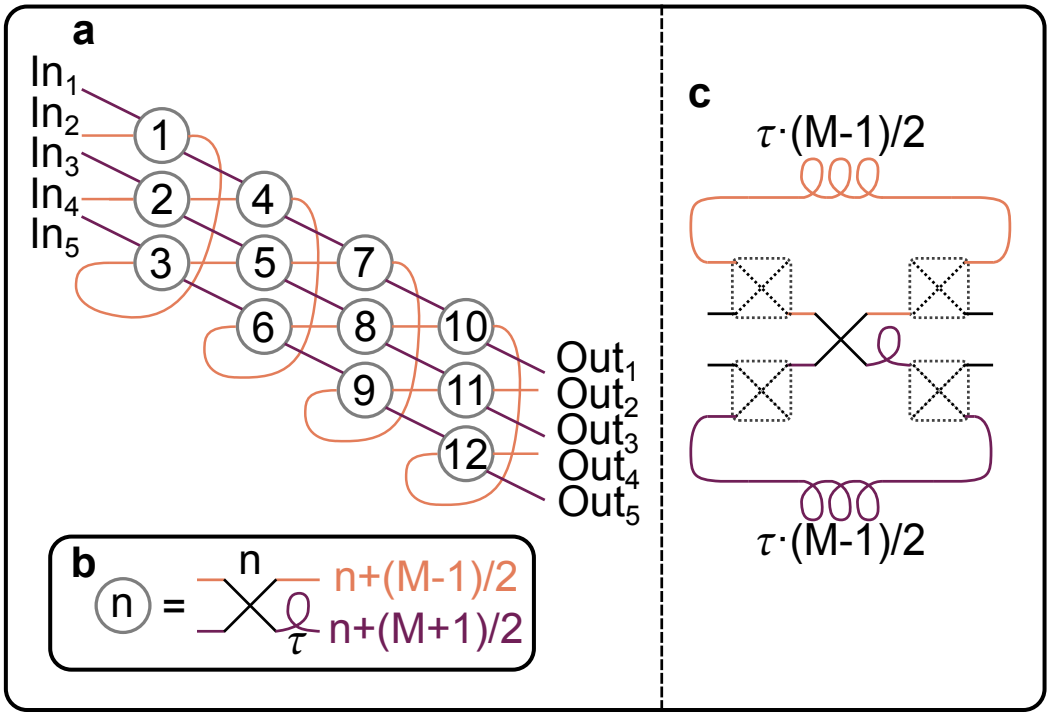

FIGURE B.2: A five-mode example of an odd-numbered two-path time-bin interferometer with periodic boundary conditions. **a** Line-and-circle representation of a five-mode interferometer. **b** Schematic showing how different MZI events are connected. **c** Physical implementation as a loop interferometer for an arbitrary odd number of modes M.

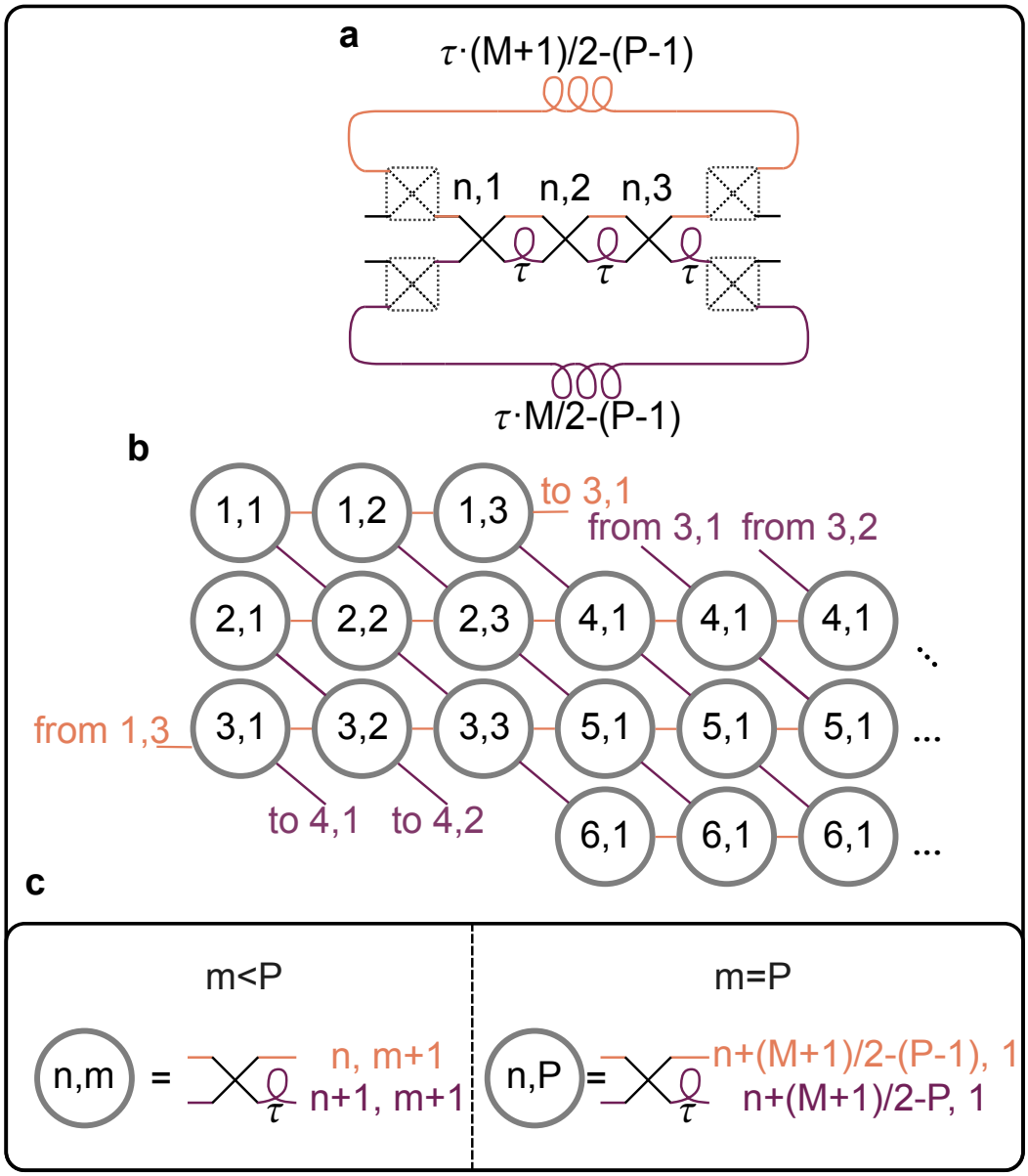

FIGURE B.3: A six-mode example of a two-path partially-cascaded interferometer architecture with three physical MZIs. **a** Physical implementation of the interferometer. **b** Line-and-circle representation of the interferometer. **c** Schematic showing how different MZI events are connected. The index n refers to the the time-bin whereas the index m refers to the physical MZI. the connection for the last physical MZI is different, as this connects to the first physical MZI through a delay loop.

numbers to be able to specify an arbitrary unitary transformation. This is indeed the case for both the Reck architecture and Clements architecture, comprised of $M(M-1)/2$ MZIs each containing two phase-shifters and a phase-screeen comprised of M phase shifters at the start or end of the interferometer (depending on the position of the external phase-shifter in the individual MZIs) for a total of

$$M(M-1)+M=M^2$$

phase-shifters, allowing for a single phase-shifter to be removed. As a phase-screen can always be added to the input or output, then an interferometer architecture with $M(M-1)/2$ MZIs should, from a resource counting perspective, be able to specify an arbitrary M-mode unitary transformation. It should be noted that there are some additional constraints that are not captured by this conjecture. For instance, placing M^2 phase-shifters in a row in a single-mode will effectively implement a single-phase shift. Similarly, any two-mode unitary transformation can be described by a single MZI with two external phase-shifters, and thus chaining together two MZIs in the same two modes effectively only implements a single MZI. Thus, the geometry of the architecture plays an important role, and such considerations must be taken into account before claiming that an interferometer architecture is universal. The rest of the section will assume that the resource counting conjecture holds for all cases except for one where there are other reasons to believe that it doesn't.

B.3.1 A conjectured optimal path-encoded universal interferometer architecture

If an interferometer architecture makes use of MZIs arranged as a series of columns, as is done e.g. in the Clements architecture, then every column can at most contain $M/2$ MZIs. This is indeed the case for every other column in the Clements architecture, however, half of the columns in this architecture contains one fewer MZI, where the first and last modes do not interfere with any other modes. If we were to have periodic boundary conditions however, we could implement the same number of MZIs in every column by interfering the first mode with the last mode when appropriate. As every column would contain $M/2$ MZIs, this would allow for an interferometer with $(M-1)$ columns, exactly one less than in the Clements interferometer. Fig. B.4 shows an example of how such an interferometer could be implemented with six modes. By arranging the modes radially rather than in a line, every mode will have two nearest-neighbors. A downside of this architecture is that it requires the ability to construct the interferometer in three dimensions, or on the two-dimensional surface of e.g. a cylinder, which is incompatible with conventional photonic integrated circuits.

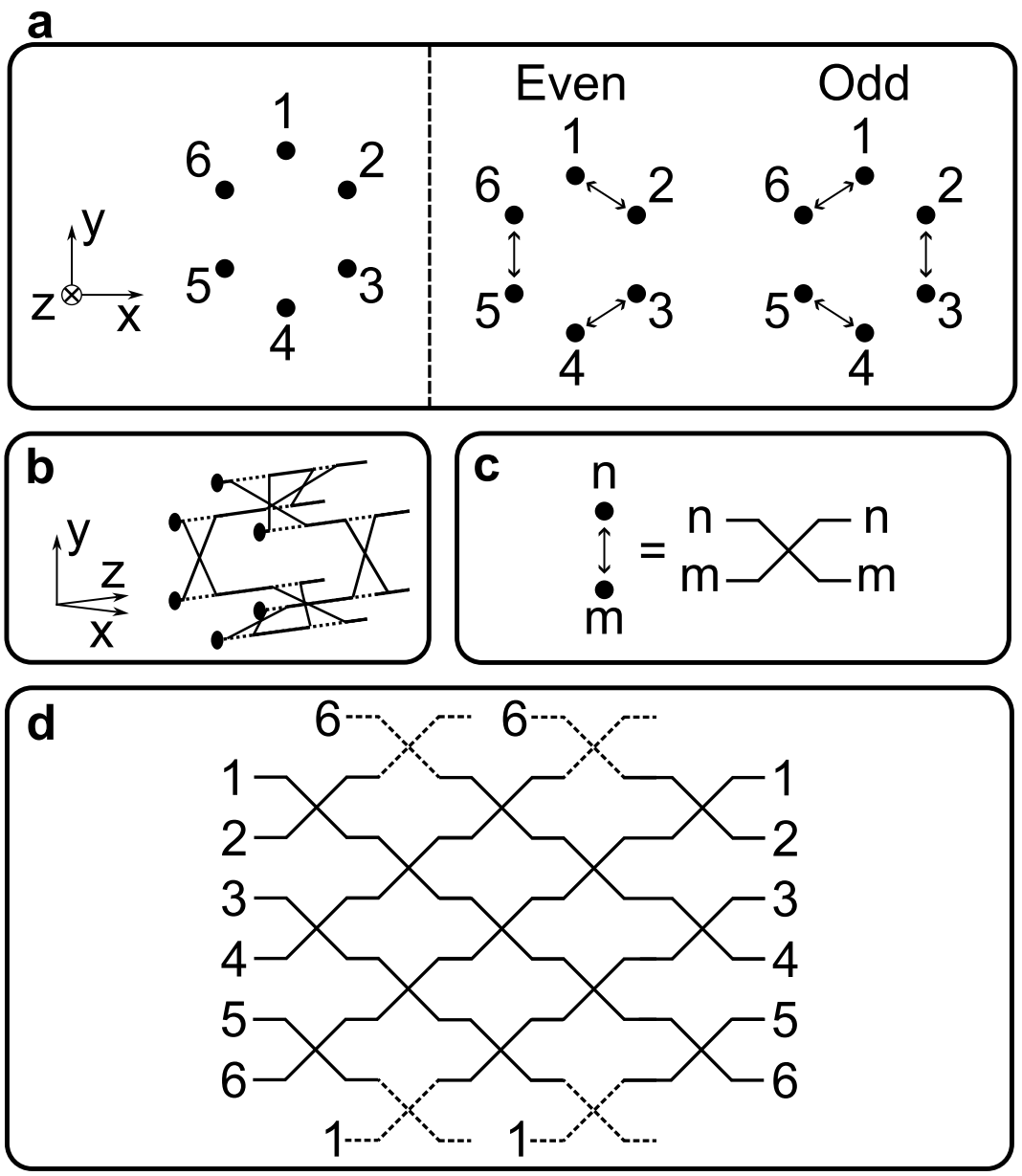

FIGURE B.4: A six-mode example of a conjectured optimal path-encoded interferometer architecture with periodic boundary conditions. The interferometer has six modes arranged in a hexagonal shape, as shown in **a** and **b**. In the illustration in **a** the modes extend into the plane. Both even and odd columns enact $M/2$ MZIs, according to the congfigurations illustrated in the right panel of **a**, where MZIs are represented using $\leftrightarrow$ symbols, as shown in **c**. **d** Schematic of the implemented interferometer architecture. The two dashed crosses in every odd column (counting from 0 and up) represent a single MZI between the first and last mode.

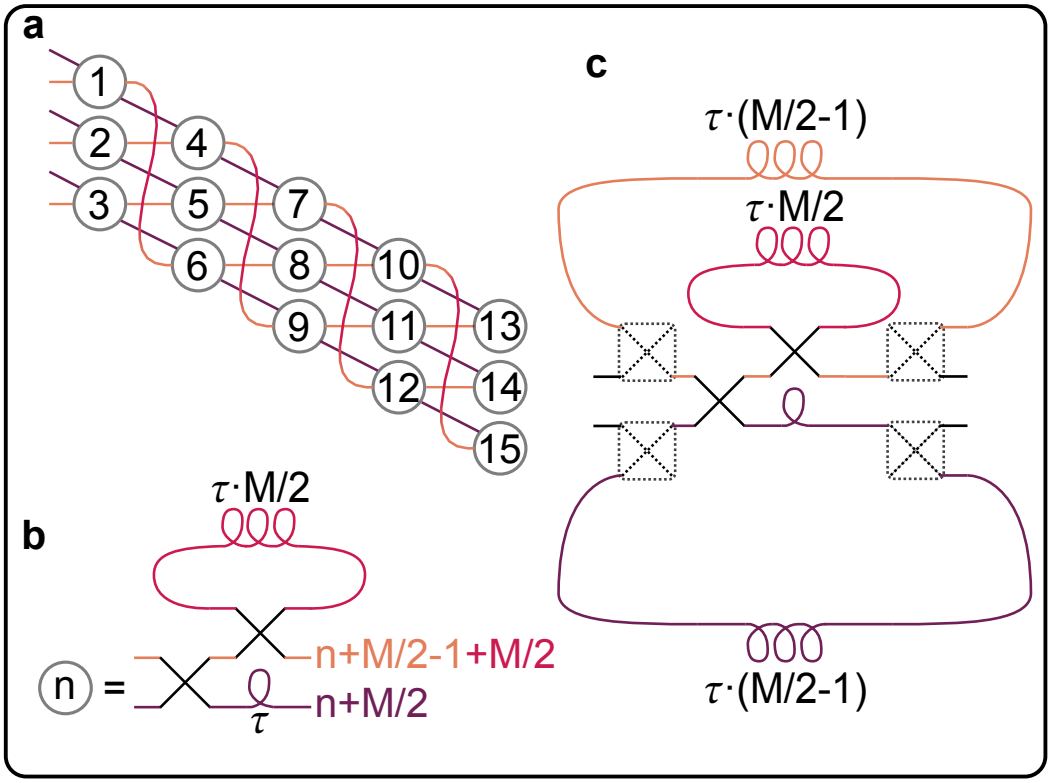

FIGURE B.5: A six-mode example of a two-path loop interferometer architecture with periodic boundary conditions. An exchange permutation is used after every MZI column to permute the first input time-bin in the top mode to occur after the last input time-bin. **a** Line-and-circle representation of a six-mode interferometer. **b** Schematic showing how different MZI events are connected. **c** Physical implementation for an arbitrary even number of modes M.

B.3.2 Conjectured optimal loop interferometer architecture for the two-path time-bin encoding

As was established in the main text, time-bin interferometer architectures allow for permutations between MZI columns, which we can use to introduce periodic boundary conditions to our interferometer architecture. Fig. B.5 shows an example of a loop interferometer with six modes. As before, this allows for fewer MZI columns, which in the case of the loop interferometer translates to less propagation in the delay loop connecting the output to the input. The number of MZI events are reduced further as every column now consists of $M/2$ MZI events compared to the Clements case where the number alternates between $M/2$ and $M/2+1$ MZI events. However, it is important to note that the exchange permutation requires the addition of an MZI in the top mode, which is not necessary for the Clements architecture. Thus, the exact benefit depends on how the MZI insertion loss required for the additional switch compares to the higher propagation loss of the Clements interferometer.

B.3.3 Conjectured optimal-delay cascaded interferometer architecture for the two-path time-bin encoding

For cascaded interferometers, the periodic boundary conditions lead to higher propagation loss compared to the Clements architecture. This is because the architecture with periodic boundary conditions adds a single time-bin of delay for every column, whereas the Clements architecture adds a single time-bin of delay for every *pair* of columns. Though the cascaded Clements architecture has significantly lower delay than the cascaded version of the interferometer in Fig. B.5, it is still one time-bin short of optimal delay, as explained in Section 3.3. To improve upon the architecture, we can take inspiration from the Reck time-bin architecture, which we know does have optimal delay. Indeed, if we implement a single Reck MZI in each spatial path after the first MZI, we can implement exactly $M(M-1)/2$ MZIs with optimal delay. To see this, consider than each of the two physical Reck MZIs implements $M/2-1$ MZI events for a total of $M-2$ MZI events, while adding one time-bin of delay. Additionally, we can sandwich the Reck MZI between two MZIs with no additional delay to implement an additional M MZI events. After this, we need to implement an additional

$$\frac{M(M-1)}{2} - 2(M-1)$$

MZI events while adding $M/2-2$ time-bins of delay. As every pair of odd and even MZI columns will add $(M-1)$ MZIs for every time-bin, we can see that adding $M/2-2$ pairs results in a total number of MZIs equal to

$$2(M-1) + (M-1)(M/2-2) = 2(M-1) - 2(M-1) + \frac{M(M-1)}{2},$$

i.e. the desired number of MZIs with optimal delay. An illustration of the interferometer for six modes is shown in Fig. B.6.

Curiously, we could have added an even higher number of MZIs to the architecture presented in Fig. B.6 for the same amount of delay by repeating the first two columns and adding a single physical MZI at the end. Every pair of MZI and double Reck MZI would add $M-2+M/2$ MZIs while delaying the state by one time-bin. Including the MZI at end, the total number of MZIs for p pairs would be

$$p\frac{3M-4}{2} + M/2,$$

allowing for the desired number of MZIs to be reached with a total delay of

$$p = \frac{M^2}{3M-4}.$$

For $M > 10$ this allows for the sufficient amount of MZIs to be reached before the last input time-bin has reached the first output time-bin, which could not possibly allow for the implementation of an arbitrary unitary

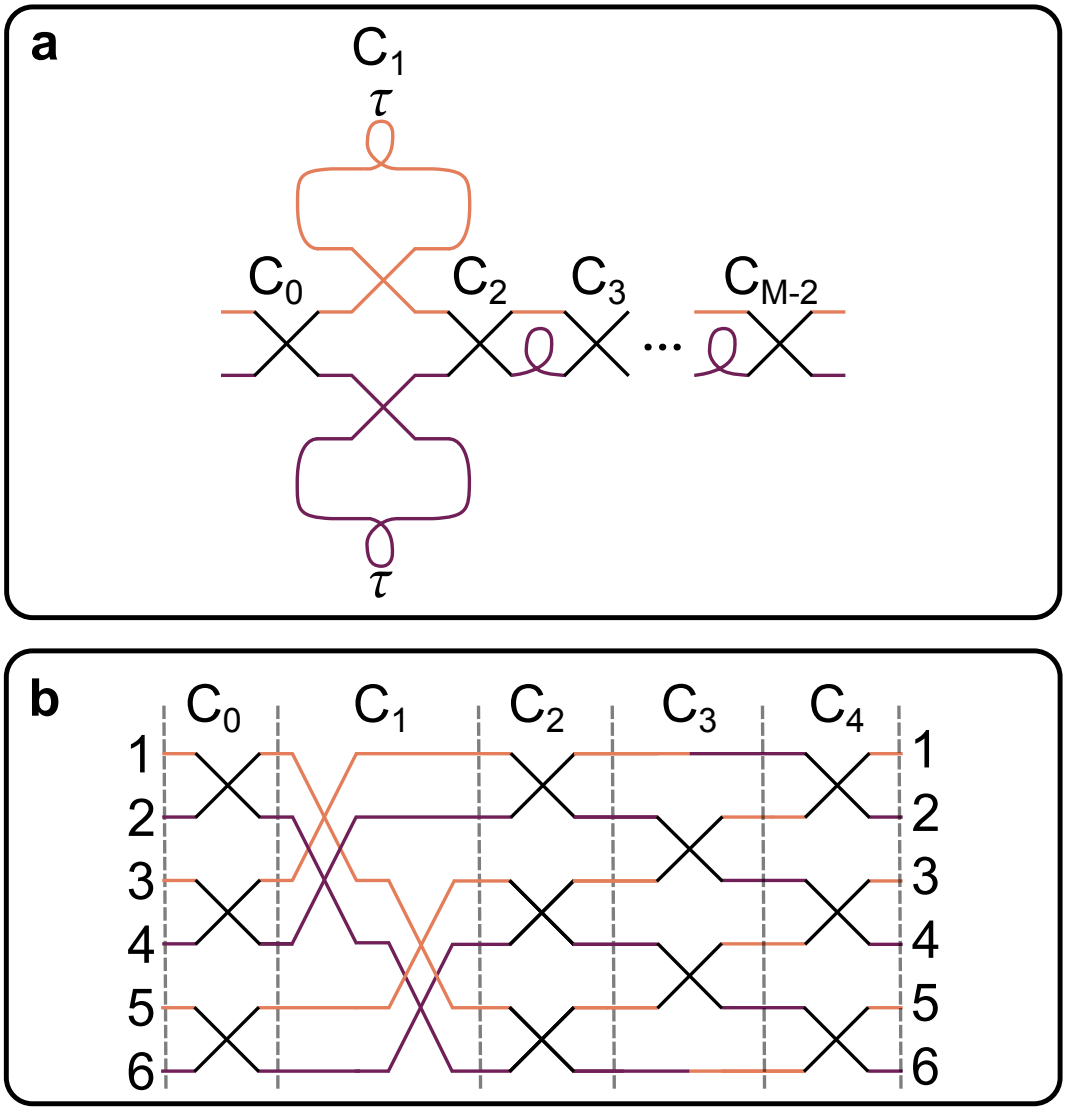

FIGURE B.6: A six-mode example of a cascaded two-path loop interferometer architecture with optimal delay. **a** Line-and-circle representation of a six-mode interferometer. **b** Schematic showing how different MZI events are connected. **c** Physical implementation for an arbitrary even number of modes M.

transformation. Thus, we can conclude that the resource counting conjecture does not hold for this modified interferometer architecture.

B.4 Towards time-bin interferometer architectures with more than two spatial paths

The single-path and two-path interferometer architectures are well-suited for use with a single on-demand source. What if we want to add more sources? For n sources it would be ideal to have a time-bin interferometer with n or $2n$ paths. To this, end we need an interferometer architectures with n paths, where we can insert delays in order to interfere modes across time-bins. Here, I would like to highlight to potential types of interferometer architectures, the spatial architecture with periodic boundary conditions shown in Fig. B.4, which makes use of three dimensions, and a new type of architecture, sketched in Fig. B.7, which makes use of two dimensions. The former seems ideal to implementing cascaded architectures, which could be achieved by judiciously delaying modes in-between the layers of a path-encoded interferometer. In the latter approach, two-path time-bin interferometers (TBIs) are applied to alternating configurations of spatial paths to facilitate interference across all spatial and temporal degrees of freedom. This approach can also be readily extended to larger even number of paths where for every two additional two paths, an additional two two-path TBIs are added (one for input and one for output). By arranging the input and output TBIs in an alternating order (as illustrated for four modes in Fig B.7), all modes should be able to see one another provided a sufficient number of loop iterations. The optimal arrangement of interferometers and delays, which may include mode permutations, and whether or not this results in a useful interferometer remains to be discovered.

B.5 Python code for generating DFT matrices with logarithmic time-bin interferometers for power-of-2 numbers of modes

```python
import numpy as np
import scipy as sp
import matplotlib.pyplot as plt
from scipy.special import factorial
import seaborn as sns

def dft_matrix(N):
    # Create an empty N x N matrix
    F = np.zeros((N, N), dtype=complex)

    # Populate the matrix with DFT coefficients
    for n in range(N):
```

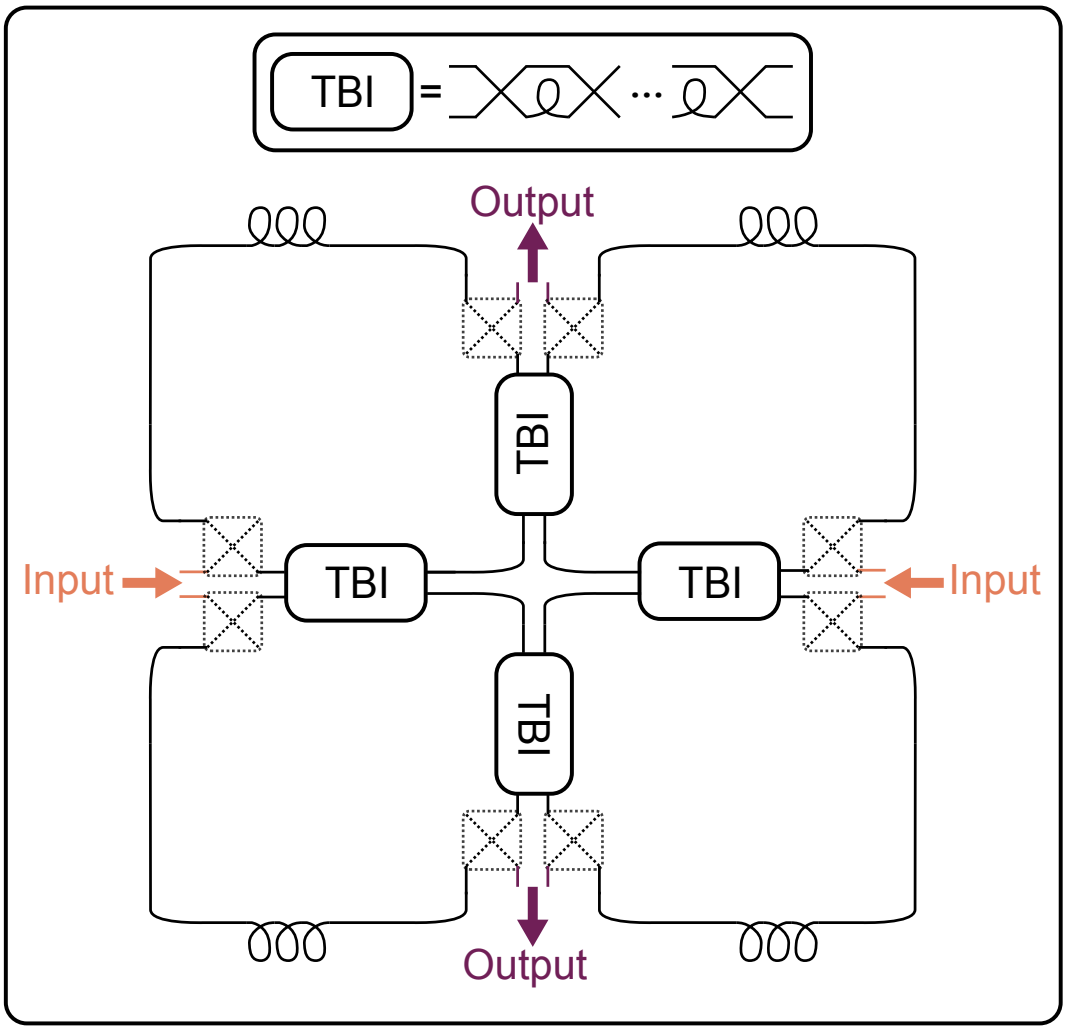

FIGURE B.7: A sketch of a four-path loop interferometer architecture. The interferometer applies two-path time-bin interferometers to alternating configurations of paths.

```
        for k in range(N):
            F[n, k] = np.exp(-2j * np.pi * n * k / N) /
             ↪  np.sqrt(N)

    return F

def bba_phase(number, k):
    # Inverted with respect to BBA as this goes in
     ↪  reverse order
    # Convert the number to its binary representation
    binary_representation = bin(number)[2:]

    # Calculate the number of bits to add (if necessary)
    num_missing_bits = k - len(binary_representation)

    if num_missing_bits > 0:
        # Add leading zeros to make it k bits long
        binary_representation = '0' * num_missing_bits +
         ↪  binary_representation

    # reverse the indices and turn it back into decimal
    new_number = int(binary_representation[::-1], 2)

    return np.exp(-1j*np.pi*new_number/2**(k))

def bba_phase_screen(num_modes, current_k):
    max_k = int(np.log2(num_modes))
    group_size = 2**(max_k-(current_k-1))
    group_idx = 0
    current_group = 0
    phase_mat = np.eye(num_modes, dtype=complex)
    for idx in range(num_modes):
        if idx%2 == 0:
            group_idx+=1
        else:
            phase_mat[idx, idx] =
             ↪  bba_phase(current_group, current_k)
            group_idx+=1
        if group_idx == group_size:
            current_group+=1
            group_idx=0
    return phase_mat

def bba_even_screen(num_modes):
    M = np.eye(num_modes, dtype=complex)
    for i in range(int(num_modes/2)):
        BS_mat = np.ones((2,2), dtype=complex)
        BS_mat[1, 1] = -1
        M[i*2:i*2+2, i*2:i*2+2] = BS_mat/np.sqrt(2)
```

```
    return M

def demux_permutation_matrix(num_modes, column):
    permutation_matrix = np.zeros((num_modes,
    ↪  num_modes), dtype=complex)
    if column == 1:
        return np.eye(num_modes)
    jump = 2**(column-1)
    group_size = 2**(column)
    for group_idx in range(int(num_modes/group_size)):
        for idx in range(0, int(group_size/2)):
            pre = group_idx*(group_size)
            permutation_matrix[pre+2*idx, pre+idx] = 1
            permutation_matrix[pre+2*idx+1,
            ↪  pre+idx+jump] = 1
    return permutation_matrix

def bba_input_output_matrix(num_modes):
    permutation_matrix = np.zeros((num_modes,
    ↪  num_modes))
    jump = int(num_modes/2)
    for row_idx in range(0, int(num_modes/2), 2):
        permutation_matrix[row_idx, row_idx] = 1
        permutation_matrix[row_idx+1, row_idx+jump] = 1
    for row_idx in range(1, int(num_modes/2), 2):
        permutation_matrix[jump+row_idx-1, row_idx] = 1
        permutation_matrix[jump+row_idx, row_idx+jump] =
        ↪  1
    return permutation_matrix

def convert_phase(arr):
    """ Sets all elements with phase -pi to have phase
    ↪  pi """
    # Find elements with phase -pi
    mask = np.isclose(np.angle(arr), -np.pi)

    # Change phase to pi while preserving the magnitude
    magnitudes = np.abs(arr)
    arr[mask] = magnitudes[mask] * np.exp(1j * np.pi)
    return arr

def double_matrix(old_mat):
    new_size = 2*len(old_mat)
    new_mat = np.zeros((new_size, new_size))
    for row_idx in range(len(old_mat)):
        for col_idx in range(len(old_mat)):
            new_mat[2*row_idx, 2*col_idx] =
            ↪  old_mat[row_idx, col_idx]
    return new_mat
```

```

def fourier_input_output_permutation(num_modes):
    if num_modes==1:
        return np.array([[1]])
    if num_modes==2:
        return np.eye(2)
    else:
        f1 = double_matrix(
            fourier_input_output_permutation(
                int(num_modes/4)
                )
            )
        full_perm = np.zeros((num_modes, num_modes))
        half_length = int(num_modes/2)
        # top left
        full_perm[:half_length,:half_length] = f1
        # bottom right
        full_perm[half_length+1:, half_length+1:] =
        ↪  f1[:-1, :-1]
        # top right
        full_perm[1:half_length+1, half_length:] = f1
        # bottom left
        full_perm[half_length:, 1:half_length+1] = f1
        return full_perm

def demux_dft_matrix(num_modes, permuted = True):
    max_k = int(np.log2(num_modes))
    M = np.eye(num_modes, dtype=complex)
    for k in range(1, max_k+1):
        phase_screen = bba_phase_screen(num_modes,
        ↪  (max_k-k)+1)
        perm_mat = demux_permutation_matrix(num_modes,
        ↪  k)
        M =
        ↪  phase_screen@bba_even_screen(num_modes)@perm_mat@M
    if permuted:
        permutation =
        ↪  fourier_input_output_permutation(num_modes)
        return permutation@M@permutation
    else:
        return M

if __name__ == "__main__":
    num_modes=64

    A = convert_phase(dft_matrix(num_modes))
    B = convert_phase(demux_dft_matrix(num_modes,
     ↪  permuted=False))
```

```
143     C = convert_phase(demux_dft_matrix(num_modes,
        ↪ permuted=True))
144
145     print("A and C are the same", np.isclose(A,
        ↪ C).all())
146
147     # permutation =
        ↪ fourier_input_output_permutation(num_modes)
148     fig, ax = plt.subplots(1,3)
149     im = ax[0].imshow(np.angle(A), cmap="rocket",
        ↪ vmin=-np.pi, vmax=np.pi)
150     ax[1].imshow(np.angle(B), cmap="rocket",
        ↪ vmin=-np.pi, vmax=np.pi)
151     ax[2].imshow(np.angle(C), cmap="rocket",
        ↪ vmin=-np.pi, vmax=np.pi)
152     # fig.colorbar(im)
153     fig.savefig('dft_fig_'+str(num_modes)+'modes.svg')
```

C Appendix for Chapter 4

C.1 Phase insensitivity of the postselected Bell state generator

In this appendix we will show that our target two-photon experiments using the interferometers shown in Fig. 4.2 are insensitive to the phase instability that will occur for this type of interferometer. As pointed out in the main chapter, phase-drifts will mainly affect different paths. Thus, we only need to concern ourselves with phase drifts between undelayed and delayed paths.

At the start of the interferometer, the photons will be in the same polarization of two different time-bins, i.e.

$$|psi\rangle_{\text{in}} = \frac{1}{\sqrt{2}}\hat{a}_0^\dagger \hat{a}_2^\dagger. \tag{C.1}$$

Transforming the creation operators with the first set of beamsplitters yields

$$\frac{1}{2\sqrt{2}}(\hat{a}_0^\dagger + \hat{a}_1^\dagger)(\hat{a}_2^\dagger + \hat{a}_3^\dagger) \tag{C.2}$$

where modes 1 and 3 are delayed, introducing the same, arbitrary phase shift, ϕ_0, on both modes with regard to modes 0 and 2

$$\frac{1}{2\sqrt{2}}(\hat{a}_0^\dagger + e^{i\phi_0}\hat{a}_1^\dagger)(\hat{a}_2^\dagger + e^{i\phi_0}\hat{a}_3^\dagger). \tag{C.3}$$

after the swap transformation we have

$$\frac{1}{2\sqrt{2}}(\hat{a}_0^\dagger + e^{i\phi_0}\hat{a}_2^\dagger)(\hat{a}_1^\dagger + e^{i\phi_0}\hat{a}_3^\dagger). \tag{C.4}$$

at which point modes 0 and 2 are delayed, introducing a global phase shift that can be neglected. For the ZZ-basis, this is already the end-point, and we can write out the entire output state as

$$|\psi\rangle_{\text{out, ZZ}} = \frac{1}{2\sqrt{2}}(\hat{a}_0^\dagger \hat{a}_1^\dagger + e^{i\phi_0}\hat{a}_0^\dagger \hat{a}_1^\dagger + e^{i\phi_0}\hat{a}_2^\dagger \hat{a}_1^\dagger + e^{i2\phi_0}\hat{a}_2^\dagger \hat{a}_3^\dagger). \tag{C.5}$$

As all terms contain unique combinations of creation operators, the phases

do not affect the output statistics. In the XX and YY basis, an additional beamsplitter transformation is added. The difference between the two bases comes down to a phase shift added to the first and third mode, which as before leads to a global phase on our state, which we neglect. Thus, in both of these bases we get

$$|\psi\rangle_{\text{out, XX}} = \frac{1}{4}\left((\hat{a}_0^\dagger + \hat{a}_1^\dagger) + e^{i\phi_0}(\hat{a}_2^\dagger + \hat{a}_3^\dagger)\right)\left((\hat{a}_0^\dagger - \hat{a}_1^\dagger) + e^{i\phi_0}(\hat{a}_2^\dagger - \hat{a}_3^\dagger)\right) \tag{C.6}$$

$$= \frac{1}{4}(\hat{a}_0^\dagger\hat{a}_0^\dagger - \hat{a}_1^\dagger\hat{a}_1^\dagger + e^{i2\phi_0}\hat{a}_2^\dagger\hat{a}_2^\dagger - e^{i2\phi_0}\hat{a}_3^\dagger\hat{a}_3^\dagger + e^{i\phi_0}\hat{a}_0^\dagger\hat{a}_2^\dagger - e^{i\phi_0}\hat{a}_1^\dagger\hat{a}_3^\dagger). \tag{C.7}$$

In the final expression all terms again contain unique combinations of creation operators, and as such, phase-instability does not affect the output probability distributions.

D Appendices for Chapter 4

D.1 Classical characterization of electro-optic modulators on the LNOI chip

There were two main issues encountered in using the electro-optic modulators on the LNOI chip: 1. The DC bias drift preventing any DC signals or DC biased AC signals and 2. Seemingly high load impedance. We will tackle the two issues in order.

The DC bias drift problem was characterized in two different ways, shown in Fig. D.1. First, the effective high-pass filter effect can be seen by recording the modulated signal low-frequency square waves. As a square wave stays on the high or low voltage for an extended period of time, the bias drift starts to kick in, reverting the modulated signal back towards that for 0 applied voltage, as seen in Fig. D.1a. This effect can alternatively be measured by measuring the modulation depth of an optical signal modulated using sine-waves with increasing frequency. Fig. D.1b shows how the modulated amplitude changes for a sine-wave frequency spanning from $1\,\mathrm{kHz}$ to over $10\,\mathrm{MHz}$, measured using a lock-in amplifier from Zurich Instruments. The behavior towards the higher frequencies is attributed to the limited bandwidth of the lock-in amplifier. As can be seen from the plot, sine-wave signals with frequencies less than approximately $20\,\mathrm{kHz}$ are attenuated. Thus, square waves with a frequency of $100\,\mathrm{kHz}$ were used to simulate DC signals in the experiments detailed in Chapter 5.

The second problem became clear when we tried to drive the modulators on either the MZI or demux structure using the AWG from Active Technologies (Arb Rider AWG-5064). Once the amplitude of the applied signal passed a certain threshold, the waveform of the modulated signal would distort, as shown in Fig. D.2. This AWG had a setting for expected load impedance, which attenuated the voltage that the AWG outputted. We found that operating the AWG with the attenuated voltages did not result in any distorted modulated waveforms, indicating that the modulators had a high impedance. Thus, we chose to use a different AWG (Rigol DG 4202) capable of driving the high-impedance modulators at sufficiently high voltages in the final experiments.

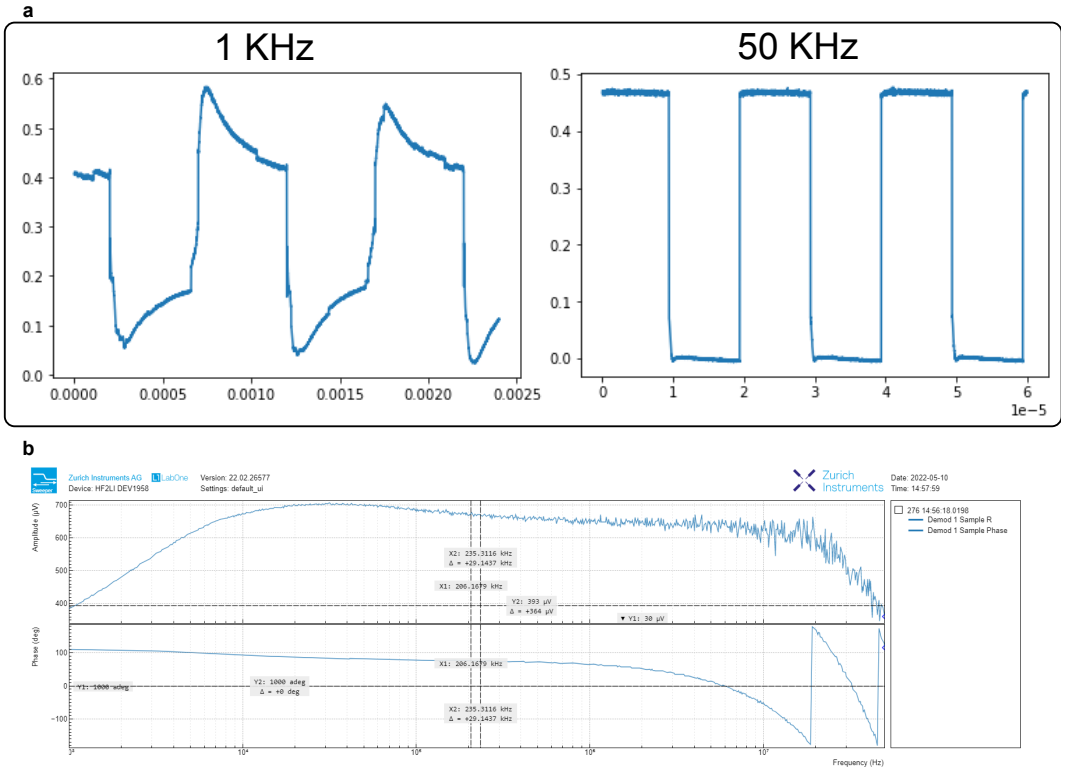

FIGURE D.1: Experimental characterization of the DC bias drift effect on electro-optic modulation on our chip. **a** The two graphs show a modulated optical signal obtained by applying a square wave signal with two different frequencies to the modulator of an MZI and recording the modulated signal with a photodioide. **b** Recorded amplitude (y-axis, top) and phase (y-axis, bottom) of a modulated optical signal for sinusoidal drive signals with increasing frequency (x-axis).

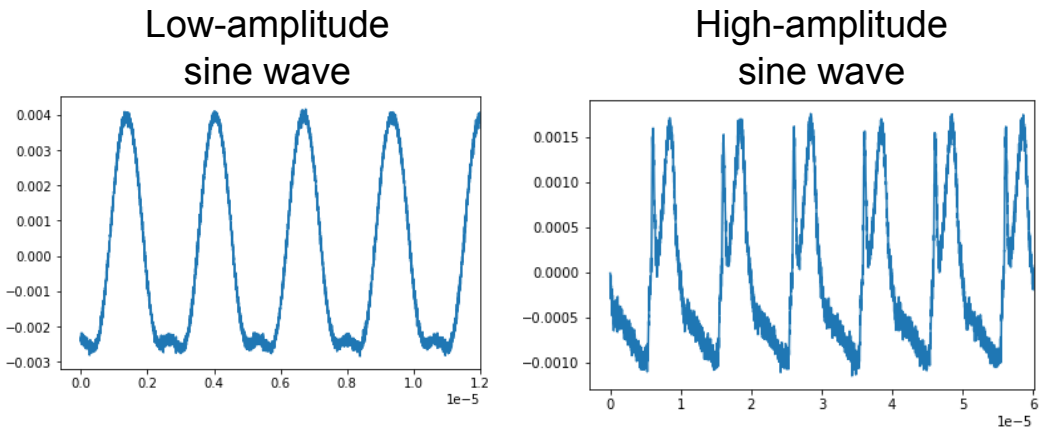

FIGURE D.2: Experimental observation of high load-impedance of electro-optic modulators. The two graphs show a modulated optical signal obtained by applying a sinusoidal signal to the modulator of an MZI and recording the modulated signal with a photodioide. The left panel shows the observed modulation for a low-amplitude sine wave, whereas the right panel shows modulation for a high-ampltiude sine wave, where the modulated waveform is heavily distorted and attenuated. Note that the y-axis on the right plot has lower values than on the left plot.

D.2 Alignment procedure for the LNOI chip

In order to align the fiber array and electrodes to the correct positions, we made use of a setup illustrated in Fig. D.3. By switching between the top view and side view, all angles of the fiber array could be coarsely aligned to the grating couplers on the chip. We could also ensure that no optics crashed into the chip from the side view. As visible in the photo from the side view shown in Fig. D.3d, the fiber array will block the position of the light on the chip as seen from the top if it is close to be well-aligned. In order to position the fiber array, we first moved the fiber array far up from the chip such that the laser spot on the chip could be seen on the camera from the top view. This allowed for us to weakly couple the fiber arrays to the grating couplers. The coupling could then be improved by iteratively moving the fiber array downwards and laterally towards the grating coupler. The lateral movement of the fiber array was necessary to compensate for the lateral displacement of the beam due to the angle of the fiber-array.

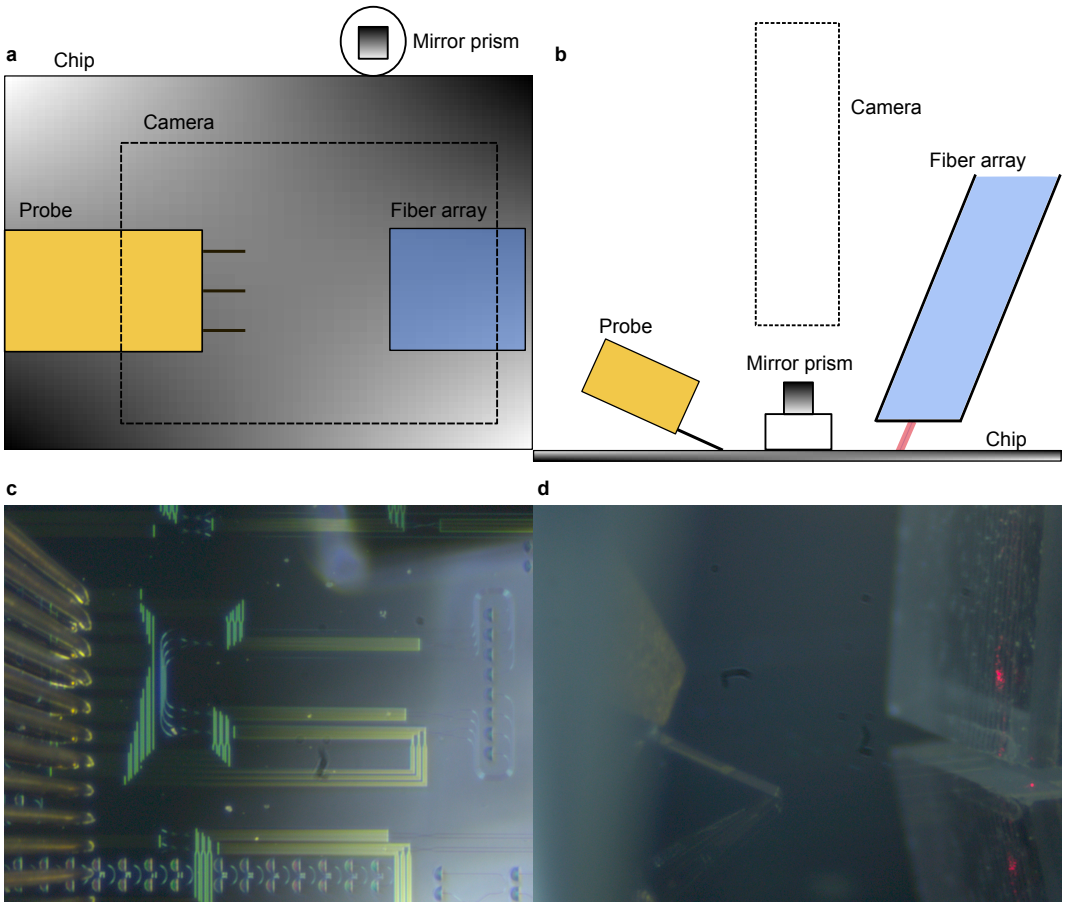

FIGURE D.3: Schematics and photos of the chip setup from a top view (**a** and **c**) and side view (**b** and **c**). The top view can be recorded by focusing camera on the chip from the top, whereas the side-view was obtained by focusing the camera on the mirror prism to the side of the chip. **c** Photo taken from the top view during the alignment of an electronic probe connected to the modulators of the on-chip demultiplexer structure. **d** Photo taken from the side view during the alignment of an electronic probe to the modulator on an on-chip MZI. The fiber array is also visible on the right-hand side.

E Appendices for Chapter 5

E.1 On the computational complexity of boson sampling with collisions

Here we will evaluate the computational complexity of boson sampling with collisions, which is relevant in the case of boson sampling with added lost photons where photon collisions and photon loss are indistinguishable due to the use of threshold detectors. To do so, we employ the approach used in Ref. Chin et al. 2018 which we summarize below. In this approach, the minimal computation time $\mathcal{T}_{\text{min}}(\vec{n}, \vec{m})$ is given as a function of the input state $\vec{n}$ and output state $\vec{m}$ in the Fock basis, where a state is defined as

$$\vec{n} = (n_1, n_2, ..., n_M), \quad \sum_i n_i = N \tag{E.1}$$

where n_i is the number of photons in the ith mode, M is the total number of modes, and N is the total number of photons.

The minimal computation time, $\mathcal{T}_{\text{min}}(\vec{n}, \vec{m})$ with input state $\vec{n}$ and output state $\vec{m}$ is found to be

$$\mathcal{T}_{\text{min}}(\vec{n}, \vec{m}) = \mathcal{O}\left(\min\left\{\sum_{k=0}^{\alpha_{\vec{n}}} X_k(\vec{n}), \sum_{l=0}^{\alpha_{\vec{m}}} X_l(\vec{m})\right\} \alpha_{\vec{n}}\alpha_{\vec{m}}\right). \tag{E.2}$$

Here, $\alpha_{\vec{n}}$ is the number of nonzero elements in the Fock state vector $\vec{n}$, called the Fock state coherence rank, and $X_k(\vec{n})$ is the k-th elementary symmetric potential defined as

$$X_k(\vec{n}) = \sum_{i_1<i_2<...<i_k=1}^{\alpha_{\vec{n}}} n_{i1}n_{i2}...n_{ik}, (0 \leq k \leq \alpha_{\vec{n}} \leq M). \tag{E.3}$$

The minimal computation time is then determined by the quantity $\sum_{k=0}^{\alpha_{\vec{n}}} X_k(\vec{n})$ for the input state and the output state. The input state will be collision-free, $\vec{n}_{\text{collision-free}}$ for which the following holds Chin et al. 2018

$$\sum_{k=0}^{\alpha_{\vec{n}}} X_k(\vec{n}_{\text{collision-free}}) = 2^N = 2^{\alpha_{\vec{n}}}. \tag{E.4}$$

Adding a collision to a collision-free state corresponds to increasing one of the nonzero numbers n_i in $\vec{n}$. From the definition of Eq. (E.3), we can see that the value of $\sum_{k=0}^{\alpha_{\vec{n}}} X_k(\vec{n})$ then has to increase. As such, the following inequality will be true for any state $\vec{n}$

$$\sum_{k=0}^{\alpha_{\vec{n}}} X_k(\vec{n}) \geq 2^{\alpha_{\vec{n}}}. \tag{E.5}$$

Thus we can say that the minimal computation time has to scale at least as $\mathcal{O}(2^{\alpha_{\vec{m}}}\alpha_{\vec{n}}\alpha_{\vec{m}})$. Accordingly, we can conclude that the computational complexity of boson sampling with collisions is not diminished compared to the computational complexity of collision-free boson sampling with the same number of nonzero elements.

E.2 The size of the Hilbert subspace for a given number of photon collisions.

The number of basis states in the Hilbert space with a given number of collisions is equal to the product of the number of ways one can distribute d nonzero modes in m modes, and the number of ways one can place $p-l-d$ collisions into d nonzero modes. The first number is equal to the number of combinations without replacements with d choices from m possibilities:

$$\binom{m}{d}.$$

The second number is equal to the number of combinations with replacements with $p-l-d$ choices from d possibilities

$$\begin{aligned}&\binom{(p-l-d)+d-1}{p-l-d}\\ =&\binom{p-l-1}{p-l-d}\end{aligned}$$

Consequently the size of the Hilbert subspace with $p-d-l$ collisions, $n_{\text{collisions}}(p,d,l,m)$, will be

$$n_{\text{collisions}}(p,d,l,m) = \binom{m}{d}\cdot\binom{p-l-1}{p-l-d}. \tag{E.6}$$

The size of the full Hilbert space, n_{full} will be the number of ways one can place $p-l$ photons into m modes. This is equivalent to the number of combinations with replacements of $p-l$ choices with m possibilities:

$$n_{\text{full}}(m,p,l) = \binom{m+p-l-1}{p-l}. \tag{E.7}$$

We can then take the ratio between Eqs. (E.6) and (E.7) to find Eq. (6.8)

E.3 The downsides of using loop architectures for time-bin interferometer

Though it is possible to implement large multimode interferometers using only a single physical MZI connected to fiber delay loops, as in Refs. Motes et al. 2014; He et al. 2017, this has two major downsides: higher propagation loss and severely reduced input state rate. Much in the same way as in the cascaded case, a column of MZIs in the Clements or Rectangular scheme can be implemented by sending the time-bins through the MZI one by one and reconfiguring the MZI transformation for each time-bin. In order to reuse the same physical MZI to implement additional columns, we can connect the outputs to the inputs through a delay loop, where the delay is sufficiently long that all output modes back at the input after the previous MZI column has been finished. As each column processes up to $m/2$ time-bins, this requires that the loops have a delay of at least $m/2$ time-bins. This is in comparison to the cascaded scheme where no such delay is necessary apart from the delay of one time-bin in one of the modes, which will still be present in the loop architecture. To see the difference, we can compare the total delay, t_{delay} for the worst case of the Clements scheme with a cascaded architecture and a loop architecture

$$t_{\text{delay, cascaded}} = \frac{m}{2} - 1 \cdot \tau, \tag{E.8}$$

$$t_{\text{delay, loop}} = (m-1)(\frac{m}{2} - 1) \cdot \tau, \tag{E.9}$$

where τ corresponds to the separation between time-bins. In other words, the total propagation loss scales linearly with the number of modes for cascaded time-bin interferometers, whereas it scales quadratically with the number of modes for loop time-bin interferometers.

The second downside is that one has to wait for the full output state to come out of the interferometer before processing a new input state. The time difference between the first time-bin in the input state and the last time-bin of the output state is equivalent to the delay in Eq. (E.9). As the time-bin separation is related to the rate of the single-photon source, the input generation rate, r_{input} for the loop time-bin interferometer will be given by

$$r_{\text{input}} = \frac{2r_{\text{single-photon}}}{m(m-1))}. \tag{E.10}$$

This is approximately a factor $1/m$ worse than the corresponding rate for a cascaded interferometer.

E.4 Increasing the input state generation rate by running multiple time-bin interferometers in parallel

Though the input state generation rate given by Eq. (6.11) applies to a single time-bin interferometer, we can increase this rate by employing multiple time-bin interferometers in parallel. In this approach, the single-photon source first produces all photons for one interferometer, and produces input state for other interferometers while waiting for the first interferometer to be available for a new input state. The number of interferometer required for this approach will be equal to $\lceil m/2p \rceil$. Additionally, a switch—equivalent to a demultiplexer without delays at the end—will be required to configure which interferometer the single-photon source addresses at any given time. This approach should only be considered for the demultiplexing interferometer architecture, as the main benefit of the other architectures is that a demultiplexer is not required. Fig. E.1 shows the MZI hardware requirements for a single demultiplexing time-bin interferometer compared to a series of interferometers run in parallel.

E.5 The importance of distributing input photons for demultiplexing interferometers

A consequence of the lower optical depth of demultiplexing interferometers is that we have access to fewer phase shifters to specify the unitary transformation, limiting the unitary transformations that can be implemented using the interferometer. As an example of how this can reduce the computational hardness of simulation, consider the case where the input photons occupy the first p time-bins, such that only the first $2p$ modes are occupied in the input state. After $l = \lceil \log_2(2p) \rceil$ layers of MZIs, every input photon will have seen every other input photon, and all modes containing photons will only encounter new empty modes. This means that there will be no more interference for the remainder of the interferometer. Thus, this case is equivalent to applying a smaller $l \times l$ interferometer with p input photons, and distributing the resulting probability output distribution across the remaining modes. However, as this second distribution stage does not involve any interference, we can model it classically by considering the probabilities (as opposed to the complex probability amplitudes), which is classically trivial. Thus, in practice the problem only as hard as simulating a boson sampling experiment with p input photons in $2p \leq 2^{1+\lceil \log_2(p) \rceil} < 4p$ modes, where we cannot post-select on collision-free outputs (as collisional outputs from the first stage could become collision-free in the second distribution stage). In order to avoid this reduction of computational hardness, the input photons should be uniformly distributed among the input modes.

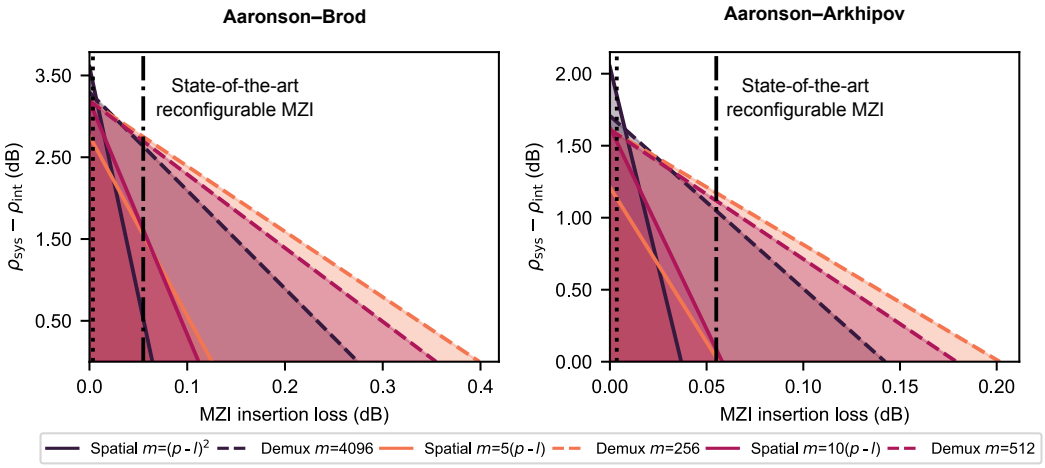

FIGURE E.1: Plot of the requirements on MZI insertion loss (x-axis) and $\rho_{\text{sys}} - \rho_{\text{int}}$ (y-axis) with photon indistinguishability set to $x^2 = 0.96$. The plot to the left shows the requirements for Aaronson–Brod boson sampling, where the input state consists of 59 photons with the outputs post-selected to contain 50 photon detection events. The plot to the right shows the requirements for Aaronson–Arkhipov boson sampling, where we send in 50 photons and detect 50 photons, not allowing for photon loss or collisions. The solid lines correspond to the requirements for a single demultiplexing interferometer, whereas dashed lines correspond to the requirements for a series of demultiplexing time-bin interferometers run in parallel in conjunction with a switch. The dotted vertical lines mark the estimated MZI loss for a state-of-the-art experimental realization with static, nonprogrammable MZIs Wang et al. 2019. The dash-dotted vertical line marks the estimated MZI loss for a state-of-the-art experimental realization with programmable MZIs Taballione et al. 2023.

Bibliography

AARONSON, S. and A. Arkhipov (2011). "The computational complexity of linear optics". *Proceedings of the forty-third annual ACM symposium on Theory of computing*, 333–342 (cited on pp. 2, 28, 109–111, 117, 128).

AARONSON, S. and D. J. Brod (2016). "BosonSampling with lost photons". *Physical Review A* **93**.1, 012335 (cited on pp. 115, 117, 126).

ADCOCK, J. C., S. Morley-Short, J. W. Silverstone, and M. G. Thompson (2018). "Hard limits on the postselectability of optical graph states". *Quantum Science and Technology* **4**.1, 015010 (cited on p. 88).

ADCOCK, J. C., C. Vigliar, R. Santagati, J. W. Silverstone, and M. G. Thompson (2019). "Programmable four-photon graph states on a silicon chip". *Nature Communications* **10**.1, 1–6. DOI: https://doi.org/10.1038/s41467-019-11489-y (cited on p. 103).

AGHAEIMEIBODI, S., B. Desiatov, J.-H. Kim, C.-M. Lee, M. A. Buyukkaya, A. Karasahin, C. J. Richardson, R. P. Leavitt, M. Lončar, and E. Waks (2018). "Integration of quantum dots with lithium niobate photonics". *Applied Physics Letters* **113**.22, 221102. DOI: https://doi.org/10.1063/1.5054865 (cited on p. 107).

APPEL, M. H. (2021). "A Quantum Dot Source of Time-Bin Multi-Photon Entanglement". PhD thesis. University of Copenhagen (cited on p. 80).

ARKHIPOV, A. and G. Kuperberg (2012). "The bosonic birthday paradox". *Geometry & Topology Monographs* **18**.1, 10–2140 (cited on p. 111).

ARUTE, F., K. Arya, R. Babbush, D. Bacon, J. C. Bardin, R. Barends, R. Biswas, S. Boixo, F. G. Brandao, D. A. Buell, et al. (2019). "Quantum supremacy using a programmable superconducting processor". *Nature* **574**.7779, 505–510. DOI: https://doi.org/10.1038/s41586-019-1666-5 (cited on p. 109).

BAO, J., Z. Fu, T. Pramanik, J. Mao, Y. Chi, Y. Cao, C. Zhai, Y. Mao, T. Dai, X. Chen, et al. (2023). "Very-large-scale integrated quantum graph photonics". *Nature Photonics*, 1–9 (cited on p. 110).

BARAK, R. and Y. Ben-Aryeh (2007). "Quantum fast Fourier transform and quantum computation by linear optics". *JOSA B* **24**.2, 231–240 (cited on pp. 67, 69, 70).

BARTOLUCCI, S., P. Birchall, H. Bombin, H. Cable, C. Dawson, M. Gimeno-Segovia, E. Johnston, K. Kieling, N. Nickerson, M. Pant, et al. (2023). "Fusion-based quantum computation". *Nature Communications*

14.1, 912. DOI: https://doi.org/10.1038/s41467-023-36493-1 (cited on pp. 2, 33, 40, 45, 91, 106, 108, 109).

BARTOLUCCI, S., P. Birchall, D. Bonneau, H. Cable, M. Gimeno-Segovia, K. Kieling, N. Nickerson, T. Rudolph, and C. Sparrow (2021). *Switch networks for photonic fusion-based quantum computing*. arXiv: 2109.13760 [quant-ph] (cited on p. 114).

BENNETT, C. H. and G. Brassard (1984). "Quantum cryptography: Public key distribution and coin tossing". *Proceedings of the IEEE International Conference on Computers, Systems, and Signal Processing* (cited on p. 1).

BOIXO, S., S. V. Isakov, V. N. Smelyanskiy, R. Babbush, N. Ding, Z. Jiang, M. J. Bremner, J. M. Martinis, and H. Neven (2018). "Characterizing quantum supremacy in near-term devices". *Nature Physics* **14**.6, 595–600 (cited on p. 109).

BOMBIN, H., I. H. Kim, D. Litinski, N. Nickerson, M. Pant, F. Pastawski, S. Roberts, and T. Rudolph (2021). "Interleaving: Modular architectures for fault-tolerant photonic quantum computing". *arXiv preprint arXiv:2103.08612*. DOI: https://doi.org/10.48550/arXiv.2103.08612 (cited on pp. 103, 108).

BORREGAARD, J., H. Pichler, T. Schröder, M. D. Lukin, P. Lodahl, and A. S. Sørensen (2020). "One-Way Quantum Repeater Based on Near-Deterministic Photon-Emitter Interfaces". *Phys. Rev. X* **10** (2), 021071. DOI: 10.1103/PhysRevX.10.021071 (cited on pp. 33, 108).

BOURASSA, J. E., R. N. Alexander, M. Vasmer, A. Patil, I. Tzitrin, T. Matsuura, D. Su, B. Q. Baragiola, S. Guha, G. Dauphinais, et al. (2021). "Blueprint for a scalable photonic fault-tolerant quantum computer". *Quantum* **5**, 392 (cited on p. 2).

BROD, D. J., E. F. Galvão, A. Crespi, R. Osellame, N. Spagnolo, and F. Sciarrino (2019). "Photonic implementation of boson sampling: a review". *Advanced Photonics* **1**.3, 034001 (cited on pp. 110, 111).

BROOME, M. A., A. Fedrizzi, S. Rahimi-Keshari, J. Dove, S. Aaronson, T. C. Ralph, and A. G. White (2013). "Photonic boson sampling in a tunable circuit". *Science* **339**.6121, 794–798 (cited on p. 110).

BROWNE, D. E. and T. Rudolph (2005). "Resource-efficient linear optical quantum computation". *Physical Review Letters* **95**.1, 010501 (cited on p. 74).

BULMER, J. F. F., S. Paesani, R. S. Chadwick, and N. Quesada (2022). "Threshold detection statistics of bosonic states". *Phys. Rev. A* **106** (4), 043712. DOI: 10.1103/PhysRevA.106.043712 (cited on p. 111).

CAROLAN, J., C. Harrold, C. Sparrow, E. Martín-López, N. J. Russell, J. W. Silverstone, P. J. Shadbolt, N. Matsuda, M. Oguma, M. Itoh, et al. (2015a). "Universal linear optics". *Science* **349**.6249, 711–716 (cited on p. 74).

— (2015b). "Universal linear optics". *Science* **349**.6249, 711–716. DOI: https://doi.org/10.1126/science.aab3642 (cited on p. 106).

CAROSINI, L., V. Oddi, F. Giorgino, L. M. Hansen, B. Seron, S. Piacentini, T. Guggemos, I. Agresti, J. C. Loredo, and P. Walther (2023). "Programmable multi-photon quantum interference in a single spatial mode". *arXiv preprint arXiv:2305.11157* (cited on pp. 48, 120).

CHEN, B., Z. Ruan, X. Fan, Z. Wang, J. Liu, C. Li, K. Chen, and L. Liu (2022). "Low-loss fiber grating coupler on thin film lithium niobate platform". *APL Photonics* **7**.7, 076103. DOI: https://doi.org/10.1063/5.0093033 (cited on p. 102).

CHEN, S., L.-C. Peng, Y.-P. Guo, X.-M. Gu, X. Ding, R.-Z. Liu, X. You, J. Qin, Y.-F. Wang, Y.-M. He, J. J. Renema, Y.-H. Huo, H. Wang, C.-Y. Lu, and J.-W. Pan (2023). *Heralded three-photon entanglement from a single-photon source on a photonic chip*. DOI: https://doi.org/10.48550/arXiv.2307.02189. arXiv: 2307.02189 [quant-ph] (cited on pp. 128, 133).

CHIN, S. and J. Huh (2018). "Generalized concurrence in boson sampling". *Scientific reports* **8**.1, 6101 (cited on pp. 116, 163).

CLEMENTS, W. R., P. C. Humphreys, B. J. Metcalf, W. S. Kolthammer, and I. A. Walmsley (2016). "Optimal design for universal multiport interferometers". *Optica* **3**.12, 1460–1465 (cited on pp. 26, 71, 106, 116, 118, 119).

CRESPI, A., R. Osellame, R. Ramponi, M. Bentivegna, F. Flamini, N. Spagnolo, N. Viggianiello, L. Innocenti, P. Mataloni, and F. Sciarrino (2016). "Suppression law of quantum states in a 3D photonic fast Fourier transform chip". *Nature communications* **7**.1, 10469 (cited on pp. 67, 74).

CRESPI, A., R. Osellame, R. Ramponi, D. J. Brod, E. F. Galvao, N. Spagnolo, C. Vitelli, E. Maiorino, P. Mataloni, and F. Sciarrino (2013). "Integrated multimode interferometers with arbitrary designs for photonic boson sampling". *Nature photonics* **7**.7, 545–549 (cited on p. 110).

DEGEN, C. L., F. Reinhard, and P. Cappellaro (2017). "Quantum sensing". *Reviews of modern physics* **89**.3, 035002 (cited on p. 20).

DING, X., Y.-P. Guo, M.-C. Xu, R.-Z. Liu, G.-Y. Zou, J.-Y. Zhao, Z.-X. Ge, Q.-H. Zhang, H.-L. Liu, M.-C. Chen, et al. (2023). "High-efficiency single-photon source above the loss-tolerant threshold for efficient linear optical quantum computing". *arXiv preprint arXiv:2311.08347* (cited on pp. 2, 17, 128).

DING, X., Y. He, Z.-C. Duan, N. Gregersen, M.-C. Chen, S. Unsleber, S. Maier, C. Schneider, M. Kamp, S. Höfling, C.-Y. Lu, and J.-W. Pan (2016). "On-Demand Single Photons with High Extraction Efficiency and Near-Unity Indistinguishability from a Resonantly Driven Quantum Dot in a Micropillar". *Phys. Rev. Lett.* **116** (2), 020401. DOI: 10.1103/PhysRevLett.116.020401 (cited on pp. 126, 128).

DREESSEN, C. L., C Ouellet-Plamondon, P Tighineanu, X Zhou, L Midolo, A. S. Sørensen, and P Lodahl (2018). "Suppressing phonon decoherence of high performance single-photon sources in nanophotonic waveguides". *Quantum Science and Technology* **4**.1, 015003. DOI: 10.1088/2058-9565/aadbb8 (cited on p. 126).

ELSHAARI, A. W., W. Pernice, K. Srinivasan, O. Benson, and V. Zwiller (2020). "Hybrid integrated quantum photonic circuits". *Nat. Photon.* **14**.5, 285–298 (cited on p. 110).

FERRANTE, M. and N. Frigo (2012). "A note on the coupon-collector's problem with multiple arrivals and the random sampling". *arXiv preprint arXiv:1209.2667* (cited on p. 123).

GERRY, C. and P. L. Knight (2005). *Introductory quantum optics*. Cambridge university press (cited on pp. 12–14).

GIMENO-SEGOVIA, M., P. Shadbolt, D. E. Browne, and T. Rudolph (2015). "From Three-Photon Greenberger-Horne-Zeilinger States to Ballistic Universal Quantum Computation". *Phys. Rev. Lett.* **115** (2), 020502. DOI: 10.1103/PhysRevLett.115.020502 (cited on p. 103).

HAMILTON, C. S., R. Kruse, L. Sansoni, S. Barkhofen, C. Silberhorn, and I. Jex (2017). "Gaussian boson sampling". *Physical review letters* **119**.17, 170501 (cited on pp. 109, 114).

HE, Y., X Ding, Z.-E. Su, H.-L. Huang, J Qin, C Wang, S Unsleber, C Chen, H Wang, Y.-M. He, et al. (2017). "Time-bin-encoded boson sampling with a single-photon device". *Physical review letters* **118**.19, 190501. DOI: https://doi.org/10.1103/PhysRevLett.118.190501 (cited on pp. 50, 54, 120, 141, 165).

HECHT, E. (2002). *Optics*. Addison Wesley (cited on p. 38).

HOLZGRAFE, J. C. (2022). "Cavity electro-optics in thin-film lithium niobate". PhD thesis. Harvard University (cited on pp. 92, 93, 107).

HONG, C.-K., Z.-Y. Ou, and L. Mandel (1987). "Measurement of subpicosecond time intervals between two photons by interference". *Physical review letters* **59**.18, 2044. DOI: https://doi.org/10.1103/PhysRevLett.59.2044 (cited on pp. 10, 113).

HUH, J., G. G. Guerreschi, B. Peropadre, J. Mcclean, and A. Aspuru-Guzik (Dec. 2014). "Boson Sampling for Molecular Vibronic Spectra". *Nature Photonics* **9**. DOI: 10.1038/nphoton.2015.153 (cited on p. 106).

HUMMEL, T., C. Ouellet-Plamondon, E. Ugur, I. Kulkova, T. Lund-Hansen, M. A. Broome, R. Uppu, and P. Lodahl (2019). "Efficient demultiplexed single-photon source with a quantum dot coupled to a nanophotonic waveguide". *Applied Physics Letters* **115**.2 (cited on p. 89).

KAUSHALRAM, A., G. Hegde, and S. Talabattula (2020). "Mode hybridization analysis in thin film lithium niobate strip multimode waveguides". *Scientific Reports* **10**.1, 1–13. DOI: https://doi.org/10.1038/s41598-020-73936-x (cited on p. 103).

KNILL, E., R. Laflamme, and G. J. Milburn (2001). "A scheme for efficient quantum computation with linear optics". *nature* **409**.6816, 46–52 (cited on pp. 2, 44, 45).

LACEY, J. and F. Payne (1990). "Radiation loss from planar waveguides with random wall imperfections". *IEE Proceedings J (Optoelectronics)* **137**.4, 282–289. DOI: 10.1049/ip-j.1990.0047 (cited on p. 100).

LAU, J. H. (2019). *Heterogeneous integrations*. Springer (cited on p. 137).

LI, J.-P., J. Qin, A. Chen, Z.-C. Duan, Y. Yu, Y. Huo, S. Höfling, C.-Y. Lu, K. Chen, and J.-W. Pan (2020). "Multiphoton graph states from a solid-state single-photon source". *ACS Photonics* **7**.7, 1603–1610 (cited on pp. 74, 89).

LINDENMANN, N, G Balthasar, D Hillerkuss, R Schmogrow, M Jordan, J. Leuthold, W Freude, and C Koos (2012). "Photonic wire bonding: a novel concept for chip-scale interconnects". *Optics Express* **20**.16, 17667–17677. DOI: 10.1364/OE.20.017667 (cited on p. 107).

LODAHL, P., A. Ludwig, and R. J. Warburton (2022). "A deterministic source of". *Physics Today* **75**, 3–44. DOI: https://doi.org/10.1063/PT.3.4962 (cited on pp. 115, 125).

LODAHL, P., S. Mahmoodian, and S. Stobbe (2015). "Interfacing single photons and single quantum dots with photonic nanostructures". *Reviews of Modern Physics* **87**.2, 347. DOI: https://doi.org/10.1103/RevModPhys.87.347 (cited on pp. 15, 16, 18).

LOMONTE, E, M Stappers, F Lenzini, and W. Pernice (2022). "Highly efficient silicon nitride grating couplers with metal back-reflector enabled by cryogenic deep silicon etching". *Integrated Photonics Platforms II*. Vol. 12148. SPIE, 14–18. DOI: https://doi:10.1117/12.2621230 (cited on p. 107).

LOMONTE, E., F. Lenzini, and W. H. Pernice (2021a). "Efficient self-imaging grating couplers on a lithium-niobate-on-insulator platform at near-visible and telecom wavelengths". *Optics Express* **29**.13, 20205–20216. DOI: https://doi.org/10.1364/OE.428138 (cited on p. 102).

LOMONTE, E., M. A. Wolff, F. Beutel, S. Ferrari, C. Schuck, W. H. Pernice, and F. Lenzini (2021b). "Single-photon detection and cryogenic reconfigurability in lithium niobate nanophotonic circuits". *Nature Communications* **12**.1, 1–10. DOI: https://doi.org/10.1038/s41467-021-27205-8 (cited on pp. 92, 93, 107, 136).

MADSEN, L. S., F. Laudenbach, M. F. Askarani, F. Rortais, T. Vincent, J. F. Bulmer, F. M. Miatto, L. Neuhaus, L. G. Helt, M. J. Collins, et al. (2022). "Quantum computational advantage with a programmable photonic processor". *Nature* **606**.7912, 75–81. DOI: https://doi.org/10.1038/s41586-022-04725-x (cited on pp. 106, 109, 114, 117, 119, 128).

MARCHETTI, R., C. Lacava, L. Carroll, K. Gradkowski, and P. Minzioni (2019). "Coupling strategies for silicon photonics integrated chips". *Photonics Research* **7**.2, 201–239 (cited on pp. 133, 137).

MARING, N., A. Fyrillas, M. Pont, E. Ivanov, P. Stepanov, N. Margaria, W. Hease, A. Pishchagin, T. H. Au, S. Boissier, et al. (2023). *A general-purpose single-photon-based quantum computing platform*. DOI: https://doi.org/10.48550/arXiv.2306.00874. arXiv: 2306.00874 [quant-ph] (cited on pp. 109, 128).

MIGDALL, A. L., D. Branning, and S. Castelletto (2002). "Tailoring single-photon and multiphoton probabilities of a single-photon on-demand source". *Phys. Rev. A* **66** (5), 053805. DOI: 10.1103/PhysRevA.66.053805 (cited on pp. 103, 114).

MOODY, G., V. J. Sorger, D. J. Blumenthal, P. W. Juodawlkis, W. Loh, C. Sorace-Agaskar, A. E. Jones, K. C. Balram, J. C. F. Matthews, A. Laing, et al. (2022). "2022 Roadmap on integrated quantum photonics". *J. Phys. Photonics* **4**, 012501. DOI: 10.1088/2515-7647/ac1ef4 (cited on p. 110).

MORVAN, A, B Villalonga, X Mi, S Mandrà, A Bengtsson, P. Klimov, Z Chen, S Hong, C Erickson, I. Drozdov, et al. (2023). "Phase transition in Random Circuit Sampling". *arXiv preprint arXiv:2304.11119* (cited on p. 109).

MOTES, K. R., A. Gilchrist, J. P. Dowling, and P. P. Rohde (2014). "Scalable boson sampling with time-bin encoding using a loop-based architecture". *Physical review letters* **113**.12, 120501. DOI: https://doi.org/10.1103/PhysRevLett.113.120501 (cited on pp. 48, 50, 120, 165).

NIELSEN, K. H. (2022). "Towards programmable nonlinear photonic quantum simulation". Master thesis. University of Copenhagen (cited on pp. 50, 73).

NIELSEN, M. A. and I. L. Chuang (2000). *Quantum information and quantum computation* (cited on p. 33).

NOTAROS, J., F. Pavanello, M. T. Wade, C. M. Gentry, A. Atabaki, L. Alloatti, R. J. Ram, and M. A. Popović (2016). "Ultra-efficient CMOS fiber-to-chip grating couplers". *2016 Optical Fiber Communications Conference and Exhibition (OFC)*. IEEE, 1–3 (cited on pp. 133, 136).

O'BRIEN, J. L., A. Furusawa, and J. Vučković (2009). "Photonic quantum technologies". *Nature Photonics* **3**.12, 687–695 (cited on p. 20).

PAESANI, S., M. Borghi, S. Signorini, A. Maïnos, L. Pavesi, and A. Laing (2020). "Near-ideal spontaneous photon sources in silicon quantum photonics". *Nature Communications* **11**.1, 1–6. DOI: https://doi.org/10.1038/s41467-020-16187-8 (cited on p. 103).

PAESANI, S. and B. J. Brown (2023). "High-Threshold Quantum Computing by Fusing One-Dimensional Cluster States". *Phys. Rev. Lett.* **131** (12), 120603. DOI: 10.1103/PhysRevLett.131.120603 (cited on p. 109).

PAPON, C., Y. Wang, R. Uppu, S. Scholz, A. D. Wieck, A. Ludwig, P. Lodahl, and L. Midolo (2022). *Independent operation of two waveguide-integrated single-photon sources*. DOI: https://doi.org/10.48550/arXiv.2210.09826. arXiv: 2210.09826 [quant-ph] (cited on p. 114).

PEDERSEN, F. T. (2020). "Deterministic Single and Multi-Photon Sources with Quantum dots in Planar Nanostructures". PhD thesis. University of Copenhagen (cited on p. 128).

PELUCCHI, E., G. Fagas, I. Aharonovich, D. Englund, E. Figueroa, Q. Gong, H. Hannes, J. Liu, C.-Y. Lu, N. Matsuda, et al. (2021). "The potential and global outlook of integrated photonics for quantum technologies". *Nat. Rev. Phys.* **4**, 194–208. DOI: 10.1038/s42254-021-00398-z (cited on p. 110).

PONT, M., G. Corrielli, A. Fyrillas, I. Agresti, G. Carvacho, N. Maring, P.-E. Emeriau, F. Ceccarelli, R. Albiero, P. H. Ferreira, et al. (2022). "High-fidelity generation of four-photon GHZ states on-chip". *arXiv preprint arXiv:2211.15626* (cited on p. 74).

PRESKILL, J. (2012). "Quantum computing and the entanglement frontier". *arXiv preprint arXiv:1203.5813* (cited on p. 109).

— (2018). "Quantum computing in the NISQ era and beyond". *Quantum* **2**, 79. DOI: https://doi.org/10.22331/q-2018-08-06-79 (cited on p. 109).

PUMA, E., R. Cheng, J. Holzgrafe, A. Shams-Ansari, R. Shankar, and M. Loncar (2022). "Mitigating anomalous sub-megahertz frequency response of electro-optic phase modulators in X-cut lithium niobate on insulator". *CLEO: Science and Innovations*. Optica Publishing Group, SF2O–1 (cited on pp. 107, 136).

QI, H., L. G. Helt, D. Su, Z. Vernon, and K. Brádler (2018). "Linear multiport photonic interferometers: loss analysis of temporally-encoded architectures". *arXiv preprint arXiv:1812.07015*. DOI: https://doi.org/10.48550/arXiv.1812.07015 (cited on pp. 50, 120).

QUANTUM, G. A., Collaborators*†, F. Arute, K. Arya, R. Babbush, D. Bacon, J. C. Bardin, R. Barends, S. Boixo, M. Broughton, B. B. Buckley, et al. (2020). "Hartree-Fock on a superconducting qubit quantum computer". *Science* **369**.6507, 1084–1089. DOI: DOI:10.1126/science.abb9811 (cited on p. 109).

RARITY, J., P. Tapster, E Jakeman, T Larchuk, R. Campos, M. Teich, and B. Saleh (1990). "Two-photon interference in a Mach-Zehnder interferometer". *Phys. Rev. Lett.* **65**.11, 1348. DOI: 10.1103/PhysRevLett.65.1348 (cited on p. 103).

RECK, M., A. Zeilinger, H. J. Bernstein, and P. Bertani (1994). "Experimental realization of any discrete unitary operator". *Physical review letters* **73**.1, 58 (cited on p. 71).

RENEMA, J., V. Shchesnovich, and R. Garcia-Patron (2018a). "Classical simulability of noisy boson sampling". *arXiv preprint arXiv:1809.01953* (cited on pp. 103, 110, 115).

RENEMA, J. J., A. Menssen, W. R. Clements, G. Triginer, W. S. Kolthammer, and I. A. Walmsley (2018b). "Efficient classical algorithm for boson sampling with partially distinguishable photons". *Physical review letters* **120**.22, 220502 (cited on p. 110).

RUDOLPH, T. (2017). "Why I am optimistic about the silicon-photonic route to quantum computing". *APL Photonics* **2**.3, 030901. DOI: https://doi.org/10.1063/1.4976737 (cited on p. 103).

SALEH, B. E. and M. C. Teich (2007). *Fundamentals of photonics*. John Wiley & Sons (cited on pp. 40, 92).

SALVESTRINI, J. P., L. Guilbert, M. Fontana, M. Abarkan, and S. Gille (2011). "Analysis and control of the DC drift in LiNbO 3 based Mach–Zehnder modulators". *Journal of lightwave technology* **29**.10, 1522–1534 (cited on p. 93).

SCHEEL, S. (2004). "Permanents in linear optical networks". *arXiv preprint quant-ph/0406127*. DOI: https://doi.org/10.48550/arXiv.quant-ph/0406127 (cited on p. 110).

SHOR, P. W. (1999). "Polynomial-time algorithms for prime factorization and discrete logarithms on a quantum computer". *SIAM review* **41**.2, 303–332 (cited on p. 1).

SPARROW, C., E. Martín-López, N. Maraviglia, A. Neville, C. Harrold, J. Carolan, Y. Joglekar, T. Hashimoto, N. Matsuda, J. O'Brien, D. Tew, and A. Laing (May 2018). "Simulating the vibrational quantum dynamics of molecules using photonics". *Nature* **557**. DOI: 10.1038/s41586-018-0152-9 (cited on p. 106).

SPRING, J. B., B. J. Metcalf, P. C. Humphreys, W. S. Kolthammer, X.-M. Jin, M. Barbieri, A. Datta, N. Thomas-Peter, N. K. Langford, D. Kundys, et al. (2013). "Boson sampling on a photonic chip". *Science* **339**.6121, 798–801 (cited on p. 110).

STOJANOVIĆ, V., R. J. Ram, M. Popović, S. Lin, S. Moazeni, M. Wade, C. Sun, L. Alloatti, A. Atabaki, F. Pavanello, et al. (2018). "Monolithic silicon-photonic platforms in state-of-the-art CMOS SOI processes". *Optics express* **26**.10, 13106–13121 (cited on p. 110).

SU, D., I. Dhand, L. G. Helt, Z. Vernon, and K. Brádler (2019). "Hybrid spatiotemporal architectures for universal linear optics". *Physical Review A* **99**.6, 062301 (cited on p. 71).

SUND, P. I., E. Lomonte, S. Paesani, Y. Wang, J. Carolan, N. Bart, A. D. Wieck, A. Ludwig, L. Midolo, W. H. Pernice, et al. (2023a). "High-speed thin-film lithium niobate quantum processor driven by a solid-state quantum emitter". *Science Advances* **9**.19, eadg7268 (cited on pp. 91–94, 98–100).

SUND, P. I., R. Uppu, S. Paesani, and P. Lodahl (2023b). "Hardware requirements for realizing a quantum advantage with deterministic single-photon sources". *arXiv preprint arXiv:2310.10185* (cited on pp. 50, 109).

TABALLIONE, C., M. C. Anguita, M. de Goede, P. Venderbosch, B. Kassenberg, H. Snijders, N. Kannan, W. L. Vleeshouwers, D. Smith, J. P. Epping, et al. (2023). "20-mode universal quantum photonic processor". *Quantum* **7**, 1071 (cited on pp. 127, 129, 131, 167).

TICHY, M. C., M. Tiersch, F. Mintert, and A. Buchleitner (2012). "Many-particle interference beyond many-boson and many-fermion statistics". *New Journal of Physics* **14**.9, 093015 (cited on p. 74).

TICHY, M. C., M. Tiersch, F. de Melo, F. Mintert, and A. Buchleitner (2010). "Zero-transmission law for multiport beam splitters". *Physical review letters* **104**.22, 220405 (cited on p. 74).

TIECKE, T., K. Nayak, J. D. Thompson, T Peyronel, N. P. de Leon, V Vuletić, and M. Lukin (2015). "Efficient fiber-optical interface for nanophotonic devices". *Optica* **2**.2, 70–75 (cited on pp. 133, 136).

TILLMANN, M., B. Dakić, R. Heilmann, S. Nolte, A. Szameit, and P. Walther (2013). "Experimental boson sampling". *Nature photonics* **7**.7, 540–544 (cited on p. 110).

TOMM, N., A. Javadi, N. O. Antoniadis, D. Najer, M. C. Löbl, A. R. Korsch, R. Schott, S. R. Valentin, A. D. Wieck, A. Ludwig, et al. (2021). "A bright and fast source of coherent single photons". *Nature Nanotechnology* **16**.4, 399–403. DOI: https://doi.org/10.1038/s41565-020-00831-x (cited on p. 110).

UPPU, R., L. Midolo, X. Zhou, J. Carolan, and P. Lodahl (2021). "Quantum-dot-based deterministic photon–emitter interfaces for scalable photonic quantum technology". *Nature Nanotechnology* **16**.12, 1308–1317. DOI: https://doi.org/10.1038/s41565-021-00965-6 (cited on pp. 110, 133, 137).

UPPU, R., F. T. Pedersen, Y. Wang, C. T. Olesen, C. Papon, X. Zhou, L. Midolo, S. Scholz, A. D. Wieck, A. Ludwig, et al. (2020). "Scalable integrated single-photon source". *Science advances* **6**.50, eabc8268 (cited on pp. 2, 18, 19, 103, 110, 114, 123, 128, 132, 135).

VALIANT, L. G. (1979). "The complexity of computing the permanent". *Theoretical computer science* **8**.2, 189–201 (cited on p. 110).

VARNAVA, M., D. E. Browne, and T. Rudolph (2008). "How Good Must Single Photon Sources and Detectors Be for Efficient Linear Optical Quantum Computation?" *Phys. Rev. Lett.* **100** (6), 060502. DOI: 10.1103/PhysRevLett.100.060502 (cited on p. 103).

VIGLIAR, C., S. Paesani, Y. Ding, J. C. Adcock, J. Wang, S. Morley-Short, D. Bacco, L. K. Oxenløwe, M. G. Thompson, J. G. Rarity, et al. (2021). "Error-protected qubits in a silicon photonic chip". *Nature Physics* **17**.10, 1137–1143 (cited on p. 86).

WANG, C., M. Zhang, X. Chen, M. Bertrand, A. Shams-Ansari, S. Chandrasekhar, P. Winzer, and M. Lončar (2018a). "Integrated lithium niobate electro-optic modulators operating at CMOS-compatible voltages". *Nature* **562**.7725, 101–104. DOI: https://doi.org/10.1038/s41586-018-0551-y (cited on pp. 92, 102).

WANG, C., M. Zhang, B. Stern, M. Lipson, and M. Lončar (2018b). "Nanophotonic lithium niobate electro-optic modulators". *Optics Express* **26**.2, 1547–1555 (cited on p. 102).

WANG, H., J. Qin, X. Ding, M.-C. Chen, S. Chen, X. You, Y.-M. He, X. Jiang, L. You, Z. Wang, C. Schneider, J. J. Renema, S. Höfling, C.-Y. Lu, and J.-W. Pan (2019). "Boson Sampling with 20 Input Photons and a 60-Mode Interferometer in a 10^{14}-Dimensional Hilbert Space". *Phys. Rev. Lett.* **123** (25), 250503. DOI: 10.1103/PhysRevLett.123.250503 (cited on pp. 106, 110, 111, 117, 119, 123, 127, 128, 131, 133, 135, 167).

WANG, J., F. Sciarrino, A. Laing, and M. G. Thompson (2020). "Integrated photonic quantum technologies". *Nature Photonics* **14**.5, 273–284 (cited on p. 20).

WANG, Y., C. F. Faurby, F. Ruf, P. I. Sund, K. Nielsen, N. Volet, M. J. Heck, N. Bart, A. D. Wieck, A. Ludwig, et al. (2023). "Deterministic photon source interfaced with a programmable silicon-nitride integrated circuit". *npj Quantum Information* **9**.1, 94 (cited on pp. 19, 21, 67, 74, 79, 81, 128).

ZAHIDY, M., M. T. Mikkelsen, R. Müller, B. Da Lio, M. Krehbiel, Y. Wang, M. Galili, S. Forchhammer, P. Lodahl, L. K. Oxenløwe, et al. (2023). "Quantum Key Distribution using Deterministic Single-Photon Sources over a Field-Installed Fibre Link". *arXiv preprint arXiv:2301.09399* (cited on p. 1).

ZHAI, L., G. N. Nguyen, C. Spinnler, J. Ritzmann, M. C. Löbl, A. D. Wieck, A. Ludwig, A. Javadi, and R. J. Warburton (2022). "Quantum interference of identical photons from remote GaAs quantum dots". *Nature Nanotechnology* **17**.8, 829–833 (cited on p. 114).

ZHANG, M., C. Wang, R. Cheng, A. Shams-Ansari, and M. Lončar (2017). "Monolithic ultra-high-Q lithium niobate microring resonator". *Optica* **4**.12, 1536–1537. DOI: https://doi.org/10.1364/OPTICA.4.001536 (cited on p. 92).

ZHONG, H.-S., H. Wang, Y.-H. Deng, M.-C. Chen, L.-C. Peng, Y.-H. Luo, J. Qin, D. Wu, X. Ding, Y. Hu, et al. (2020). "Quantum computational advantage using photons". *Science* **370**.6523, 1460–1463. DOI: https://doi.org/10.1126/science.abe8770 (cited on pp. 106, 110, 111, 114, 117, 119, 128, 132, 133).

ZHOU, X., I. Kulkova, T. Lund-Hansen, S. L. Hansen, P. Lodahl, and L. Midolo (2018). "High-efficiency shallow-etched grating on GaAs membranes for quantum photonic applications". *Applied Physics Letters* **113**.25. DOI: https://doi.org/10.1063/1.5055622 (cited on p. 140).

ZHOU, X., P. Lodahl, and L. Midolo (2022). "In-plane resonant excitation of quantum dots in a dual-mode photonic-crystal waveguide with high β-factor". *Quantum Science and Technology* **7**.2, 025023 (cited on pp. 17, 19).

ZHU, D., L. Shao, M. Yu, R. Cheng, B. Desiatov, C. Xin, Y. Hu, J. Holzgrafe, S. Ghosh, A. Shams-Ansari, et al. (2021). "Integrated photonics on thin-film lithium niobate". *Advances in Optics and Photonics* **13**.2, 242–352 (cited on p. 94).